Design of Spin-Crossover Complexes for Chiral and Soft Molecular Materials

Kay Eva Jane Burrows

Submitted in accordance with the requirements for the degree of

Doctor of Philosophy

The University of Leeds

School of Chemistry

August 2019

The candidate confirms that the work submitted is his/her own, except where work which has formed part of jointly-authored publications has been included. The contribution of the candidate and the other authors to this work has been explicitly indicated below. The candidate confirms that appropriate credit has been given within the thesis where reference has been made to the work of others.

Chapter 2 includes work from

Kay E. Burrows, Sarah E. McGrath, Rafal Kulmaczewski, Oscar Cespedes, Simon A. Barrett and Malcolm A. Halcrow, Spin States of Homochiral and Heterochiral Isomers of $[Fe(PyBox)_2]^{2+}$ Derivatives, **2017**, *Chem. Eur. J.*, 23, 9067-9075.

Chapter 3 includes work from

Kay E. Burrows; Rafal Kulmaczewski, Oscar Cespedes, Simon A Barrett and Malcolm A. Halcrow, The Speciation of Homochiral and Heterochiral Diastereomers of Homoleptic Cobalt(II) and Zinc(II) PyBox Complexes, **2018**, *Polyhedron*, 149, 134-141.

In the case of Burrows *et al.* Spin States of Homochiral and Heterochiral Isomers of $[Fe(PyBox)_2]^{2+}$ Derivatives, **2017**, *Chem. Eur. J.*, 23, 9067-9075, all of the synthesis and analysis of the complexes was completed by myself. S. McGrath did a preliminary synthesis of two complexes for her MChem project. R. Kulmaczewski obtained SQUID measurements and O. Cespedes maintained the instrument. S. Barrett collected variable temperature Evans Method NMR spectroscopy data. M. Halcrow prepared the final manuscript for publication and is the PI.

In the case of Burrows *et al.* The Speciation of Homochiral and Heterochiral Diastereomers of Homoleptic Cobalt(II) and Zinc(II) PyBox Complexes, **2018**, *Polyhedron*, 149, 134-141, all of the synthesis and analysis of the complexes and the first draft of the manuscript was completed by myself. S. McGrath did a preliminary synthesis of two complexes for her MChem project. R. Kulmaczewski obtained SQUID measurements and O. Cespedes maintained the instrument. S. Barrett collected variable temperature Evans Method NMR spectroscopy data. M. Halcrow prepared the final manuscript for publication and is the PI.

“Without deviation from the norm,

progress is not possible”

Frank Zappa

Acknowledgements

There have been one or two moments over the years when it would have been farfetched to suggest that that I would end up being in the position of writing a PhD thesis in chemistry. As such, I believe it is of the utmost importance to express my gratitude to the wonderful people who have helped me along the way.

First and foremost, Professor Malcolm Halcrow has been a truly fantastic supervisor, ever present with wisdom, guidance and patience. I couldn't have asked for a better PhD supervisor and I'm grateful for the support and opportunities that I've had whilst working in his research group.

I am also very grateful to Professor Patrick McGowan for his supervision, particularly during the polymers project. Thank you for all of the ideas, support and incredible vegetarian cooking skills!

Much of the work in this thesis, particularly the VT Evans method and NOESY NMR could not have been completed without the NMR wizardry of Dr Mark Howard, and his predecessor Simon Barrett. I'm also grateful to Dr Raf Kulmaczewski, Namrah Shahid and Izar Capel Berdiell for running my SQUID samples and to Dr Chris Pask for 3 years of crystallography magic! I'd also like to thank Dr Stuart Warriner for direct injection high resolution mass spectrometry and Stephen Boyer at London Metropolitan University for elemental microanalysis.

Thank you to Dr Nick Warren in the School of Chemical and Process Engineering for his advice on the polymers project, as well as Andy Leeson for tips for successful synthesis and Sam Parkinson for running my GPC samples. I'm also grateful to Saskia Boardman here in Chemistry for her general advice on working with polymers.

This thesis would almost certainly never have made it to fruition without the friendship, support and kindness of Dr Chris Pask, who truly lives up to his reputation as the nicest man in chemistry! I cannot thank you enough for the copious supplies of tea, cake and Chocolate Oranges, the ranting opportunities and the discussions about just how many books it is appropriate to buy - all of which have truly kept me sane over the last few years. I am also indebted to your patience for my endless questions about the finer points of modelling solvent disorder, setting up solvent stills and dealing with mercury!

To my lab comrades, past and present – Frances, who has solidly been my person throughout everything the last few years have thrown at me, including the occurrence of bizarre chemistry phenomena, love for The Guilty Feminist and, of course, eating lunch at 12 every day! Thank you for being an amazing friend – we made it!! Laura, for our C&B sessions, ability to eat our own body weight in biscuits

and for being a wonderful human being. Jonny, you're probably the most dedicated chemist I've ever met! I miss our gym sessions, love of trips to Diamond and shared opinion on the wonder that is Leicester Forest East services. Heba, habibty, I miss you and our frequent Wagamama trips every single day. Namrah, you're always so optimistic about everything and never let my cynicism get in the way of that. I'll really miss our trips to get coffee and chatting about absolutely everything, including the finer points of PyBox! Abi, I'm still not sure I'm over you abandoning me in the lab! Thank you for your fume hood quotes and amazing ability to always cheer me up. Ravi, my token organic friend; your love for pKa is second to none and you've been a true friend, despite your insistence on driving a BMW. Shout out to the Bradford massive! Flora, the font of so much knowledge about everything. I miss you loads and can't thank you enough for your help. Finally Em, my mini-me! Thank you for cheering me up every day during my final year.

Last, but not least, shout outs must go to all the other members of Team Inorganic; the Halcrow, McGowan, Hardie and Willans group members, past and present. There are too many to name, but you've made it a truly interesting place to work for the last few years, and there's never been a dull moment! I'm also eternally grateful to the 'True Lunch Crew' – Kev, Chris, Emma, Becky and Tom. It's truly been a pleasure to get out of the office for lunch with you all for the last few years! It is also important to recognise the series of Very Important Meetings I've shared with Chris and Mark; a plethora of gin and tonics, opportunities to rant about the lunacy of human condition and the search for the ultimate guitar setup have made my final year much more tolerable!

Outside and away from the University, there is a long, long list of people who have made life more exciting and more beautiful. To Karen, for all the phone calls and rants, being able to have conversations through glances and sign language, going 'out out', road trips, dress swapping, inability to manage our faces and for an entire lifetime of friendship. You really are three days wiser and I'm truly proud of you and love you to pieces. Perm, Greg, Amy, Trebor, Ed and Georgina, for Christmas Eve shenanigans, trips to the zoo and laughing at chemistry mishaps. Sam G, for our random drives to find the Men in Black, discussions on the finer points of laminating ham and always having a house I can drop into. We will win the lottery one day! Sam H for catch up chats about how we're definitely not grown ups and comparing PhD life and Mike H for his eternal optimism about life, music and London, even if the true lyrics to the song are '…floating out to sea'. Otavio, for our deep, deep discussions on superhero films and trips to The Eldon (where you always have gammon!) and the rest of the Medieval History crew for tolerating the token scientist among you. And finally to Sergey, Natasha, Peter and Simon for trusting me in their

research lab all those years ago as an undergrad and for kickstarting my love of research.

And finally, to my family, whose unwavering belief in me, often despite the odds, has meant more to me than I can possibly coherently express. Mum, for our culture days turned holidays, mutual appreciation of a fine G&T and for your advice, which is always is second to none - you really were always right about everything. Columns and arches! Dad, for a lifetime of 'the long version', a true appreciation of the extended back catalogue of Uncle Frank and Uncle Bob and for always, always having my back. And to Mike (Dr Burrows the First), who is the best sibling, friend and thesis proof-reader I could possibly ask for. I am so proud of you! Cheers to the democratisation of pub seating arrangements, Christmases ruled with an iron fist with Lenin on the tree and wandering the hills at night with sticks, looking for wildlife.

And last, but absolutely not least, to my grandma, who is wise, welcoming and wonderful and has given me so much support throughout the (many!) years of my education. Grandad always said I would get there, and here I am!! I could not have done this PhD without you, and therefore it only seems fit to dedicate my thesis to you.

Abstract

The focus of this thesis is the design of spin-crossover complexes for inclusion into chiral or soft materials. A variety of ligand and complex architectures have been investigated and a method for functionalising polymers with such complexes has been explored.

Chapter 2 discusses the spin states of a family of homochiral and heterochiral iron(II) PyBox complexes in the solid state and in solution. Solution phase results show the first example of chiral discrimination between spin states, which is a promising development towards the incorporation of such complexes in functional materials.

Chapter 3 provides a computational approach to these iron(II) PyBox complexes and reinforces the experimental data presented in Chapter 2. Further insights into the contribution of the PyBox ligands are discussed and predictions on the spin states of a family of analogous iron(II) thio-PyBox complexes are made.

Chapter 4 is an investigation into cobalt(II) and zinc(II) PyBox complexes and looks at the speciation of these in solution and compares these trends to those seen in their iron(II) counterparts. In addition, NOESY NMR studies of the zinc(II) complexes and the magnetic behaviour of the cobalt(II) complexes are reviewed.

Chapter 5 explores the structure and spin-crossover behaviour of a family of iron(II) tripodal pseudoclathrochelate complexes. During the synthesis, a pair of multimetallic clusters were serendipitously discovered, and these are also reviewed.

Chapter 6 is an exploration into the incorporation of a functionalised bpp ligand into polymers. The RAFT polymerisation and copolymerisation of acrylates and this ligand derivative are presented.

Chapter 7 details the synthetic procedures and analysis for each compound discussed in this thesis.

Table of Contents

List of Figures

List of Tables

Abbreviations

1-bpp	2,6-*bis*[pyrazol-1-yl]pyridine
2,5-bpp	2,5-bis (pyrid-4-yl)pyridine
3-bpp	2,6-*bis*[1H-pyrazol-3-yl]pyridine
4-4'-bipy	4,4'-bipyridine
ACVA	4,4'-azobis(4-cyanovaleric acid)
AIBN	azobisisobutyronitrile
Alatrz	4H-1,2,4-triazol-4-yl-propionate (β-amino acid ester 1,2,4-triazole)
azpy	4,4'-azopyridine
bpt	2,4-di(pyrazol-1-yl)-1,3,5-triazine
bpym	2,6-di(pyrazol-1-yl)pyrimidine
bpyz	2,6-di(pyrazol-1-yl)pyrazine
CFSE	crystal field stabilisation energy
C_n-trenH	tris[3-aza-4-((5-C_n)(6-H)(2-pyridyl))but-3-enyl]amine
CSIRO	Commonwealth Scientific and Industrial Research Organisation
CTA	charge transfer agent
DCM	dichloromethane
DFT	Density Functional Theory
DHP	dihexadecyl phosphate
DMF	dimethylformamide
DMSO	dimethylsulfoxide
DOSY	Diffusion-ordered spectroscopy
EXAFS	Extended X-ray absorption fine structure
Hmptpy	3-methyl-2-(5-(4-(pyridin-4-yl)phenyl)-4H-1,2,4-triazol-3-yl)-pyridine
HS	high-spin

Htrz	1,2,4-triazole
hyetrz	4-(2’-hydroxy-ethyl)-1,2,4-triazole
LB	Langmuir-Blodgett
LC	liquid crystal
LS	low-spin
Mebip	2,6-bis(1’-methylbenzimidazolyl)-pyridine
MeCN	acetonitrile
MLCT	metal to ligand charge transfer
MOF	metal-organic framework
PBA	poly (butyl acrylate)
PBzMA	poly (benzyl methacrylate)
PD	polydispersity
phen	phenanthroline
phtptrz	4-(3’-N-phtalimido-propyl)-1,2,4-triazole
ptol	para-tolylsulfonate
py	pyridine
PyBox	bis(oxazolinyl) pyridine
pz	pyrazine
RAFT	reversible addition-fragmentation chain transfer
SCO	spin-crossover
Terpy	terpyridine
TINM	tetrakis(isonicotinoxymethyl)methane)
Tpc-OMe	tris(2-pyridyl)methoxymethane
trz	1,2,4-triazolato

Chapter 1 - An Introduction to Spin-Crossover

1.1 Spin-crossover

An interesting property of d^4-d^7 transition metal complexes of octahedral geometry is that they can exist in either a low-spin (LS) or high-spin (HS) state, depending on the energy difference between the d orbitals. The low-spin state is obtained when the pairing energy between the electrons is less than that of the ligand field strength (Δ_o) leading to the minimum number of unpaired electrons. Conversely, the high-spin state features the maximum number of unpaired electrons as the ligand field strength is greater than the electron pairing energy.

Whether the high-spin or the low-spin form is adopted is a property of the metal centre and the ligands. Ligands which bond primarily through the donation of a lone pair of electrons, such as halides, H_2O and NH_3, act as σ bond donors to the metal centre which gives a small splitting between the t_{2g} and e_g d orbitals. This small splitting means that the pairing energy may be greater than the ligand field strength, resulting in high-spin complexes as it is more energetically favourable for electrons to occupy the e_g orbital than to pair with another electron. Conversely, ligands such as CO and CN^- which use π orbitals to form strong bonds with the t_{2g} metal orbitals often form low-spin complexes. This is because the strong π bonds lower the energy of the t_{2g} orbitals which increases the ligand field strength. Thus it becomes more favourable for electrons to pair in the t_{2g} orbitals than to occupy the e_g levels. Figure 1.1 shows a schematic representation of the high-spin and low-spin forms of iron(II) d^6 complexes.

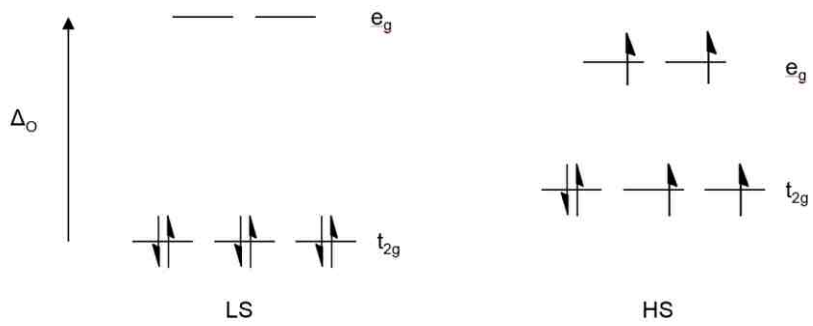

Figure 1.1 - Schematic representation of the electron configuration seen in the low-spin and high-spin forms of iron(II) complexes. Δo is the ligand field strength. P is the pairing energy.

When ligands which strongly favour neither low-spin nor high-spin states are coordinated to metals, the resulting complexes can have a small energy difference between the low-spin and high-spin forms. In these complexes, a physical or chemical stimulus can trigger a transition between the high-spin and low-spin states; this is known as spin-crossover (SCO). SCO can be considered a balance between the low-spin state, which is enthalpically favoured due to stronger metal-ligand bonds and greater crystal field stabilisation energy (CFSE), and the high-spin form which has more favourable entropy due to the electronic and vibrational contributions.[1] At low temperatures, the low-spin state is favoured. However as the temperature increases the high-spin form stabilises, leading to the high-spin state becoming the thermodynamic ground state at higher temperatures.[2] $T_{1/2}$ is an important measure of SCO behaviour and is defined as the temperature at which half of the sites in a sample have made the transition.

Iron(II) complexes have a d^6 electron configuration. In the low-spin form the electrons occupy the lower energy orbitals (t_{2g}^6) whereas the high-spin form arises from electrons in a combination of both sets of orbitals (t_{2g}^4 e_g^2). Both low and high-spin configurations of iron(II) complexes are shown in Figure 1.1. The properties of iron(II) make its SCO behaviour particularly interesting and it is the most commonly studied metal ion in this context, usually in a complex with six nitrogen donors.[3] Iron(II) complexes exhibit a dramatic change in magnetic behaviour when a spin-crossover transition occurs. Low-spin iron(II) complexes are diamagnetic whereas high-spin complexes are paramagnetic; this leads to a large change in magnetic response which is easy to detect and characterise, often using a magnetometer although other methods can be used.[1] Iron(II) complexes undergo a strong colour change when a spin-transition takes place; low-spin complexes are strongly coloured yet those in the high-spin state are pale or colourless. In addition, the low-spin state features Fe-N bonds which are shorter than Fe-N bonds in the high-spin state (~1.8-2.0 Å and ~2.0-2.2 Å respectively).[1] Furthermore, iron(II) compounds are the most useful for spin-trapping experiments which entail trapping a material in its excited form at a low temperature; this is known as Light-Induced Excited Spin-State Trapping (LIESST) and is covered in more detail later in this section. The presence of all of these changes makes it easy to detect SCO.

SCO in solid samples can occur in various forms which can be plotted on spin transition curves. These are obtained by plotting the high-spin fraction (γ_{HS}) versus the temperature onto a graph. The degree of cooperativity between sites is crucial in SCO. Cooperativity can be defined as the extent to which the effects of spin transition, especially the changes in metal-ligand distances, are propagated through the solid.[4] Cooperativity is a result of the intermolecular packing of a solid and thus different crystal polymorphs of the same compound can show different SCO types.[3] Three synthetic strategies have been developed which increase cooperativity; these are the inclusion of π-stacking systems, the incorporation of a hydrogen bond network and the coordination of bridging ligands.[5]

The different types of SCO are shown in Figure 1.2. Gradual SCO (Figure 1.2a) is seen when cooperativity is weak and is the most common type. It occurs over a range of tens or hundreds of degrees and is consistent with a Boltzmann distribution.[1] Gradual SCO also appears in solution, since the complex molecules are well-separated and there is almost no cooperativity.[5] Abrupt SCO (Figure 1.2b) takes place over a few degrees and indicates strong cooperativity. Figure 1.2c shows an SCO hysteresis loop. Hysteresis occurs when the LS-HS and HS-LS transitions take place at different temperatures.[6] The $T_{1/2}$ on the cooling cycle ($T_{1/2}\downarrow$) is different to the $T_{1/2}$ on the warming cycle ($T_{1/2}\uparrow$) and this loop confers bistability on the compound. The spin-state depends on the thermal history of the compound; if the sample enters the loop at a high temperature it remains in the high-spin state whereas if it enters the loop at a low temperature it retains the low-spin state.[1] As a result, SCO compounds which exhibit hysteresis can be considered to have a memory function which mimics binary code. The memory is activated by returning the compound to room temperature, after heating or cooling, and the last spin state will be 'remembered'. The potential applications of hysteresis in storage, memory and display devices are considerable. Figure 1.2d shows multi-step SCO which suggests a step towards a ternary (or greater) switch if it could be harnessed.[1] Gradual and incomplete SCO, as seen in Figure 1.2e, is of less interest than other forms.

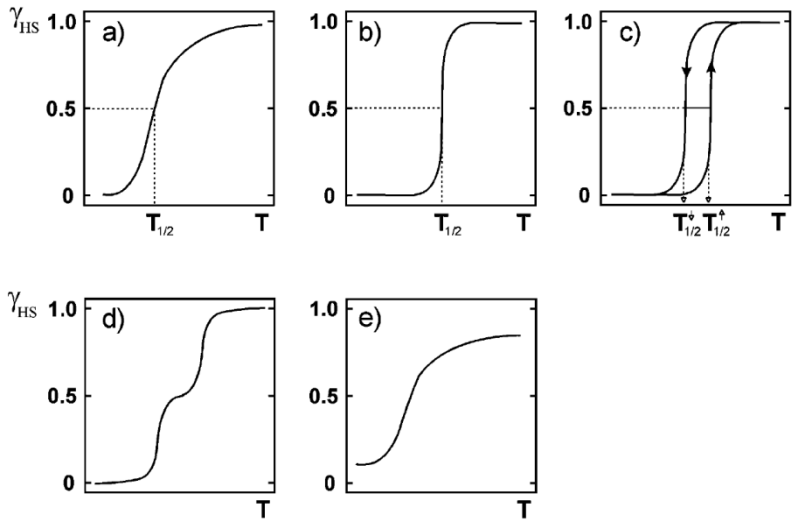

Figure 1.2 - Schematic representations of different types of SCO where γHS is the fraction of the sample that is high-spin and T is temperature. a) gradual SCO; b) abrupt SCO; c) SCO with hysteresis d) two step SCO; e) incomplete SCO.[4]

There are several stimuli which can trigger SCO; these can be physical (thermal, pressure, light) and chemical (ligand substitution and anion or solvate presence) in nature.

Spin crossover can be triggered by changes in temperature. An increase in temperature favours the high-spin state whereas decreases in temperature favour the low-spin state. For thermal SCO to occur, the difference in Gibb's free energy between the two spin-states must be on the order of thermal energy, k_BT. Thermal SCO behaviour can be seen when molecular changes, such as alterations in magnetic behaviour and colour, occur. These changes can be monitored by magnetic susceptibility measurements, X-ray crystallography, optical and vibrational spectroscopy, Mössbauer spectroscopy and heat capacity measurements.[5]

The application of pressure can cause SCO because it shortens the metal-ligand bond distance which increases the ligand field strength at the metal atom. This favours the low-spin state and increases the temperature at which a spin transition will occur. In addition, an increase in pressure can cause changes to thermal SCO behaviour. It can induce a spin transition in a high-spin system in which a thermal transition does not

occur, change the width of a hysteresis loop and 'even out' a transition, giving increasing amounts of residual low and high-spin species.[4]

LIESST is usually achieved by irradiating a solid, low-spin iron(II) complex sample with a green laser at a temperature around 10 K.[2] Irreversible SCO from low-spin to high-spin is observed. The metastable high-spin form exhibits reasonably long lifetimes, sometimes in the order of days, when the temperature remains below 50 K.[7] The LIESST phenomenon could be used as an optical switch system with applications in information storage and optical data processing. A reverse-LIESST process is also possible; light of a longer wavelength can induce a transition from the metastable high-spin state back to the low-spin form.[5]

Substitution of different ligands onto the iron(II) centre can alter the spin-state of the complex. One example which highlights this is $[Fe(py)_4(NCS)_2]$, which is high-spin at room temperature and does not show thermal SCO. When two of the pyridine ligands are substituted by phenanthroline, to give $[Fe(phen)(py)(NCS)_2]$, the spin-state behaviour changes and the complex undergoes thermal SCO with a $T_{1/2}$ of 106 K. When another phenanthroline is substituted into the complex, giving $[Fe(phen)_2(NCS)_2]$, a thermal SCO is also seen with a higher $T_{1/2}$ of 176 K. One final substitution of phenanthroline in place of both NCS ligands, forming $[Fe(phen)_3]^{2+}$, produces a low-spin complex.[4]

A second chemical stimulus which affects the spin-state is the type of solvent present or the anion associated with a cationic complex, both of which can affect the temperature at which SCO occurs and the type of transition seen. Anions, such as halides, can have a significant influence on the SCO behaviour of a complex. For example, for the series of complexes $[Fe(2\text{-pic})_3]X_2 \cdot EtOH$ (where 2-pic = 2-picolylamine), the extent of completion and gradient of the spin-transition curve increases in the order iodide<bromide<chloride.[4] Within the same $[Fe(2\text{-pic})_3]X_2 \cdot$solvent system, different solvent molecules (ethanol, methanol and water) influence the temperature of the spin transition. In these solvates, SCO is observed but there is an increasing stabilisation of the low-spin state.[4] However it is important to consider that the effect of anions and solvent molecules is not consistent across all SCO systems.

1.2 The relevance of incorporating spin-crossover properties into functional materials

The area of spin-crossover has developed significantly since its inception. It was initially considered an interesting area of coordination chemistry, but ongoing research has shown that it is of interest to multiple fields, including chemistry, physics, materials science, biochemistry and spectroscopy. Research has diversified from the search for fundamental information about the behaviour of SCO compounds and is now extended to include different types of materials with a broad range of potential applications.[4]

A fundamental concept that underpins the design and function of new molecular materials is bistability.[8] To be successfully harnessed into materials this bistability must be accompanied by an observable response, such as a change in colour or magnetism, which makes materials based on SCO ideal candidates.

Since the origins of the spin-crossover phenomenon, solid-state and solution examples have been actively researched. More recently, research has begun to include the incorporation of spin-crossover properties into other materials, such as polymers, liquid crystals, gels and thin films. This research seeks to design new materials with additional properties and to explore the possibility that bulk SCO properties could be transferred into such materials.[9] The potential uses of such research are numerous and include materials with switchable states, memory function [10], sensors [11, 12] and optical devices.[9] Current research into a range of materials, including polymers, liquid crystals, gels and thin films, which incorporate spin-crossover behaviour, are reviewed in the remainder of this section.

1.3 Spin-crossover in polymers

1.3.1 Background

A polymer is made up of many repeating units, known as monomers. Organic polymers are typically composed of long hydrocarbon chains which provide the material with its interesting and unique properties. The development of synthetic organic polymers revolutionised the materials available in the 20th century; thermoplastics and elastomers were of particular significance.[13] The simplest definition of an inorganic polymer is one which has repeating inorganic monomeric units, although there is much debate about how to define the term more precisely.[14] The first polymer with a metal centre (also known as metallopolymers), was reported in 1955,[13] however polymers with a high molecular weight and good solubility were difficult to make. It was not until the 1990s that new synthetic techniques enabled a rapid growth in the numbers of metal-based polymers reported.[13]

Metal-based polymers can exist in different structural formations based on the location of the metal atom which can be present on either the main chain or the side chain as shown in Figure 1.3. At present, there are no SCO polymers which have the metal centre on the side chain. The bonds that link the metal centres are also key; covalent bonds form linkages that are effectively irreversible whilst non-covalent interactions lead to reversible, 'dynamic' binding.[13]

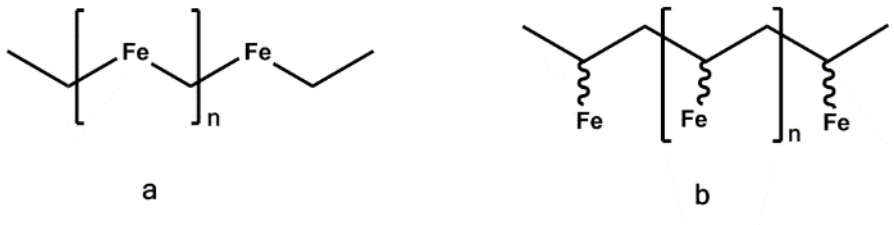

Figure 1.3 - Schematic representation of a main chain and b side chain iron metallopolymers.

Polymers can also be classified by dimensionality. A polymer with a linear chain can be classed as a one-dimensional (1D) polymer, although there may be twists in the

chain. Two-dimensional (2D) polymers have a sheet structure, where parallel layers 'sit' above and below each other. Three-dimensional (3D) polymers have bonding which occurs in three dimensions, giving 3D structures.[14]

Metal-based polymers have become an important class of materials with many practical uses as well as being of fundamental interest. They have numerous applications including conductive, semiconductive, optically active and stimuli-responsive materials, thin films, biometallopolymers and nanomaterials.[13]

The use of polymers to encapsulate a separate cargo is common in a variety of applications which include biomedical/biological uses,[15, 16] heterogeneous catalysis[17] and delivery of active cosmetic ingredients.[18] Inorganic nanoparticles can be encapsulated inside a polymeric matrix, a technique which has given novel materials with interesting properties, such as fluorescence and superparamagnetism.[15] Heterogeneous catalysis can be activated for organic reactions that would ordinarily be catalysed by homogeneous catalysis, by enclosing metallic nanoparticles inside a polymer.[17] The delivery of active cosmetics ingredients, which requires both a safe and non-toxic method of reaching the target and removal by normal metabolic pathways, can be achieved when the ingredients are enclosed in a polymer.[18]

This short, yet varied list highlights the real-world potential for novel materials which can encapsulate and release a molecular cargo. Polymers which incorporate a SCO centre would achieve a combination of the functionality of polymers and the properties of the iron(II) centre, such as paramagnetism and a colour change.

1.3.2 Spin-crossover in polymers

1.3.2.1 1,2,4-triazole-based polymers

One-dimensional spin-crossover polymers based on 1,2,4-triazoles are of much interest as they are easy to prepare, chemically stable and easy to process. They tend to display abrupt thermal SCO and have wide hysteresis loops at ambient temperatures.[10] The use of triazoles in SCO metallopolymers has led to the design of

optical device prototypes, thin films, liquid crystals, supramolecular gels and contrast agents for Magnetic Resonance Imaging.[19]

The first 1,2,4-triazole-based SCO polymer with the general formula $[Fe(Htrz)_2(trz)](anion)$ (where Htrz is 1,2,4-triazole and trz is 1,2,4-triazolato) was reported by Haasnoot *et al.* in 1977.[20] The possibilities for modification of the triazole at the N4 position makes it possible to synthesise a family of compounds with the same core structure. This chemical flexibility makes it possible to tune the SCO temperature and cooperativity of each compound. The structure is a linear chain where the iron atoms are linked by three N1,N2 bridges (Figure 1.4). This bridging system is rigid and the polymer therefore exhibits strong cooperative behaviour as a result of effective propagation of short range elastic interactions between neighbouring Fe(II) ions.[10] Abrupt SCO and thermal hysteresis with a loop of about 10 K are seen. EXAFS and powder diffraction studies confirmed that the rigidity of the chain is preserved in both the low-spin and high-spin state.[4] A correlation between the SCO temperature and the radii of the anion has been observed in some triazole based systems. For the complex $[Fe(hyetrz)_2(trz)](anion)_2$ (where hyetrz is 4-(2'-hydroxy-ethyl)-1,2,4-triazole), when the anion size is increased, the temperature at which SCO occurs decreases, which stabilises the high-spin state. The use of different solvents can stabilise the low-spin state.[4] Triazole systems exhibit thermochromic behaviour; low-spin systems are purple and high-spin systems are white.[19] This gives an observable response that contributes to the successful bistable systems of these types of polymers.

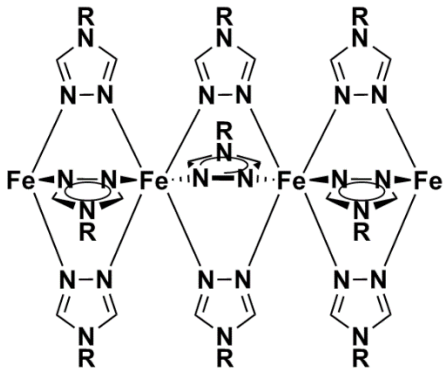

Figure 1.4 - The linear 1D structure of a 1,2,4-triazole based polymer.

Although some triazole systems show abrupt SCO, other types of SCO have been reported. In 2015, Dirtu *et al.* reported a 1D 1,2,4-triazole polymer, $[Fe(bAlatrz)_3](BF_4)_2 \cdot 2H_2O$, which exhibits an abrupt two-step SCO with hysteresis.[21] The ligand used is 4H-1,2,4-triazol-4-yl-propionate; a 1,2,4-triazole with a β-amino acid ester substituent at the N4 position. The hysteresis loop occurs at $T_{1/2}\downarrow$ = 230 K and $T_{1/2}\uparrow$ = 235 K for step 1 and at $T_{1/2}\downarrow$ = 172 K and $T_{1/2}\uparrow$ = 188 K for step 2. However when the complex is dehydrated, one-step SCO is observed with $T_{1/2}\downarrow$ = 199 K and $T_{1/2}\uparrow$ = 202 K. It is suggested that the reason for this difference is due to the lack of hydrogen bonding network from non-coordinated H_2O present in the latter complex. The polymer also exhibits thermochromism, meaning this material has potential as a sensor which can be used to detect two temperature thresholds.

The family of $[Fe(phtptrz)_3]$ complexes exhibit a gradual and incomplete SCO profile.[22] The phtptrz ligand (Figure 1.5) has a bulky substituent group which results in a loss of cooperativity. There is some evidence to suggest that the cooperativity of SCO in triazole systems is dependent on the substituent that is attached to the N4 position. The cooperative behaviour will decrease when this substituent is a bulky or long alkyl group.[10] However, it is suggested that the aromatic group participates in π-π stacking interactions and that the carbonyl group forms hydrogen bonding networks which promote the weak cooperativity that is seen and which gives the complex its gradual and incomplete SCO behaviour.[22]

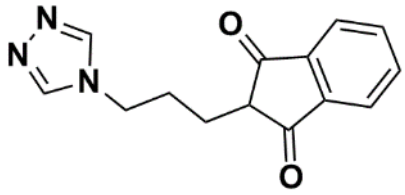

Figure 1.5 - The 4-(3'-N-phtalimido-propyl)-1,2,4-triazole (phtptrz) ligand.

A triazole-based polymer $[Fe(A\text{-}Trz)_3SO_4]$, where A-Trz = 4-amino-1,2,4-triazole), has recently been combined with an organosilica-reinforced nanocomposite gel. This material exhibits similar solid state SCO properties to the polymer itself, but has been

shown to be more stable to time and temperature cycling experiments. This combination shows the potential of such materials to be used in functional devices.[23]

1.3.2.2 Pyridine-based polymers

Spin-crossover polymers with pyridine ligands have been developed. They are typically of the formula $[FeL_2(NCS)_2]\cdot nSolv$, where L is a pyridine-based ligand. A common feature of these polymers is that they exhibit complete and relatively gradual SCO with T_{SCO} typically of 176-220 K.[10] The two-dimensonal framework of these polymers is defined by the location of the $[FeN_6]$ pseudo-octahedral sites which make a square or rhombus-shaped grid structure. The layers are alternated so that the iron atom of one layer is vertically above the centre of the square or rhombus formed by the iron atoms of the layers above and below. A schematic representation of this structure is shown in Figure 1.6. Ligand size and crystal packing efficiency affect the stacking of the layers.[24]

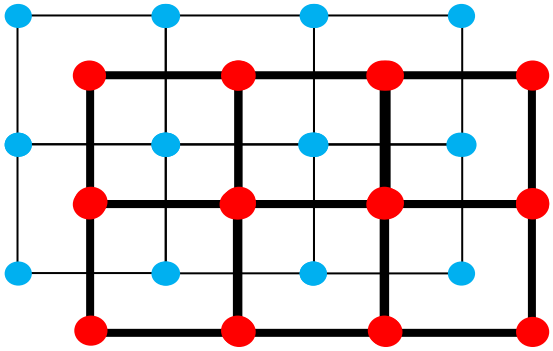

Figure 1.6 - Schematic diagram of the lattice structure of the iron atoms in these 2D polymers. The iron atoms of the bottom layer are shown in blue and the iron atoms of the top layer are shown in red. The squares are included for clarity within this diagram.

Two prominent families of 2D and 3D pyridine-based SCO polymers are the Hofmann-type and Spin-Crossover Framework (SCOF) systems. The structures of the monomeric units which combine to make the polymers are shown in Figure 1.7.

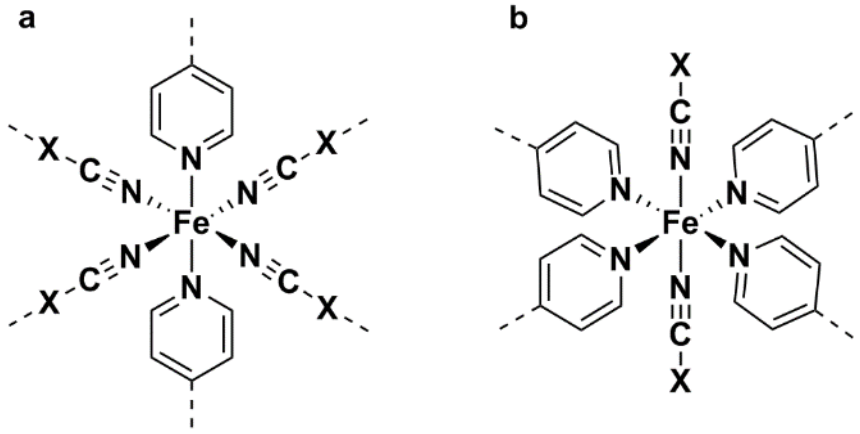

Figure 1.7 - The typical coordination frameworks for a) Hofmann-type monomer units where X = S, Se or BH_3 and b) SCOF monomer units where X = Ni, Pt, Pd, Au or Ag.

Hofmann-type polymers contain distorted octahedral iron(II) centres coordinated to parallel metallocyanate 2D layers and axially coordinated N-donating aromatic rings. This metallocyanate layer provides the framework for the long-range interactions that provide these polymers with cooperativity and hysteresis. The Hofmann family of polymers often exhibit room temperature SCO and are considered more structurally robust and have greater SCO communication potential. This cooperativity is a result of the short, rigid framework provided by the metallocyanate layer, whilst the space between layers provides the opportunity for the tuning of SCO behaviour.[25]

SCOF polymers contain iron(II) octahedral metal centres which are axially coordinated by N-donor NCX ligands and equatorially by bridging aromatic N-donor ligands. The linear linking ligands mean that the material is composed of square shapes in a 2D structure. Depending on the ligand size and flexibility, pores can be seen in these materials which can accommodate guest molecules. A number of porous scaffolds have been produced and the role of guest molecules can be easily assessed as altering the guest molecules present in these frameworks is relatively simple.[25] There are examples of 2D SCO frameworks[26] and molecular sensing[27] materials in SCOF materials.

In 2002, Kepert *et al.* reported a SCOF which displays tuneable SCO behaviour which is dependent on the solvent molecule present in the guest site of the polymer.[27]

The structure $[Fe(azpy)_2(NCS)_2]\cdot 1/2(guest)$ (azpy is 4,4'-azopyridine) displays one-step half SCO when the guest site is occupied by ethanol whereas when the guest solvent is 1-propanol, two-step SCO is seen. Similarly, Li *et al.* made a Hofmann-type polymer, $[Fe(2,5\text{-bpp})(Au(CN)_2)_2]\cdot x$Solvent (bpp is 2,5-bis(pyrid-4-yl)pyridine) which exhibits a similar solvent dependent SCO.[28] When there is no solvent, the polymer exhibits abrupt, two-step SCO with a hysteresis loop. The structure of this polymer contains a one-dimensional channel which a solvent molecule can occupy. The uncoordinated pyridyl group of the ligand is accessible to the solvent which sits in the channel and this mediates interactions which alter the SCO behaviour. When protic solvents (such as ethanol and isobutanol) occupy the solvent position, complete and abrupt SCO with hysteresis and higher temperatures are seen. This is a result of the hydrogen bond interactions between the nitrogen of the pyridyl group in the ligand and the OH group of the solvent which improve cooperativity. In the case of aprotic solvents in this position there is little cooperativity, due to a lack of hydrogen bonding, and a gradual half-spin SCO with lower critical temperatures is seen. This SCO behaviour can be seen in Figure 1.8. The presence of this solvent dependent SCO in different polymers shows that the chemically stimulated SCO which occurs in non-polymeric SCO compounds, such as those reported by Gütlich *et al.*[4], is also seen in polymeric SCO materials.

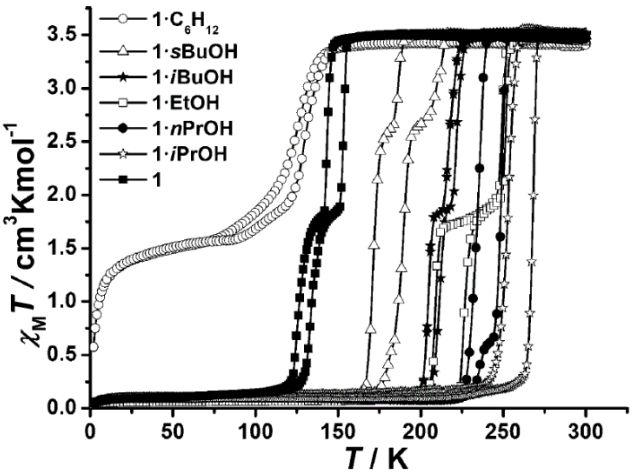

Figure 1.8 - Plots of variable-temperature $\chi_M T$ for complexes loaded with different solvents.[28]

Recently, a polymer composed of $[Fe(II)[Hg(II)(SCN)_3]_2(\mu\text{-}4,4'\text{-bipy})_2]_n$, (where 4-4'-bipy = 4,4'-bipyridine) was shown to have six distinct phases over a range of temperatures. The material is made up of linear $[Fe(\mu\text{-}4,4'\text{-bipy})_2]_n^{2n+}$ chains linked by $[Hg(SCN)_3]_2(\mu\text{-}4,4'\text{-bipy})_2]^{2n-}$ anionic dimers. The polymer has four different magnetic states which are a result of different fractions of the material being in the high-spin state. There are then two lower temperature phases which occur as a result of spontaneous symmetry breaking and photoirradiaton. This competition between spin-crossover and structural ligand ordering highlights the complexities which can be involved in the rational design and control of such materials.[29]

1.3.2.3 Polymers based on other ligand systems

Whilst polymers based on triazoles and those with Hoffman and SCOF motifs are common, the exploration of more unusual architectures is increasingly common.

An unconventional iron (II) one-dimensional coordination polymer, with an FeN_5S coordination sphere was recently reported. This material is based around a tris(2-pyridyl)methoxymethane (tpc-OMe) ligand and three thiocyanate groups. One of these thiocyanate groups acts as a linker between individual complex units and coordinates one iron through the sulfur and a second iron through the nitrogen. This polymer shows a sharp cooperative spin transition with a narrow hysteresis and a $T_{1/2}$ of 199 K.[30]

A combination of a Schiff-base ligand, which was functionalised with a phenazine fluorophore, and 4,4'-bipyridine with iron (II) formed a coordination polymer which combines fluorescence and spin-crossover. The polymer undergoes an above temperature spin transition with a 48 K wide hysteresis. This hysteresis loop is stable for several cycles and occurs at $T_{1/2}\downarrow$ = 323 K and $T_{1/2}\uparrow$ = 371 K. The changes in spin state is mirrored by changes in fluorescence, as the low-spin state is green and the high-spin state is yellow. This example highlights the possibilities for harnessing multiple functions in spin-crossover materials.[31]

An unusual coordination polymer based on the tetradentate ligand tetrakis(isonicotinoxymethyl)methane) (TINM) was recently reported. The complex is

composed of one iron(II) cation which is coordinated by two thiocyanate ligands in the axial positions and four nitrogens from four different TINM ligands in the equatorial positions. This coordination polymer undergoes both thermal and pressure regulated gradual, incomplete spin-crossover.[32]

1.4 Spin crossover in liquid crystals

1.4.1 Background

Mesogens, also known as liquid crystals, are materials in an intermediate state of matter (mesophase) between the liquid and the crystalline form. Liquid crystals combine properties from the crystalline state, such as electrical and optical anisotropy, with properties associated with liquids, for example molecular fluidity and mobility. To exhibit liquid crystal behaviour, mesogenic molecules must fulfil a specific set of structural and electronic properties; these include a rigid core, strongly polarisable functional groups and long, flexible chains.[9] These features ensure appropriate packing of the molecules which enables the necessary intermolecular interactions, such as π-π stacking, hydrogen bonding, van der Waals and electrostatic interactions, to occur.[33] In addition, the presence of a permanent dipole, its magnitude or the anisotropy of the molecular polarisability has a strong impact on whether liquid crystals will be formed.[33, 34]

Discussion of liquid crystals requires the use of specific terminology. Mesophases can be formed in two ways. The first is when pure or mixtures of compounds are influenced by temperature and form thermotropic liquid crystals. Secondly, mesophases can be formed when amphiphilic species form anisotropic aggregates in a solvent (frequently water); these are known as lyotropic liquid crystals. Thermotropic crystals can be sub-divided based on their structural features into discotic (disk-like) and calamitic (rod-like) crystals. The latter can be further split based on the order in the mesophase into nematic (least ordered) and smectic (most ordered) crystals. The nematic phase contains molecules which are almost parallel aligned in the *n* director. The *n* director is

the preferred axis for orientation within the material. These molecules can move within the phase and rotate around the long molecular axis giving them orientational order but not positional order. The degree of order found in the smectic crystals gives a number of possible phases (A, B, C, E, G, H, J and K). The S_A and S_C phases are the most common and least ordered. In these phases, molecules in layers are randomly distributed and can rotate along the long axis. The S_A phase exists with the director *n* perpendicular to the layers. The S_C phase has a tilted director *n* so that the molecules are not aligned perpendicular to the layers. In most cases, temperature determines the angle of this tilt.[35]

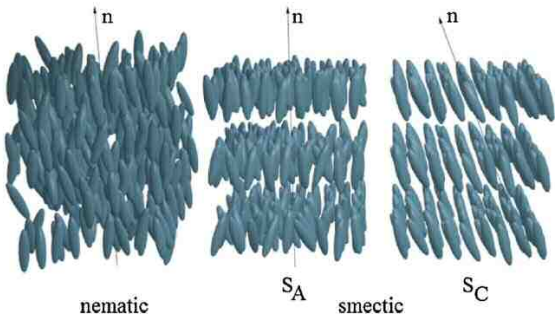

Figure 1.9 - Illustration of the molecular order in nematic (left), smectic A (middle) and smectic C (right) subclasses of the calimitic mesophases aligned along the n director.[9]

Metallomesogens are molecules which contain a metal centre and exhibit liquid crystal behaviour. They combine the interesting properties of liquid crystals with the range and variety of coordination chemistry compounds. The presence of a metal centre extends the properties seen in organic liquid crystals and offers the possibility of tuning the physical aspects, such as electrical, optical, magnetic and mesomorphic behaviour.[33] This extension is due to the increased geometries which are available, compared to those in organic metallomesogens, as well as the addition of paramagnetism, colour, conductivity and optics.[9] In addition, the large, easily polarisable centre of electron density of the metal atom increases the likelihood that the molecule will exhibit liquid crystal behaviour.[34]

It is likely that technological developments in the future will demand materials with a range of chemical and physical properties, such as those found in

metallomesogens, for a variety of purposes which include memory storage and optical devices.[36]

1.4.2 Spin-crossover in liquid crystals

The first spin-crossover liquid crystal was reported by Galyametdinov *et al*. in 2001. The complex was an N-alkyloxysalicyldenyl-N'-ethyl-N-ethylenediamine ligand (Figure 1.10) with an Fe^{3+} centre and a PF_6^- counterion. Results from magnetic susceptibility experiments and X-ray crystallography showed a compound which exhibited gradual SCO over the temperature range 4.5-460K and had calamitic molecules in a smectic A mesophase structure.[37]

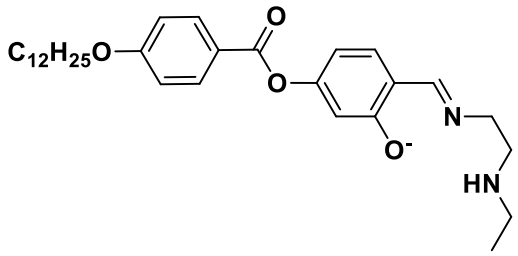

Figure 1.10 - Structure of the ligand from the first reported spin-crossover liquid crystal.[37]

Hayami *et al*. worked on a 2,6-*bis*(benzimidazolyl)pyridine-based liquid crystal system with R groups of varying alkyl chain length.[38] The structure and the R groups used are shown in Figure 1.11. For an unsubstituted [Fe(2,6-*bis*(benzimidazolyl)pyridine)$_2$]$^{2+}$ complex, abrupt SCO at 400 K is observed, however the addition of alkoxy substituents decreases the ligand field strength which alters the magnetic properties. When R_1 = $OC_{16}H_{33}$ and R_2 = H, the complex has a large fraction which is HS at low temperature, but undergoes gradual SCO with $T_{1/2}$ = 225 K. SCO in this complex can also be triggered using LIESST. However, when the substituents are changed to R_1 = H and R_2 = $C_{16}H_{33}$ the resultant complex is LS at temperatures up to 400 K. For the complex with R_1 = OAlk and R_2 = Alk, a SCO hysteresis loop is seen with $T_{1/2}\uparrow$ = 236 K and $T_{1/2}\downarrow$ = 230 K.

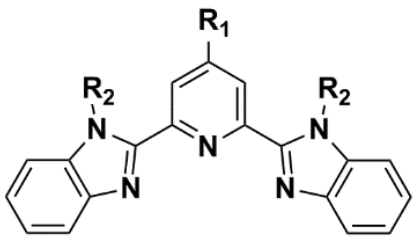

$R_1 = OC_{16}H_{33}$ or H or OAlk

$R_2 = C_{16}H_{33}$ or H or Alk

Alk =

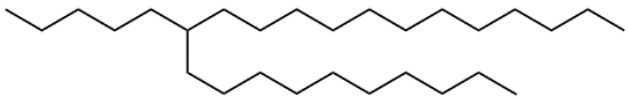

Figure 1.11 - Structure of 2,6-*bis*(benzimidazolyl)pyridine-based liquid crystal structure. The different R groups are shown below the molecular structure.

A series of complexes derived from a (tris(2-aminoethyl)amine Schiff base ligand with an Fe(II) centre were reported by Seredyuk (Figure 1.12).[39] The ligand field strength of the complex depends on the counterion. For the counterions ClO_4^- and BF_4^-, the complexes are LS. When the halide counterions are incorporated, the SCO behaviour is dependent on which halide is present. For I^- and Br^-, the iron centre is LS up to 400 K. For Cl^- and F^-, the spin state depends on the amount of water present and the complexes are LS up to the temperature at which the compounds are dehydrated.

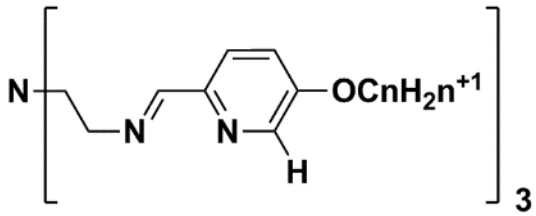

Figure 1.12 - Structure of triamine tren(tris(2-aminoethyl)amine.

Liquid crystals based on a triazole system were first reported by Fujigaya *et al.* and the structure is shown in Figure 1.13.[40] When n = 8,12 or 16, the spin transition and liquid crystal behaviour coexist as the SCO occurred above the crystalline→liquid crystal transition of the alkyl chains. In addition, the complexes were reacted with Fe(II) tosylate, $CF_3SO_3^-$ and BF_4^-. The family of tosylate complexes, with n = 4, 6, 8, 10, 12 and 16, showed SCO at the temperature where the compound shows the discotic columnar mesophase, Col_h. When these complexes are dehydrated, the type of SCO changes to give incomplete, abrupt SCO with hysteretic and thermochromic behaviour.

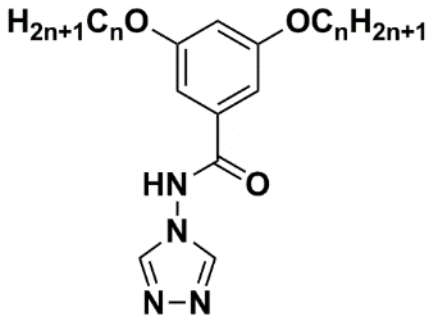

Figure 1.13 - Structure of triazole-based liquid crystals.

A rare example of an iron(II) complex with liquid crystalline behaviour which undergoes spin-crossover with a wide hysteresis around room temperature has been reported recently. The complex is based on a pyridyl-benzohydrazonate ligand with C_{10} alkyl chains. The positioning of these chains give a more bent structure than that seen in many complexes of this type. This structure, alongside the iron/pyridyl-benzohydrazonate centre which can deviate from a classic octahedral geometry, are thought to contribute to the unusually cooperative spin transition.[41]

1.5 Spin-crossover in gels

When a large amount of liquid and a smaller amount of solid are mixed, a gel may be formed due to the development of a solid 3D network within the liquid. The presence of this solid network restricts the movement of the liquid phase. Gels which contain metals, or metallogels, are formed when metals or metal complexes are introduced into the liquid or solid phase. The addition of metals to gels can modify the aggregation and gelation of the gel as well as incorporating a method of tuning the properties of the gel.[42] Gels can be classed as physical gels (where the formation is based on non-covalent interactions such as hydrogen bonds and π-stacking and the liquid phase can be recovered upon heating) and chemical gels (which are covalently bonded and the liquid form is thermally irreversible).[9]

Several SCO gels based on a 1,2,4-triazole framework have been developed. These gel systems typically have the same 1D linear structure as the 1,2,4-triazole-based polymers discussed previously (Figure 1.4) with the liquid phase provided by a solvent. The first gels with SCO behaviour were the structures based on $[Fe(C_{18}trz)_3]$-$(ptol)_2 \cdot 2H_2O$ reported by Roubeau *et al.*[43] The structure of the triazole-based polymer was functionalised with long alkyl chains and different SCO temperatures were achieved by using different solvents. This is consistent with the solvent dependent spin transition temperatures seen in SCO compounds, polymers and liquid crystals.

A series of triazole-based gels have been reported that exhibit thermochromism and SCO behaviour and show no thermal deterioration when subjected to repeated heating/cooling cycles. In addition to the hydrogen bonding network between the triazole and sulfonate counterions which improves cooperativity, it is thought that lipophilic interactions between the counterions and the long hydrocarbon chains on the triazole R groups also contribute to the rapid response in spin transition.[44]

1.6 Spin-crossover in thin films

Thin films made from SCO compounds are of significant interest, as they would incorporate the useful properties of bulk SCO solids and transfer them to a much smaller surface.[9] The most commonly used method of making these thin films is the Langmuir-Blodgett (LB) technique. To make thin films in this way, a Langmuir monolayer is formed when a single layer of molecules is placed onto a liquid (usually water) layer. This monolayer is transferred to a solid support which forms a thin film that is the thickness of one of the molecules; this is known as a LB film. To make multi-layer films, these steps are repeated. LB films have several advantages over other types; these include control over monolayer thickness, homogeneous coverage of the monolayer of large areas, deposition onto most solid surfaces and the potential for the formation of multiple layers which vary in composition.[9]

The first LB thin film of an SCO compound was reported in 1988.[45] The compound has the formula $[Fe(L1)_2(NCS)_2$, where the structure of L1 is shown in Figure 1.14. The bulk solid of the same structure is HS, whilst the thin film does exhibit a spin transition. However the thin film was not pure and showed traces of the *tris* complex.

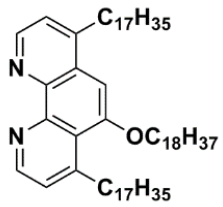

Figure 1.14 - Structure of the ligand used in the LB thin film made from $[Fe(L1)_2(NCS)_2$.

A related compound, $[Fe(L2)_2(NCS)_2$, with the ligand, L2, shown in Figure 1.15 showed good stability in the LB film.[46] The SCO properties are interesting and show some insight into the structural constraints on SCO molecules in thin films. The bulk solid undergoes a spin transition centred at 230 K. There are a small number of residual LS sites, but SCO is almost complete. The first time that the thin film form is heated, only a small number of sites exhibit SCO; the rest remain LS. However successive

heating cycles appear to 'induce' spin transitions to occur, as on subsequent cycles, SCO similar to that of the bulk solid is seen. The authors hypothesise that this is a result of the heating releasing some of the stress imposed by the structure, especially when the alkyl chains melt.[46] SCO in this compound could also be triggered by the LIESST effect.

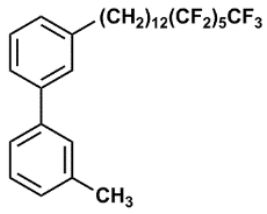

Figure 1.15 - Structure of the ligand L2 in $[Fe(L2)_2(NCS)_2]$.

Some thin films made of a nanoporous 3D framework of the structure $[Fe(pz)Ni(CN)_4]$ have been reported which could be used for the sensing of gas and vapour molecules.[11] The SCO behaviour was found to be dependent on the guest molecule in the system and the spin transition could be induced by the adsoption and desorption of vapour molecules.[12]

Kurth *et al.* reported a thin film made using a bis-terpyridine ligand framework (Figure 1.16) and dihexadecyl phosphate (DHP).[47] The terpyridine complexes are LS, regardless of the anion present. However, the when the amphiphilic phase transition occurs, mechanical stress within the molecules is induced. this decreases the ligand field strength causing SCO behaviour to be exhibited.[9]

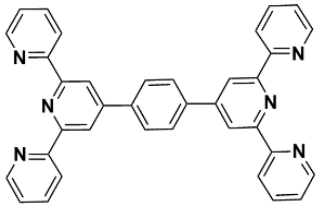

Figure 1.16 - Structure of the bis-terpyridine ligand L3.

1.7 Conclusion

Although the types of soft materials discussed have different structures and properties, there are clear trends in structure and substituents which influence the spin-crossover behaviour exhibited. A critical factor in SCO behaviour across polymers, liquid crystals, gels and thin films are the intermolecular interactions which occur between SCO centres within the materials. These include π-π interactions, hydrogen bond networks and lipophilic interactions. Similarly, the presence of different substituents, ligands, counterions and solvents has an impact on the type and temperature at which SCO occurs. All of these factors lead to the potential for the design of a range of structurally diverse materials with a range of types of SCO behaviour, temperatures at which SCO occurs and widths of hysteresis loops. As a result of this diversity, SCO can effectively be tuned giving the potential for rational materials design which incorporates both the structure of the framework and the properties and functions of the materials involved. This gives potential for materials which could function for a range of purposes, including optical, magnetic, sensing[9] and sorbtive[12] applications.

1.8 Aims

This project encompasses a broad range of chemistry with a focus on the design of spin-crossover complexes with chiral and soft materials in mind. The inherent bistability of systems capable of spin-crossover make them strong candidates for interesting functional materials and the proposed uses include materials for optical, biomedical and environmental purposes, storage devices, molecular sensors and catalysts. A variety of ligand and complex architectures have been identified and investigated, as well as the preparation of a functionalised ligand and its incorporation into polymers.

The first three chapters focus a series of iron, cobalt and zinc PyBox complexes (Figure 1.17). The first example of chiral discrimination in iron(II) spin-crossover complexes is herein reported and follow up studies include a theoretical Density Functional treatment of such complexes, the PyBox ligands and an analogous set of thio-PyBox complexes, as well as solution phase studies into the speciation of cobalt(II) and zinc(II) PyBox complexes.

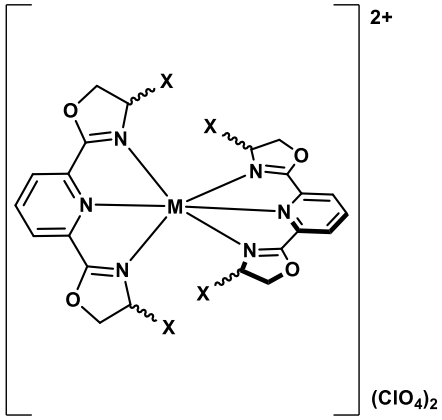

Figure 1.17 - General structure of $[M(PyBox)_2]^{2+}$ complexes, where M = Fe, Co or Zn and X = H, Me, Ph, iPr or indanol substituents.

A family of tripodal pseudoclathrochelate complexes were prepared and their spin-crossover behaviour has been analysed. No novel research is complete without

some serendipitous results, therefore the discovery of two multimetallic clusters is also discussed.

Finally, a synthetic methodology has been established to begin to work toward the incorporation of spin-crossover complexes into a polymer backbone. This initial exploration provides a beginning to this project and the future of this strategy is discussed.

1.9 References

1. S. Brooker, *Chem. Soc. Rev.*, 2015, **44**, 2880-2892.
2. M. A. Halcrow, *Chem. Commun. (Camb)*, 2013, **49**, 10890-10892.
3. M. A. Halcrow, *Polyhedron*, 2007, **26**, 3523-3576.
4. P. Gütlich and H. A. Goodwin, in *Spin Crossover in Transition Metal Compounds I*, eds. P. Gütlich and H. A. Goodwin, Springer-Verlag Berlin Heidelberg, Berlin, Germany, Editon edn., 2004, pp. 1-48.
5. P. Gütlich, A. B. Gaspar and Y. Garcia, *Beilstein J. Org. Chem.*, 2013, **9**, 342-391.
6. I. Šalitroš, N. T. Madhu, R. Boča, J. Pavlik and M. Ruben, *Monatsh. Chem.*, 2009, **140**, 695-733.
7. P. Gütlich and A. Hauser, *Coord. Chem. Rev.*, 1990, **97**, 1-22.
8. O. Kahn and C. J. Martinez, *Science*, 1998, **279**, 44-48.
9. A. B. Gaspar and M. Seredyuk, *Coord. Chem. Rev.*, 2014, **268**, 41-58.
10. M. Carmen Muñoz and J. Antonio Real, in *Spin-Crossover Materials: Properties and Applications*, ed. M. A. Halcrow, John Wiley & Sons Ltd, Oxford, UK, Editon edn., 2013, pp. 121-146.
11. A. Bousseksou, G. Molnar, L. Salmon and W. Nicolazzi, *Chem. Soc. Rev.*, 2011, **40**, 3313-3335.
12. P. D. Southon, L. Liu, E. A. Fellows, D. J. Price, G. J. Halder, K. W. Chapman, B. Moubaraki, K. S. Murray, J.-F. Létard and C. J. Kepert, *J. Am. Chem. Soc.*, 2009, **131**, 10998-11009.
13. G. R. Whittell and I. Manners, *Adv. Mater.*, 2007, **19**, 3439-3468.
14. R. D. Archer, *Inorganic and Organometallic Polymers*, Wiley-VCH, New York, 2001.
15. R. Ladj, A. Bitar, M. M. Eissa, H. Fessi, Y. Mugnier, R. Le Dantec and A. Elaissari, *Int. J. Pharm.*, 2013, **458**, 230-241.
16. A. Musyanovych and K. Landfester, *Macromol. Biosci.*, 2014, **14**, 458-477.
17. E. Gross, F. D. Toste and G. A. Somorjai, *Catal. Lett.*, 2014, **145**, 126-138.

18. A. Ammala, *Int. J. Cosmetic. Sci.*, 2013, **35**, 113-124.
19. O. Roubeau, *Chem. Eur. J.*, 2012, **18**, 15230-15244.
20. J. G. Haasnoot, G. Vos and W. L. Groeneveld, *Z. Naturforsch., B: Chem. Sci.*, 1977, **32**, 1421-1430.
21. M. M. Dirtu, F. Schmit, A. D. Naik, I. Rusu, A. Rotaru, S. Rackwitz, J. A. Wolny, V. Schunemann, L. Spinu and Y. Garcia, *Chem. Eur. J.*, 2015, **21**, 5843-5855.
22. M. M. Dîrtu, D. Gillard, A. D. Naik, A. Rotaru and Y. Garcia, *Hyperfine Interact.*, 2011, **205**, 75-79.
23. H. Voisin, C. Aimé, A. Vallée, T. Coradin and C. Roux, *Inorg. Chem. Front.*, 2018, **5**, 2140-2147.
24. Y. Garcia, V. Niel, M. C. Munoz and J. A. Real, in *Spin Crossover in Transition Metal Compounds I*, eds. P. Gütlich and H. A. Goodwin, Springer-Verlag Berlin Heidelberg, Berlin, Germany, Editon edn., 2004, pp. 229-259.
25. N. F. Sciortino and S. M. Neville, *Aust. J. Chem.*, 2014, **67**, 1553-1562.
26. J. A. Real, E. Andres, M. C. Munoz, M. Julve, T. Granier, A. Bousseksou and F. Varret, *Science*, 1995, **268**, 265-267.
27. G. J. Halder, C. J. Kepert, B. Moubaraki, K. S. Murray and J. D. Cashion, *Science*, 2002, **298**, 1762-1765.
28. J. Y. Li, Y. C. Chen, Z. M. Zhang, W. Liu, Z. P. Ni and M. L. Tong, *Chem. Eur. J.*, 2015, **21**, 1645-1651.
29. D. Zhang, E. Trzop, F. J. Valverde-Muñoz, L. Piñeiro-López, M. C. Muñoz, E. Collet and J. A. Real, *Cryst. Growth Des.*, 2017, **17**, 2736-2745.
30. K. Nebbali, C. D. Mekuimemba, C. Charles, S. Yefsah, G. Chastanet, A. J. Mota, E. Colacio and S. Triki, *Inorg. Chem.*, 2018, **57**, 12338-12346.
31. C. Lochenie, K. Schotz, F. Panzer, H. Kurz, B. Maier, F. Puchtler, S. Agarwal, A. Kohler and B. Weber, *J. Am. Chem. Soc.*, 2018, **140**, 700-709.
32. J. Li, S. Chen, L. Jiang, Y. Li and B. Li, *Cryst. Growth Des.*, 2018, **18**, 1931-1934.
33. J. L. Serrano, in *Metallomesogens: Synthesis, Properties and Applications*, ed. J. L. Serrano, John Wiley and Sons Ltd, Oxford, UK, Editon edn., 2008, pp. 1-22.

34. P. M. Maitlis and A.-M. Giroud-Godquin, *Angew. Chem. Int. Ed.*, 2003, **30**, 375-402.
35. S. Kumar and T. L. Polgreen, in *Liquid Crystals and Ordered Fluids*, eds. A. C. Griffin and J. F. Johnson, Plenum Press, New York, USA, Editon edn., 1982, vol. 4, pp. 1131-1139.
36. A. B. Gaspar, M. Seredyuk and P. Gütlich, *Coord. Chem. Rev.*, 2009, **253**, 2399-2413.
37. Y. Galyametdinov, V. Ksenofontov, A. Prosvirin, I. Ovchinnikov, G. Ivanova, P. Gütlich and W. Haase, *Angew. Chem. Int. Ed.*, 2001, **40**, 4269-4271.
38. S. Hayami, N. Motokawa, A. Shuto, R. Moriyama, N. Masuhara, K. Inoue and Y. Maeda, *Polyhedron*, 2007, **26**, 2375-2380.
39. M. Seredyuk, *Inorg. Chim. Acta*, 2012, **380**, 65-71.
40. T. Fujigaya, D.-L. Jiang and T. Aida, *J. Am. Chem. Soc.*, 2003, **125**, 14690-14691.
41. D. Rosario-Amorin, P. Dechambenoit, A. Bentaleb, M. Rouzieres, C. Mathoniere and R. Clerac, *J. Am. Chem. Soc.*, 2018, **140**, 98-101.
42. P. Grondin, O. Roubeau, M. Castro, H. Saadaoui, A. Colin and R. Clérac, *Langmuir*, 2010, **26**, 5184-5195.
43. O. Roubeau, A. Colin, V. Schmitt and R. Clerac, *Angew. Chem. Int. Ed.*, 2004, **43**, 3283-3286.
44. T. Fujigaya, D. L. Jiang and T. Aida, *Chem. Asian. J.*, 2007, **2**, 106-113.
45. A. Ruaudel-Teixier, A. Barraud, P. Coronel and O. Kahn, *Thin Solid Films*, 1988, **160**, 107-115.
46. H. Soyer, E. Dupart, C. J. Gómez-García, C. Mingotaud and P. Delha, *Adv. Mater. Processes*, 1999, **11**, 382-384.
47. Y. Bodenthin, U. Pietsch, H. Mohwald and D. G. Kurth, *J. Am. Chem. Soc.*, 2005, **127**, 3110 - 3114.

Chapter 2 - The Impact of Chirality on the Spin States of Iron(II) PyBox Complexes

2.1 Introduction

2.1.1 Spin-crossover and chirality

The combination of chirality and the spin-crossover phenomenon has the potential to give rise to a range of multifunctional materials with interesting properties such as magneto chiral dichroism and ferroelectric behaviour.[1] However, it can be challenging to combine these two properties in both the molecular structure and the crystal structure.[1]

Schiff-base ligands are a common motif in attempts to combine spin-crossover and chirality. Such ligands based on an imidazole moiety can be tuned to have different properties as the acidic hydrogen on the imidazole ring can be easily replaced with a variety of substituents.[2] Gu *et al.* (2013) sought to harness these properties *via* the rational design of the bidentate Schiff base ligand, 1-phenyl-N-(1-methyl-imidazol-2-ylmethylene) ethanamine (Figure 2.1).[1]

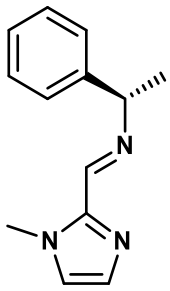

Figure 2.1 - Structure of (*S*)-1-phenyl-N-(1-methyl-imidazol-2-ylmethylene) ethanamine.

Two Fe(II) complexes, *fac*-Λ-$[Fe(R\text{-}L)_3](BF_4)_2$.MeCN and *fac*-Δ-$[Fe(S\text{-}L)_3](BF_4)_2$.MeCN, were synthesised and characterised. Both enantiomers crystallise in the chiral $P2_1$ space group, showing that the chirality of the ligand is retained in the complex. The crystal structure suggests π-π interactions occur between the imidazole and phenyl rings of adjacent ligands. This is thought to avoid any steric hindrance and stabilise both the *fac*-Λ and *fac*-Δ structures. The complexes undergo gradual SCO with $T_{1/2}$ = 365 K in the acetonitrile solvate (Figure 2.2). However, when the accompanying

acetonitrile is removed, the nature of the spin transition changes to include a narrow hysteresis loop.

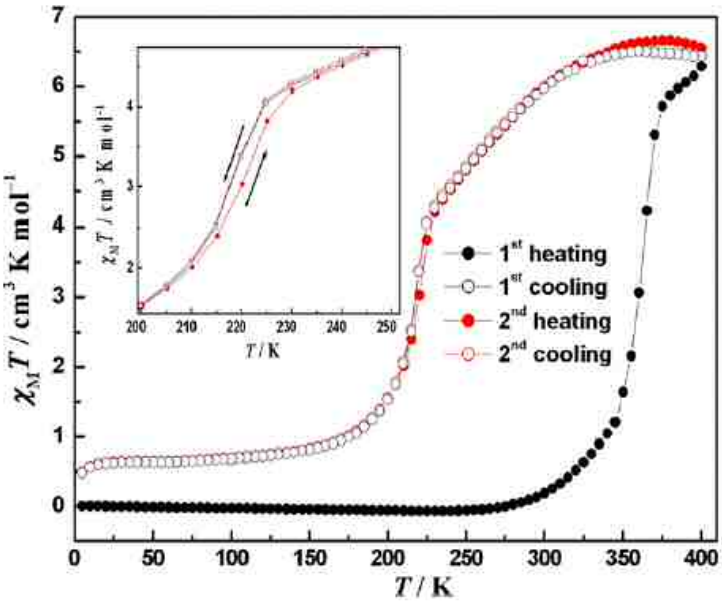

Figure 2.2 - Magnetic susceptibility of *fac*-Λ-[Fe(R-L)$_3$](BF$_4$)$_2$ in a 0.5 T field.[1] The black line indicates the gradual spin-crossover of the acetonitrile solvate. The red and white lines show the gradual spin-crossover with narrow hysteresis loop of the complex without acetonitrile.

Ren *et al.* (2015) used Schiff-base ligands with different substituents on the imidazole and phenyl rings to make Fe(II) complexes that are both chiral and exhibit SCO behaviour (Figure 2.3).[2]

a)

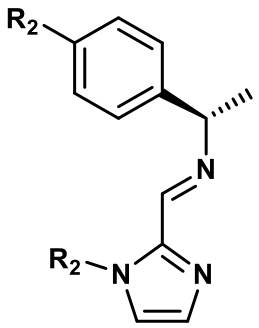

b)

Ligand number	R_1	R_2	SCO $T_{1/2}$ / K
1	n-Propylenyl	H	257
2	Isobutenyl	Cl	375
3	n-Pentenyl	OCH_3	137
4	n-Hexenyl	H	282

Figure 2.3 - a) General structure of the Schiff-base ligands. b) Information on the substituents and $T_{1/2}$ of the Schiff-base complexes.[2]

Three effects were reported to have an impact on SCO behaviour; substitution effect, packing mode and intermolecular interactions. The different substituents on both rings led to a change in ligand field strength which altered SCO trends. Complexes made with ligands **2** and **4** crystallised in lower symmetry space groups ($P2_12_12_1$ rather than $P6_3$ or $P2_13$) and also showed SCO at a higher temperature than complexes with **1** and **3** as ligands, suggesting that the packing of the complex in the solid state influenced the SCO. In addition, the complex made with ligand **2** exhibits SCO at a higher temperature than the others. The authors suggest that this is a result of the strong C-Cl···π interactions.

As well as the synthesis and characterisation of chiral SCO complexes for fundamental purposes, the design of multi-functional materials which exhibit the same properties has been targeted.

A similar set of Schiff-base ligands, featuring a naphthyl rather than phenyl group, formed chiral complexes with Fe(II) and were found to exhibit SCO behaviour. These complexes were grafted on to Merrifield's resin in an attempt to make chiral materials with SCO behaviour for potential use in catalysis.[3] However, the ability to undergo a spin transition was lost upon attachment to the solid support and the Fe(II) remained in the high-spin form. Although this particular example was unsuccessful, it highlights the interest in coupling SCO with other properties, such as chirality and incorporating them into functional materials.

A metal-organic framework (MOF) with SCO behaviour has also been developed by Liu *et al.* (2014) using 3-methyl-2-(5-(4-(pyridin-4-yl)phenyl)-4H-1,2,4-triazol-3-yl)-pyridine as a ligand.[4] The resulting chiral MOF exhibits two-step SCO with the plateau between the spin states at room temperature (Figure 2.4).

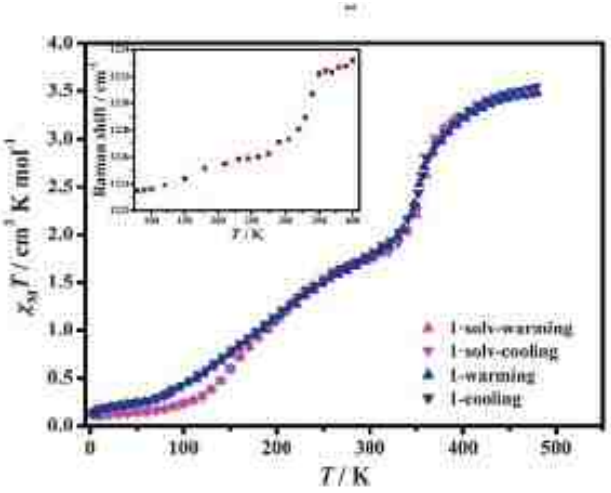

Figure 2.4 - Plots of variable-temperature $\chi_M T$ for the SCO-MOF, prepared by Liu *et al*..[4]

The significance of combining SCO with other inherent molecular properties such as chirality, has the potential to lead to a range of interesting possibilities, including increasing fundamental knowledge, the development of functional materials and the design of novel catalysts. At present, the majority of the literature precedent is based around iron(II) complexes with Schiff-base ligands, however an investigation into SCO in iron(II) PyBox complexes offers a relatively unexplored alternative. The common themes which influence SCO in other ligand systems are still present; the examples of SCO-chiral compounds show that cooperativity, intermolecular interactions and the effects of packing, substituents and solvents remain critical to SCO behaviour. As with other SCO active compounds, it may be possible to incorporate iron(II) PyBox complexes into switchable materials.

2.1.2 Bis(oxazolinyl) pyridine (PyBox) ligands and complexes

Bis(oxazolinyl) pyridine (PyBox) ligands were first reported by Nishiyama *et al.* (1989) who were interested in designing chiral organic molecules to be used in transition metal catalysis.[5] Since then, this class of ligand has been of interest due to their ease of preparation and ready availability of chiral precursor materials.[6] PyBox ligands (Figure 2.5) have a tridentate structure which traditionally coordinates to a metal through the lone pairs of electrons on each of the three nitrogen donors,

although several examples of bidentate[7] or monodentate[8] coordination have been reported.

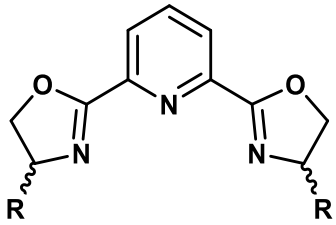

Figure 2.5 - General structure of bis(oxazolinyl) pyridine ligands

Asymmetric, also known as chiral or enantioselective, synthesis occurs when a chiral starting material is used and stereoisomeric products are formed in different amounts. This principle can be extended to catalysis, whereby a chiral coordination compound is used as a catalyst. If a ligand is chiral, it will impart this chirality onto a metal complex. Assuming that the metal is capable of catalytic activity, the combination of metal and ligand is the basis of asymmetric catalysis. There is a significant advantage in developing one ligand class which can be rationally tuned both electronically and sterically, as this gives a simple method of designing catalysts suitable for a number of applications.[9] The structure of the PyBox complexes makes them ideal for this purpose as the substituents can easily be altered. In addition, the planar rigidity of the system and the coordination versatility with a variety of d and f block metals makes them excellent asymmetric catalysts for a variety of reactions, including reduction, oxidation, aldol-type, Diels-Alder, polymerisation and cross-coupling reactions.[9] Although PyBox complexes using a range of transition metal (rhodium[8], ruthenium[9], copper[10] and scandium[11]) and lanthanide (samarium, lanthanum and ytterbium[11, 12]) metal centres have been described, there is a focus on the development of iron complexes for catalysis, as iron catalysts are associated with lower costs, toxicity and environmental impact.[6]

2.1.3 Spin-crossover in $[Fe(PyBox)_2]^{2+}$ complexes

Although PyBox ligands have been used to form complexes with a range of d and f block metals, their application in the field of spin-crossover has been little explored until very recently.

The achiral PyBox ligand 2,6-bis[4,4-dimethyl-4,5-dihydrooxazol-2-yl]pyridine (**L1**) was first explored as an iron(II) complex exhibiting spin-crossover in 2015 by Gao *et al.*[13] Two complexes, $[Fe(L1)_2][ClO_4]_2$ and $[Fe(L1)_2][ClO_4]_2$.MeCN, were synthesised and the solid state magnetic susceptibility measured. $[Fe(L1)_2][ClO_4]_2$ undergoes a spin transition within a narrow temperature band with half of the iron(II) centres transitioning. In contrast $[Fe(L1)_2][ClO_4]_2$.MeCN remains high-spin across the temperature range. Pressure and light-induced spin-crossover were also observed for $[Fe(L1)_2][ClO_4]_2$.

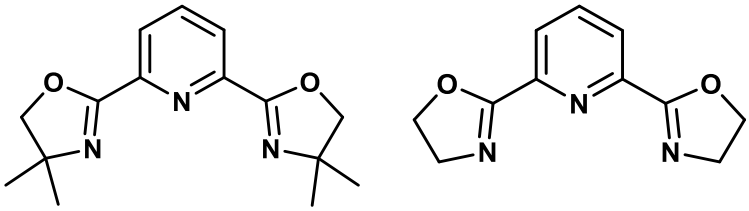

Figure 2.6 - The structure of L1 and L2.

In a subsequent publication, Gao *et al.* investigated $[Fe(PyBox)_2]^{2+}$ complexes using both **L1** and **L2** (Figure 2.6) in conjunction with Fe(II) salts with four different counterions; tetrafluoroborate (BF_4), perchlorate (ClO_4), hexafluorophosphate (PF_6) and tetraphenylborate (BPh_4) to attempt to clarify the effect of ligand design, counter anion and solvent influence on spin-crossover in the solid state.[14] The spin-crossover behaviour of the complexes is summarised in Table 2.1.

Table 2.1 - Information on the spin-crossover behaviour of $[Fe(PyBox)_2]^{2+}$ complexes.[14]

	BF_4	ClO_4	PF_6	BPh_4
L1	Abrupt SCO with 50% completeness. Structural phase transition. $[Fe(L1)_2][BF_4]_2$. MeCN is high spin.	Abrupt SCO with 50% completeness. Structural phase transition. $[Fe(L1)_2][ClO_4]_2$. MeCN is high spin.	High spin. $[Fe(L1)_2[PF_6]_2$. $MeCN.Et_2O$ is high spin.	High spin. $[Fe(L1)_2[BPh_4]_2$. MeCN shows gradual, complete SCO.
L2	Gradual, complete SCO.	Gradual, complete SCO.	Two-step SCO. $L1(PF_6)$.MeCN shows two-step SCO.	Two-step SCO.

$[Fe(L2)_2]^{2+}$ complexes, regardless of counterion and solvent, all undergo spin-crossover, although the $T_{1/2}$ values are all above 300K. It appears that the addition of the dimethyl moiety to the oxazoline ring alters the predictability of a spin transition occurring. This is an effect of the increase in steric bulk of the ligand which weakens the ligand field. $[Fe(L1)_2]^{2+}$ complexes are able to undergo spin-crossover, however the counterion and solvent present in the solid lattice appear to have an increased effect. Some complexes exhibit spin-crossover with a reduced $T_{1/2}$ temperature, although $[Fe(L1)_2][BF_4]_2$.MeCN, $[Fe(L1)_2][PF_6]_2$, $[Fe(L1)_2][ClO_4]_2$.MeCN, $[Fe(L1)_2][BPh_4]_2$ and $[Fe(L1)_2][PF_6]_2$.$MeCN.Et_2O$ are all high-spin. Both $[Fe(L1)_2][BF_4]_2$ and $[Fe(L1)_2][ClO_4]_2$ show a structural phase transition in conjunction with a 50% complete abrupt spin transition. This is a result of two crystallographically independent Fe(II) centres which can adopt opposite spin states.

The similar size, charge and geometry of the tetrafluoroborate and perchlorate counterions result in very similar solid state structures, leading these complexes to exhibit similar spin-crossover behaviour. However due to their larger size and differing geometries, hexafluorophosphate and tetraphenylborate counterions lead to a very different packing arrangement in the solid state, resulting in different magnetic responses.

Complexes which were co-crystallised with solvent molecules, such as $[Fe(L1)_2][BF_4]_2$.MeCN and $[Fe(L1)_2][ClO_4]_2$.MeCN, remained high spin across the temperature range measured. In these cases, the presence of the solvent causes the

lattice to become more rigid and the complexes do not have the capacity to undergo the structural changes needed to undergo a spin transition. However, both $[Fe(L1)_2][PF_6]_2$ and $[Fe(L1)_2][PF_6]_2.MeCN.Et_2O$ are high spin, which indicates this solvent effect is not consistent between complexes.

The results highlighted in this publication indicate that ligand design, counterion and solvent molecules all contribute to the spin-crossover behaviour, but that results are not necessarily predictable.

These initial studies of $[Fe(PyBox)_2]^{2+}$ complexes highlight the suitability of PyBox ligands as a viable system for complexes which undergo spin-crossover. However, these investigations do not harness chiral PyBox ligands to form chiral spin-crossover complexes, which have the potential for useful applications such as non-linear optical materials. In addition, the complexes have only been investigated in the solid state. It can be difficult to fully determine the effects of ligand design on spin-crossover in the solid state, as the effects of the crystal lattice on spin transitions cannot be separated from those of the ligand, thus an investigation of spin-crossover behaviour in the solution state is also important.

2.1.4 Fe(II) *bis*-pyrazolylpyridine complexes: insights into the geometry of spin-crossover complexes

The spin-crossover behaviour of the iron(II) complexes of *bis*-pyrazolylpyridine ligands (2,6-*bis*[pyrazol-1-yl]pyridine = 1-bpp and 2,6-*bis*[1H-pyrazol-3-yl]pyridine = 3-bpp) (Figure 2.7) has been intensively studied.[15-20]

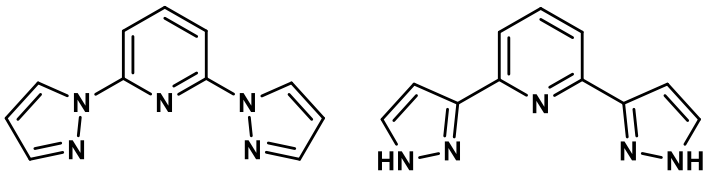

Figure 2.7 - The structures of 1-bpp and 3-bpp.

A particularly interesting study investigated $[Fe(bpp)_2]^{2+}$ complexes in terms of the octahedral geometry around the metal centre by looking at the trans-N(pyridine)-Fe-N(pyridine) angle (ϕ) and the dihedral angle between the two ligands (θ) (Figure 2.8).[17] It was found that where there was a significant distortion of the octahedron from the ideal 180° ϕ angle and/or from the ideal 90° θ angle, the complex remained high spin and exhibited Jahn-Teller distortion as a result of the degenerate orbitals of the high spin state. Since the low-spin form of the complex cannot have Jahn-Teller distortion, in order to undergo spin-crossover, the complex must rearrange to its low-spin form. If this rearrangement is prevented by the rigidity of the solid lattice, then the complex cannot make the high-spin to low-spin transition and thus remains high-spin.

Figure 2.8 - The ϕ and θ distortion angles exhibited by some high-spin $[Fe(1\text{-}bpp)_2]^{2+}$ and $[Fe(3\text{-}bpp)_2]^{2+}$ complexes.[17]

PyBox ligands have parallels with the structure of bpp; both ligands are tridentate with a symmetrical shape, consisting of a central pyridine ring with an aromatic five-membered ring attached in the 2- and 6-pyridyl positions. The rigidity imposed by the aromatic ring systems ensures that the ligands remain relatively planar, although steric bulk imposed by substituents on the pyrazolyl or oxazolinyl moieties can impact the octahedral geometry of the resulting complexes significantly. These structural similarities allow parallels to be drawn from the existing bank of literature on bpp complexes towards the hitherto little-investigated PyBox complexes to help interpret the spin-crossover trends of $[Fe(PyBox)_2]^{2+}$ complexes.

2.2 Aims

The bi-stability of spin-crossover complexes makes them targets for molecular materials, optical and storage devices. If the properties of such complexes could be harnessed, they could be successfully utilised as functional materials. The aim of this work seeks to investigate the impact of chirality on the spin states of a family of $[Fe(PyBox)_2]^{2+}$ complexes in the hope of finding candidates for non-linear optical materials.

2.3 Preparation of PyBox ligands

A range of PyBox ligands were used during the course of this project. The structures and nomenclature used within this chapter are shown in Figure 2.9.

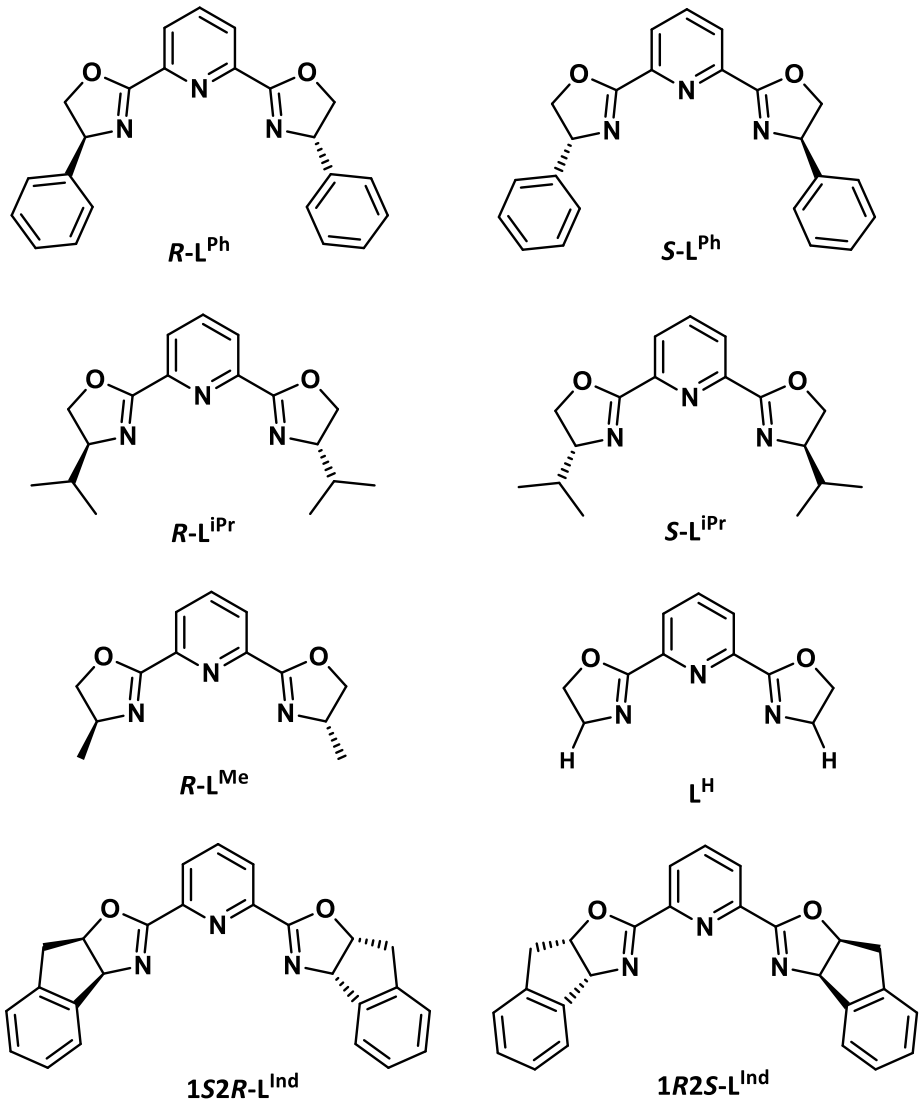

Figure 2.9 - Structures of PyBox ligands.

Ligands ***R*-L^{Ph}**, ***S*-L^{Ph}**, ***R*-L^{iPr}** and ***S*-L^{iPr}** were obtained from Sigma Aldrich, Fluorochem or Insight Biotechnology and were used without further purification. ***R*-L^{Me}**, **L^{H}**, **1*R*2*S*-L^{Ind} and 1*S*2*R*-L^{Ind}** were synthesised according to modified literature

procedures.[9, 21] The original synthesis of compounds ***R*-L^{Me}** and **L^{H}** was undertaken by Sarah McGrath, although the synthetic procedures were repeated by the author.

2.4 Synthesis of iron(II) PyBox complexes

The synthesis of homochiral iron(II) PyBox complexes was achieved by stirring two equivalents of ***R*-L^{Ph}**, ***R*-L^{iPr}** or ***R*-L^{Me}** with one equivalent of iron(II) perchlorate hydrate in acetonitrile at room temperature. The heterochiral complexes were similarly prepared, using one equivalent of ***R*-L^{Ph}** or ***R*-L^{iPr}**, one equivalent of ***S*-L^{Ph}** or ***S*-L^{iPr}** and one equivalent of iron(II) perchlorate hydrate in acetonitrile at room temperature. The achiral complex was synthesised using two equivalents of **L^{H}** and iron(II) perchlorate hydrate in acetonitrile at room temperature. The structures of complexes ***R*-1** - ***R*-3**, ***RS*-1** - ***RS*-2**, **4**, ***R*-5** and ***RS*-5** which feature in this chapter, are shown in Figure 2.10.

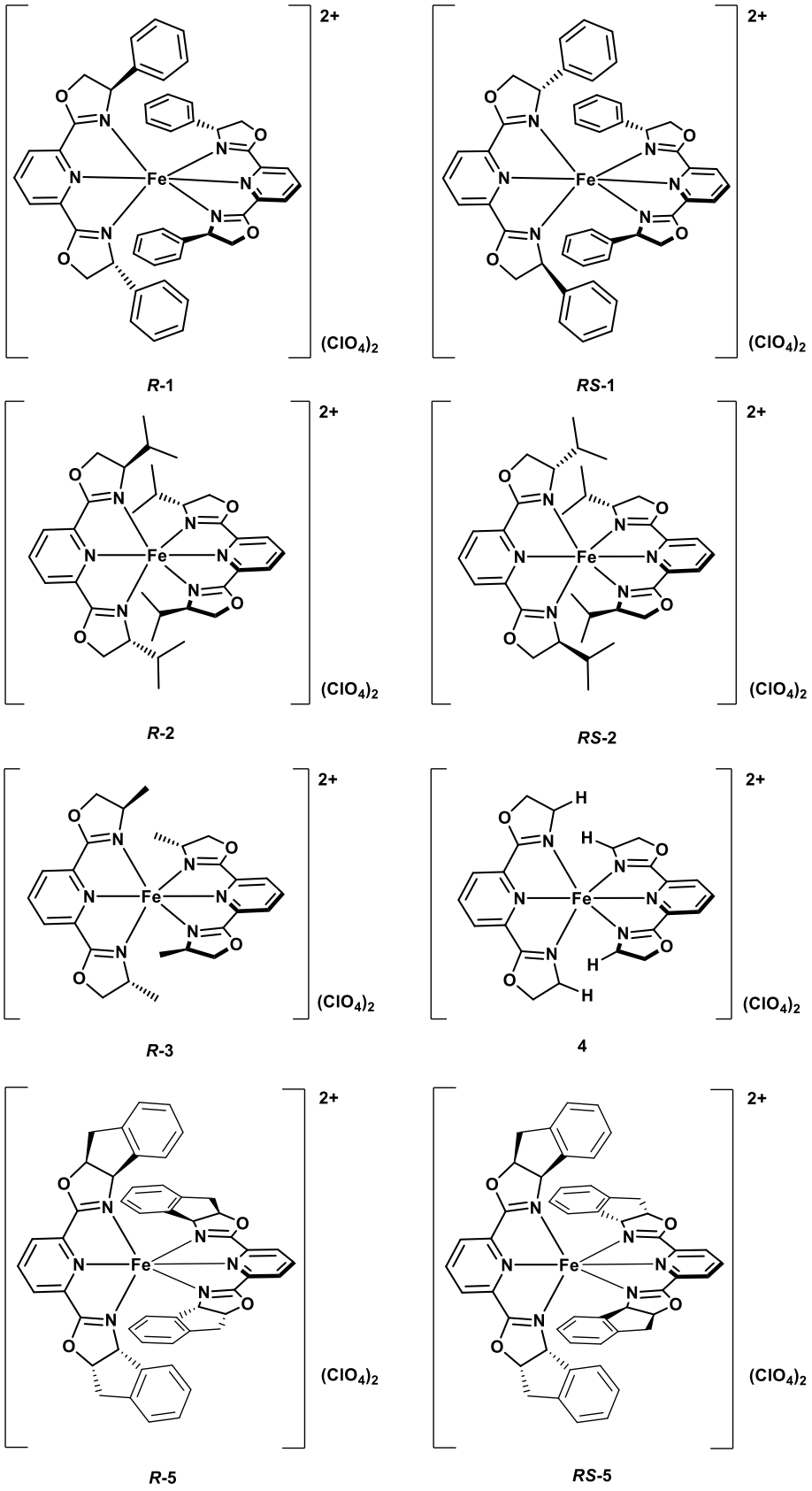

Figure 2.10 - Structures of iron(II) PyBox complexes in this chapter.

Once formed, each complex was structurally characterised by NMR spectroscopy and X-ray crystallography and the magnetic susceptibility in both solution and the solid state was investigated, using Evans method variable temperature NMR spectroscopy and SQUID magnetometry respectively.

2.5 Solid state studies of iron(II) PyBox complexes

2.5.1 Details of single crystal crystallography

Single crystals suitable for x-ray diffraction were grown using vapour diffusion of diethyl ether into a concentrated solution of each complex in acetonitrile or nitromethane. Suitable crystals of **RS-5** could not be grown, despite repeated attempts in different solvents. All data were collected, solved and refined by the author, unless otherwise stated. Structure solutions were achieved using intrinsic phasing through SHELXT[22] and the model was refined using the least squares method using SHELXL[23] interfaced through Olex2.[24] Images were also obtained through Olex2. All non-H atoms were modelled anisotropically at the final least-squares refinement cycles and hydrogen atoms were placed in calculated positions and refined using a riding model.

2.5.2 X-ray-crystallography of homochiral (*R*-1) and heterochiral (*RS*-1)

Homochiral ***R*-1** was crystallised from slow vapour diffusion of diethyl ether into a concentrated nitromethane solution and a full dataset was collected on the same crystal every 10 K between 125 K and 275 K. Selected metric parameters for all of these structures appear in Table 2.2. From 275 K to 175 K, the crystal structure of ***R*-1** solves in the $C222_1$ space group with half a complex cation, one perchlorate anion and one molecule of nitromethane in the asymmetric unit. Disorder was present in both the counterion and solvent molecules. As a result, the oxygen atoms in the counterion were modelled over three positions with occupancies of 0.33. Cl-O bond length restraints of 1.45 Å were applied to the perchlorate molecule. The nitromethane was refined as half a molecule, with both oxygen atoms split with occupancies of 0.25 and the carbon atom

split with occupancies of 0.2 and 0.3. Restraints on the N-C and N-O bond lengths of 1.45 Å and 1.22 Å respectively were used to model the solvent molecule. In addition, bond angle restraints of O-O (2.09 Å) and C-O (2.3 Å) distances were applied. Disorder was also observed on one, or both, crystallographically independent phenyl rings. However, thermal ellipsoids became increasingly enlarged with lower temperatures, reaching maximum disorder at 195 K, which is near the temperature at which the complex becomes fully low-spin. Below 195 K, the trend of disorder is reversed, with thermal ellipsoids becoming smaller and more regular in shape as expected. Between 195 and 175 K, initial anisotropic refinements of the cation gave unreasonably large, elongated thermal ellipsoids, implying that the whole molecule was disordered across the symmetry axis. To account for this, the whole complex cation was modelled across two positions without restraints. The perchlorate counterion showed significant disorder and was modelled across 3 positions with occupancies of 0.3. Fixed bond length restraints of 1.42(2) Å were applied to all Cl-O bonds. The nitromethane molecule was modelled as discussed above. Between 165 and 125 K, ***R*-1** was solved in the space group $P2_12_12_1$, with three complex cations, six perchlorate counterions and three molecules of nitromethane in the asymmetric unit. The only crystallographic restraints used in refinement were fixed bond length restraints applied to disordered phenyl rings. Datasets at 120 K, 250 K and 350 K were collected on the same crystal of ***RS*-1**. At 120 and 250 K, the structure solves in the *P*bca space group and the asymmetric unit contains one complex cation, two perchlorate counterions and three molecules of acetonitrile. As expected, the higher temperature structure shows larger thermal ellipsoids, but does not suffer from unreasonable disorder. As a result, both structures were refined without disorder models.

Figure 2.11 shows that the phenyl substituents of ***R*-1** are angled towards one another in two diagonally opposing quadrants, causing close steric contact. As a result of this contact, two of the phenyl rings are twisted out of the plane, causing ortho C-H groups to be angled towards the pyridyl motif of the opposing ligand. The second pair of phenyl rings are almost parallel to the pyridyl of the other ligand, causing a slightly offset, stacked π–π interaction. Both twisted phenyl rings are on one PyBox ligand, whilst both stacked phenyl moieties are substituents of the other ligand. This is

consistent with other $[M(R\text{-}L^{Ph})_2]^{2+}$ complexes, where M = Co and Cu and the triflate salt of the zinc(II) complex.[25-28] In contrast, the $[Zn(R\text{-}L^{Ph})_2][BF_4]_2$ complex shows a different pattern, with one twisted and one stacked phenyl moiety on each ligand. This is discussed further in Chapter 3. ***RS*-1 (**Figure 2.11**,** right) shows no steric clash between phenyl rings, as the moieties are all oriented away from each other into different quadrants of the complex. This geometry is also seen in cobalt(II) and zinc(II) analogues of the complex (Chapter 3).

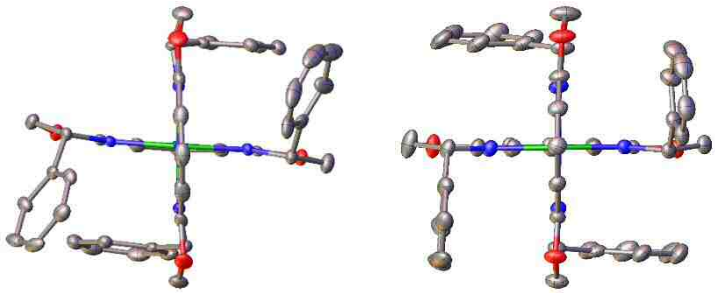

Figure 2.11 - Crystal structures of *R*-1 at 125 K (left) and *RS*-1 at 120 K (right). Counterions and hydrogen atoms are omitted for clarity. Colour code: Fe, green; C, grey; N, blue; O, red.

Selected bond lengths are given in Table 2.2 and analysis of Fe-N bond lengths can be used to gain an insight into the spin states of the complexes. Iron(II) low-spin complexes typically have Fe-N bond lengths of 1.8-2.0 Å, whereas the Fe-N bond lengths of high-spin complexes are 2.0-2.2 Å.[29]

The Fe-N bond lengths of ***R*-1** show a gradual increase between 125 and 275 K, which indicate that a spin transition is occurring, although a definitive high-spin state is not seen. The crystal structure data for ***RS*-1** at both 120 K and 250 K indicate that the complex is low-spin at both of these temperatures. Thus the crystallographic data for both complexes are consistent with the solid state magnetic behaviour discussed in Section 2.5.7.

2.5.3 X-ray crystallography of homochiral (*R*-2) and heterochiral (*RS*-2)

The dataset of homochiral ***R*-2** was collected at 120 K and was solved in the $P2_12_12_1$ space group. There are two complex molecules, four perchlorate counterions and one molecule of acetonitrile in the asymmetric unit. One perchlorate counterion showed significant disorder and was modelled over two positions using oxygen occupancies of 0.5 and fixed bond restraints of Cl-O - 1.42 Å (2). Heterochiral ***RS*-2** was solved in the $P2_1/n$ space group with one complex and two perchlorate counterions in the asymmetric unit. All non-H atoms and the ordered perchlorate counterions were refined anisotropically. This dataset refined with no significant disorder and therefore no restraints were necessary.

Figure 2.12 shows the crystal structures of ***R*-2** and ***RS*-2** in which trends similar to those seen in ***R*-1** and ***RS*-1** can be observed. In ***R*-2**, the isopropyl substituents are oriented into two opposite quadrants of the complex, exerting a steric influence on the PyBox ligand framework. The rotational flexibility of isopropyl groups is greater than that of phenyl rings and therefore a steric clash similar to that seen in **R-1** is precluded. However, a CH-π interaction between one isopropyl group and pyridyl or oxazolinyl ring is present and it is this repulsion that leads to a significant distortion of the octahedral geometry of the complex which is much greater than that seen for ***R*-1**. In contrast, the isopropyl groups of ***RS*-2** are angled into four separate quadrants, reducing the steric impact of the substituents. These geometries are also seen in zinc(II) and cobalt(II) analogues, as discussed in Chapter 3. The Fe-N bond lengths in Table 2.2 for ***R*-2** and ***RS*-2** are between 2.1 and 2.2 Å and thus show both complexes are high-spin at 120 K. This observation is consistent with the solid state magnetic behaviour discussed in section 2.5.7.

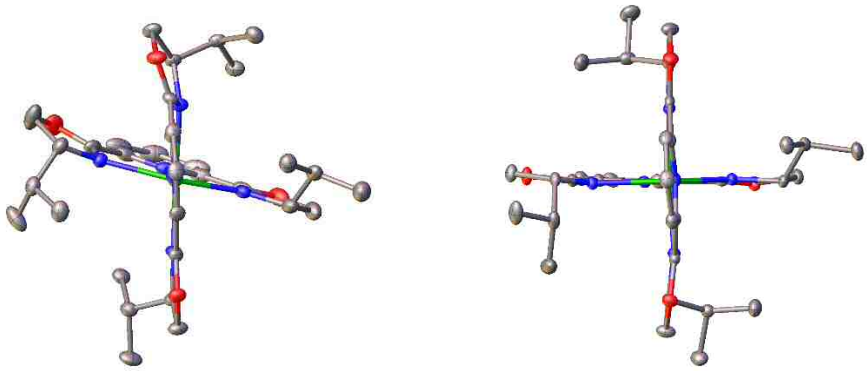

Figure 2.12 - Crystal structures of R-2 (left) and RS-2 (right). Counterions and hydrogen atoms are omitted for clarity. Colour code: Fe, green; C, grey; N, blue; O, red.

2.5.4 X-ray crystallography of homochiral (*R*-3) and achiral 4

Complexes ***R*-3** and **4** were first synthesised by Sarah McGrath, crystallographic data collection was carried out by Dr Rafal Kulmaczewski and the structures were solved and refined by Professor Malcolm Halcrow.

Homchiral ***R*-3** was crystallised from vapour diffusion of diethyl ether into a concentrated solution of the complex in acetonitrile. A dataset was collected at 130 K. The structure solves in the $P3_121$ space group with half a complex cation and one perchlorate counterion in the asymmetric unit. Achiral **4** was crystallised from vapour diffusion of diethyl ether into a concentrated solution of the complex in acetonitrile. A dataset was collected on the same crystal at 240 K and 350 K. At both temperatures, the structures solved in the space group $P2_1/n$, with one complex cation and two perchlorate counterions in the asymmetric unit. One counterion is disordered at both temperatures and was modelled over two positions with chlorine and oxygen occupancies of 0.5 and with refined restraints Cl-O - 1.42(2) and O…O = 2.32(2) Å.

***R*-3** has methyl substituents on opposite ligands oriented to the same quadrant. However, methyl groups have a much reduced steric bulk compared to phenyl and isopropyl groups, thus minimising the steric clash of the substituents. There is no geometric distortion as a direct result of the substituents, although there are electronic ramifications on the spin state as a result of the electron donating nature of the methyl groups. Achiral **4** bears no substituents and as such the geometry is unaffected by steric

effects. Table 2.2 indicates that ***R*-3** is high-spin at 130 K as the bond lengths are between 2.1 and 2.2 Å. The lower temperature dataset of **4** indicates that the complex is low-spin, whilst the data from 350 K shows the longer bond lengths associated with a high-spin complex. The observations for both ***R*-3** and **4** are consistent with the solid state magnetic behaviour discussed in Section 2.5.7.

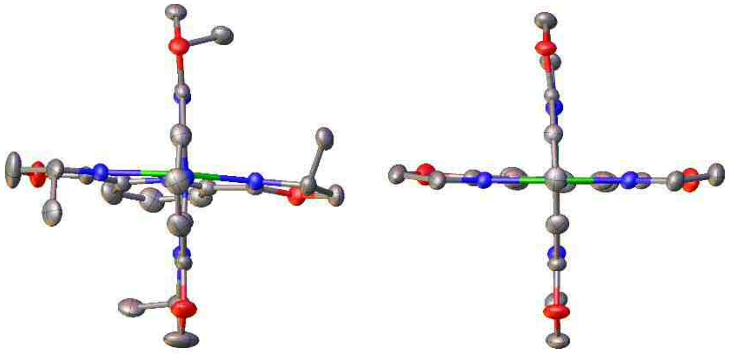

Figure 2.13 - Crystal structures of *R*-3 at 130 K (left) and 4 at 240 K (right). Counterions and hydrogen atoms are omitted for clarity. Colour code: Fe, green; C, grey; N, blue; O, red.

2.5.5 X-ray crystallography of homochiral (*R*-5)

The dataset of homochiral ***R*-5** was collected at 125 K and the structure was solved in the $P3_121$ space group. The asymmetric unit contains two half complex cations and two perchlorate counterions. The dataset refined with no significant disorder and therefore no constraints or restraints were necessary. The Fe-N bonds lengths indicate a high-spin complex.

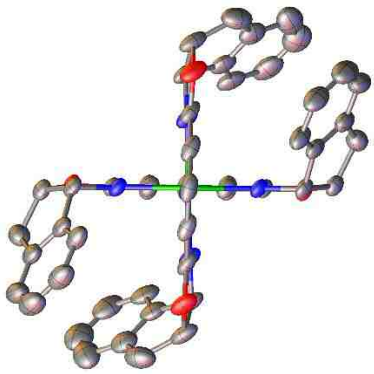

Figure 2.14 - Crystal structure of *R*-5 at 125 K. Counterions and hydrogen atoms are omitted for clarity. Colour code: Fe, green; C, grey; N, blue; O, red.

Table 2.2 - Selected crystallographic metric parameters for *R*-1, *RS*-1, *R*-2, *RS*-2, *R*-3, 4, *R*-5 and *RS*-5.

	***R*-1 Molecule 1 125 K**	***R*-1 Molecule 2 125 K**	***R*-1 Molecule 3 125 K**	***R*-1 Molecule 1 135 K**	***R*-1 Molecule 2 135 K**	***R*-1 Molecule 3 135 K**	***R*-1 Molecule 1 145 K**	***R*-1 Molecule 2 145 K**	***R*-1 Molecule 3 145 K**
Crystal system	Orthorhombic	-	-	Orthorhombic	-	-	Orthorhombic	-	-
Space group	$P2_12_12_1$	-	-	$P2_12_12_1$	-	-	$P2_12_12_1$	-	-
a / Å	13.5606(2)	-	-	13.5653(2)	-	-	13.5722(2)	-	-
b / Å	21.9177(3)	-	-	21.9353(3)	-	-	21.9562(3)	-	-
c / Å	46.1753(6)	-	-	46.2136(6)	-	-	46.2235(7)	-	-
α / Å	90	-	-	90	-	-	90	-	-
β / Å	90	-	-	90	-	-	90	-	-
γ / Å	90	-	-	90	-	-	90	-	-
Volume / Å^3	13724.1(3)	-	-	13751.3(3)	-	-	13774.3(3)	-	-
Fe-N(pyridyl)	1.897(3) - 1.908(3)	1.902(3) - 1.908(3)	1.901(3) - 1.908(3)	1.898(4) - 1.906(3)	1.906(3) - 1.910(3)	1.899(4) - 1.905(4)	1.896 (3) - 1.907(3)	1.906(3) - 1.910(3)	1.898(3) - 1.902(3)
Fe-N(oxazolinyl)	1.983(3) - 2.011(3)	1.981(4) - 2.018(4)	1.976(3) - 2.014(3)	1.976(4) - 2.005(4)	1.978(3) - 2.014(4)	1.973(4) - 2.012(4)	1.979(3) - 2.008(3)	1.986(3) - 2.015(3)	1.973(3) - 2.012(3)
ϕ	178.25(14)	179.45(13)	177.66(15)	178.30(16)	179.44(14)	177.71(16)	178.24(15)	179.56(13)	177.99(15)
θ	88.97(14)	89.96(13)	88.29(14)	84.86(14)	85.37(14)	84.84(14)	89.10(14)	89.92(13)	88.22(14)

	***R*-1 Molecule 1 155 K**	***R*-1 Molecule 2 155 K**	***R*-1 Molecule 3 155 K**	***R*-1 Molecule 1 165 K**	***R*-1 Molecule 2 165 K**	***R*-1 Molecule 3 165 K**	***R*-1 175 K**	***R*-1 185 K**	***R*-1 195 K**
Crystal system	Orthorhombic	-	-	Orthorhombic	-	-	Orthorhombic	Orthorhombic	Orthorhombic
Space group	$P2_12_12_1$	-	-	$P2_12_12_1$	-	-	$C222_1$	$C222_1$	$C222_1$
a / Å	13.5830(3)	-	-	13.5894(2)	-	-	13.6091(7)	13.6121(5)	13.6440(7)
b / Å	21.9776(4)	-	-	21.9877(3)	-	-	15.4458(5)	15.4521(3)	15.4556(5)
c / Å	46.2647(10)	-	-	46.2804(6)	-	-	22.0008(6)	22.0403(4)	22.0532(9)
α / Å	90	-	-	90	-	-	90	90	90
β / Å	90	-	-	90	-	-	90	90	90
γ / Å	90	-	-	90	-	-	90	90	90
Volume / Å^3	13811.0(5)	-	-	13828.6(3)	-	-	4624.6(3)	4635.9(2)	4650.5(3)
Fe-N(pyridyl)	1.897(4) - 1.902(4)	1.905(4) - 1.910(4)	1.898(4) - 1.903(4)	1.894(4) - 1.903(4)	1.904(4) - 1.908(4)	1.987(4) - 1.904(4)	1.908(7) - 1.913(9)	1.902(6) - 1.915(8)	1.903(6) - 1.928(8)
Fe-N(oxazolinyl)	1.978(4) - 2.008(4)	1.978(4) - 2.018(4)	1.972(4) - 2.013(4)	1.977(4) - 2.009(4)	1.980(4) - 2.016(4)	1.972(4) - 2.013(4)	1.921(18) - 2.090(18)	1.963(13) - 2.050(13)	1.911(14) - 2.052(15)
Φ	178.43(16)	179.54(15)	178.11(17)	178.43(17)	179.57(15)	178.29(17)	175.0(11)	176.0(7)	172.5(7)
Θ	85.95(15)	85.29(15)	84.86(15)	85.74(15)	85.26(15)	84.86(15)	87.3(8)	88.8(5)	87.3(5)

	***R*-1** **205 K**	***R*-1** **215 K**	***R*-1** **225 K**	***R*-1** **235 K**	***R*-1** **245 K**	***R*-1** **255 K**	***R*-1** **265 K**	***R*-1** **275 K**
Crystal system	Orthorhombic	Orthorhombic	Orthorhombic	Orthorhombic	Orthorhombic	Orthorhombic	Orthorhombic	Orthorhombic
Space group	$C222_1$	$C222_1$	$C222_1$	$C222_1$	$C222_1$	$C222_1$	$C222_1$	$C222_1$
a / Å	13.6394(4)	13.6536(8)	13.6597(2)	13.6774(2)	13.6981(2)	13.7187(2)	13.7381(2)	13.7609(2)
b / Å	15.4799(6)	15.5170(13)	15.5090(3)	15.5213(2)	15.5267(2)	15.5385(2)	15.5434(2)	15.5459(2)
c / Å	22.1071(7)	22.1583(15)	22.2122(3)	22.2671(3)	22.2986(3)	22.3009(2)	22.3120(2)	22.3234(3)
α / Å	90	90	90	90	90	90	90	90
β / Å	90	90	90	90	90	90	90	90
γ / Å	90	90	90	90	90	90	90	90
Volume / Å^3	4667.6(3)	4694.5(6)	4705.62(13)	4727.11(11)	4742.61(11)	4753.84(10)	4764.43(10)	4775.55(11)
Fe-N(pyridyl)	1.902(7) - 1.910(7)	1.910(8) - 1.913(7)	1.914(6) - 1.926(6)	1.927(5) - 1.933(6)	1.934(5) - 1.937(6)	1.939(5) - 1.945(6)	1.945(5) - 1.948(6)	1.948(5) - 1.955(5)
Fe-N(oxazolinyl)	1.988(5) - 2.014(6)	1.992(5) - 2.023(6)	1.984(4) - 2.022(5)	1.997(4) - 2.034(4)	2.002(4) - 2.040(4)	2.005(4) - 2.043(4)	2.008(4) - 2.046(4)	2.013(4) - 2.052(4)
Φ	180.0	180.0	180.0	180.0	180.0	180.0	180.0	180.0
Θ	88.8(2)	84.6(2)	88.48(17)	78.75(12)	84.24(16)	84.21(17)	84.10(16)	84.03(15)

	***RS*-1** **120 K**	***RS*-1** **250 K**	***R*-2** **Molecule 1** **120 K**	***R*-2** **Molecule 2** **120 K**	***RS*-2** **120 K**	***R*-3 *** **130 K**	**4** **240 K**	**4** **350 K**
Crystal system	Orthorhombic	Orthorhombic	Orthorhombic	-	Monoclinic	Trigonal	Monoclinic	Monoclinic
Space group	*P*bca	*P*bca	$P2_12_12_1$	-	$P2_1/n$	$P3_121$	$P2_1/n$	$P2_1/n$
a / Å	20.58612(19)	20.7512(3)	12.61331(17)	-	9.21136(10)	10.4565(2)	15.4989(2)	15.8967(5)
b / Å	21.4992(2)	21.7685(4)	15.4887(3)	-	23.2381(2)	10.4565(2)	10.7135(1)	10.8528(3)
c / Å	22.5026(2)	22.6230(3)	41.0876(7)	-	17.78023(17)	24.7573(4)	17.0653(2)	1878.1038(6)
α / Å	90	90	90	-	90	90.00	90.00	90.00
β / Å	90	90	90	-	95.5540(10)	90.00	103.426(1)	103.323(4)
γ / Å	90	90	90	-	90	120.00	90.00	90.00
Volume / Å^3	9959.34(17)	10219.3(3)	8027.0(2)	-	3788.07(7)	2344.26(7)	2756.21(5)	2871.39(16)
Fe-N(pyridyl)	1.9054(18) - 1.9123(18)	1.9103(19) - 1.9116(19)	2.188(4) - 2.121(4)	2.119(4) - 2.132(4)	2.1171(14) - 2.1344(14)	2.137(2)	1.899(3) - 1.905(3)	1.993(4) - 2.003(5)
Fe-N(oxazolinyl)	1.978(2) - 1.9861(19)	1.979(2) - 1.992(2)	2.245(4) - 2.277(4)	2.226(4) - 2.296(4)	2.2009(14) - 2.2770(15)	2.1883(19) - 2.207(2)	1.977(3) - 1.994(3)	2.068(5) - 2.081(5)
ϕ	178.19(8)	178.37(9)	175.35(16)	165.47(17)	163.63(6)	170.91(11)	179.05(11)	178.07(18)
θ	88.72(7)	92.26(8)	76.75(16)	78.68(16)	89.23(5)	86.50(3)	87.30(11)	85.60(19)

***** The complex cation in this crystal has crystallographic C_2 symmetry, with half a molecule in its asymmetric unit.

	***R*-5 * Molecule 1 125 K**	***R*-5 * Molecule 2 125 K**
Crystal system	Trigonal	Trigonal
Space group	$P3_121$	$P3_121$
a / Å	14.64476(13)	14.64476(13)
b / Å	14.64476(13)	14.64476(13)
c / Å	38.2045(4)	38.2045(4)
α / Å	90	90
β / Å	90	90
γ / Å	120	120
Volume / Å^3	7095.92(14)	7095.92(14)
Fe-N(pyridyl)	2.120(5) - 2.123 (5)	2.121(6) - 2.123(5)
Fe-N(oxazolinyl)	2.220(4) - 2.227(4)	2.213(4) - 2.232(4)
ϕ	180.0	180.0
θ	87.36(14)	88.39(14)

***** ***R*-5** contains two half complex cations in the asymmetric unit.

2.5.6 X-ray powder diffraction

X-ray powder diffraction data were obtained for all complexes in this chapter. The simulated powder patterns were obtained using Mercury[30, 31] and were based on the crystal structures discussed above. Powder diffraction experiments were performed on samples of fresh material. Where a single crystal x-ray diffraction experiment had been gathered at more than one temperature, the dataset closest to room temperature was used to simulate the powder pattern.

The powder patterns and simulated patterns for complexes ***R*-1**, ***R*-2**, ***RS*-1**, ***RS*-2**, ***R*-3** and **4** are shown in Figure 2.15. The powder pattern for each complex shows good agreement with the simulated patterns. This indicates that the bulk solid sample has the same structure as the single crystals. In particular, there is no evidence for contamination of ***RS*-1** and ***RS*-2** by their homochiral counterparts.

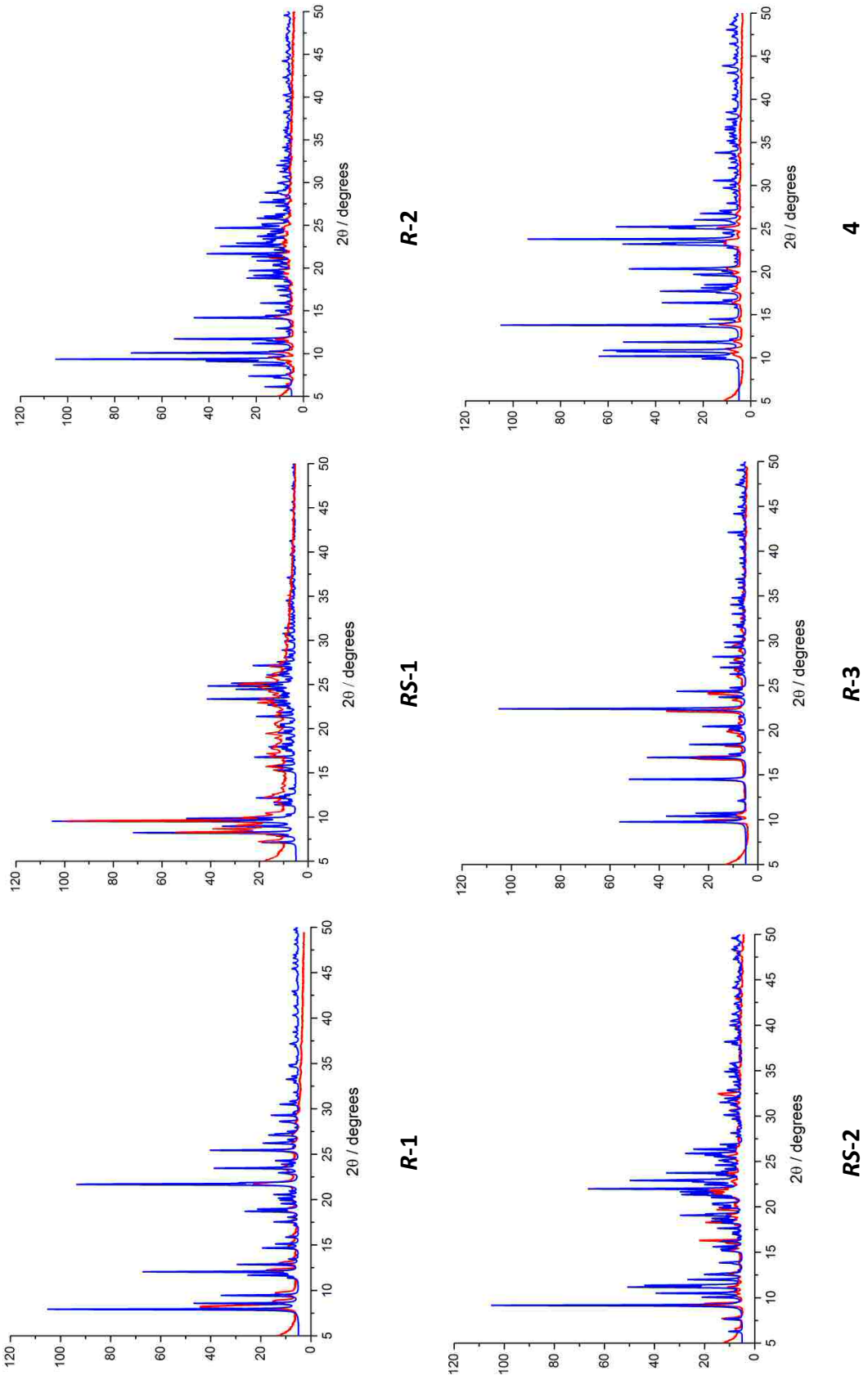

Figure 2.15 - Powder diffraction patterns (red) and simulated powder patterns (blue) for all complexes.

2.5.7 Solid state magnetic susceptibility

Solid state magnetic susceptibility measurements for ***R*-1**, ***RS*-1**, ***R*-2**, ***RS*-2**, ***R*-3**, **4**, ***R*-5** and ***RS*-5** were measured using a Super-Conducting Quantum Interference Device (SQUID) in a magnetic field of 0.5 T. These results are shown in Figure 2.16, alongside the $T_{1/2}$ values for each complex. Measurements were performed on samples of fresh material, which had been analysed by x-ray powder diffraction to ensure it was structurally identical to the samples used for single crystal x-ray diffraction and showed bulk phase purity.

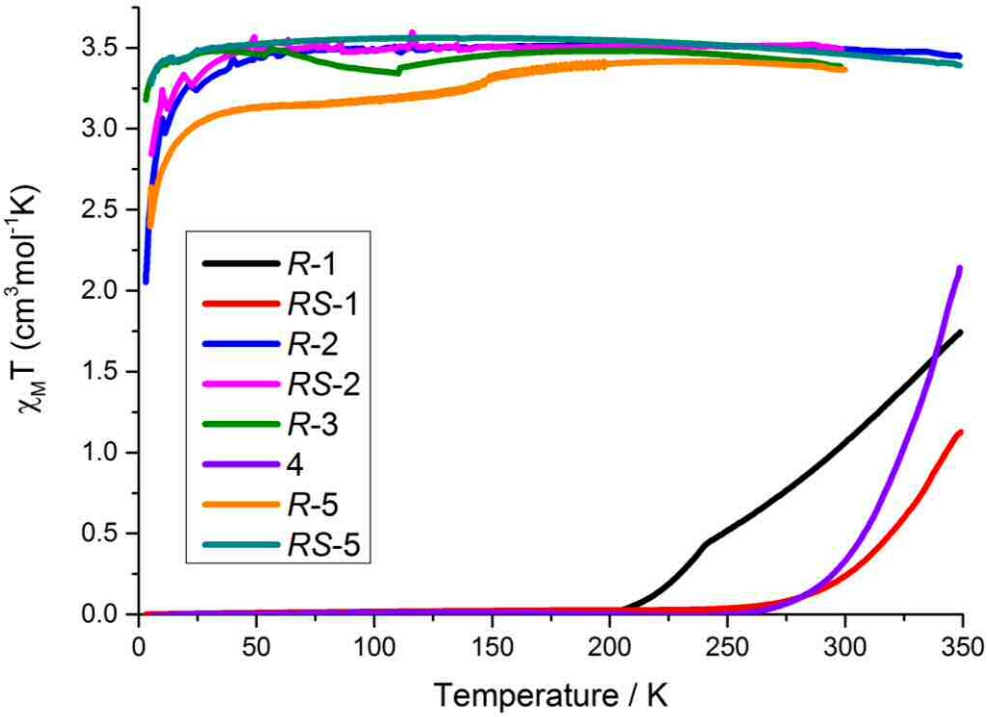

Complex	$T_{1/2}$ / K	Complex	$T_{1/2}$ / K	Complex	$T_{1/2}$ / K	Complex	$T_{1/2}$ / K
***R*-1**	~ 350	***R*-2**	HS	***R*-3**	HS	***R*-5**	HS
***RS*-1**	~400	***RS*-2**	HS	**4**	~ 350	***RS*-5**	HS

Figure 2.16 - Solid state magnetic susceptibility of complexes *R*-1 (black), *RS*-1 (red), *R*-2 (blue), *RS*-2 (magenta), *R*-3 (green), 4 (purple), *R*-5 (orange) and *RS*-5 (cyan), measured by SQUID. $T_{1/2}$ values for all complexes are given in the accompanying table. Complexes *R*-1, *RS*-1, *R*-2, 4 and *RS*-5 were measured between 5 K and 350 K. *R*-2, *RS*-2, *R*-3 and *R*-5 were measured between 5 K and 300 K.

Complexes ***R*-2**, ***RS*-2**, ***R*-3** and ***RS*-5** remain high-spin across the measured temperature range. The apparent decrease in magnetic susceptibility at very low temperatures is the effect of zero field splitting and thus does not indicate a transition in spin-state. ***R*-5** remains high-spin, although there is a small drop in $\chi_M T$ at around 150 K, which is likely to be the result of a small proportion of the sample (~ 5%) changing spin state. In contrast, ***R*-1**, ***RS*-1** and **4** undergo gradual, thermal spin-crossover. All three complexes have $T_{1/2}$ values which are significantly above room temperature.

***R*-1** undergoes gradual, non-hysteretic thermal spin-crossover with a discontinuity at approximately 240 K. The $T_{1/2}$ temperature is ~350 K, estimated from the $\chi_M T$ value of 1.8 $cm^3mol^{-1}K$ at that temperature. Discontinuous spin-crossover transitions such as these are not uncommon and can be the result of various features of solid state samples, including the presence of multiple independent switching sites in the lattice[32-34], a crystallographic phase transition during spin-crossover[35] or an order:disorder transition in the ligand or anion.[36, 37] This discontinuity was probed further using x-ray diffraction experiments of ***R*-1** on the same crystal which were collected every 10 K between 125 K and 275 K. The crystallographic phase change, discussed in section 2.5.2, which was discovered during refinement occurs independently of the discontinuity observed in the magnetic measurements.

Figure 2.17 shows the magnetic and crystallographic measurements plotted together, which show excellent agreement despite some scatter. The temperature at which the crystallographic phase change occurs is also marked. It is particularly interesting that the crystallographic measurements, plotted as the octahedral volume of the cations, reproduce the discontinuity near 240 K. Also observed at around 220 K is a slight inflection which can be associated with a decrease in the *c* dimension which occurs on cooling from 240 K to 200 K (Table 2.2).

In phase 2, the complex cations have C_2 symmetry and the unique axes align with the *b* axis. The meridional ligands are oriented on the (010) plane with the most disordered phenyl rings parallel to the *c* axis. This indicates that the decrease in *c* when the sample is cooled from 240 K to 200 K is the result of the increased ligand disorder over that temperature range. The size and arrangement of the thermal ellipsoids is

consistent with this observation. Therefore the spin-crossover discontinuity at 240 K shown by both the crystallographic and magnetic measurements reflects the increased ligand disorder below 240 K. This may be indicative of a mismatch between the spin transition and the contraction of the crystal lattice on cooling the sample below 240 K

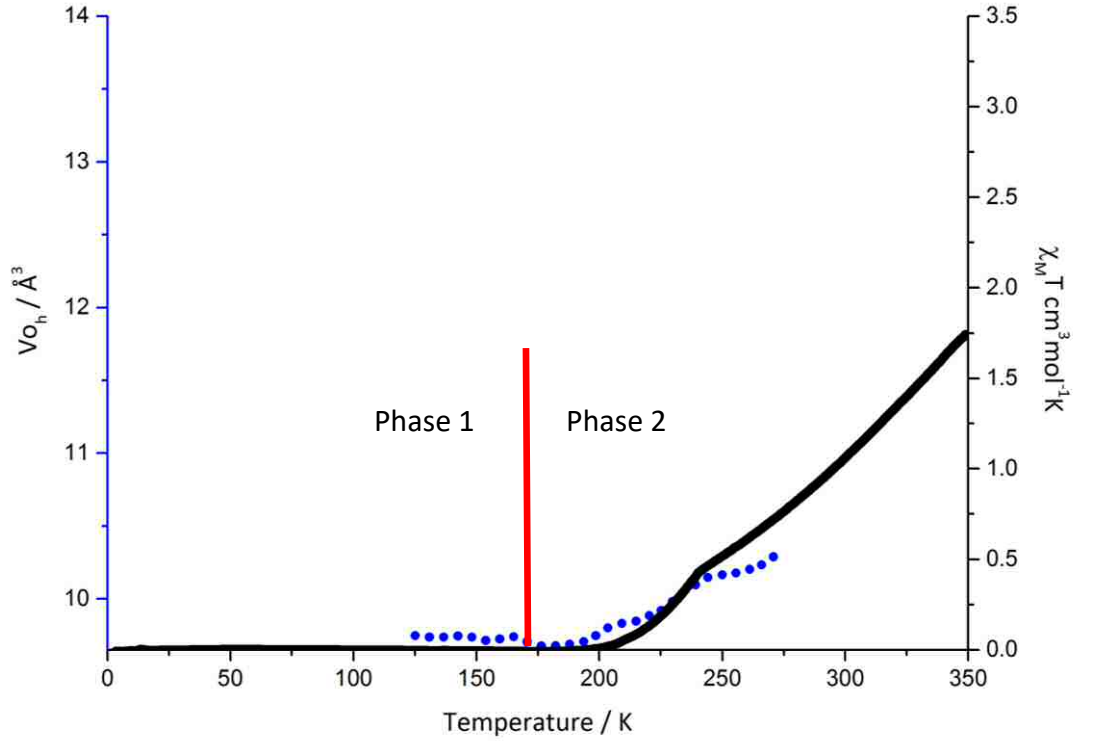

Figure 2.17 - The spin-crossover behaviour of *R*-1 monitored by magnetic susceptibility (black line) and V_{Oh} (blue dotted line). The crystallographic phase change temperature is shown by the red line.

2.5.8 Magneto-structural correlations of $[Fe(PyBox)_2]^{2+}$ complexes

As discussed in 2.1.4, an extensive study into the spin states of $[Fe(bpp)_2]^{2+}$ complexes revealed a link between a distorted geometry, stemming from the trans N-Fe-N (ϕ) and dihedral angles (θ), and a trapped high-spin state.[17] Such complexes are effectively trapped in this state by the inability of the complex to undergo a physical rearrangement as a result of Jahn-Teller distortion imposed by the electronic configuration of the high-spin state. As a result, these complexes rarely undergo spin-crossover upon cooling. Given the parallels between ligand structure and octahedral

geometry experienced by $[Fe(bpp)_2]^{2+}$ and $[Fe(PyBox)_2]^{2+}$ complexes, the above reasoning, in conjunction with the solid state magnetic and crystallographic behaviour previously discussed, can be applied to the $[Fe(PyBox)_2]^{2+}$ complexes in this work to explain the observed spin state behaviour.

Table 2.3 shows ϕ and θ angles for complexes ***R*-1** - ***R*-5**. Despite numerous attempts, ***RS*-5** could not be crystallised. Complexes ***R*-2** and ***RS*-2** exhibit ϕ and θ angles which would disfavour spin-crossover, explaining their high-spin state. Homochiral ***R*-2** also suffers from steric interactions between isopropyl substituents oriented into the same quadrant which further exacerbates the distortion of the complex, whilst heterochiral ***RS*-2** does not experience this steric effect. ***R*-1** and ***RS*-1** do not show significant Jahn-Teller distortion and are therefore capable of undergoing spin-crossover, which is indeed observed in the magnetic behaviour. However, as with ***R*-2**, the steric clash between the phenyl substituents of ***R*-1** impacts the geometry of the complex, as homochiral ***R*-1** shows slightly more distortion than the heterochiral diastereomer. The low temperature, low-spin structure of **4** shows almost no deviation of the geometry, although as expected there is a slight increase in distortion at 350 K when the complex has transitioned to its high-spin form. Given the lack of substituents, there are no substituent effects at play for this complex. Homochiral ***R*-3** shows ϕ and θ angles which suggest a trapped high-spin state. Whilst there are no steric, substituent effects in this complex due to the small size of the methyl groups, the electron donating nature of the substituent would likely reduce M-L back bonding into the oxazolinyl ring. This would have the effect of weakening the ligand field and thus favouring the observed high spin form. This fully high-spin behaviour is contrary to the solution phase data, in which the complex does undergo spin-crossover. This discrepancy will be discussed further in Section 2.6.2. Complexes ***R*-2** and ***RS*-2** are also likely to experience this electronic effect due to the electron donating nature of the isopropyl substituents. ***R*-5** does not show particularly profound distortion of θ and ϕ is strictly 180° due to the N-Fe-N unit lying on a mirror plane. Significant distortion of the complex as a whole is not present. The lack of crystallographic parameters for the heterochiral counterpart, ***RS*-5**, means that a comparison of the two geometries is not possible, however the high-

spin behaviour in the solid state could be a result of π-π interactions between the extended aromatic system of the substituents locking the complex in its geometry.

Table 2.3 - Crystallographic data showing trans N-Fe-N angle (ϕ) and dihedral angles (θ).

	***R*-1 Molecule 1 125 K**	***R*-1 Molecule 2 125 K**	***R*-1 Molecule 3 125 K**	***RS*-1 120 K**	***RS*-1 250 K**	***R*-2 Molecule 1 120 K**	***R*-2 Molecule 2 120 K**
ϕ	178.25(14)	179.45(13)	177.66(15)	178.19(8)	178.37(9)	175.35(16)	165.47(17)
θ	88.97(14)	89.96(13)	88.29(14)	88.72(7)	92.26(8)	76.75(16)	78.68(16)
	***RS*-2 120 K**	***R*-3 *[1] 130 K**	**4 240 K**	**4 350 K**	***R*-5**	***RS*-5 *[2]**	
ϕ	163.63(6)	170.91(11)	179.05(11)	178.07(18)	180.0	180.0	
Θ	89.23(5)	86.50(3)	87.3(11)	85.60(19)	87.36(14)	88.39(14)	

*[1] ***R*-3** has crystallographic C_2 symmetry, with half a molecule in its asymmetric unit. *[2] ***R*-5** contains two half complex cations in the asymmetric unit.

2.6 Solution phase studies of iron(II) PyBox complexes

2.6.1 Solution phase stability of *RS*-1 and *RS*-2

Previous ^{1}H NMR studies have shown that heterochiral *RS*-$[M(L^{Ph})_2]^{2+}$ PyBox complexes, where M = Co and Zn, do not racemise by undergoing ligand exchange to form *R*-$[M(L^{Ph})_2]^{2+}$ and *S*-$[M(L^{Ph})_2]^{2+}$, and are therefore are stable in solution.[25, 28] This trend has also been seen in the gas phase by mass spectrometry.[38]

In order to fully understand the solution phase behaviour of the iron(II) complexes contained in this chapter, an NMR investigation into the solution phase stability of *RS*-$[Fe(L^{Ph})_2]^{2+}$ and *RS*-$[Fe(L^{iPr})_2]^{2+}$ was conducted. NMR samples were prepared by dissolving 5mg of ***R*-1**, ***RS*-1**, ***R*-2** and ***RS*-2** in acetontitrile-d_3. Additional samples, which contained 2.5 mg of both ***R*-1** and ***RS*-1**, and 2.5 mg of both ***R*-2** and ***RS*-2** were also prepared. Figure 2.18 shows the NMR spectra for ***R*-1**, ***RS*-1** and the mixed sample. The NMR spectra for the homochiral and heterochiral complexes are different, and thus the peaks are characteristic of the environments in each complex. Comparison of the spectra for ***R*-1** and ***RS*-1** reveal that there are no peaks present in the spectrum for heterochiral ***RS*-1** that can be attributed to homochiral ***R*-1**. Examination of the bottom spectrum in Figure 2.18 reveals a 1:1 ratio of both homochiral and heterochiral complexes, which is as expected given the method of sample preparation.

The NMR sample for ***R*-2**, ***RS*-2** and the mixed samples can be seen in Figure 2.19. In contrast to the spectra seen in Figure 2.18, the spectrum for ***RS*-2** shows peaks that are attributed to homochiral ***R*-2**. This suggests that ligand redistribution had occurred, causing some formation of ***R*-2** and its equivalent ***S*-2**.

The discrepancies in observable partial racemisation between ***RS*-1** and ***RS*-2** can be accounted for by differences in substituent effects between the isopropyl and phenyl groups. As discussed, the homochiral complexes show interactions between the substituents which are oriented towards the same quadrant. The extent of these interactions is different depending on the steric qualities of the substituent in

question. CH-π interactions are seen between the isopropyl groups and pyridyl or oxazolinyl rings in complex ***R*-2**, whereas the phenyl groups of ***R*-1** are in such close proximity to one another that two of the phenyl rings are twisted out of the plane. It is therefore likely that the proximity of these phenyl moieties in ***R*-1** is enough to disfavour the long-term formation of the homochiral complex when the option of forming the heterochiral analogue is present, although clearly it is not sufficient to preclude formation of the homochiral complex. In contrast though, there is reduced steric clash between isopropyl substituents which allows the exchange of homochiral and heterochiral products in solution.

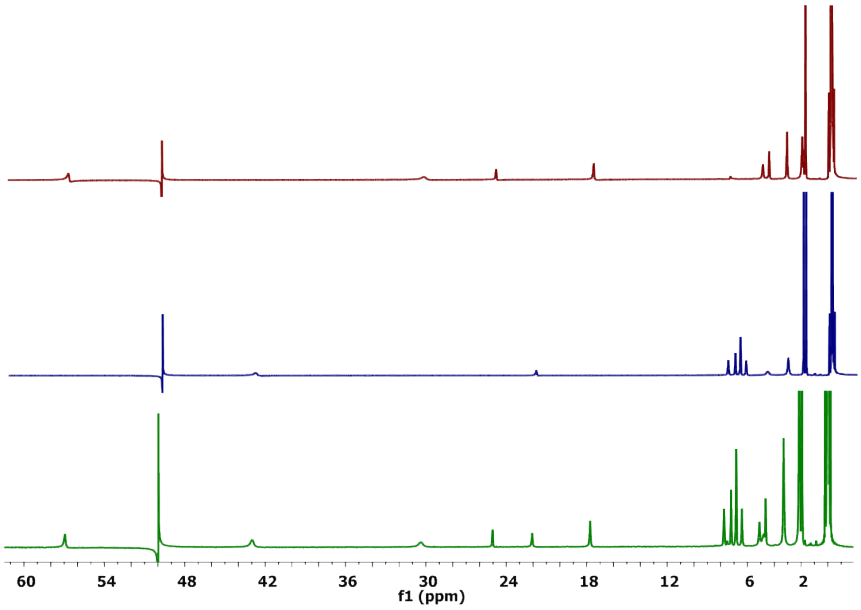

Figure 2.18 - ^{1}H NMR spectra of *R*-1 (red, top), *RS*-1 (blue, middle) and a 1:1 ratio of both *R*-1 and *RS*-1 (green, bottom) in CD_3CN. The feature at ~50 ppm is a spectrometer artefact.

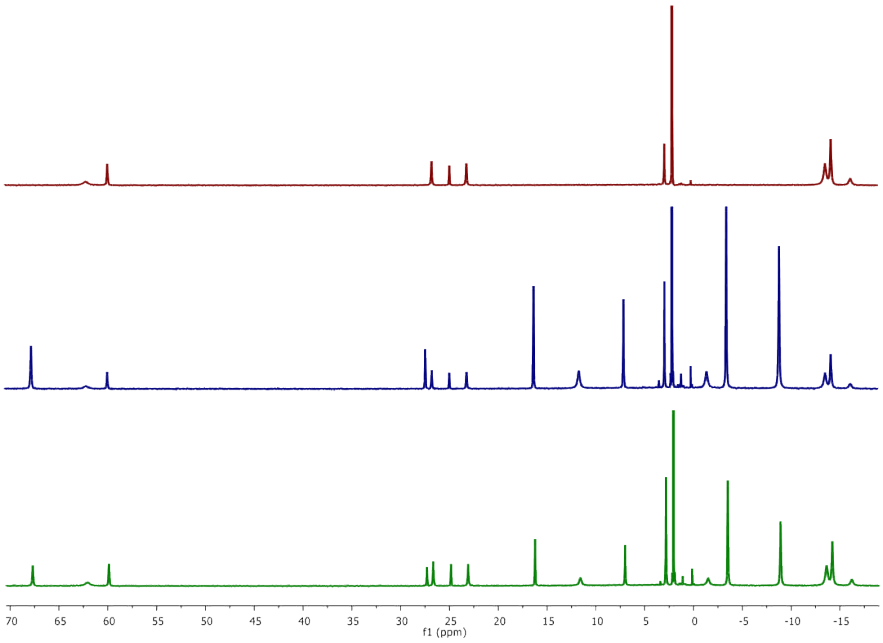

Figure 2.19 - ^{1}H NMR spectra of R-2 (red, top), RS-2 (blue, middle) and a 1:1 ratio of both R-2 and RS-2 (green, bottom) in $(CD_3)_2CO$.

It was apparent from the initial NMR experiment that the racemisation of ***RS*-2** did not go to completion. To monitor this, further NMR experiments were conducted on the same sample at 5 minutes, 1 hour, 5 hour and 24 hour intervals after sample preparation. The spectra for these experiments can be seen in Figure 2.20 and show that partial racemisation occurs almost immediately, giving a homochiral to heterochiral ratio of ~1:5, which does not progress further over the 24 hour period.

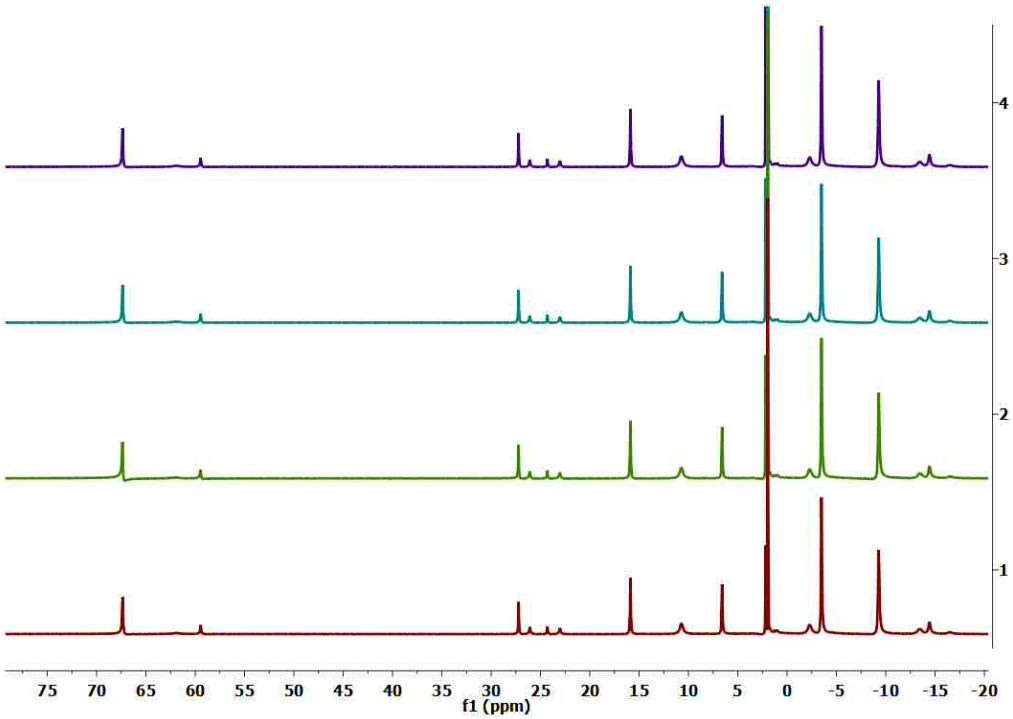

Figure 2.20 - ^{1}H NMR spectra taken at intervals to observe ligand redistribution of RS-2. 5 minutes (red), 1 hour (green), 5 hours (turquoise), 24 hours (blue).

2.6.2 Solution phase paramagnetic susceptibility of iron(II) PyBox complexes

The paramagnetic susceptibility of ***R*-1**, ***RS*-1**, ***R*-2**, ***RS*-2**, ***R*-3**, **4**, ***R*-5** and ***RS*-5** in solution was measured using variable temperature Evans' method NMR spectroscopy[39, 40] and the results can be seen in Figure 2.21. The stability of high-spin state relative to low-spin state follows order ***RS*-1** < ***R*-1** < **4** < ***R*-3** < ***R*-2**/***RS*-2**/***R*-5**/***RS*-5**.

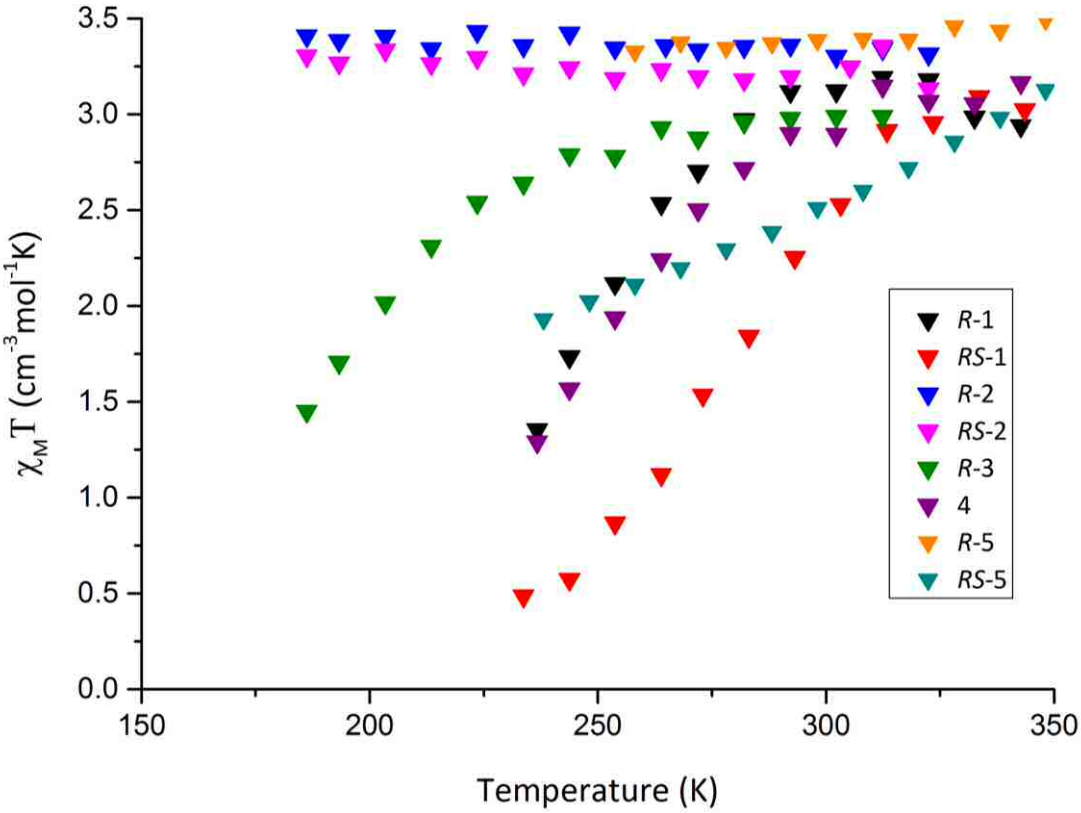

Complex	$T_{1/2}$ / K	Complex	$T_{1/2}$ / K	Complex	$T_{1/2}$ / K	Complex	$T_{1/2}$ / K
***R*-1**	244	***R*-2**	HS	***R*-3**	192	***R*-5**	HS
***RS*-1**	278	***RS*-2**	HS	**4**	245	***RS*-5**	200

Figure 2.21 - Variable temperature Evan's method NMR spectroscopy of complexes *R*-1 (black), *RS*-1 (red), *R*-2 (blue), *RS*-2 (magenta), *R*-3 (purple), 4 (green), *R*-5 (orange) and *RS*-5 (cyan). Complexes *R*-1, *RS*-1, *R*-3, *R*-5 and *RS*-5 have been measured in acetonitrile-d_3. Complexes *R*-2, *RS*-2 and 4 have been measured in acetone-d_6.

***R*-2** and ***RS*-2** remain high spin between 180 and 320 K, which is consistent with their thermal spin-crossover behaviour in the solid state. As previously discussed, the distorted octahedral geometry experienced by the complexes prevents spin-crossover from occurring. This trend is consistent with analogous $Fe[bpp]^{2+}$ complexes with distal isopropyl substituents, which were all high-spin.[41, 42]

In contrast to this, ***R*-1**, ***RS*-1**, ***R*-3** and **4** all undergo thermal spin-crossover in solution. The differences in spin state behaviour of ***R*-3** between the solid state and

solution is particularly interesting, and serves to highlight the importance of measuring magnetic susceptibility in both phases. Had measurements been taken only in the solid state, the natural conclusion would have been that the complex was incapable of spin crossover. However, the results shown in solution indicate that the complex itself is capable of the physical changes required to undergo a spin transition, despite the electronic effects of the methyl group which stabilize the high-spin form. This indicates that the complex must therefore be subject to solid state lattice effects which preclude a switch between the high-spin and low-spin state in the solid phase.

Additionally, the differences in $T_{1/2}$ between ***R*-3** and **4** indicate that there must be an electronic influence on the spin states of these complexes. ***R*-3** shows a significantly lower $T_{1/2}$ than **4**, despite the lack of steric effects contributed by the methyl substituents. The methyl substituents of ***R*-3** are weakly electron donating which may reduce Fe-L backbonding into the oxazolinyl ring system. This weakens the ligand field and therefore stabilises the high-spin state of ***R*-3**, accounting for the significant differences in $T_{1/2}$ temperature.

The most important and novel conclusion to be drawn from this set of results though, is the difference in temperature at which homochiral ***R*-1** and heterochiral ***RS*-1** undergo spin crossover. This observation highlights the first, unequivocal proof that chirality can impact the spin-crossover behaviour of a complex.

The iron centre of homochiral diasteromer, ***R*-1**, is more congested due to the steric bulk of the phenyl substituents which are oriented into the same quadrant of the complex. This causes a slight twist in the octahedral geometry of the complex. In contrast, the heterochiral ***RS*-1** experiences almost no distortion because the substituents are all oriented towards separate quadrants. As a result, the high-spin state of ***R*-1** is stabilised in comparison to that of ***RS*-1** and thus the temperature at which it begins to switch to a low-spin state upon cooling is lower, as indicated by the lower $T_{1/2}$ value for ***R*-1** compared to ***RS*-1**. This effect gives discrimination in spin state switching based on the chirality of the complexes, which is an effect hitherto unreported.

The effect of chirality on the spin states of this type of complex was further observed with solution phase measurements of homochiral ***R*-5** and heterochiral ***RS*-5**. ***R*-5** is high-spin across the temperature range measured, whereas ***RS*-5** appears to undergo thermal spin-crossover. If so, this effect is even more profound than that seen for complexes ***R*-1** and ***RS*-1**, given that the behaviour is completely different in each diastereomer. However, given the propensity of heterochiral Fe[PyBox]$^{2+}$, from ***RS*-1**, complexes to undergo solution phase racemisation, it is likely that the sample was undergoing this racemisation process during the measurements. This means that the data contain some contribution from the high-spin portion of the complex, making it difficult to give a precise $T_{1/2}$ temperature and stability of the low-spin form, relative to the other complexes.

2.7 Conclusion

The impact of chirality on the spin states of Fe[PyBox]$^{2+}$ complexes have been thoroughly explored in this chapter. Solid state magnetic susceptibility data show that some complexes undergo spin-crossover, whilst some remain trapped in their high-spin form. This behaviour was rationalised through a detailed investigation of the solid state structures.

Solution phase data show that chirality can have a clear impact on the spin states of these complexes, when appropriately bulky substituents are present. This chiral discrimination is a promising avenue into the development of thermal sensors and non-linear optical materials.

2.8 Further work

Fe[PyBox]$^{2+}$ complexes can be synthesised quickly, easily and on a relatively large scale. These factors, combined with their thermal spin state switching properties make them interesting candidates for functional materials. Future work could involve investigation of their non-linear optical properties as well as incorporation onto bulk surfaces to form temperature sensitive molecular switches.

2.9 References

1. Z.-G. Gu, C.-Y. Pang, D. Qiu, J. Zhang, J.-L. Huang, L.-F. Qin, A.-Q. Sun and Z. Li, *Inorg. Chem. Commun.*, 2013, **35**, 164-168.
2. D. H. Ren, X. L. Sun, L. Gu, D. Qiu, Z. Li and Z. G. Gu, *Inorg. Chem. Commun.*, 2015, **51**, 50-54.
3. L. Tian, C.-Y. Pang, F.-L. Zhang, L.-F. Qin, Z.-G. Gu and Z. Li, *Inorg. Chem. Commun.*, 2015, **53**, 55-59.
4. W. Liu, X. Bao, L. L. Mao, J. Tucek, R. Zboril, J. L. Liu, F. S. Guo, Z. P. Ni and M. L. Tong, *Chem. Commun. (Camb)*, 2014, **50**, 4059-4061.
5. H. Nishiyama, H. Sakaguchi, T. Nakamura, M. Horlhata, M. Kondo and K. Itoh, *Organometallics* 1989, **8** 846-848.
6. T. Chen, L. Yang, D. Gong and K.-W. Huang, *Inorg. Chim. Acta*, 2014, **423**, 320-325.
7. P. J. Heard and C. Jones, *J. Chem. Soc., Dalton Trans.*, 1997, 1083-1092.
8. D. Cuervo, J. Diez, M. P. Gamasa, S. Garcia-Granda and J. Gimeno, *Inorg. Chem.*, 2002, **41**, 4999-5001.
9. M. K. Tse, S. Bhor, M. Klawonn, G. Anilkumar, H. Jiao, C. Dobler, A. Spannenberg, W. Magerlein, H. Hugl and M. Beller, *Chem. Eur. J.*, 2006, **12**, 1855-1874.
10. A. D. Steinkamp, M. Frings, I. Thome, I. Schiffers and C. Bolm, *Chem. Eur. J.*, 2015, **21**, 7705-7708.
11. B. D. Ward and L. H. Gade, *Chem. Commun. (Camb)*, 2012, **48**, 10587-10599.
12. G. Pereira, M. F. Ferreira, E. M. S. Castanheira, J. A. Martins and P. M. T. Ferreira, *Eur. J. Org. Chem.*, 2012, **2012**, 3905-3910.
13. Y. Y. Zhu, C. W. Liu, J. Yin, Z. S. Meng, Q. Yang, J. Wang, T. Liu and S. Gao, *Dalton Trans.*, 2015, **44**, 20906-20912.
14. Y.-Y. Zhu, H.-Q. Li, Z.-Y. Ding, X.-J. Lü, L. Zhao, Y.-S. Meng, T. Liu and S. Gao, *Inorg. Chem. Front.*, 2016, **3**, 1624-1636.

15. L. J. K. Cook, R. Kulmaczewski, R. Mohammed, S. Dudley, S. A. Barrett, M. A. Little, R. J. Deeth and M. A. Halcrow, *Angew. Chem. Int. Ed.*, 2016, **55**, 4327 - 4331
16. L. J. Kershaw Cook, F. L. Thorp-Greenwood, T. P. Comyn, O. Cespedes, G. Chastanet and M. A. Halcrow, *Inorg. Chem.*, 2015, **54**, 6319-6330.
17. L. J. Kershaw Cook, R. Mohammed, G. Sherborne, T. D. Roberts, S. Alvarez and M. A. Halcrow, *Coord. Chem. Rev.*, 2015, **289-290**, 2-12.
18. M. Clemente-Leon, E. Coronado, M. C. Gimenez-Lopez, F. M. Romero, S. Asthana, C. Desplanches and J. F. Letard, *Dalton Trans.*, 2009, 8087-8095.
19. S. A. Barrett, C. A. Kilner and M. A. Halcrow, *Dalton Trans.*, 2011, **40**, 12021-12024.
20. S. Vela, J. J. Novoa and J. Ribas-Arino, *Phys. Chem. Chem. Phys.*, 2014, **16**, 27012-27024.
21. M. Jiang, S. Dalgarno, C. A. Kilner, M. A. Halcrow and T. P. Kee, *Polyhedron*, 2001, **20**, 2151-2162.
22. G. M. Sheldrick, *Acta Cryst. A*, 2015, **71**, 3-8.
23. G. M. Sheldrick, *Acta Cryst. C*, 2015, **71**, 3-8.
24. O. V. Dolomanov, L. J. Bourhis, R. J. Gildea, J. A. K. Howard and H. Puschmann, *J. Appl. Crystallogr.*, 2009, **42**, 339-341.
25. C. Provent, G. Bernardinelli, A. F. Williams and N. Vulliermet, *Eur. J. Inorg. Chem.*, 2001, 1963-1967.
26. J. Guo, B. Wang, J. Bi, C. Zhang, H. Zhang, C. Bai, Y. Hu and X. Zhang, *Polymer*, 2015, **59**, 124-132.
27. D. A. Evans, M. C. Kozlowski, J. A. Murry, C. S. Burgey, K. R. Campos, B. T. Connell and R. J. Staples, *J. Am. Chem. Soc.*, **121**, 669-685.
28. S. Saaby, K. Nakama, M. A. Lie, R. G. Hazell and K. A. Jorgensen, *Chem. Eur. J.*, 2003, **9**, 6145-6154.
29. S. Brooker, *Chem. Soc. Rev.*, 2015, **44**, 2880-2892.
30. C. F. Macrae, P. R. Edgington, P. McCabe, E. Pidcock, G. P. Shields, R. Taylor, M. Towler and J. van de Streek, *J. Appl. Crystallogr.*, 2006, **39**, 453-457.

31. C. F. Macrae, I. J. Bruno, J. A. Chisholm, P. R. Edgington, P. McCabe, E. Pidcock, L. Rodriguez-Monge, R. Taylor, J. van de Streek and P. A. Wood, *J. Appl. Crystallogr.*, 2008, **41**, 466-470.
32. M. Yamada, M. Ooidemizu, Y. Ikuta, S. Osa, N. Matsumoto, S. Iijima, M. Kojima, F. o. Dahan and J.-P. Tuchagues, *Inorg. Chem.*, 2003, **42**, 8406-8416.
33. B. Weber, C. Carbonera, C. Desplances and J.-F. Létard, *Eur. J. Inorg. Chem.*, 2008, 1589-1598.
34. J. Tang, J. S. Costa, S. Smulders, G. Molna, A. Bousseksou, S. J. Teat, Y. Li, G. A. v. Albada, P. Gamez and J. Reedijk, *Inorg. Chem.*, 2009, **48**, 2128-2135.
35. M. Shatruk, H. Phana, B. A. Chrisostomoa and A. Suleimenova, *Coord. Chem. Rev.*, 2015, **289-290**, 62-73.
36. V. A. Money, J. Elhaïk, I. R. Evans, M. A. Halcrow and J. A. K. Howard, *Dalton Trans.*, 2004, 65-69.
37. G. S. Matouzenko, D. Luneau, G. Molnár, N. Ould-Moussa, S. Zein, S. A. Borshch, A. Bousseksou and F. Averseng, *Eur. J. Inorg. Chem.*, 2006, 2671-2682.
38. H. Sato, Y. Suzuki, Y. Takai, H. Kawasaki, R. Arakawa and M. Shizuma, *Chem. Lett.*, 2010, **39**, 564-566.
39. D. F. Evans, *J. Chem. Soc.*, 1959, 2003-2005.
40. E. M. Schubert, *J. Chem. Educ.*, 1992, 62.
41. J. M. Holland, S. A. Barrett, C. A. Kilner and M. A. Halcrow, *Inorg. Chem. Commun.*, 2002, **5**, 328-332.
42. T. D. Roberts, M. A. Little, L. J. Kershaw Cook, S. A. Barrett, F. Tuna and M. A. Halcrow, *Polyhedron*, 2013, **64**, 4-12.

Chapter 3 - A Density Functional Theory Treatment of Iron(II) PyBox Complexes

3.1 Introduction to Density Functional Theory calculations of spin-states in iron(II) complexes

Density Functional Theory (DFT) is a computational, quantum mechanical model used to investigate the electronic structure of molecules. Appropriate choice of functionals, which perform the exchange-correlation function, and basis set, which represents the electronic wavefunction, is the subject of much research in the field of computational chemistry. Applying such calculations to transition metal complexes can be challenging, as are all calculations where d electrons are concerned, as well as accurately predicting the stability of the high or low-spin form.

Traditionally, the propensity of a complex to take a low-spin or high-spin form is governed by the spectrochemical series, which organises ligands in order of their strong to weak-field nature. The combination of these ligands with a transition metal ion capable of either a high-spin or low-spin electronic configuration allows the complex to adopt either spin state. However, it is difficult for density functionals to predict this subtle interplay. In addition, real spin-states are also the product of orbital pairing and vibrational entropies which are not accounted for in the spectrochemical series,[1] as well as more quantum mechanical effects such as zero point energies, relativistic effects and dispersion forces.[2] These additional contributions make quantum mechanical calculations of these complexes more difficult. This is particularly relevant in the investigation of spin-crossover systems which are inherently delicately balanced to adopt their high-spin and low-spin states.

The theoretical treatment of spin-crossover systems is an active area of research, although there are many challenges involved in the calculations of absolute spin-state energies. Correlated wavefunction methods are much more accurate, however they are correspondingly computationally expensive.[3] DFT methods are faster and able to describe the electron correlation well,[4] although the accuracy of such calculations has been found to be variable.[3] In addition, different density functionals produce different HS - LS energy gaps.[5] As a result of these challenges, the focus of

many investigations has been on predicting the trends and relative spin-state energies of families of complexes.

In this work, the combination of the B86PW91 functional and def-SVP2 basis set was chosen as it was the closest available analogue of BP86/def-SVP2 in SPARTAN'16.[9] The combination of BP86/def-SVP2 has been shown to work well in calculations of comparative spin state energies in iron complexes[1, 3, 6], including $[Fe(bpp)_2]^{2+}$ derivatives, where bpp = 2,6-di(pyrazol-1-yl)pyridine.[6] In addition, the B86PW91/def-SVP2 combination employed here has recently been used in the Halcrow group to successfully look at the comparative spin-states of several families of iron(II) complexes, including $[Fe(bpp)_2]^{2+}$, $[Fe(bpt)_2]^{2+}$, $[Fe(bpym)_2]^{2+}$ and $[Fe(bpyz)_2]^{2+}$, where bpt = 2,4-di(pyrazol-1-yl)-1,3,5-triazine, bpym = 2,6-di(pyrazol-1-yl)pyrimidine and bpyz = 2,6-di(pyrazol-1-yl)pyrazine.[7] The choice of this combination of basis set and functional for this type of calculation is therefore appropriate and indicates that the results from these calculations will be accurate. In terms of precision, calculations will yield the same result, assuming that the same starting point is used, and the results are given to a standard level of precision. These are one decimal place for energies in kcal mol^{-1} and calculated bond angles, and three decimal places for calculated bond lengths.

A thorough investigation into the solid and solution phase magnetic data of $[Fe(bpp)_2]X_2$ complexes, (X = BF_4^- or PF_6^-), identified differences in spin state behaviour between the two salts.[8] In contrast to $[Fe(bpp)_2][BF_4]_2$, $[Fe(bpp)_2][PF_6]_2$ shows high-spin behaviour. Using DFT calculations, this was rationalised as a Jahn-Teller distortion of the type subsequently observed in other $[Fe(bpp)_2]^{2+}$ [9] and $[Fe(PyBox)_2]^{2+}$ complexes.[11]

A subsequent investigation of $[Fe(bpp)_2]^{2+}$ complexes with substituents on the pyridyl or pyrazolyl moiety sought to rationalise the impact of electron-donating and electron-withdrawing groups on the SCO behaviour of the complexes. DFT calculations using BP86/def-SVP2 were successfully employed to reproduce the observed experimental trends.[6]

Recent work has used DFT calculations alongside experimental data to look at the $T_{1/2}$ temperature of 4-pyridyl substituted $[Fe(PyBox)_2]^{2+}$ complexes.[10] B3LYP/6-311+G was used initially to perform geometry optimisations on the ligands only,

showing that the electron density lifts the energy level of the t_{2g} orbital, narrowing the t_{2g}-e_g energy gap which leads to stabilisation of the high-spin state. Data from this model were then compared with experimental findings, showing a good correlation between the two.

3.2 Computational methods

DFT calculations were performed using SPARTAN'16 for Windows with the B86PW91 functional and def-SVP2 basis set. Low-spin calculations were conducted as spin-restricted, whilst high-spin systems were treated as spin-unrestricted. Calculations were performed in the gas phase as a solvent gradient for iron was not available in SPARTAN'16 at the time the work was carried out. The fractional atomic coordinates for $[Fe(PyBox)_2]^{2+}$ complexes in the low-spin or high-spin crystal structures of $[Fe(PyBox)_2][ClO_4]_2$ complexes were used as a starting point for the undistorted geometry minimisations. Calculations on free ligands were performed on both free ligand coordinates, which had been drawn within SPARTAN'16 or on ligand structures from previous calculations where one ligand and the iron had been removed from the model. Jahn-Teller distortion calculations were performed on unminimised crystallographic models with the trans-N(PyBox)-Fe-N(PyBox) angle (ϕ) fixed at 155°, 160° and 165°. This restraint was necessary to prevent the structures from relaxing back toward their undistorted conformations. The $[Fe(Thio\text{-}PyBox)_2]^{2+}$ calculations were performed on unminimised fractional atomic coordinates for $[Fe(PyBox)_2]^{2+}$ complexes, where the ligand O atoms were replaced with S atoms as appropriate for each complex.

3.3 Aims

Computational chemistry has shown itself to be a powerful ally to experimental chemistry, even in areas in which it has traditionally proven challenging to gain a computational insight, such as spin state calculations. This work seeks to corroborate the experimentally determined work discussed in Chapter 2 and delve into the effects

of Jahn-Teller distortion and PyBox ligand conformation. It also extends into theoretical models of a family of related $[Fe(Thio\text{-}PyBox)_2]^{2+}$ complexes and aims to predict the spin states of such complexes, prior to experimental work being undertaken by another member of the group.

3.4 Prediction of spin states in $[Fe(PyBox)_2]^{2+}$ complexes

Density Functional Theory (DFT) calculations were performed using SPARTAN'16 with the B86PW91 functional and def2-SVP basis set. A geometry optimisation calculation was performed on each complex (***R*-1**, ***RS*-1**, ***R*-2**, ***RS*-2**, ***R*-3** and **4**), in both the low-spin and high-spin state, by setting the number of unpaired electrons in the system. Additional calculations were performed for the low-spin and high-spin form of $[Fe(R\text{-}L^{Me})(S\text{-}L^{Me})]^{2+}$, herein referred to as ***RS*-3**, which had not been experimentally prepared. The crystal structure files containing the fractional atomic coordinates for each complex were used as the starting point for the calculations. Counterions and solvent molecules were removed. For complex **4**, a crystal structure of the complex in both the low-spin and high-spin form was available and these were used as the basis for the relevant optimisation. For all other complexes, crystal structures were available in the low-spin or high-spin form only and all optimisations were performed from this starting point.

Table 3.1 shows all of the calculated energies in kcal mol^{-1}. Given the tendency of pure density functionals to stabilise the low-spin form of complexes,[11] it is difficult to use the absolute numbers given out by geometry optimisation calculations to draw conclusions. Therefore the difference between the energies of the low-spin and high-spin forms of each complex was calculated and this number was scaled relative to the energy of the low-spin form of **4**. These values (ΔE_{rel}(HS-LS)) are given in the final column of Table 3.1.

Table 3.1 - Calculated energies from geometry optimised structures of $[Fe(PyBox)_2]^{2+}$ complexes.

Complex	*E*(HS) / kcal mol^{-1}	*E*(LS) / kcal mol^{-1}	*E*(HS) - *E*(LS) / kcal mol^{-1}	ΔE_{rel} (HS-LS)* / kcal mol^{-1}
4	-1721715.7	-1721731.5	15.8	0.0
***R*-1**	-2301476.7	-2301492.0	15.4	-0.5
***RS*-1**	-2301481.2	-2301497.3	16.1	0.2
***R*-2**	-2017637.1	-2017639.1	2.0	-13.8
***RS*-2**	-2017639.5	-2017647.8	8.3	-7.6
***R*-3**	-1820365.9	-1820379.8	13.9	-1.9
***RS*-3**	-1820366.3	-1820379.4	13.1	-2.7

* ΔE_{rel} (HS-LS) refers to the energy difference between the high-spin and low-spin states, relative to **4**.

The ΔE_{rel}(HS-LS) values can be compared and conclusions about the stabilities of the low-spin states can be drawn. These conclusions can then be compared with experimental data and will provide an indication of the accuracy of the computational models chosen. A more positive ΔE_{rel}(HS-LS) value indicates that the complex has a more stable low-spin form. Thus the predicted stabilities of the low-spin forms of the complexes are:

***RS*-1 > 4 > *R*-1 >> *R*-3 > *RS*-3 > *RS*-2 > *R*-2**

This trend is entirely consistent with the solution phase data measured for these complexes. Figure 3.1 shows the variable temperature NMR spectroscopy data for this set of complexes which was first discussed in Chapter 2. Complexes ***R*-2** and ***RS*-2** are exclusively high-spin, which is expected given that DFT calculations predict the instability of their low-spin forms. Complexes ***R*-1**, ***RS*-1**, ***R*-3** and **4** all undergo spin-crossover, with the $T_{1/2}$ temperatures providing a measure of the ease with which the spin transition will occur. Given that the $T_{1/2}$ temperatures decrease in the order ***RS*-1** > **4** > ***R*-1** >> ***R*-3**, the predictions from the DFT calculations match the experimental results. This match between experimental and computational results provide confidence in the accuracy in the computational model used for this set of complexes.

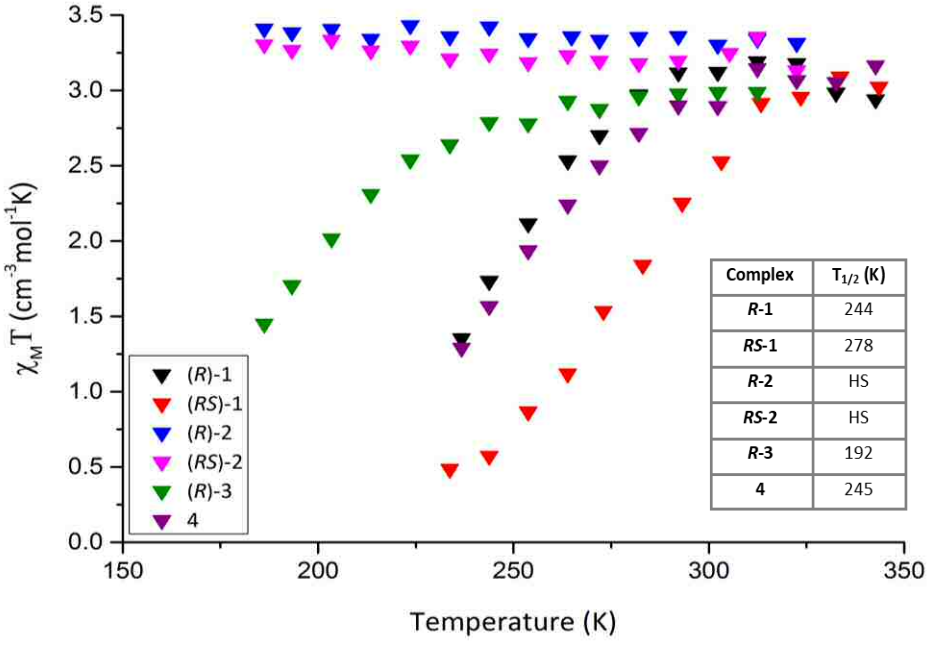

Figure 3.1 - Variable temperature Evan's method NMR spectroscopy of $[Fe(PyBox)_2]^{2+}$ complexes. This graph was originally discussed in Chapter 2.

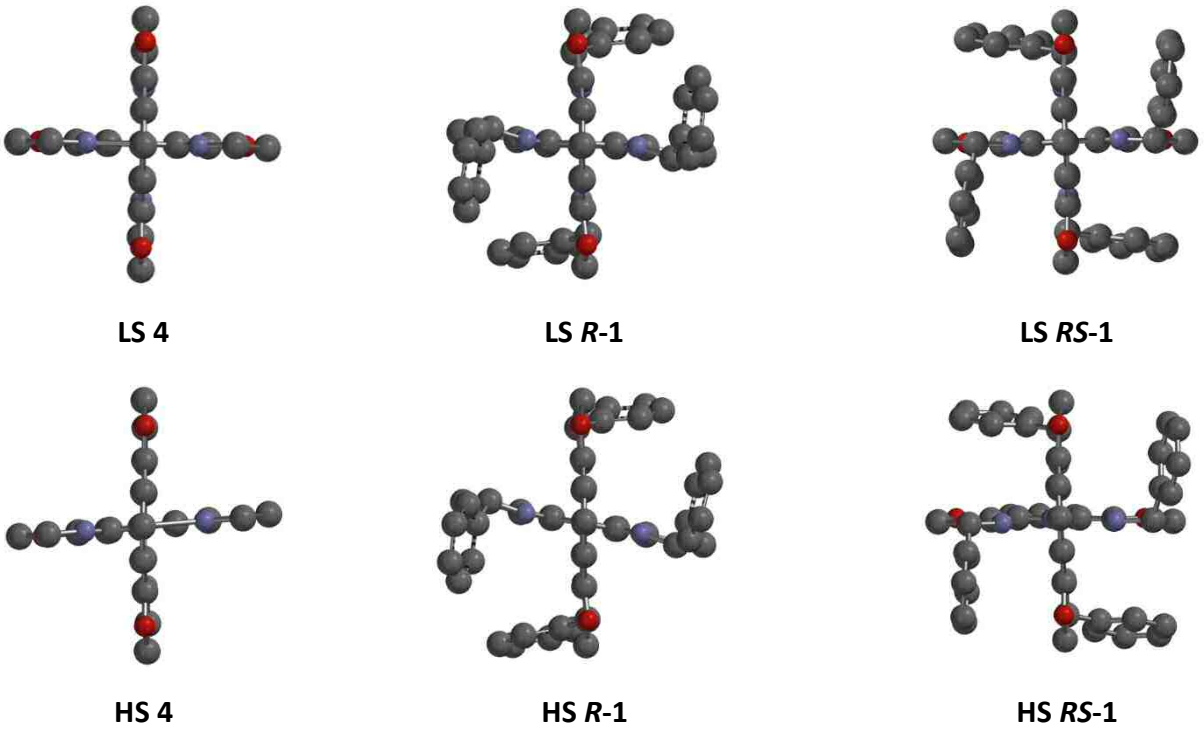

Figure 3.2 - Structures of geometry optimised $[Fe(PyBox)_2]^{2+}$ complexes.

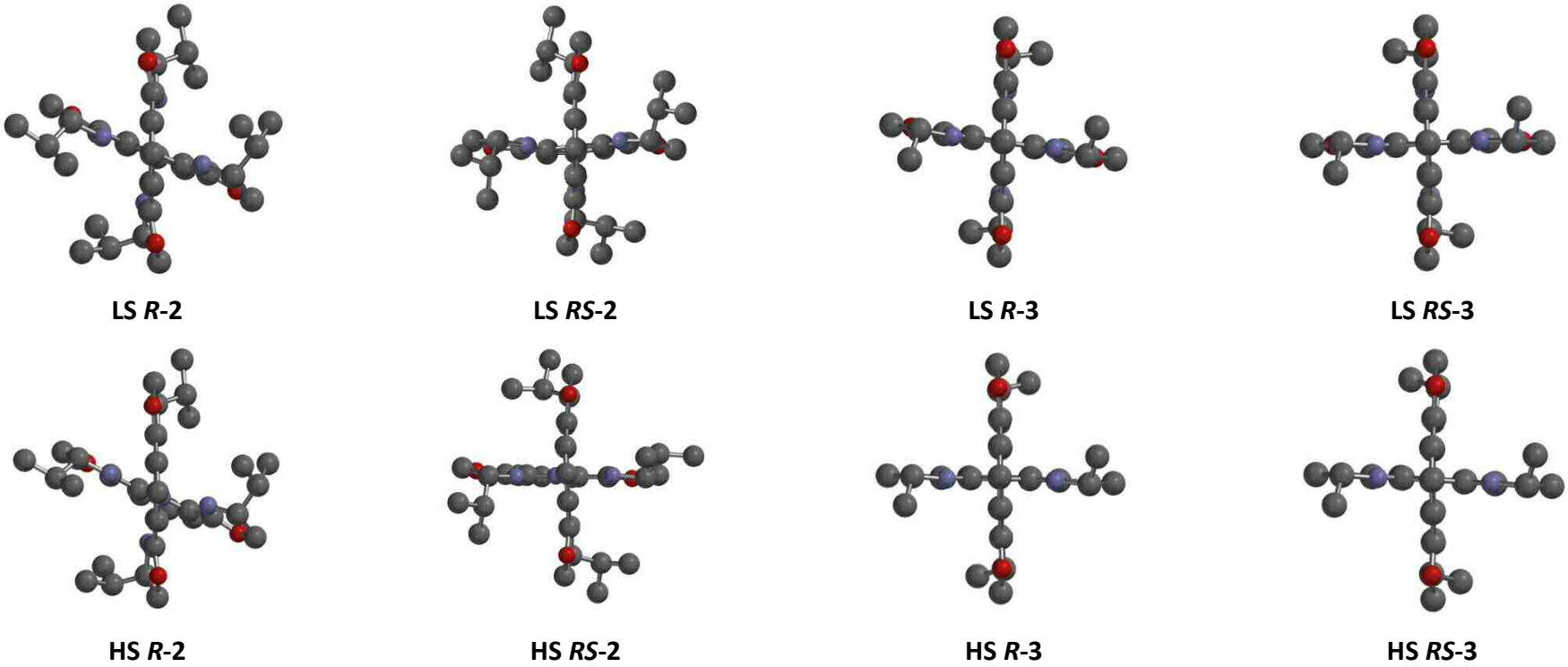

Figure 2 (continued) - Structures of geometry optimised $[Fe(PyBox)_2]^{2+}$ complexes.

Table 3.2 - Comparison of bond lengths and angles from crystal structures and computational models. Data from crystallographic models are shown in the grey columns and computational data are shown in white columns.

	***R*-1 *[1]**			***R*-1**		***RS*-1**	***RS*-1**	
	LS			**LS**	**HS**	**LS**	**LS**	**HS**
Fe-N(pyridyl)	1.905(3)	1.902(3)	1.904(3)	1.912	2.150	1.909(18)	1.916	2.156
Fe-N(oxazolinyl)	1.994(3)	1.992(3)	1.997(3)	2.010	2.238	1.984(19)	2.013	2.225
ϕ	178.25(14)	179.45(13)	177.66(15)	179.3	178.1	178.19(8)	179.8	169.0
θ	88.97(14)	89.96(13)	88.29(14)	88.3	85.4	88.72(7)	88.1	89.1
	***R*-2 *[2]**		***R*-2**		***RS*-2**	***RS*-2**		
	HS		**LS**	**HS**	**HS**	**LS**	**HS**	
Fe-N(pyridyl)	2.120(4)	2.198(4)	1.915	2.139	2.126(14)	1.916	2.147	
Fe-N(oxazolinyl)	2.258(4)	2.214(4)	2.079	2.305	2.230(15)	2.043	2.272	
ϕ	175.35(16)	165.47(17)	176.5	166.5	163.63(6)	174.8	167.1	
θ	76.75(16)	78.68(16)	83.7	84.7	89.23(5)	87.3	84.1	

*[1] This complex has three crystallographically unique molecules in the asymmetric unit. *[2] This complex has two crystallographically unique molecules in the asymmetric unit.

	***R*-3 ***	***R*-3**		***RS*-3**	
	HS	**LS**	**HS**	**LS**	**HS**
Fe-N(pyridyl)	2.137(2)	1.916	2.150	1.917	2.151
Fe-N(oxazolinyl)	2.198(2)	2.015	2.246	2.019	2.246
ϕ	170.91(11)	179.57	177.9	179.78	177.66
θ	86.50(3)	88.63	86.57	87.99	87.52
	4	**4**	**4**		
	LS	**HS**	**LS**	**HS**	
Fe-N(pyridyl)	1.902(3)	1.998(5)	1.918	2.152	
Fe-N(oxazolinyl)	1.985(3)	2.074(5)	1.996	2.231	
ϕ	179.05(11)	178.07(18)	179.75	176.94	
θ	87.30(11)	85.60(19)	88.31	82.17	

* This molecule has half a molecule in its asymmetric unit.

Table 3.2 shows selected bond lengths and angles for all the complexes discussed here. These data have been extracted from the crystallographic data, as discussed previously in Chapter 2, and from the geometry optimised structures discussed in this chapter. Computationally calculated bond lengths have been given as a mean value of either Fe-N(pyridyl) or Fe-N(oxazolinyl) lengths and the angles discussed are the trans-N(pyridyl)-Fe-N(pyridyl) angle (ϕ) or the dihedral angle (θ). Comparing the similarities between experimental and computational data will give an indication as to the accuracy of the DFT model.

The agreement between the computational data for ***R*-1** and the crystallographic parameters at 125 K is generally excellent. ***R*-1** is low-spin at 125 K and the bond lengths and angles match very well with the minimised structure in the low-spin form. A crystal structure of ***R*-1** in its high-spin form is not available, as the complex has a $T_{1/2}$ temperature of around 350 K and the challenges of obtaining a good quality single crystal x-ray diffraction data collection at even higher temperatures would be significant. That said, the calculated bond lengths of the complex in its high-spin form are appropriate for a typical high-spin iron(II) complex. Both angles in homochiral ***R*-1** show slightly more deviation from their ideal values (180° and 90°) in the high-spin form than those for the low-spin form.

The crystallographic model of the low-spin form of ***RS*-1** at 120 K is used for comparison with the results from the low-spin DFT calculations and these show good agreement. A crystal structure of high-spin ***RS*-1** is unavailable for the same reasons as ***R*-1**, but again, the calculated bond lengths fall within the typical range of high-spin iron(II) complexes. The θ distortion parameter for both high and low-spin forms are similar and indicate little distortion of the geometry.

The differences between the calculated angles (ϕ and θ) in ***R*-1** and ***RS*-1** reinforce the experimental magnetic behaviour. As discussed in Chapter 2, the $T_{1/2}$ temperature of ***R*-1** is lower than that for ***RS*-1** (~350 K and ~400 K respectively), indicating that the high-spin state of ***R*-1** is stabilised when compared to that of ***RS*-1**. The additional distortion of θ in ***R*-1** in the minimised structure suggests that the high-

spin form is stabilised over a wider temperature range than ***RS*-1** and therefore ***R*-1** has a lower $T_{1/2}$ temperature.

The minimised structure of ***R*-2** is compared with a crystallographic model of the high-spin form of the complex at 120 K. As a result of the extreme Jahn-Teller distortion exhibited by the complex, the low-spin state is experimentally inaccessible. The computational data for the high-spin complex is in excellent agreement with the experimental data, although the Fe-N(oxazolinyl) bond lengths are a little long for typical high-spin iron(II) complexes. There are two unique molecules in the asymmetric unit of the crystal structure which have very different ϕ values (175.35°(16) and 165.47°(17)). The calculated value for this parameter (166.50°) agrees well with the latter experimental value, although it is clearly significantly different to the former. Interestingly, the ϕ value for the calculated low-spin form is 176.45°, which is much closer to the former crystallographic value. The calculated bond lengths for ***R*-2** are consistent with low-spin iron(II) complexes, although the angles clearly show significant distortion of the octahedral geometry, which could reflect the inherent inaccessibility of the low-spin state.

The crystal structure of ***RS*-2** at 120 K shows the high-spin form of the complex. When compared with the computational values, the high-spin forms compare well, although the distortion of the ϕ angle is under-emphasised, whilst the θ angle is over-distorted. The low-spin optimised structure shows typical bond lengths and, similarly to ***R*-2**, suggests geometry distortion.

Solid state ***R*-3** was high-spin and the crystallographic values listed in Table 3.2 reflect this. The high-spin computational model shows excellent agreement for the bond lengths and θ angle, although ϕ shows a value much closer to ideal than that observed crystallographically. The calculated values for the low-spin form of ***R*-3** show appropriate bond lengths for a low-spin iron(II) structure and there is not a great deal of distortion observed in the octahedral geometry. The ϕ and θ values here are reminiscent of the angles seen for ***R*-1**, a complex which successfully undergoes solid state spin-crossover, which may reflect the dichotomy of the spin-state behaviour of ***R*-3**. As discussed in Chapter 2, the complex undergoes a spin-transition in solution, whilst

solid state effects preclude this switch in the solid state. The lack of distortion in the low-spin computational model suggests that the low-spin state is indeed accessible for the complex and indicates that the high-spin state trapping in the solid state is indeed the result of lattice effects, rather than the properties of the complex itself.

As there are no experimental data for ***RS*-3** to be considered, the data from the computational model will be considered in isolation. The bond lengths for both the high and low-spin forms are in good agreement with typical iron(II) complexes. In terms of the distortion parameters, there are no significant differences between the ϕ and θ values in the high and low-spin states. Additionally, the values are similar to those observed for ***R*-3**. This suggests that both spin-states may be accessible thus the complex may be capable of undergoing spin-crossover.

Complex **4** is unique in that both high and low-spin states could be characterised crystallographically. Therefore there is the opportunity to compare computational and crystallographic models of both spin states directly. The low-spin states compare well and both bond lengths and angles are in good agreement. The calculated high-spin Fe-N(pyridyl) bond lengths are slightly shorter than both the crystallographic values and bond lengths of typical iron(II) complexes. The computational model also predicts slightly more distortion in the high-spin form than that seen in the crystal structure data.

3.5 PyBox ligand conformation calculations

To investigate the extent to which incorporation of the PyBox ligand into a complex causes conformational strain of the ligand, and the effect of such strain on the geometry of the complexes, DFT calculations were performed on PyBox ligand structures. Structures of the free ligand were drawn in SPARTAN'16 and geometry optimisation calculations were performed, giving the both the conformation and energy of ligands which were completely independent of complexes. To obtain the energies of ligands from the complexes, hereafter referred to as strained ligand, the structures of

previously calculated $[Fe(PyBox)_2]^{2+}$ complexes were altered. This was achieved by deleting the iron centre and one ligand and conducting energy minimisation calculations, thus retaining the geometry imposed by the geometry of the complex. The resultant energies from all calculations can be seen in Table 3.3. The complex from which the ligand originates is given in brackets in the first column.

Overall it can be seen that the strained ligands are higher in energy than the free ligand, which is to be expected given the constrained geometry imposed by metal coordination. The difference in energy between free ligand and strained ligand (ΔE_{rel}) can be placed in the following sequence.

***R*-L^{Me} (*RS*-3)** < ***R*-L^{iPr} (*R*-2)** < ***R*-L^{Me} (*R*-3)** < **L^{H} (4)** < ***R*-L^{iPr} (*RS*-2)** < ***R*-L^{Ph} (*RS*-1)** < ***R*-L^{Ph} (*R*-1)**

Ligands from homochiral complexes with phenyl and methyl substituents have a larger ΔE_{rel} than equivalent ligands from heterochiral complexes. In contrast, this pattern is reversed for ligands with isopropyl substituents. The difference between the free and strained structures of ***R*-L^{Ph} (*R*-1)** shows the most difference in strain, which is to be expected given the steric clash of the phenyl substituents in the complex. As discussed in Chapter 2, this clash causes two of the phenyl rings to twist away from the opposing ring causing some strain of the coordination geometry. This twist is not observed in the heterochiral complex. That said, there is relatively little difference between the ΔE_{rel} of ***R*-L^{Me} (*RS*-3)** and ***R*-L^{Ph} (*R*-1)** (~3 kcal mol^{-1}), which suggests that, despite the observed trend, the majority of observed behaviour in these complexes is not attributable to ligand strain.

To further explore this, the difference between the energies of the high-spin structures of homochiral and heterochiral diastereomers of each complex (Column 6 of Table 3.5) were compared with the difference in energies between ligands from homochiral and heterochiral complexes (Column 5 of Table 3.5). Given that there are two ligands per complex, the energy difference between the ligands is multiplied by two and this value compared with that of the complexes.

For complexes with isopropyl or methyl substituents, there is a 0.8 or 1.0 kcal mol^{-1} difference between the ligand and complex. In the case of phenyl substituents,

there is a 7.1 kcal mol^{-1} difference between the ligand and complex. These discrepancies suggest that the geometry of the complexes is a result of more than the conformational strain of the ligand and that, as previously suggested, the steric factors involved between substituents is a strong influencing factor.

Table 3.3 - Table of energies of free and strained ligand.

Ligand	*E*(free ligand) / kcal mol^{-1}	*E*(strained ligand) / kcal mol^{-1}	ΔE_{rel} (strained ligand - free ligand) / kcal mol^{-1}	Δ*E*(Heterochiral - homochiral isomer) / kcal mol^{-1}	Δ*E*(Heterochiral - homochiral complex) / kcal mol^{-1}
L^{H} from **4**	-464461.3	-464441.5	-19.9		
R-L^{Ph} from ***R*-1**	-754338.9	-754316.7	-22.2	1.3	-4.5
R-L^{Ph} from ***RS*-1**	-754338.8	-754317.9	-20.9		
R-L^{iPr} from ***R*-2**	-612423.5	-612404.4	-19.2	-0.8	-2.5
R-L^{iPr} from ***RS*-2**	-612422.5	-612402.5	-19.9		
R-L^{Me} from ***R*-3**	-513785.7	-513766.5	-19.2	0.3	-0.4
R-L^{Me} from ***RS*-3**	-513785.6	-513766.8	-18.9		

3.6 Jahn-Teller distortion in $[Fe(PyBox)_2]^{2+}$ complexes

As discussed in Chapter 2, a structural Jahn-Teller distortion in $[Fe(L)_2]^{2+}$ complexes can lead to complexes which are trapped in a high-spin state. This phenomenon has been observed in complexes where L = 1-bpp, 3-bpp,[9] PyBox[11] or bpt.[7] This distortion can be quantified by referring to the trans-N(pyridine)-Fe-N(pyridine) angle (ϕ) and the dihedral angle between the two ligands (θ). When these angles deviate from their ideal values of 180° and 90° respectively, the complex becomes distorted from its octahedral geometry and can become trapped in its high-spin form, due to its inability to undergo the necessary structural contraction to attain its low-spin form. The effects of this distortion are limited to the solid state and high-spin trapped complexes can be capable of spin-transitions in solution, as a result of the rapid conversion between the distorted and undistorted geometries in the labile high-spin state.[9] Whilst the effect is easily explored experimentally using crystal structures, density functional theory has been increasingly used as a tool to explore the phenomenon.[7, 8]

Jahn-Teller distortion calculations were performed on unminimised crystallographic models of ***R*-1**, ***RS*-1** and **4** with the trans-N(PyBox)-Fe-N(PyBox) angle (ϕ) fixed at 155°, 160° and 165°. This restraint was necessary to prevent the structures from relaxing back toward their undistorted conformations. Values of ϕ > 165° are treated as "almost linear" by SPARTAN'16 and default to ϕ = 180°. As a result, calculations where 165 ≥ ϕ ≥ 180° could not be performed. A ϕ distortion of 155° is close to the minimum value observed in practise.

Table 3.4 shows the calculated energies for each complex where the trans-N(PyBox)-Fe-N(PyBox) angle has been fixed. The figure for ΔE_{dist} is calculated by subtracting the energy of the undistorted structure from that of the energy of the restrained structure.

Table 3.4 - Jahn-Teller distortion of $[Fe(PyBox)_2]^{2+}$ complexes.

Complex	Restrained trans-N(PyBox)-Fe-N(PyBox) angle (ϕ)	E / kcal mol^{-1}	ΔE_{dist} / kcal mol^{-1}
4	Undistorted	-1721715.7	
	165	-1721715.3	0.4
	160	-1721714.9	0.8
	155	-1721715.7	-0.0069
***R*-1**	Undistorted	-2301476.7	
	165	-2301392.2	84.4
	160	-2301391.8	84.8
	155	-2301391.1	85.5
***RS*-1**	Undistorted	-2301481.2	
	165	-2301481.1	0.1
	160	-2301480.6	0.6
	155	-2301479.7	1.5

The results in Table 3.4 show that there is little difference between the distorted and undistorted structures of both ***RS*-1** and **4**. For ***RS*-1**, each of the three distorted molecules lie ≤ 1.4 kcal mol^{-1} above the undistorted structures. In the case of **4**, where ϕ = 160° or 165°, the distorted complexes are ≤ 0.8 kcal mol^{-1} above the undistorted configuration, whereas for ϕ = 155° the distorted structure lies 0.0069 kcal mol^{-1} below the undistorted molecule. In contrast, the values for the distorted molecules of ***R*-1** lie ≤ 85.5 kcal mol^{-1} above the undistorted structure, which is a significant difference in energy.

For complexes ***RS*-1** and **4**, the ΔE_{dist} values suggest that the distorted complexes have a shallow potential energy surface, meaning that there is little difference in energy between the distorted and undistorted configurations of these two complexes. This indicates that it is comparatively easy to distort the complexes along the dihedral angle of the ligands. In contrast, it is much harder to distort ***R*-1**, as shown by the large energy difference between the distorted and undistorted structures. These energy differences can be explained by the contrasting sterics of the complexes.

As discussed in Chapter 2, homochiral ***R*-1** has phenyl substituents angled towards each other in the same quadrant. As a result of this steric clash, a distortion of the complex *via* the dihedral angle is difficult to attain, requiring much higher energy to distort the complex. As expected, the energy required to twist the complexes reduces slightly as the angle is relaxed (Table 3.4).

The opposing argument can be made for complexes ***RS*-1** and **4**. As a result of the orientation of the phenyl rings into separate quadrants in ***RS*-1,** and the lack of substituents in **4**, the dihedral angle of these complexes can be easily distorted. This means there are a negligible differences in energy between the artificially distorted and geometry optimised models of these complexes. Space-filling models of the distorted structures for each angle (Figure 3.3) highlight this well; the models of ***RS*-1** and **4** show that the complexes can be distorted without steric interference, whereas the models for ***R*-1** show the impact of the steric clash between the phenyl rings. Once again, these data lend support to the proposal that much of the structural behaviour of these

$[Fe(PyBox)_2]^{2+}$ complexes can be attributed to the sterics imposed by the ligand substituents.

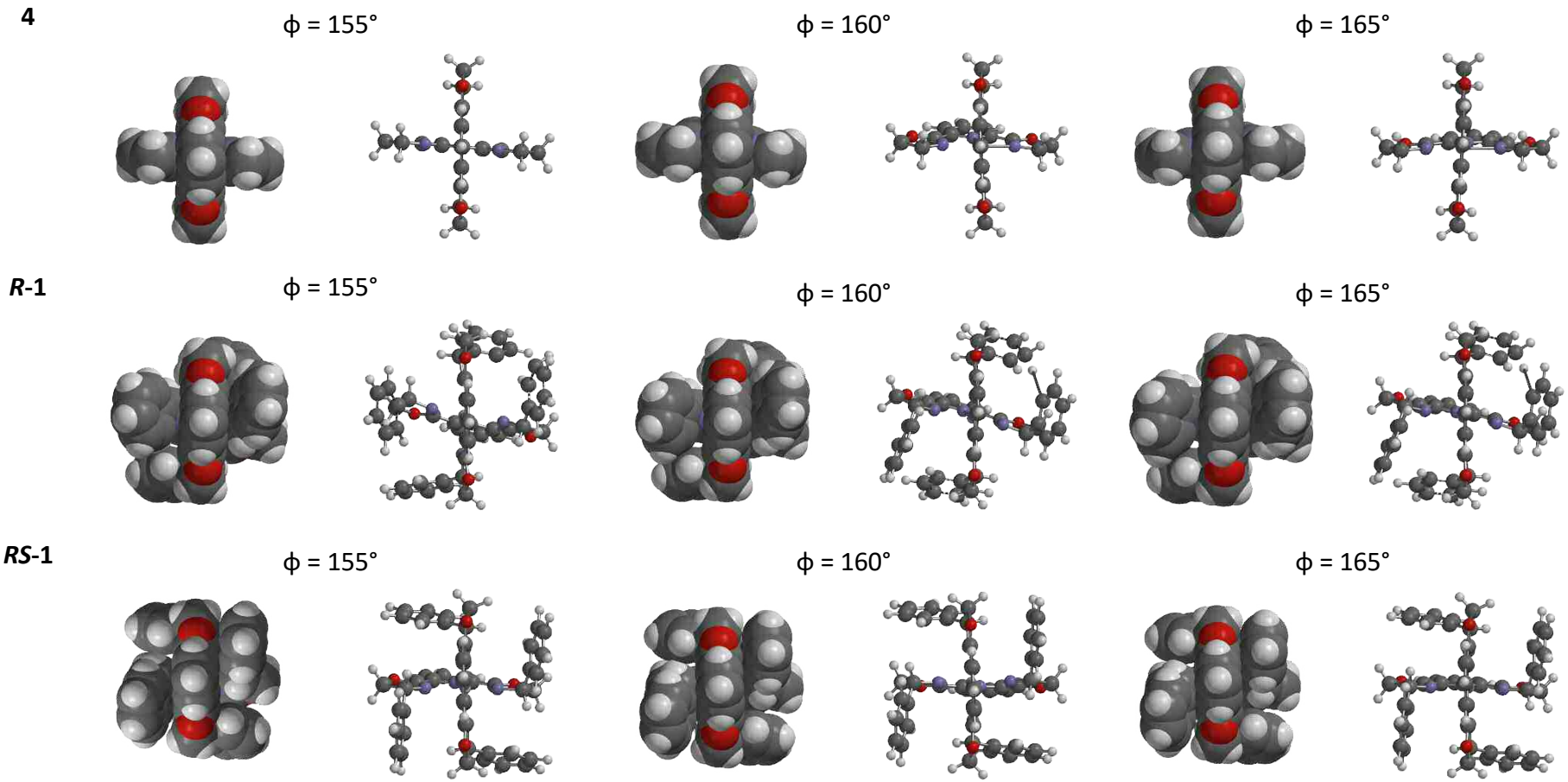

Figure 3.3 - Space filling and ball and stick models of Jahn-Teller distorted $[Fe(PyBox)_2]^{2+}$ complexes.

3.7 Prediction of spin states in $[Fe(Thio\text{-}PyBox)_2]^{2+}$ complexes

As previously discussed, PyBox ligands and complexes are of interest as asymmetric catalysts and improvements in efficiency are much sought after. A rational progression then, is to tune the electronic properties of the ligand. This can easily be achieved by switching the oxazoline ring to a thiazoline, giving thio-PyBox ligands, although these ligands have not been synthesised as part of this project. Thio-PyBox ligands could be synthesised in two steps. The first uses pyridine-2,6-dicarbonyldichloride and an appropriate amino alcohol to form a diamide. This step is the same as the one used for the synthesis of PyBox ligands. The diamide is then treated with a thiolating agent, such as Lawesson's reagent or P_2S_5, which both thiolates the ligand and closes the ring, leaving a thio-PyBox ligand.[12] As with the synthesis of PyBox ligands, the stereochemistry is retained throughout the synthesis.

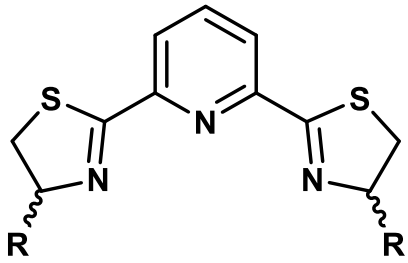

Figure 3.4 - General structure of thio-PyBox ligands.

The alteration of the electronic properties of a ligand is of interest in spin-crossover research. Sulfur is less electronegative than oxygen which reduces the electron-withdrawing nature of the thiazole ring compared with an equivalent oxazoline. This change in the electronic properties of the ligand will increase sigma-donation, thus making the ligand field stronger. Current work by another member the Halcrow group seeks to experimentally explore the spin-crossover behaviour in $[Fe(Thio\text{-}PyBox)_2]^{2+}$ complexes. However, as a precursor to this, DFT calculations were performed to predict the properties of such complexes. It is these calculations that are discussed here.

Geometry optimisation calculations for $[Fe(Thio\text{-}PyBox)_2]^{2+}$ complexes were performed on unminimised fractional atomic coordinates for $[Fe(PyBox)_2]^{2+}$ complexes, where the ligand oxygen atoms were replaced with sulfur atoms as appropriate for each complex. Calculations were conducted for both low-spin and high-spin forms of the complexes by setting the number of unpaired electrons in the system. The energy outputs of these calculations can be seen in Table 3.5. In addition, the energy difference between the low-spin and high-spin forms of each complex was calculated and this number was scaled relative to the energy of **4** ($[Fe(L^H)_2]^{2+}$). These values (ΔE_{rel}(HS-LS)) can be seen in Table 3.5, alongside their $[Fe(PyBox)_2]^{2+}$ counterparts.

As with the $[Fe(PyBox)_2]^{2+}$ complexes discussed in section 3.2, the stability of the low-spin states of the $[Fe(Thio\text{-}PyBox)_2]^{2+}$ complexes can be placed in the following order.

$$\mathbf{[Fe(LTP^{H})_2]^{2+}} > \mathbf{[Fe(\textit{R}\text{-}LTP^{iPr})(\textit{S}\text{-}LTP^{iPr})]^{2+}} > \mathbf{[Fe(\textit{R}\text{-}LTP^{Ph})(\textit{S}\text{-}LTP^{Ph})]^{2+}} >$$

$$\mathbf{[Fe(\textit{R}\text{-}LTP^{Ph})_2]^{2+}} > \mathbf{[Fe(\textit{R}\text{-}LTP^{iPr})_2]^{2+}}$$

This result shows an interesting trend which is subtly different to that observed in the $[Fe(PyBox)_2]^{2+}$ complexes. The unsubstituted complex, $\mathbf{[Fe(LTP^{H})_2]^{2+}}$, is shown to have the most stable low-spin state, followed closely by both heterochiral diasteromers, $\mathbf{[Fe(\textit{R}\text{-}LTP^{iPr})(\textit{S}\text{-}LTP^{iPr})]^{2+}}$ and $\mathbf{[Fe(\textit{R}\text{-}LTP^{Ph})(\textit{S}\text{-}LTP^{Ph})]^{2+}}$. Homochiral complexes, $\mathbf{[Fe(\textit{R}\text{-}LTP^{Ph})_2]^{2+}}$ and $\mathbf{[Fe(\textit{R}\text{-}LTP^{iPr})_2]^{2+}}$, show the least stable low-spin forms.

From these data, it can be hypothesised that the steric effects imposed by the chirality of the complexes have a stronger effect in $[Fe(Thio\text{-}PyBox)_2]^{2+}$ analogues than in $[Fe(PyBox)_2]^{2+}$ complexes. There is a very small difference (~ 0.5 kcal mol^{-1}) between the energies of $\mathbf{[Fe(\textit{R}\text{-}LTP^{iPr})(\textit{S}\text{-}LTP^{iPr})]^{2+}}$ and $\mathbf{[Fe(\textit{R}\text{-}LTP^{Ph})(\textit{S}\text{-}LTP^{Ph})]^{2+}}$, indicating only the most subtle difference in the stability of the low-spin state. Examination of the relevant calculated bond angles (Table 3.6) indicate that both ϕ and θ are very close to ideal for both low-spin forms and for the high-spin form of $\mathbf{[Fe(\textit{R}\text{-}LTP^{Ph})(\textit{S}\text{-}LTP^{Ph})]^{2+}}$, whereas high-spin $\mathbf{[Fe(\textit{R}\text{-}LTP^{iPr})(\textit{S}\text{-}LTP^{iPr})]^{2+}}$ shows a very small deviation of θ. This can also be observed from the images of the calculated structures in Figure 3.5, which show almost no geometry distortion of the type sometimes observed in this type of complex. As a result of the heterochiral diastereoisomerism, which results in substituents angled into

all four quadrants of the complex, the complexes should theoretically be free to perform the physical contraction required to switch between high- and low-spin.

In contrast, there is a much larger difference (~10 kcal mol^{-1}) between the two homochiral complexes. The calculated bond angles for low-spin **[Fe(*R*-LTP^{Ph})$_2$]$^{2+}$** are very close to ideal and some deviation of θ is seen in the high-spin form. In contrast, both high- and low-spin **[Fe(*R*-LTP^{iPr})$_2$]$^{2+}$** show distortion from the ideal geometry of both Φ and θ. The effects of these angles can be seen in Figure 3.5; the images of both complexes show some distortion, but the structure of **[Fe(*R*-LTP^{iPr})$_2$]$^{2+}$** is particularly twisted. It is reasonable then, based on these parameters, to predict that one or both of these homochiral complexes may be unable to perform spin-crossover.

The low-spin stabilities of both $[Fe(PyBox)_2]^{2+}$ and $[Fe(Thio\text{-}PyBox)_2]^{2+}$ complexes, scaled relative to complex **4**, have been combined below.

[Fe(LTP^{H})$_2$]$^{2+}$ > [Fe(*R*-LTP^{iPr})(*S*-LTP^{iPr})]$^{2+}$ > [Fe(*R*-LTP^{Ph})(*S*-LTP^{Ph})]$^{2+}$ >

[Fe(*R*-LTP^{Ph})$_2$]$^{2+}$ > *RS*-1 > 4 > *R*-1 > *RS*-2 > [Fe(*R*-LTP^{iPr})$_2$]$^{2+}$ > *R*-2

Based on the calculated energies of each complex, it may be possible to predict the likelihood of spin-crossover occurring in $[Fe(Thio\text{-}PyBox)_2]^{2+}$ complexes. Four $[Fe(Thio\text{-}PyBox)_2]^{2+}$ complexes (**[Fe(LTP^{H})$_2$]$^{2+}$**, **[Fe(*R*-LTP^{iPr})(*S*-LTP^{iPr})]$^{2+}$**, **[Fe(*R*-LTP^{Ph})(*S*-LTP^{Ph})]$^{2+}$**and **[Fe(*R*-LTP^{Ph})$_2$]$^{2+}$**) should have more stable low-spin states than ***RS*-1**. It is possible then, that some of these complexes would undergo a spin-transition with lower $T_{1/2}$ temperatures than those seen in $[Fe(PyBox)_2]^{2+}$ complexes[11], although those with the most stable low-spin forms may be exclusively low-spin. On the other hand, **[Fe(*R*-LTP^{iPr})$_2$]$^{2+}$,** which falls in between ***RS*-2** and ***R*-2** in terms of its energy, is likely to also be trapped in it's high-spin form. Clearly, experimental data is necessary to support these hypotheses, however given the accuracy of the computational model used here in predicting the spin states of $[Fe(PyBox)_2]^{2+}$complexes, it is reasonable to infer that the computational model will hold true for the $[Fe(Thio\text{-}PyBox)_2]^{2+}$ complexes.

Table 3.5 - Calculated energies from geometry optimised structures of $[Fe(PyBox)_2]^{2+}$ and $[Fe(Thio\text{-}PyBox)_2]^{2+}$ complexes.

Complex	ΔE_{rel} (HS-LS)* / kcal mol^{-1}	Thio-PyBox Complex	E(HS) / kcal mol^{-1}	E(LS) / kcal mol^{-1}	E(HS) - E(LS) / kcal mol^{-1}	ΔE_{rel} (HS-LS)* / kcal mol^{-1}
4	0.0	$[Fe(LTP^{H})_2]^{2+}$	-2532295.8	-2532317.1	21.3	5.4
***R*-1**	-0.5	$[Fe(R\text{-}LTP^{Ph})_2]^{2+}$	-3112054.9	-3112071.3	16.4	0.5
***RS*-1**	0.2	$[Fe(R\text{-}LTP^{Ph})(S\text{-}LTP^{Ph})]^{2+}$	-3112055.1	-3112073.9	18.8	2.9
***R*-2**	-13.8	$[Fe(R\text{-}LTP^{iPr})_2]^{2+}$	-2828207.2	-2828212.4	5.1	-10.7
***RS*-2**	-7.6	$[Fe(R\text{-}LTP^{iPr})(S\text{-}LTP^{iPr})]^{2+}$	-2828212.0	-2828231.3	19.3	3.5

* ΔE_{rel} (HS-LS) refers to the energy difference between the high-spin and low-spin states, relative to $[Fe(L^{H})_2]^{2+}$.

Table 3.6 - Calculated bond distances and lengths from the optimised $[Fe(Thio\text{-}PyBox)_2]^{2+}$ complex structures.

	$[Fe(R\text{-}LTP^{H})_2]^{2+}$		$[Fe(R\text{-}LTP^{Ph})_2]^{2+}$		$[Fe(R\text{-}LTP^{Ph})(S\text{-}LTP^{Ph})]^{2+}$		$[Fe(R\text{-}LTP^{iPr})_2]^{2+}$		$[Fe(R\text{-}LTP^{iPr})(S\text{-}LTP^{iPr})]^{2+}$	
	LS	**HS**	**LS**	**HS**	**LS**	**HS**	**LS**	**HS**	**LS**	**HS**
Fe-N(pyridyl)	1.905	2.173	1.899	2.117	1.902	2.128	1.900	2.101	1.903	2.129
Fe-N(oxazolinyl)	1.988	2.217	2.030	2.256	2.013	2.235	2.072	2.313	2.018	2.279
ϕ	179.6	178.1	179.5	179.3	179.7	179.4	177.6	163.0	179.5	166.9
θ	88.2	88.7	87.5	76.1	88.2	84.1	81.9	74.8	88.0	81.3

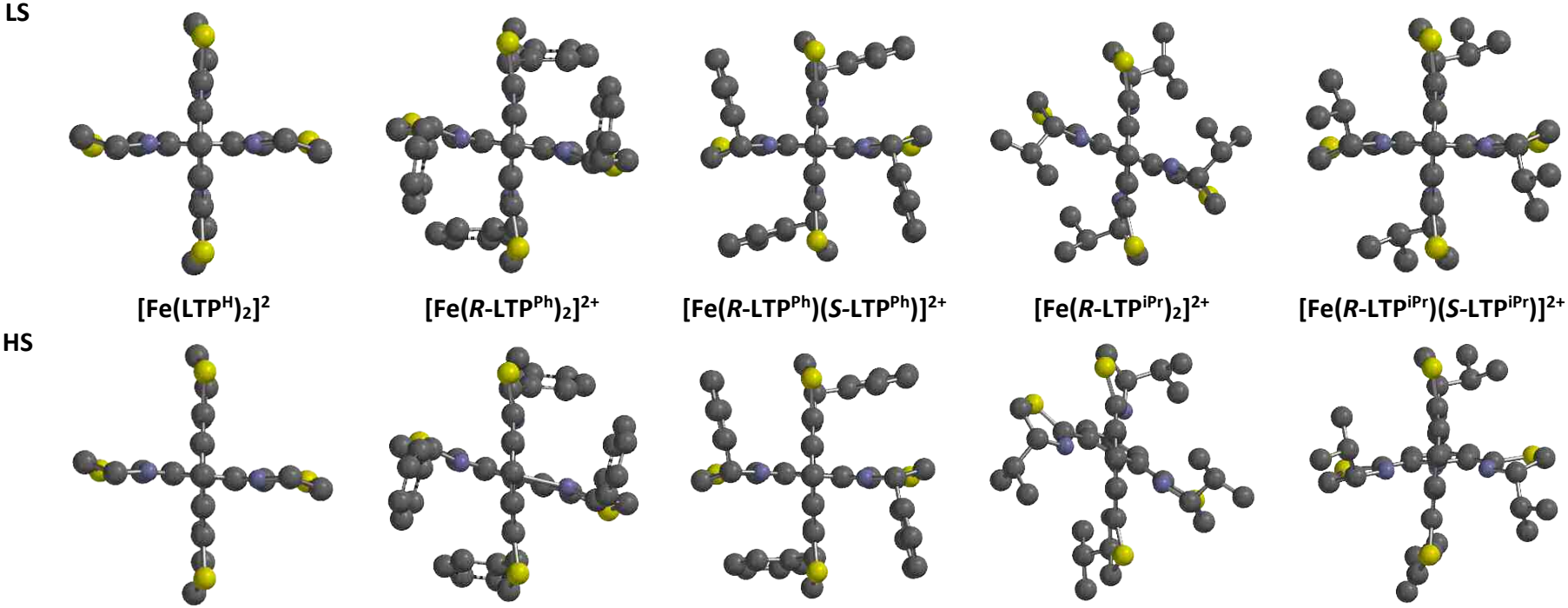

Figure 3.5 - Structures of geometry optimised [Fe(Thio-PyBox)$_2$]$^{2+}$ complexes.

3.8 Conclusion

This chapter discussed the computational methodology and results used to examine $[Fe(PyBox)_2]^{2+}$ complexes, PyBox ligands and a set of $[Fe(Thio\text{-}PyBox)_2]^{2+}$ analogues.

The spin state calculations of $[Fe(PyBox)_2]^{2+}$ complexes matched the experimental trends seen in solution in terms of the stability of the low-spin states and the corresponding $T_{1/2}$ temperatures. This shows that the combination of the B86PW91 functional and def-SVP2 basis set can be used to successfully model relative spin states in iron(II) systems.

DFT calculations performed on PyBox ligand structures show that, as expected, the strained ligands have greater energies than the free ligands as a result of conformational strain imposed upon metal coordination. In addition, the differences between the energies of the diastereomers of the complexes and two PyBox ligands show that, whilst ligand conformation almost certainly has some role to play in coordination geometry, the main factor impacting the geometry, and resultant SCO behaviour, is sterics.

The propensity of ***R*-1**, ***RS*-1** and **4** to undergo Jahn-Teller distortion as a result of restraining the dihedral angle follows the expected behaviour of these complexes, based on their steric properties. Given their lack of clashing substituents, it takes little energy to distort the dihedral angle of ***RS*-1** and **4**. In contrast, owing to the proximity of the phenyl substituents to each other, much more energy is required to distort ***R*-1**.

The predicted spin states of $[Fe(Thio\text{-}PyBox)_2]^{2+}$ complexes indicate that there is the strong possibility of interesting SCO behaviour from this class of compound, with the potential for stronger chiral discrimination than that seen in $[Fe(PyBox)_2]^{2+}$ complexes. Current work in the Halcrow group seeks to explore this area experimentally.

3.9 References

1. S. R. Mortensen and K. P. Kepp, *J. Phys. Chem. A*, 2015, **119**, 4041-4050.
2. K. P. Kepp, *Inorg. Chem.*, 2016, **55**, 2717-2727.
3. B. J. Houghton and R. J. Deeth, *Eur. J. Inorg. Chem.*, 2014, 4573-4580.
4. O. S. Siig and K. P. Kepp, *J. Phys. Chem. A*, 2018, **122**, 4208-4217.
5. H. Paulsen, V. Schünemann and J. A. Wolny, *Eur. J. Inorg. Chem.*, 2013, **2013**, 628-641.
6. L. J. Kershaw-Cook, R. Kulmaczewski, R. Mohammed, S. Dudley, S. A. Barrett, M. A. Little, R. J. Deeth and M. A. Halcrow, *Angew. Chem. Int. Ed.*, 2016, **55**, 4327-4331.
7. I. Capel Berdiell, R. Kulmaczewski and M. A. Halcrow, *Inorg. Chem.*, 2017, **56**, 8817-8828.
8. J. M. Holland, J. A. McAllister, C. A. Kilner, M. Thornton-Pett, A. J. Bridgeman and M. A. Halcrow, *J. Chem. Soc., Dalton Trans.*, 2002, 548-554.
9. L. J. Kershaw Cook, R. Mohammed, G. Sherborne, T. D. Roberts, S. Alvarez and M. A. Halcrow, *Coord. Chem. Rev.*, 2015, **289-290**, 2-12.
10. A. Kimura and T. Ishida, *ACS Omega*, 2018, **3**, 6737-6747.
11. M. Reiher, O. Salomon and B. A. Hess, *Theor. Chem. Acc.*, 2001, **107**, 48-55.
12. J. D. Nobbs, A. K. Tomov, R. Cariou, V. C. Gibson, A. J. White and G. J. Britovsek, *Dalton Trans.*, 2012, **41**, 5949-5964.

Chapter 4 - Speciation of Homochiral and Heterochiral Diastereomers of Cobalt(II) and Zinc(II) PyBox Complexes

4.1 Introduction

Recently, the chiral nature of PyBox ligands has been exploited in fields other than their application for asymmetric catalysis. This has included their spin-crossover behaviour in both achiral[1, 2] and chiral[3] complexes, molecular magnetism[4-6] and supramolecular chemistry.[7]

Previous studies have described the stability of heterochiral $[M(L^{RS\text{-}Ph})_2]^{2+}$ complexes, where M = Co, Zn and Fe.[3, 8, 9] These investigations showed that racemisation of the complexes through ligand redistribution did not occur. In contrast, for $[M(L^{RS\text{-}iPr})_2]^{2+}$ complexes, where M = Fe, this redistribution was seen to occur, causing the formation of *RR* and *SS* isomers in solution from a prepared *RS* complex.

Chapter 2 discussed the unequivocal influence of chirality on the spin states of $[Fe(L^{Ph})_2][ClO_4]_2$ complexes in solution. The $T_{1/2}$ temperature of the homochiral isomer was shown to be 34 K lower than the heterochiral analogue in acetonitrile.[3] This difference in SCO has been attributed to a steric clash between phenyl substituents in the homochiral isomer which are not present in the heterochiral complex. This work, which assesses the impact of chirality on the spin transition of iron(II) PyBox complexes, was made possible by the stability of the heterochiral diastereomer with phenyl substituents, as the spin states could be accurately probed in solution.

The geometry of octahedral complexes with tridentate ligands can be characterised by two parameters: the *trans* N(pyridyl)-M-N(pyridyl) angle (ϕ) and the dihedral angle between the plane of the two ligands (θ) which should be 180° and 90° respectively. Previous work in the Halcrow group on iron(II) *bis*(pyrazole)pyridine complexes[10] found that complexes with geometries that showed variation from these angles were high-spin and this observation was also shown to be the case for iron(II) PyBox complexes with isopropyl substituents.[3]

4.2 Aims

The thorough exploration of iron(II) PyBox complexes (Chapter 2) showcased not only an unequivocal link between chirality and spin state, but also an interesting occurrence of racemisation by ligand redistribution and differences in geometric distortion depending on substituent. To further explore these trends, cobalt(II) and zinc(II) analogues of the iron(II) complexes were synthesised and characterised using x-ray crystallography and NMR spectroscopy. A zinc(II) metal centre was chosen as it is a diamagnetic d^{10} metal, and thus ideally suited to 2D NMR experiments. Cobalt(II) complexes are capable of undergoing spin-crossover and were thus investigated for their magnetic susceptibility in addition to the aforementioned techniques.

4.3 Synthesis and characterisation of zinc(II) PyBox complexes

The PyBox ligands and shortened nomenclature used in this work are shown below in Figure 4.1.

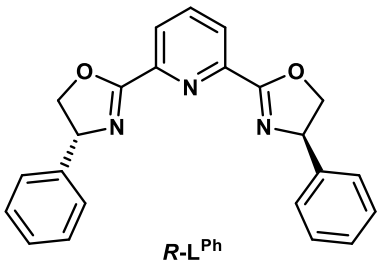

***R*-L^{Ph}**

2,6-bis[(4R)-4-phenyl-2-oxazolinyl] pyridine

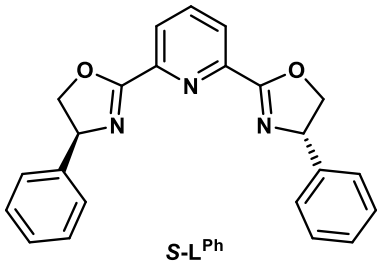

***S*-L^{Ph}**

2,6-bis[(4S)-4-phenyl-2-oxazolinyl] pyridine

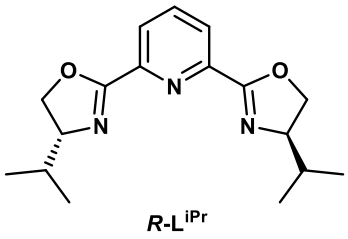

***R*-L^{iPr}**

2,6-bis[(4R)-4-isopropyl-2-oxazolinyl] pyridine

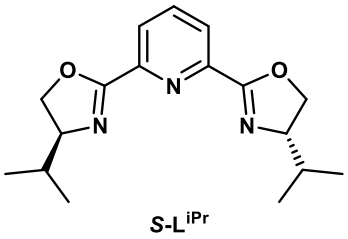

***S*-L^{iPr}**

2,6-bis[(4S)-4-isopropyl-2-oxazolinyl] pyridine

Figure 4.1 - Structures of the PyBox ligands used in this chapter.

The structures and labelling scheme used for the complexes are shown below in Figure 4.2.

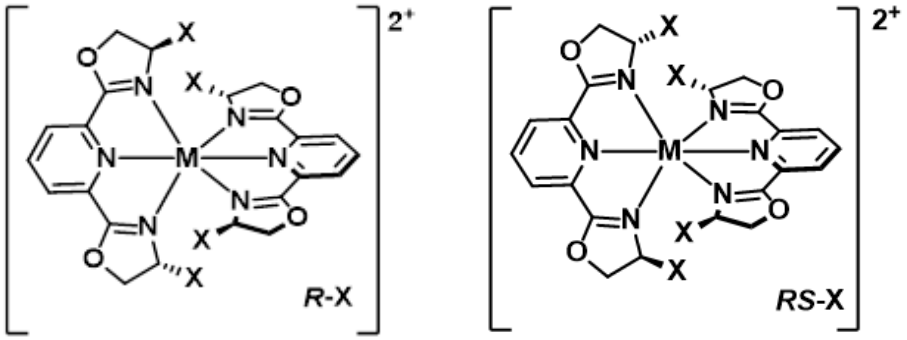

Substituent (X)	Zinc(II)		Cobalt(II)	
	Homochiral	Heterochiral	Homochiral	Heterochiral
Phenyl	***R*-6**	***RS*-6**	***R*-8**	***RS*-8**
Isopropyl	***R*-7**	***RS*-7**	***R*-9**	***RS*-9**

Figure 4.2 - Structure and labelling for complexes in this chapter. M = Zn(II) or Co(II). X = phenyl or isopropyl. All complexes have two tetrafluoroborate counterions.

The synthesis of homochiral zinc(II) or cobalt(II) PyBox complexes was achieved by stirring 2 equivalents of ***R*-L^{Ph}** or ***R*-L^{iPr}** with 1 equivalent of zinc(II) tetrafluoroborate hydrate or cobalt(II) tetrafluoroborate hydrate in acetonitrile at room temperature. The synthesis of heterochiral zinc(II) or cobalt(II) PyBox complexes was similarly achieved; 1 equivalent of both ***R*-L^{Ph}** and ***S*-L^{Ph}** or both ***R*-L^{iPr}** and ***S*-L^{iPr}** were stirred with 1 equivalent of zinc(II) tetrafluoroborate hydrate or cobalt(II) tetrafluoroborate hydrate in acetonitrile. Following precipitation and filtration, a white or orange solid was isolated which was used without further purification. Whilst several crystal structures reported here showed solvent molecules in the asymmetric unit, all elemental microanalysis results indicated all complexes were in their solvent free form once they had been dried under vacuum.

4.4 X-ray crystallography of zinc(II) PyBox complexes

Single crystals suitable for x-ray diffraction were grown using vapour diffusion of diethyl ether into a concentrated solution of each complex in acetonitrile. All data was collected, solved and refined by the author. Structure solutions were achieved using intrinsic phasing through SHELXT[11] and the model was refined using the least squares method using SHELXL[12] interfaced through Olex2.[13] Images were also obtained through Olex2. All non-H atoms were modelled anisotropically at the final least-squares refinement cycles and hydrogen atoms were placed in calculated positions and refined using a riding model.

4.4.1 Homochiral (*R*-6) and heterochiral (*RS*-6)

Homochiral ***R*-6** solved in the monoclinic $P2_1$ space group with 1 complex cation, 2 BF_4^- anions and no solvent present in the asymmetric unit. The crystal structure of heterochiral ***RS*-6** solved in the monoclinic *P*c space group with 4 complexes, 8 tetrafluoroborate anions and 10 molecules of acetonitrile in the asymmetric unit. The crystal was non-merohedrally twinned and the structure was refined using the twin law (-1, 0, 0, 0, 1, 0, 0, 0, -1) with a domain ratio of 0.25(3). Some disorder was observed; two phenyl rings were restrained using fixed bond distance restraints and two counterions were refined with restrained B-F distances.

The crystal structure for ***R*-6** shows the phenyl rings from opposite ligands are in the same quadrant and therefore have close steric contact (Figure 4.3, left). This steric clash causes one phenyl ring from each pair to twist out of the plane, causing one C-H group to be angled towards the pyridyl motif of the other ligand. The second phenyl ring of the pair is almost parallel to the pyridyl of the other ligand, which causes a slightly offset, stacked π-π interaction. In ***R*-6**, each ligand has one stacked and one twisted phenyl ring. However other reports of isostructural complexes $[M(R\text{-}L^{Ph})_2]^{2+}$ where M = Fe, Cu, Co, show that one ligand has both twisted phenyl rings, whilst the other ligand has both stacked phenyl moieties.[3, 8, 14, 15] This is also the case for the triflate salt of this complex, $\mathbf{[Zn(}\boldsymbol{R}\mathbf{\text{-}L^{Ph})_2][CF_3SO_3]_2}$.[9] The geometry of heterochiral ***RS*-6** means that all the phenyl rings are oriented away from each other, each pointing to a different

quadrant (Figure 4.3, right). Therefore there is no steric clash observed between the substituents. This geometry is also observed in the isostructural **[Zn(*R*-L^{Ph}) (*S*-L^{Ph}][CF$_3$SO$_3$]$_2$**.[9]

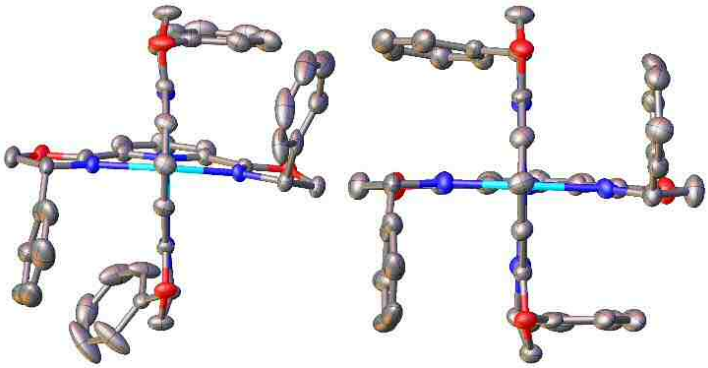

Figure 4.3 - Crystal structures of *R*-6 (left) and *RS*-6 (right). Counterions and hydrogen atoms are omitted for clarity. Colour code: Zn, turquoise; C, grey; N, blue; O, red.

Selected metric parameters from ***R*-6**, ***RS*-6** and **[Zn(*R*-L^{Ph})$_2$][CF$_3$SO$_3$]$_2$** and **[Zn(*R*-L^{Ph})(*S*-L^{Ph})][CF$_3$SO$_3$]$_2$** are shown in Table 4.1.

Table 4.1 - List of selected metric parameters for *R*-6, *RS*-6, $[Zn(R\text{-}L^{Ph})_2][CF_3SO_3]_2$ and $[Zn(R\text{-}L^{Ph})(S\text{-}L^{Ph})][CF_3SO_3]_2$.

	***R*-6**	***RS*-6 Molecule 1**	***RS*-6 Molecule 2**	***RS*-6 Molecule 3**	***RS*-6 Molecule 4**	**$[Zn(R\text{-}L^{Ph})_2][CF_3SO_3]_2.[CH_2CL_2]$**	**$[Zn(R\text{-}L^{Ph})(S\text{-}L^{Ph})][CF_3SO_3]_2.CH_2CL_2]$**
Crystal system	Monoclinic	Monoclinic	-	-	-	Monoclinic	Tetragonal
Space group	$P2_1$	Pc	-	-	-	$P2_1$	I-42d
a / Å	11.1726(2)	21.25726(19)	-	-	-	10.7259(9)	20.3707(12)
b / Å	16.6498(3)	22.4616(2)	-	-	-	21.887(2)	20.3707(12)
c / Å	12.4526(3)	20.7784(2)	-	-	-	10.8682(9)	24.178(2)
α / Å	90	90	-	-	-	90	90
β / Å	111.610(2)	91.4956(9)	-	-	-	101.624(2)	90
γ / Å	90	90	-	-	-	90	90
Volume / $Å^3$	2153.64(8)	9917.72(17)	-	-	-	2499.1(4)	10033.0(12)
Zn-N(pyridyl)	2.104(3) - 2.208(3)	2.116(7) - 2.126(7)	2.131(7) - 2.134(8)	2.109(8) - 2.128(8)	2.116(7) - 2.130(7)	2.099(3) - 2.133(3)	2.110(4) - 2.125(4)
Zn-N(oxazolinyl)	2.122(3) - 2.261(3)	2.170(8) - 2.217(7)	2.131(7) - 2.185(8)	2.178(8) - 2.209(8)	2.152(8) - 2.210(7)	2.153(3) - 2.219(3)	2.194(4) - 2.253(3)
Chelate bite angle	74.5(10) - 74.9(10)	74.4(3) - 75.4(3)	74.2(3) - 75.0(3)	73.7(3) - 75.7(3)	74.8(3) - 75.4(3)	74.2(1) - 75.1(1)	74.3(7) - 74.6(7)
ϕ	171.27(13)	177.1(3)	176.6(3)	171.6(3)	174.1(3)	176.4(1)	180.0(7)
θ	83.3(13)	87.0(3)	85.8(3)	83.4(3)	84.1(3)	86.6(1)	88.3(7)

Analysis of the ϕ and θ angles reveals key differences between ***R*-6** and **[Zn(*R*-L^{Ph})$_2$][CF_3SO_3]$_2$**. By using both ϕ and θ as a measure of distortion of the ligands around the metal centre, it can be seen that ***R*-6** is much more distorted than **[Zn(*R*-L^{Ph})$_2$][CF_3SO_3]$_2$**. As briefly discussed above, ***R*-6** shows a different pattern of phenyl substituent steric clash than other [Zn(*R*-L^{Ph})]$^{2+}$ complexes; ***R*-6** contains one twisted phenyl and one stacked phenyl per ligand, rather than both twisted phenyls appearing on the same ligand. This change in phenyl orientation is enough to alter the packing of the complexes (Figure 4.4 and Figure 4.5). The packing of ***R*-6** along the a axis shows interlocking between complex cations, where the perpendicular shape of one phenyl/oxazolinyl motif orients itself in the perpendicular structure of two opposing PyBox ligands. In contrast, no such cooperative orientation occurs in the packing of **[Zn(*R*-L^{Ph})$_2$][CF_3SO_{32}]**.

The heterochiral diastereomers show the same trends as the homochiral isomers when the metric parameters associated with distortion are considered. Although heterochiral diastereomers of this type are comparatively undistorted when placed alongside their homochiral counterparts, the ϕ and θ values for ***RS*-6** show more distortion to the complex than **[Zn(*R*-L^{Ph})(*S*-L^{Ph})][CF_3SO_3]$_2$.**

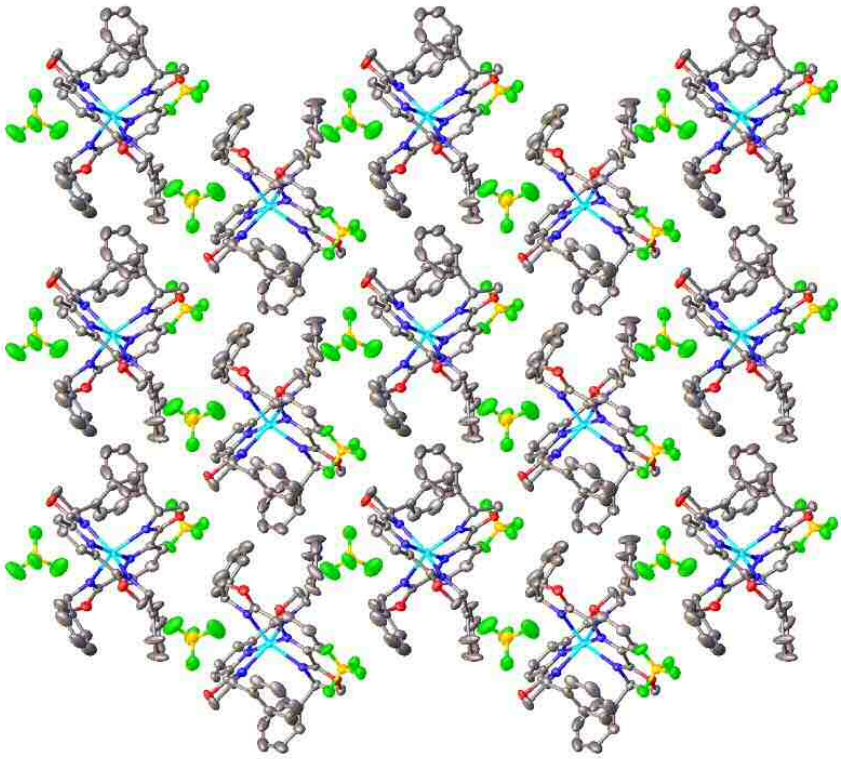

Figure 4.4 - Packing of *R*-6 along the a axis. Hydrogen atoms are omitted for clarity. Colour code: Zn, turquoise; C, grey; N, blue; O, red; B, yellow; F, green.

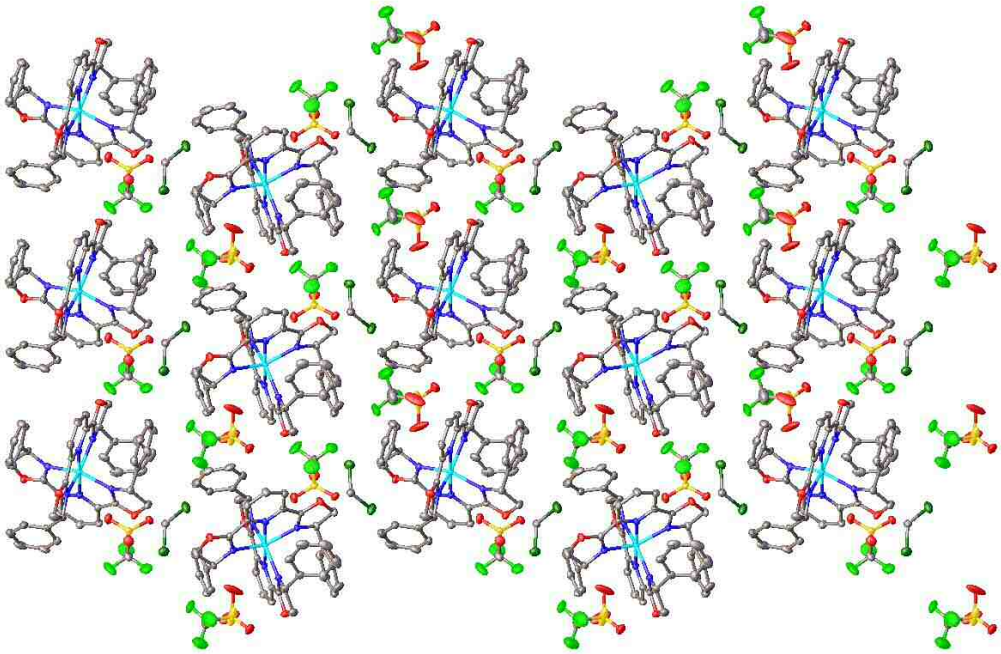

Figure 4.5 - Packing of $[Zn(R\text{-}L^{Ph})_2][CF_3SO_3]_2$ down the a axis. Hydrogen atoms are omitted for clarity. Colour code: Zn, turquoise; C, grey; N, blue; O, red; B, yellow; F, green.

4.4.2 Homochiral (*R*-7) and heterochiral (*RS*-7)

Homochiral ***R*-7** was solved in the orthorhombic $P2_12_12_1$ space group with two complex cations, four tetrafluoroborate anions and one molecule of acetonitrile in the asymmetric unit. The crystal structure for heterochiral ***RS*-7** was solved in the monoclinic $P2_1/n$ space group, with 1 complex cation and 2 tetrafluoroborate anions in the asymmetric unit.

In ***R*-7** (Figure 4.6, left), two isopropyl groups are angled towards the same quadrant, although the increased rotational flexibility of this substituent allows the avoidance of a steric clash similar to that observed in the phenyl groups for ***R*-6**. This leads to CH-π interactions between the isopropyl substituent and a pyridyl or oxazolinyl ring. Thus this repulsion leads to a large distortion of the θ angle for this complex. As a result of the opposing chirality of the ligands, the characteristics of the isopropyl groups in ***RS*-7** are different, meaning that the substituents are oriented towards four different quadrants in a similar manner to ***RS*-6**.

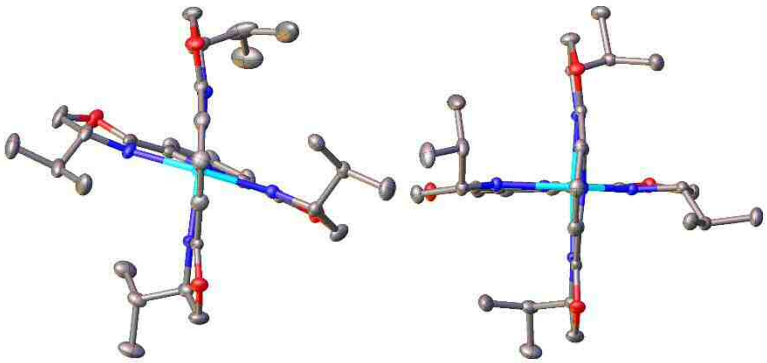

Figure 4.6 - Crystal structures of *R*-7 (left) and *RS*-7 (right). Counterions and hydrogen atoms are omitted for clarity. Colour code: Zn, turquoise; C, grey; N, blue; O, red.

Table 4.2 contains selected metric parameters for ***R*-7** and ***RS*-7**, which have not been crystallographically characterised previously. These complexes show similar trends to ***R*-6** and ***RS*-6**, in terms of distortion around the zinc metal centre. Homochiral ***R*-7** shows significant distortion of both ϕ and θ from their ideal values as a result of repulsion between isopropyl substituents oriented away from each other. In contrast,

heterochiral ***RS*-7** has an almost ideal θ angle, although ϕ is deviated to a similar extent as ***R*-7**.

In general, isopropyl substituted ***R*-7** and ***RS*-7** show much more divergence from the ideal octahedral geometry than their phenyl substituted counterparts ***R*-6** and ***RS*-6**. This trend was also observed in the previously discussed corresponding iron(II) complexes.

Table 4.2 - List of selected metric parameters for *R*-7 and *RS*-7.

	***R*-7 Molecule 1**	***R*-7 Molecule 2**	***RS*-7**
Crystal system	Orthorhombic	-	Monoclinic
Space group	$P2_12_12_1$	-	$P2_1/n$
a / Å	12.61158(13)	-	9.16507(8)
b / Å	15.39473(15)	-	23.11363(16)
c / Å	40.6472(4)	-	17.77946(14)
α / Å	90	-	90
β / Å	90	-	95.7046(8)
γ / Å	90	-	90
Volume / Å^3	7891.73(14)	-	3747.71(5)
Zn-N(pyridyl)	2.087(3) - 2.094(3)	2.073(3) - 2.082(3)	2.0928(11) - 2.1111(11)
Zn-N(oxazolinyl)	2.189 (3) - 2.345(3)	2.213(3) - 2.348(3)	2.1825(11) - 2.3295(11)
Chelate bite angle	78.38(12) - 76.65(13)	73.88(12) - 76.32(12)	73.47(4) - 76.19(4)
Φ	163.59(12)	171.97(12)	162.15(4)
Θ	77.73(10)	76.96(12)	89.52(4)

4.5 X-ray crystallographic characterisation of cobalt(II) PyBox complexes

4.5.1 Homochiral (*R*-8) and heterochiral (*RS*-8)

Homochiral ***R*-8** was solved in the $P2_1$ space group with one complex cation, two tetrafluoroborate anions and three molecules of acetonitrile in the asymmetric unit. Heterochiral ***RS*-8** was solved in the Pc space group with four complex cations, eight tetrafluoroborate counterions and eight molecules of acetonitrile in the asymmetric unit. The crystals exhibited non-merohedral twinning similar to ***RS*-6** and were refined

as a two component twin using HKL5 refinement with a domain ratio of 0.268. However the crystals were much more weakly diffracting and, whilst a structure was obtained, the data were not of sufficient quality to publish alongside the other structures in this work.[16] Fixed bond distance restraints were applied to one phenyl ring and one molecule of acetonitrile. Both ***R*-8** and ***RS*-8** have bond lengths of Co-N 2.0 - 2.2 Å, indicating that the complexes are high spin.[17]

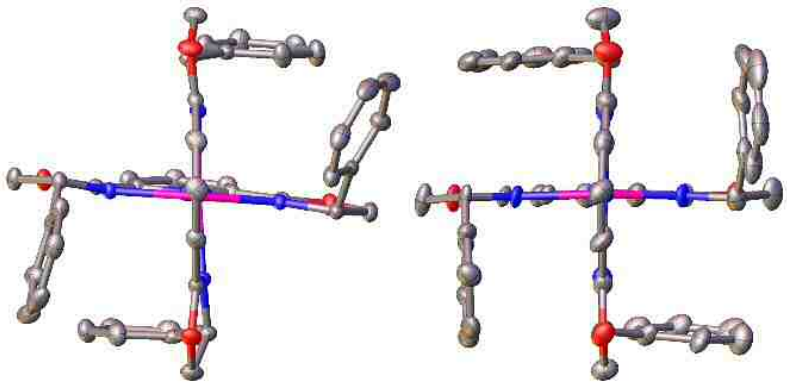

Figure 4.7 - Crystal structures of *R*-8 (left) and *RS*-8 (right). Counterions and hydrogen atoms are omitted for clarity. Colour code: Co, pink; C, grey; N, blue; O, red.

***R*-8** has the geometry typical to PyBox complexes of this type where the substituents are phenyl rings. The phenyl groups from opposing ligands are directed into the same two quadrants, causing one ring to twist due to steric clashes. ***R*-8** has two twisted and two stacked phenyl rings and each type appears on the same PyBox ligand. The stacked phenyl rings form slightly offset π–π interactions with the pyridyl moiety of the other ligand. In contrast to ***R*-6**, ***R*-8** has both twisted phenyl rings on the same ligand. This configuration is consistent with literature examples of $[M(R\text{-}L^{Ph})_2]^{2+}$ complexes, where M = Fe, Co, Cu and Zn.[3, 8, 14, 15] This difference in orientation of phenyl substituents clearly influences the long range structure of the complexes. The packing of ***R*-8** down the a axis is shown in Figure 4.8. The packing structure is different to ***R*-6** and the same as that for **$[Zn(R\text{-}L^{Ph})_2][CF_3SO_3]_2$** (Figure 4.5), which also shows both twisted and both stacked phenyl rings on the same ligand. In a similar fashion to ***RS*-6**, ***RS*-8** has all phenyl substituents oriented towards a different quadrant and therefore no steric clash between the phenyl rings is observed.

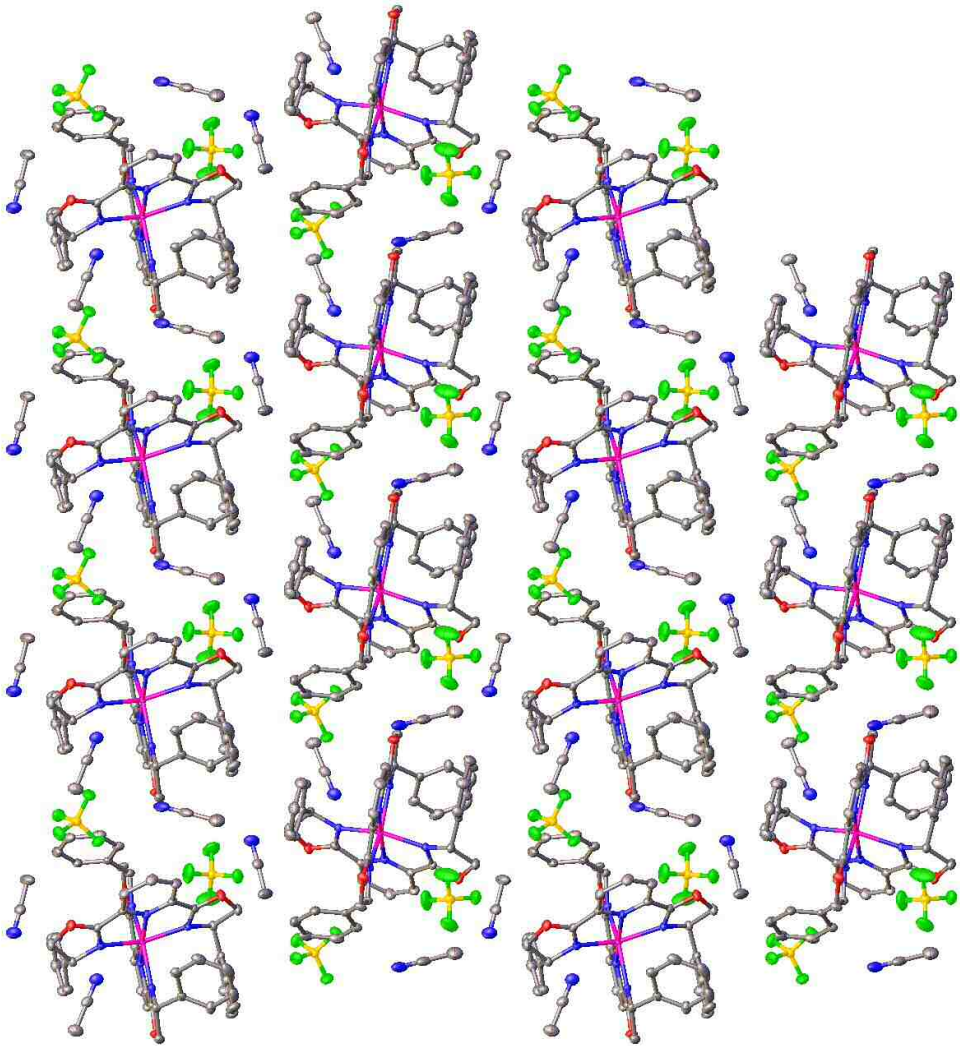

Figure 4.8 - Packing of *RS*-8 down the a axis. Hydrogen atoms are omitted for clarity. Colour code Co, pink; C, grey; N, blue; O, red; B, yellow; F, green.

The metric parameters of ***R*-8** were compared to the previously reported similar complex, **[Co(*R*-L^{Ph})$_2$][CoCl$_4$]$_2$.[2DMF]**[18] (Table 4.3). The bond lengths of the two complexes show no significant differences, but the ϕ and θ angles show an interesting difference. The distortion of both angles is greater for ***R*-8** than for **[Co(*R*-L^{Ph})$_2$][CoCl$_4$]$_2$.[2DMF]**.

As expected, ***R*-8** shows a distorted octahedral geometry; the ϕ and θ angles (Table 4.3) are deviated from the ideal values, although ***RS*-8** does show some distortion

in these parameters, particularly in ϕ. These observations about the geometry are consistent with the isostructural iron(II) and zinc(II) PyBox complexes.

4.5.2 Heterochiral (*RS*-9)

Heterochiral ***RS*-9** was solved in the P-1 space group with one complex cation, two tetrafluoroborate anions and one molecule of acetonitrile in the asymmetric unit. Despite numerous attempts, single crystals suitable for x-ray diffraction of ***R*-9** could not be grown. The Co-N bond lengths are 2.0 - 2.2 Å, which are characteristic of a high spin Co(II) complex.[17]

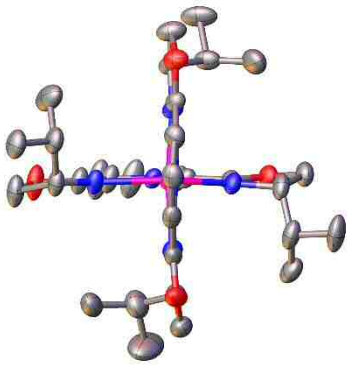

Figure 4.9 - Crystal structures of *RS*-9. Counterions and hydrogen atoms are omitted for clarity. Colour code: Co, pink; C, grey; N, blue; O, red; B, yellow; F, green.

***RS*-9** has not been previously reported. Due to the lack of crystals of sufficient quality of ***R*-9**, the homochiral and heterochiral diastereomers cannot be directly compared crystallographically. However, examination of the metric parameters in Table 4.3 shows a slight distortion as a result of the ϕ angle, although this is distorted to a much lesser extent than for the analogous zinc complex, ***RS*-7**.

Table 4.3 - List of selected metric parameters for *R*-8, *RS*-8, *RS*-9 and $[Co(R\text{-}L^{Ph})_2][CoCl_4]_2$.[2DMF].

	***R*-8**	***RS*-8 Molecule 1**	***RS*-8 Molecule 2**	***RS*-8 Molecule 3**	***RS*-8 Molecule 4**	***R*-9**	**$[Co(R\text{-}L^{Ph})_2][CoCl_4]_2$.[2DMF]**
Crystal system	Monoclinic	Monoclinic	-	-	-	Triclinic	Monoclinic
Space group	$P2_1$	Pc	-	-	-	P-1	$P2_1$
a / Å	10.81668(11)	21.2207(3)	-	-	-	11.7604(2)	10.8775(6)
b / Å	21.36754(16)	22.4647(5)	-	-	-	11.8654(2)	20.4036(10)
c / Å	11.76292(12)	20.7348(3)	-	-	-	16.0917(2)	12.9752(7)
α / Å	90	90	-	-	-	76.4350(10)	90
β / Å	112.5126(12)	91.6760(10)	-	-	-	85.9730(10)	114.0240(10)
γ / Å	90	90	-	-	-	89.8950(10)	90
Volume / $Å^3$	2511.54(5)	9880.4(3)	-	-	-	2177.19(6)	2630.3(2)
Co-N(pyridyl)	2.01(2) - 2.080(2)	2.052(8) - 2.098(10)	2.069(8) - 2.087(9)	2.054(9) - 2.105(9)	2.053(8) - 2.086(9)	2.05429(3) - 2.06579(3)	2.068(6) - 2.071(6)
Co-N(oxazolinyl)	2.123(2) - 2.180(2)	2.144(9) - 2.168(9)	2.132(9) - 2.165(9)	2.124(8) - 2.161(8)	2.132(9) - 2.168(8)	2.14785(3) - 2.18134(4)	2.173(5) - 2.199(4)
Chelate bite angle	75.408) - 75.90(8)	75.4(4) - 76.4(4)	75.1(4) - 75.9(3)	75.3(4) - 75.8(3)	75.1(3) - 76.1(3)	75.7137(11) - 76.4581(10)	75.4(2) - 75.84(18)
ϕ	171.36(9)	177.9(3)	173.7(3)	176.6(4)	174.1(3)	172.20(10)	176.1(2)
θ	80.86(8)	88.2(3)	83.5(3)	87.1(3)	84.4(3)	89.96(3)	85.7(17)

4.6 Conclusions on x-ray crystallographic characterisation

The crystallographic data collected have been used to characterise distortion of the PyBox ligand around the metal centre. From this characterisation several trends can be observed. The metal at the centre of the complex appears to have no impact on the distortion of the ligand; the relevant factors are the substituent and the diastereomer. Homochiral complexes consistently show more distortion than heterochiral complexes, which can be attributed to the steric clashes of the substituents in the same quadrant. The isopropyl substituents show the most repulsion and the homochiral isomers with isopropyl substituents are therefore the most distorted. These patterns are the same for the previously reported isostructural iron(II) complexes.

4.7 Magnetic susceptibility of cobalt(II) PyBox complexes

Previous work has investigated the spin-crossover phenomenon and molecular magnetism in PyBox complexes with various metals.[3-6] Iron(II) PyBox complexes with phenyl substituents undergo SCO in the solid state, whilst their isopropyl substituted counterparts remain high spin.[3]

Cobalt(II) complexes can take the high spin or low spin form, depending on the ligand field strength. In complexes where the ligand field strength lies on the cusp of both high and low spin, the spin-crossover phenomenon can occur when an external stimulus, such as temperature, pressure or light, is applied. Magnetic susceptibility ($\chi_M T$) is a measure of spin state and can be determined in both the solid state and in solution. The spin state of a complex may differ between phases, due to the influences of solid state lattice effects, such as hydrogen bonding and π-π stacking. The magnetic susceptibilities of cobalt(II) complexes are 0.5 cm^3 K mol^{-1} and 1.9-3.5 cm^3 K mol^{-1} for

low spin and high spin respectively.[17] Transitions between these $\chi_M T$ values would indicate that a spin transition has occurred.

The solid state magnetic susceptibility of cobalt(II) PyBox complexes, ***R*-8**, ***RS*-8**, ***R*-9** and ***RS*-9** was measured across a range of temperatures (300 - 5 K). As shown in Figure 4.10, all four complexes are high spin. The $\chi_M T$ for all four complexes remain static at approximately 2.4 cm^3 K mol^{-1}, until approximately 60 K, when the complex undergoes zero-field splitting. This high spin state of these four complexes in the solid state is in contrast to their iron(II) counterparts. Whilst the iron(II) complexes with isopropyl substituents were high spin, the phenyl substituted analogues were shown to undergo a spin transition. Similarly the solution phase data for ***R*-8** and ***RS*-8** (Figure 4.10 insert) show that the complexes remain high spin in contrast to their iron(II) analogues, which do undergo SCO. Hence, all cobalt(II) diastereomers have the same spin state, in contrast to the iron(II) complexes. This difference in spin state behaviour can be accounted for by the pairing energy (P) required for low spin cobalt(II) being higher than for iron(II), therefore a stronger field ligand is needed to induce a transition from high spin to low spin.

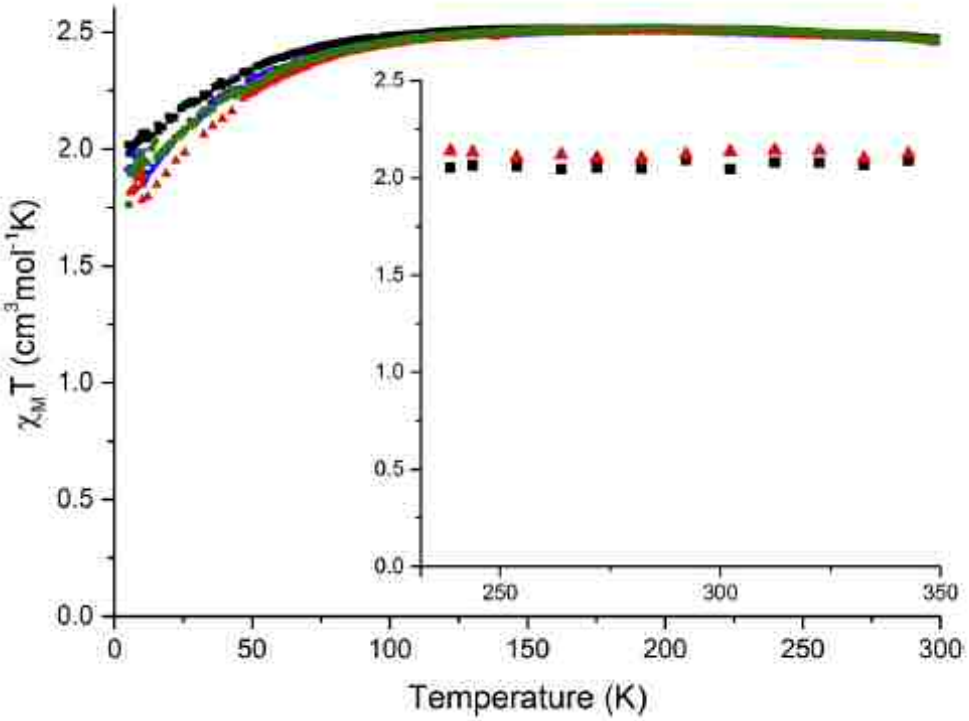

Figure 4.10 - Solid state magnetic susceptibility of cobalt(II) PyBox complexes in the solid state. *R*-8 (black squares), *RS*-8 (red triangles), *R*-9 (blue triangles) and *RS*-9 (green circles).

Insert: Solution phase magnetic susceptibility in CD_3CN. *R*-8 (black squares), *RS*-8 (red triangles).

4.8 NMR studies of zinc(II) PyBox complexes

4.8.1 Stability of heterochiral complexes in solution

^{1}H NMR studies have previously indicated that *RS*-$[M(L^{Ph})_2]^{2+}$ complexes, where M = Co, Zn or Fe, do not racemise by undergoing ligand exchange and are therefore stable in solution.[3, 8, 9] Mass spectrometry confirmed the same trend in the gas phase.[18] In contrast, when *RS*-$[M(L^{iPr})_2]^{2+}$ complexes, where M = Fe, were subjected to the same investigation, ligand exchange was observed.[18]

^{1}H NMR experiments to support this observation in zinc(II) PyBox complexes, where the substituent is a phenyl ring, and to extend the investigation to complexes with an isopropyl substituent were undertaken. Comparison of the NMR spectra for ***R***-

6 and ***RS*-6** (Figure 4.11) confirm the original observation; there are no peaks in the NMR spectrum for ***RS*-6** which would suggest racemisation to the homochiral complexes.

Conversely, Figure 4.12 shows evidence for the racemisation of ***RS*-7** to ***R*-7** due to the presence of characteristic peaks attributed to the homochiral complexes. This result is consistent with the observations of iron(II) analogues. The exchange from the phenyl substituent to an isopropyl group is clearly impacting the stability of the heterochiral complex in solution.

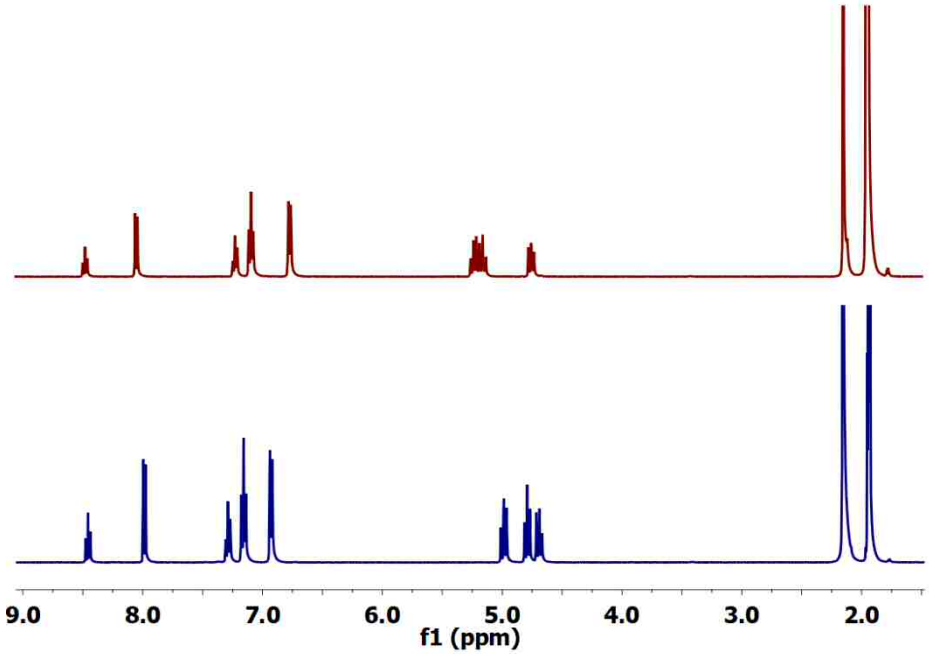

Figure 4.11 - ^{1}H NMR spectra of *R*-6 (top, red) and *RS*-6 (bottom, blue).

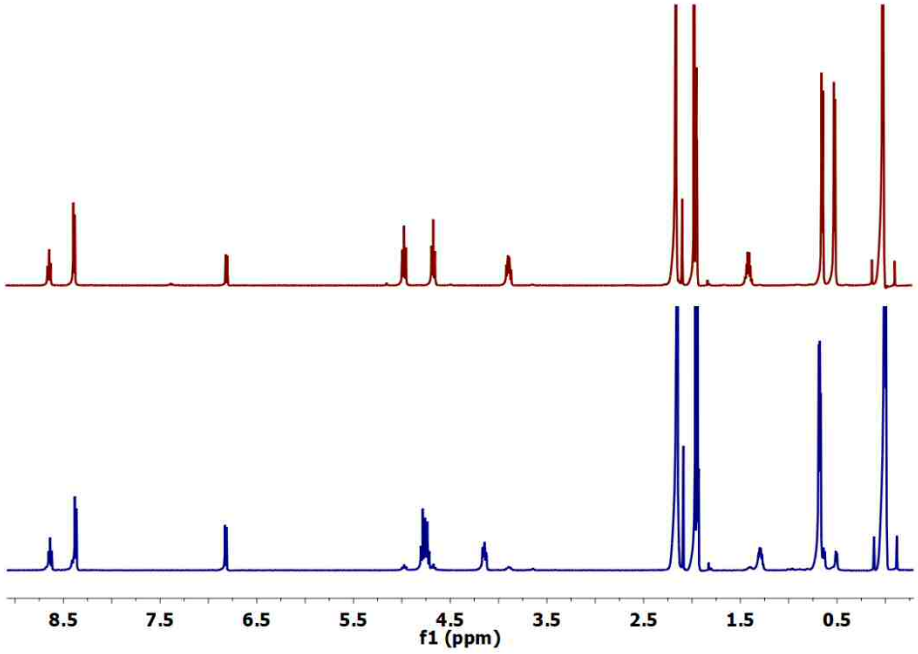

Figure 4.12 - ^{1}H NMR spectra of *R*-7 (top, red) and *RS*-7 (bottom, blue).

Experiments to ascertain the timescale of this racemisation were carried out by obtaining ^{1}H NMR spectra on ***RS*-7** at 5 minutes, 1 hour, 5 hours and 24 hours after sample preparation (Figure 4.13). However, the homochiral to heterochiral ratio remains static at ~1:4 over the 24 hour period, suggesting that some racemisation occurs almost immediately, but that the transformation from *RS* to *RR* and *SS* does not go to completion.

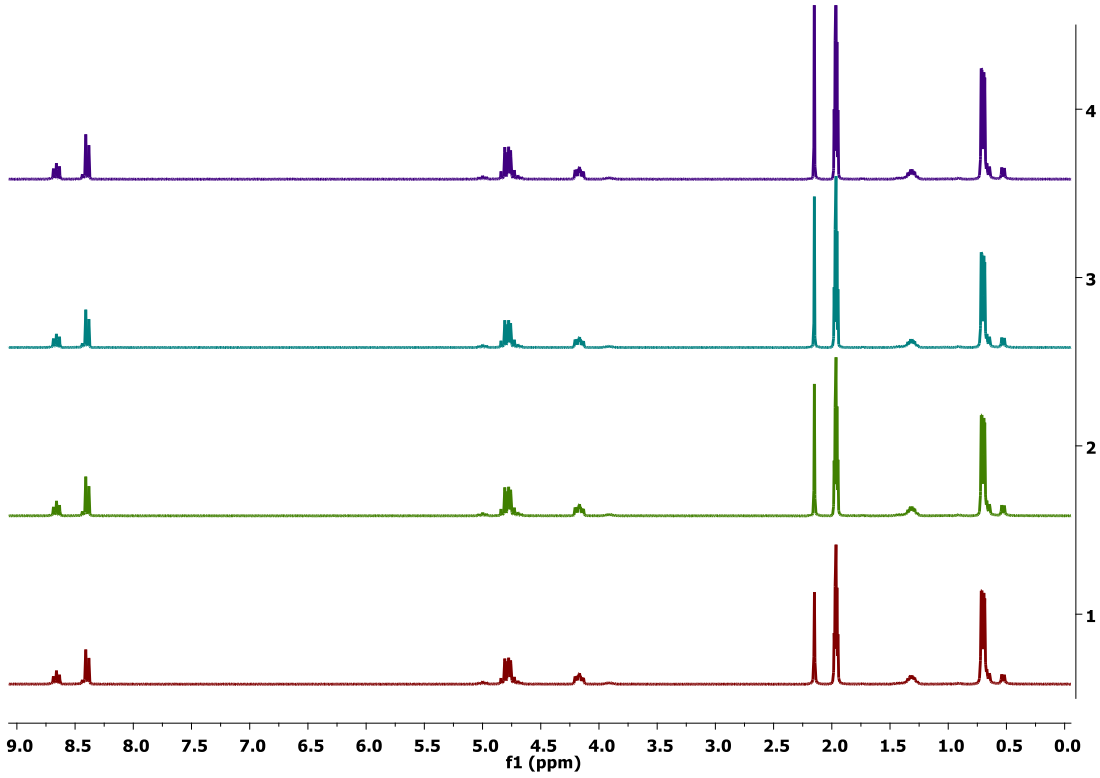

Figure 4.13 - ^{1}H NMR spectra taken at intervals to observe ligand redistribution of *RS*-7. 5 minutes (red), 1 hour (green), 5 hours (turquoise), 24 hours (blue).

4.8.2 NOESY NMR studies

Given the similarities between the structures of relevant complexes, it is likely that differences in the racemisation discussed above are a result of substituent interactions. To investigate this hypothesis further, two-dimensional NOESY NMR was employed to probe the proton-proton interactions between substituents. To elucidate the differences between isomers and to avoid verbose descriptions, this analysis is centred on interactions between the *meta* phenyl proton and the diastereotopic oxazoline protons. Interactions between the *ortho* and *para* phenyl protons and the oxazoline ring can be observed in the NOESY spectrum, however these are not discussed further.

***R*-6** shows a strong NOE between the *meta* phenyl protons and only one of the diastereotopic protons on the oxazoline rings (Figure 4.14). In contrast though, the

spectrum for ***RS*-6** (Figure 4.15) shows interactions between the *meta* phenyl protons and both oxazoline protons.

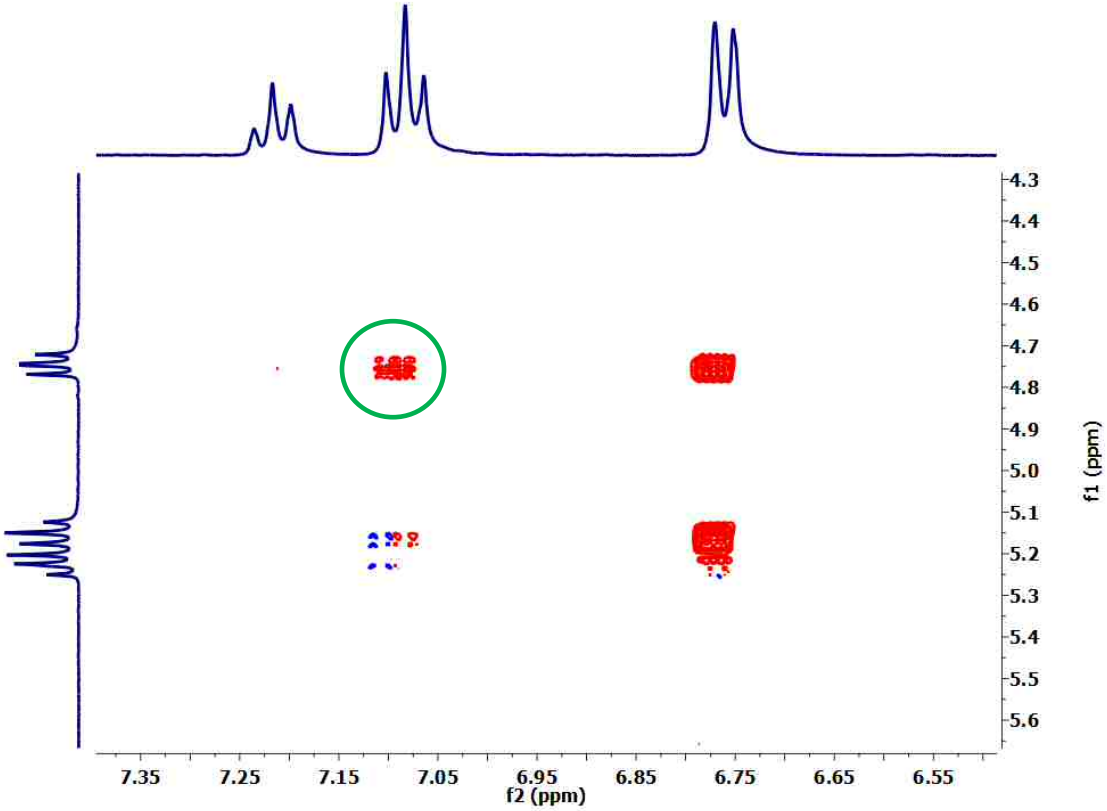

Figure 4.14 - Excerpt of the NOESY spectrum for *R*-6 in CD_3CN. The peaks between 6.6 and 7.2 ppm are phenyl protons (*ortho, meta, para*). The peaks between 4.7 and 5.3 ppm are oxazolinyl, C-H and oxazolinyl protons. The discussed single interaction between the *meta* proton and one oxazolinyl proton is indicated with a green circle.

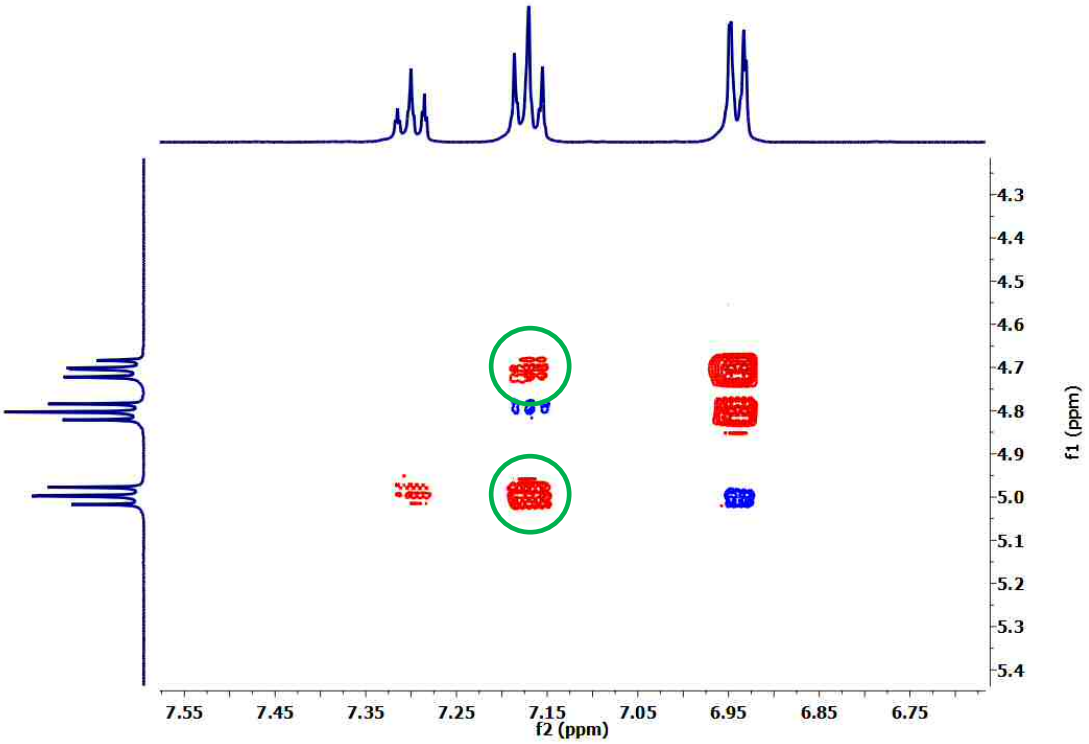

Figure 4.15 - Excerpt of the NOESY spectrum for *RS*-6 in CD_3CN. The peaks between 6.8 and 7.3 ppm are phenyl protons (*ortho*, *meta*, *para*). The peaks between 4.6 and 5.1 ppm are oxazolinyl, C-H and oxazolinyl protons. The discussed interactions between the *meta* proton and both diastereotopic oxazolinyl protons are indicated by green circles.

The patterns of the NOEs between *meta* phenyl protons and the oxazoline protons is consistent with the crystal structures for ***R*-6** and ***RS*-6** (Section 4.4.1). For ***R*-6**, only the *endo* oxazoline proton is in close proximity to the phenyl rings, hence there is only one NOE observed. In contrast, for ***RS*-6**, the change in orientation of the phenyl ring, means they lie close to both the *exo* oxazoline proton from the other ligand and the *endo* proton from the same ligand.

A similar study, using ***R*-7** and ***RS*-7**, was attempted, however the overlap between oxazoline environments in these spectra was too great and the different environments could not be distinguished.

4.9 NMR studies of cobalt(II) PyBox complexes

A previous study showed that heterochiral $[Co(L^R)_2]^{2+}$ complexes, where R = benzyl or methyl, undergo partial racemisation in solution.[8] NMR experiments to explore this for $[Co(L^R)_2]^{2+}$ complexes, where R = phenyl or isopropyl, were conducted to explore this trend further.

The paramagnetic NMR spectra for ***R*-8** and ***RS*-8** are shown in Figure 4.16. The homochiral complex, ***R*-8**, can be seen at the top of the figure in red, whilst the heterochiral complex, ***RS*-8**, is at the bottom in blue. This image shows that no peaks characteristic to ***R*-8** can be seen in the spectrum for ***RS*-8,** and that there is no partial racemisation of ***RS*-8**. This result is consistent with equivalent experiments conducted on analogous iron(II) and zinc(II) complexes with phenyl substituents.

The paramagnetic NMR spectra for ***R*-9** and ***RS*-9** are shown in Figure 4.17. Both the zinc(II) and iron(II) complexes with isopropyl substituents showed partial racemisation and this trend is continued with these cobalt(II) complexes. Peaks attributed to homochiral ***R*-9** can be seen in the spectrum of heterochiral ***RS*-9**, indicating partial ligand redistribution.

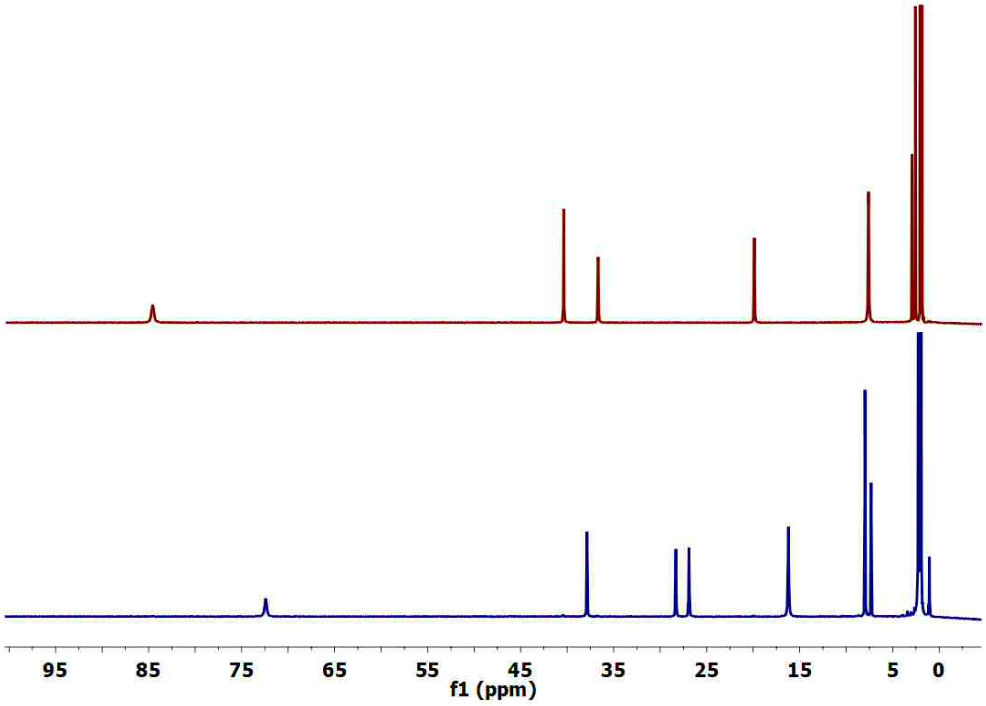

Figure 4.16 - ^{1}H paramagnetic NMR spectra of *R*-8 (top, red) and *RS*-8 (bottom, blue).

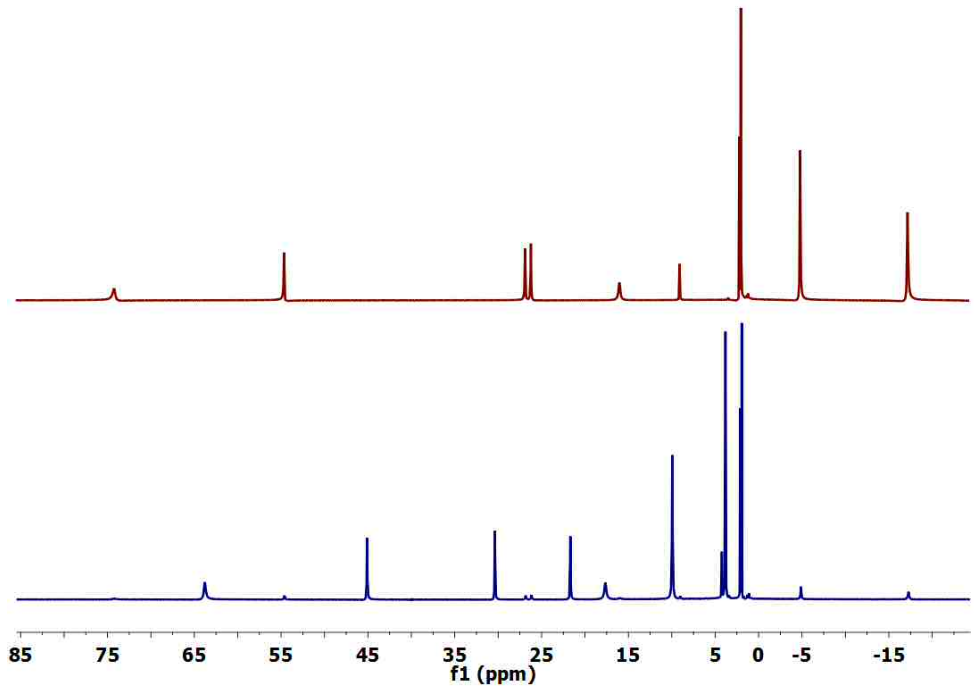

Figure 4.17 - ^{1}H paramagnetic NMR spectra of *R*-9 (top, red) and *RS*-9 (bottom, blue).

4.10 Conclusions on NMR spectroscopy experiments

NMR experiments on both zinc(II) and cobalt(II) have established a strong trend in racemisation of the heterochiral diastereomers; complexes with phenyl substituents, regardless of metal centre do not undergo ligand redistribution by racemisation in solution. Conversely, when the substituent in question is an isopropyl group, racemisation is seen to occur in both the cobalt(II) and zinc(II) complexes seen here and in the aforementioned iron(II) complexes.

The structure of homochiral and heterochiral ***R*-6** and ***RS*-6** have been explored by NOESY NMR experiments. These experiments have indicated that the substituents lie in close proximity to each other in solution, suggesting a geometry similar to that seen in the solid state.

4.11 References

1. Y. Y. Zhu, C. W. Liu, J. Yin, Z. S. Meng, Q. Yang, J. Wang, T. Liu and S. Gao, *Dalton Trans.*, 2015, **44**, 20906-20912.
2. Y.-Y. Zhu, H.-Q. Li, Z.-Y. Ding, X.-J. Lü, L. Zhao, Y.-S. Meng, T. Liu and S. Gao, *Inorg. Chem. Front.*, 2016, **3**, 1624-1636.
3. K. E. Burrows, S. E. McGrath, R. Kulmaczewski, O. Cespedes, S. A. Barrett and M. A. Halcrow, *Chem. Eur. J.*, 2017, **23**, 9067-9075.
4. S. Chorazy, K. Nakabayashi, M. Arczynski, R. Pelka, S. Ohkoshi and B. Sieklucka, *Chem. Eur. J.*, 2014, **20**, 7144-7159.
5. S. Chorazy, K. Nakabayashi, K. Imoto, J. Mlynarski, B. Sieklucka and S. Ohkoshi, *J. Am. Chem. Soc.*, 2012, **134**, 16151-16154.
6. S. Chorazy, K. Nakabayashi, N. Ozaki, R. Pełka, T. Fic, J. Mlynarski, B. Sieklucka and S.-i. Ohkoshi, *RSC Adv.*, 2013, **3**, 1065-1068.
7. T. Y. Bing, T. Kawai and J. Yuasa, *J. Am. Chem. Soc.*, 2018, **140**, 3683-3689.
8. C. Provent, G. Bernardinelli, A. F. Williams and N. Vulliermet, *Eur. J. Inorg. Chem.*, 2001, 1963-1967.
9. S. Saaby, K. Nakama, M. A. Lie, R. G. Hazell and K. A. Jorgensen, *Chem. Eur. J.*, 2003, **9**, 6145-6154.
10. L. J. Kershaw Cook, R. Mohammed, G. Sherborne, T. D. Roberts, S. Alvarez and M. A. Halcrow, *Coord. Chem. Rev.*, 2015, **289-290**, 2-12.
11. G. M. Sheldrick, *Acta Cryst. A*, 2015, **71**, 3-8.
12. G. M. Sheldrick, *Acta Cryst. C*, 2015, **71**, 3-8.
13. O. V. Dolomanov, L. J. Bourhis, R. J. Gildea, J. A. K. Howard and H. Puschmann, *J. Appl. Crystallogr.*, 2009, **42**, 339-341.
14. J. Guo, B. Wang, J. Bi, C. Zhang, H. Zhang, C. Bai, Y. Hu and X. Zhang, *Polymer*, 2015, **59**, 124-132.
15. D. A. Evans, M. C. Kozlowski, J. A. Murry, C. S. Burgey, K. R. Campos, B. T. Connell and R. J. Staples, *J. Am. Chem. Soc.*, **121**, 669-685.

16. K. E. Burrows, R. Kulmaczewski, O. Cespedes, S. A. Barrett and M. A. Halcrow, *Polyhedron*, 2018, **149**, 134-141.
17. S. Hayami, Y. Komatsu, T. Shimizu, H. Kamihata and Y. H. Lee, *Coord. Chem. Rev.*, 2011, **255**, 1981-1990.
18. H. Sato, Y. Suzuki, Y. Takai, H. Kawasaki, R. Arakawa and M. Shizuma, *Chem. Lett.*, 2010, **39**, 564-566.

Chapter 5 - Spin-Crossover in Tripodal Iron(II) Pseudoclathrochelate Complexes

5.1 Introduction

Supramolecular chemistry is a vast area of research with an incredibly diverse array of structural motifs include porphyrins[1, 2], crown ethers[3] and hexamines.[4] In 1968, Lehn, Dietrich and Sauvage contributed to this field by introducing cryptands, defined as a "*…nouvelle classe de complexes métalliques*" (a novel class of metal complexes).[5] These molecules feature large bicyclic macrocycle ligands that can encapsulate transition metals as well as alkaline earth metals and anions.[5, 6] Within this field, there is scope to investigate electron transfer, spectroscopic properties and intramolecular rearrangements without the occurrance of ligand substitution.[7]

Clathrochelate complexes (Figure 5.1) are related to cryptands and can be defined as metal complexes in which the metal centre is completely encapsulated in a ligand cage.[8] The 1960s and 1970s saw the emergence of these complexes, such as those shown in Figure 5.2 from the groups of Rose,[9] Holm,[10] Goedken[11] and Sargeson,[7] and these early examples were mostly formed by either boron-capped or hexamine architectures.

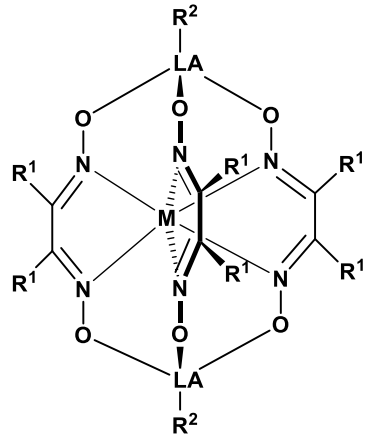

Figure 5.1 - General structure of clathrochelate complexes based on dioximate or oximehydrozonate ligands and Lewis acid capping moieties. LA = Lewis acid, R^1 and R^2 = various substituents.

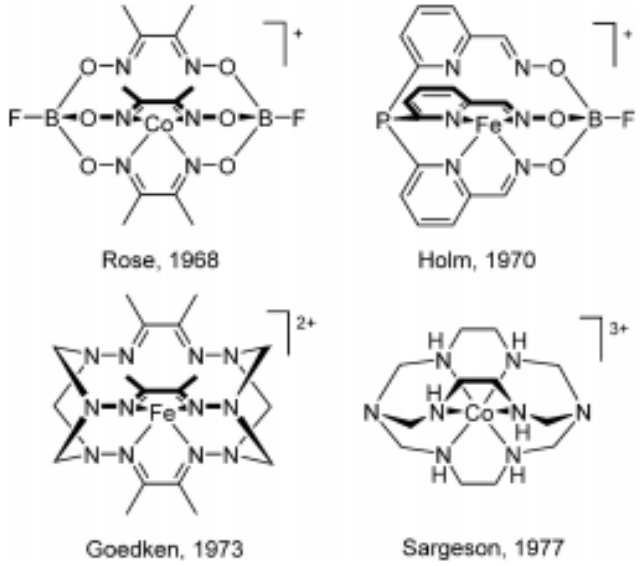

Figure 5.2 - Structures of early clathrochelate complexes.[12]

Since then, a plethora of clathrochelate complexes with different metal centres and ligand architectures have been prepared and characterised. Most of these examples focus on a dioximate or oximehydrazonate core capped by Lewis acid moieties, including boron[8, 13], antimony[14], tin[15] and germanium.[16] The most common procedure for synthesis is a metal-templated condensation reaction between the dioximate core and the capping agent. Once formed, clathrochelates typically exhibit thermodynamic and kinetic stability, tuneable redox potentials and good solubility.[12]

Numerous different architectures based on clathrochelate complexes have been reported. Dimetallic iron complexes formed from oximehydrazonate ligands which are bridged with phenyl borate, ferrocenyl borate and ferrocenyl diborate motifs have been prepared by Grzybowski and co-workers.[13] Unusual structural phase transitions of clathrochelate Fe(II) complexes from both dioximate or oximehydrazonate ligands with long alkyl chains on the boron capping ligand have been reported.[17] A cobalt diamine monoxime monoximate complex, upon double deprotonation, formed a multimetallic complexes with cobalt, zinc, cadmium, manganese and ruthenium coordination.[18] This

handful of examples highlights the diversity of clathrochelates in terms of type and number of metal ions, capping group and ligand structure.

As well as investigations into structural diversity, clathrochelate complexes with interesting magnetic properties have been reported. A cobalt (II) hexachloroclathrochelate complex with trigonal prismatic geometry was found to show single-molecule magnetic behaviour.[19] It is postulated that the cage structure of this complex adds the rigidity needed for such behaviour, as well as providing a point of functionalisation to tune the magnetic properties further in the future.

The SCO behaviour of a cobalt(II) methyl phenylboronic acid capped hexachloroclathrochelate was investigated. The complex undergoes gradual, incomplete SCO in the solid state, yet is high-spin in solution. The authors propose that the weak π-Cl intermolecular interactions cause anti-cooperative spin transitions to occur; this effect are more gradual in the solid state than in solution. This result is particularly interesting given that much SCO research focuses on the crystal engineering that governs solid state cooperativity.[20]

A variety of transition metals situated at the centre of clathrochelate complexes have been investigated. It is theorised that the encapsulation experienced by the metal could stabilise low oxidation states, and indeed some examples have been isolated. Voloshin and coworkers have extensively studied such systems and have isolated cobalt(I), (II) and (III) clathrochelate complexes[21, 22], as well as an iron(II) complex.[23] The use of ruthenium(II) and ruthenium (III) has also been reported; when ruthenium(III) is used, the complex formation triggers the *in-situ* reduction to ruthenium(II).[24] These examples highlight the exciting redox chemistry which is possible in this class of complexes.

Two practical uses for clathrochelate complexes are catalysis and biological applications. Some very recent examples include the conjugation of an iron(II) clathrochelate complex and a ruthenium tris(bipyridine) dye[25] and an iron(IV) clathrochelate complex, [26] both for water oxidation reactions. Iron(II) and cobalt(II) clathrochelates have also been shown to be effective for hydrogen evolution

reactions.[27, 28] In addition, an iron(II) clathrochelate complex has been shown to be effective against human promyelocytic leukemia cells.[29]

Clathrochelates have also been incorporated into materials, including nanostructures, polymers, thin films and metal-organic frameworks (MOFs).[12] A porous framework built from cross-linked iron(II) clathrochelate complexes showed permanent porosity. When this framework was formed from enatiopure dioximate ligands, a chiral network was formed which selectively absorbed D-tryptophan over L-tryptophan.[30] The first example of polyclathrochelates formed *via* a one-step polycondensation reaction was reported in 2017.[31] These 1D polymers formed stable gels when they were sonicated. The properties of such gels can be tuned by substituting different dioximate ligands and capping agent. A series of 1D, 2D and 3D polymers were formed from dinuclear clathrochelate complexes with two, three, four or five cyano groups on the ligand. A variety of transition metals were used, forming heterometallic Zn^{2+}/Ag^{+} and Co^{2+}/Ag^{+} coordination polymers.[32] The ability to incorporate different metal centres into the same material highlights the potential of clathrochelates for functional materials. Iron(II) clathrochelates have also been used as initiators to control the radical polymerisation of styrene and methyl methacrylate.[33]

Pseudoclathrochelate complexes are similar to clathrochelates, but have a tripodal rather than macrocyclic scaffold and are therefore not as rigid. These complexes can also be formed *via* metal-templated condensation reactions between oximate ligands, capping groups and a metal, allowing access to similar diversity as that seen in their clathrochelate counterparts.

Hörner and Breher designed a pair of pseudoclathrochelate complexes (Figure 5.3) with pendant ligands, designed to direct the complexes towards trigonal prismatic geometry, tethered with a rigid double-bonded sulfur-phosphorus capping group.[34] A detailed analysis of the relationship between the structure and electronic properties of the complexes revealed that the SCO behaviour of these complexes is dependent upon the geometry around the iron(II) centre. In its high-spin form, the geometry is trigonal prismatic whereas after undergoing a spin transition to the low-spin form, the geometry is octahedral. This change in geometry occurs *via* Bailar's trigonal twist pathway.[35]

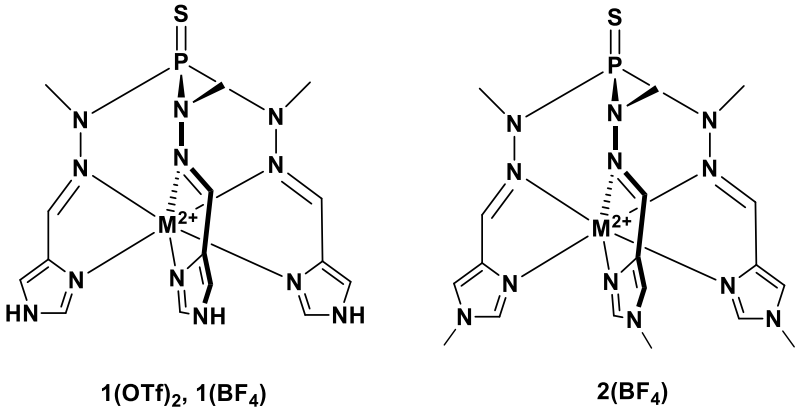

Figure 5.3 - Structures of sulfur-phosphorous tethered clathrochelate complexes.

Voloshin and coworkers explored a phenyl boronic acid capping group to form a range of pseudo-clathrochelate tris-pyrazoloximate complexes with zinc(II), cobalt(II), iron(II) and manganese(II).[36] The iron(II) complex in this series showed distorted trigonal prismatic geometry and was high-spin. The chloride ion proved to be critical in the self-assembly process and templated the complex formation by forming hydrogen bonds with the pyrazole hydrogen bonds. This process was selective for chloride ions, even in the presence of large excesses of bromide and iodide ions.

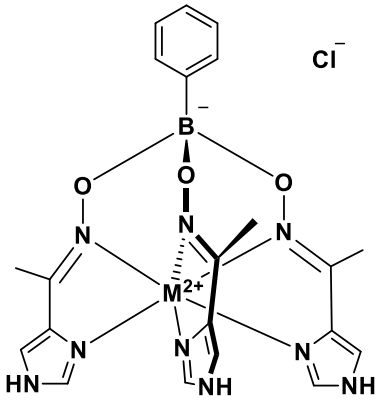

Figure 5.4 - General structure of pseudo-clathrochelate tris-pyrazoloximate complexes, where M = zinc(II), cobalt(II), iron(II) or manganese(II).

A more recent study by the same group examined the structures and magnetic behavior of iron(II), cobalt(II), manganese(II) and zinc(II) hexadecylboron-capped tri(pyrazoloximate) complexes.[37] The crystal structure of each complex indicated the

presence of hydrogen bonding between the chloride counterion and the pyrzaole-NH group in a similar manner to that seen in the complexes discussed above.[36] The iron(II), cobalt(II) and manganese(II) complexes were all high-spin.

These examples show the diversity of clathrochelate and pseudoclathrochelate complexes, both in terms of their structure and function for applications such as catalysis, pharmaceutical agents and functional materials.

5.2 Aims

The above discussion of clathrochelates and pseudoclathrochelates presents an overview of the structural diversity available in this family of complexes. This diversity makes it easy to tune the spectroscopic, redox and magnetic properties, as well as provide a scaffold to link or tether complexes for incorporation into polymeric networks or surfaces.

The aim of this work was to produce a series of novel iron(II) pseudoclathrochelate complexes, formed *via* a metal-templated self-assembly reaction between iron(II) perchlorate, phenyl boronic acid and oximate ligands with various N-donating aromatic and substituted aromatic groups. Once prepared, the magnetic behaviour in both the solid state and solution was tested to assess the capability of these complexes to undergo spin-crossover.

The long-term goal for this project was to include such complexes in polymeric functional materials. Whilst most polymers with spin-crossover capabilities are based on coordination polymers, the tripodal pseudoclathrochelate structures investigated here would give a more unusual polymeric architecture, with the complexes acting as pendant structures from an organic polymer chain. This framework could potentially allow selective encapsulation and release of molecular cargo upon the switch of spin state.

Given the available timescale and the unexpected sensitivity of these complexes to air, the successful functionalisation of these complexes could not be completed.

However the method used for ligand functionalisation discussed in Chapter 6 would be equally suitable for these complexes.

5.3 Synthesis of oxime ligands

The oxime ligands which make up the pendant groups in these complexes were synthesised using an established literature procedure, shown in Figure 5.5.[36] 2.5 equivalents of sodium acetate and 1.2 equivalents of hydroxylamine hydrochloride were dissolved in water and heated to 60° C for 1 hour. 1 equivalent of carboxaldehyde starting material was dissolved in methanol and this solution was added to the original mixture and heated at 60° C overnight. The solution was then cooled to 0° C which precipitated the oxime. This solid was then washed with water to remove any remaining sodium acetate or hydroxylamine hydrochloride and dried in a vacuum oven at 40° C. The structures and numbering system used in this chapter are shown in Figure 5.6.

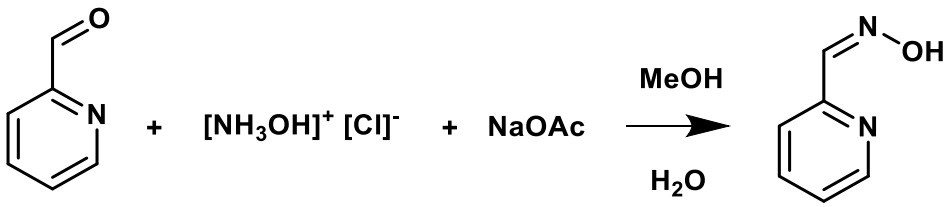

Figure 5.5 - Method of oxime formation.

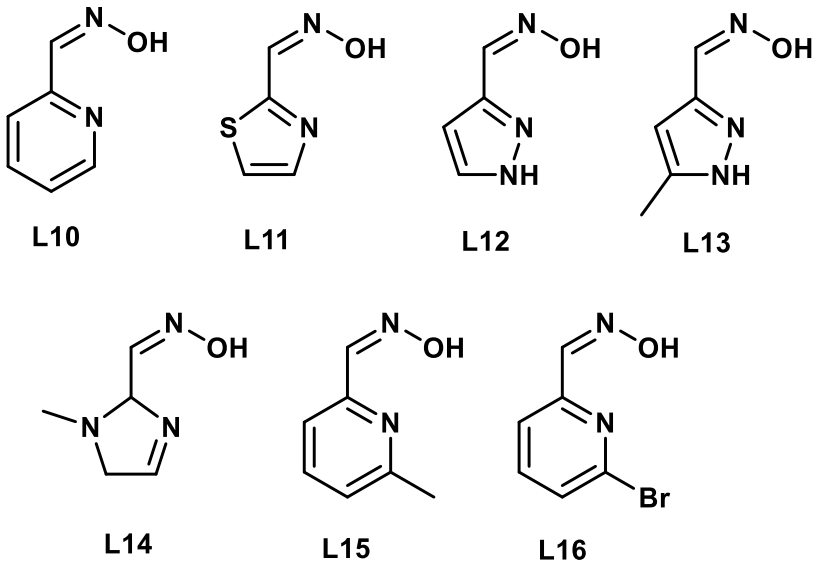

Figure 5.6 - Structures and numbering of oxime ligands discussed in Chapter 5.

All ligands were characterised by ^{1}H and ^{13}C NMR spectroscopies. The carboxaldehyde starting materials contain the peaks for the aromatic protons, along with alkyl peaks for methyl groups where appropriate. Upon conversion to the imine, a sharp singlet from the imine proton appeared in the spectrum between 7.3 and 8.10 ppm. As an example, the ^{1}H NMR for **L10** is shown below in Figure 5.7, however all the ligands showed the same trends in their spectra. The singlet at 8.10 shows the imine proton, whilst the other three peaks are the aromatic protons from the pyridine ring.

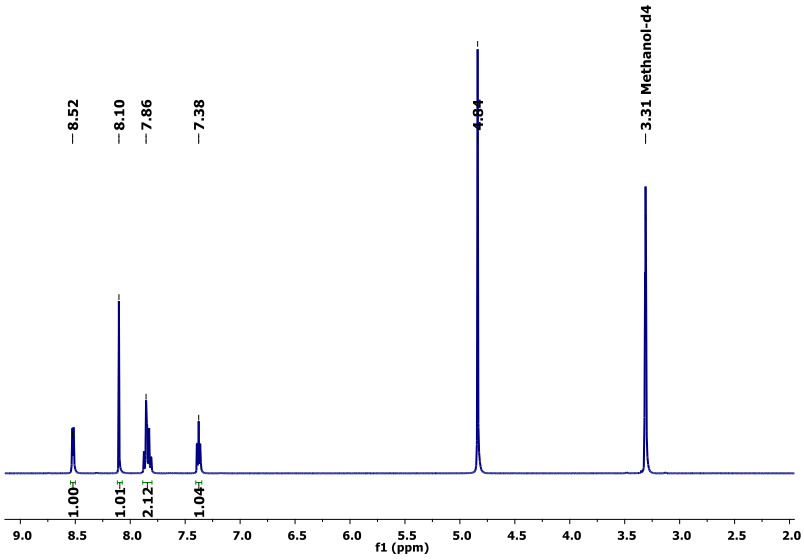

Figure 5.7 - ^{1}H NMR spectrum of L10. The peaks at 3.31 and 4.84 are residual peaks from the methanol and water in the methanol-d_4 used.

5.4 Synthesis of iron(II) pseudoclathrochelate complexes

The tripodal cage complexes discussed in this chapter were synthesised *via* a self-assembly reaction between three equivalents of oxime ligand, one equivalent of phenyl boronic acid and and one equivalent of iron(II) perchlorate in methanol. This procedure was modified from a literature preparation of similar complexes.[36] This solution was heated to reflux for 16 hours, cooled to room temperature and a red/brown solid precipitated with excess diethyl ether and isolated *via* vacuum filtration. The structures of complexes **10** - **14** are shown in Figure 5.8.

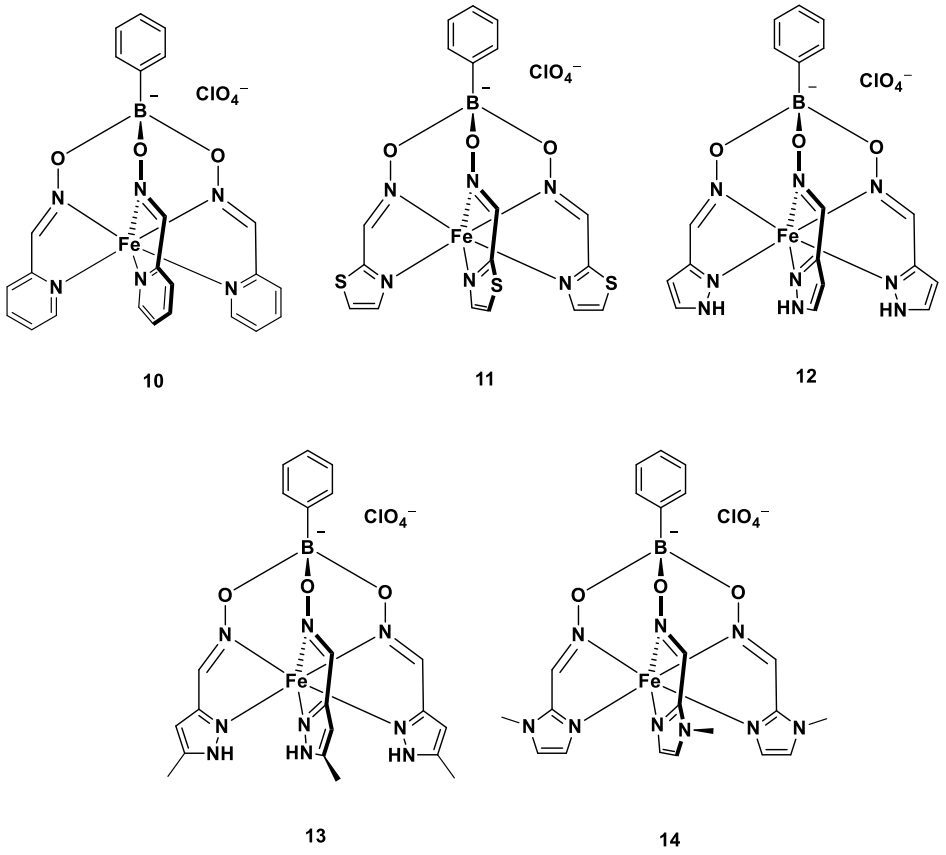

Figure 5.8 - Structures of complexes 10 - 14.

Several literature examples[20, 36, 38] of complexes which formed *via* a similar self-assembly reaction used inert conditions for the synthesis. Two test preparations of **10** were carried out to assess the necessary conditions for the complexes discussed in this chapter; one in air and one using inert conditions for both synthesis and work up. Both of these reactions gave the same product. However, subsequent reactions to form complexes **11** - **14** showed that inert conditions were required to form these compounds. Upon isolation in air, the complexes quickly decomposed leaving brown oils. Attempts to recrystallise these oils were unsuccessful, despite numerous attempts.

The synthesis of complexes **11** - **14** was repeated using the same procedure as detailed above, but with dry solvents and standard Schlenk techniques. Once the complex had been precipitated with dry diethyl ether, cannula filtration was used to isolate the solid and the Schlenk flasks were taken into the glovebox for storage of the dry samples.

Samples of complexes **11** - **14** for analysis were prepared inside the glovebox. NMR samples using dried, deuterated solvents could be made inside the glovebox. Samples for SQUID, elemental microanalysis, vapour diffusion crystallisations and mass spectrometry were weighed out into the appropriate vials in the glovebox, sealed with Parafilm and removed for further sample preparations.

The synthesis of the analogous tripodal cage complexes, **15a** and **16a** (Figure 5.9), was attempted using the same method as discussed above. However, complexes with this structure never formed; instead all products isolated from such reactions were multi-metallic clusters. These cluster complexes will be discussed further in Section 5.7.

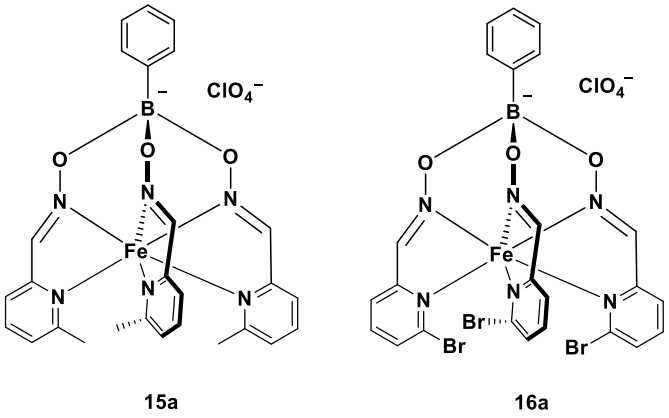

Figure 5.9 - Structures of the desired tripodal cage complexes 15a and 16a.

5.5 Solid state investigations of iron(II) pseudoclathrochelate complexes

5.5.1 Details of single crystal crystallography

Single crystals suitable for x-ray diffraction were grown using vapour diffusion of diethyl ether into a concentrated solution of each complex in acetonitrile. All data were collected, solved and refined by the author, unless otherwise stated. Structure solutions were achieved using intrinsic phasing through SHELXT[39] and the model was refined using the least squares method using SHELXL[40] interfaced through Olex2.[41] Figures were also prepared through Olex2. All non-H atoms were modelled

anisotropically at the final least-squares refinement cycles and hydrogen atoms were placed in calculated positions and refined using a riding model. Selected metric parameters for each complex are given in Table 5.1.

5.5.2 X-ray crystallography of iron(II) pseudoclathrochelate complexes (10 - 14)

Datasets of **10** were collected at 120 K, 250 K and 350 K. All three structures solved in the triclinic P-1 space group and had one complex cation and one perchlorate counterion in the asymmetric unit. At 120 K, no disorder was observed, however disorder of the perchlorate counterion was seen at 250 K and 350 K. At the temperatures, the anion was modelled isotropically over two positions with oxygen occupancies of 0.5. Fixed bond restraints of Cl-O - 1.45 Å (2) were applied in both cases. Fe-N bond lengths at all temperatures show each structure is low-spin. All three datasets show packing of the complexes occurs in the same way, regardless of temperature and that there are some offset π–π interactions between either two pendant pyridyl rings or between phenyl and pyridyl rings on adjacent complexes.

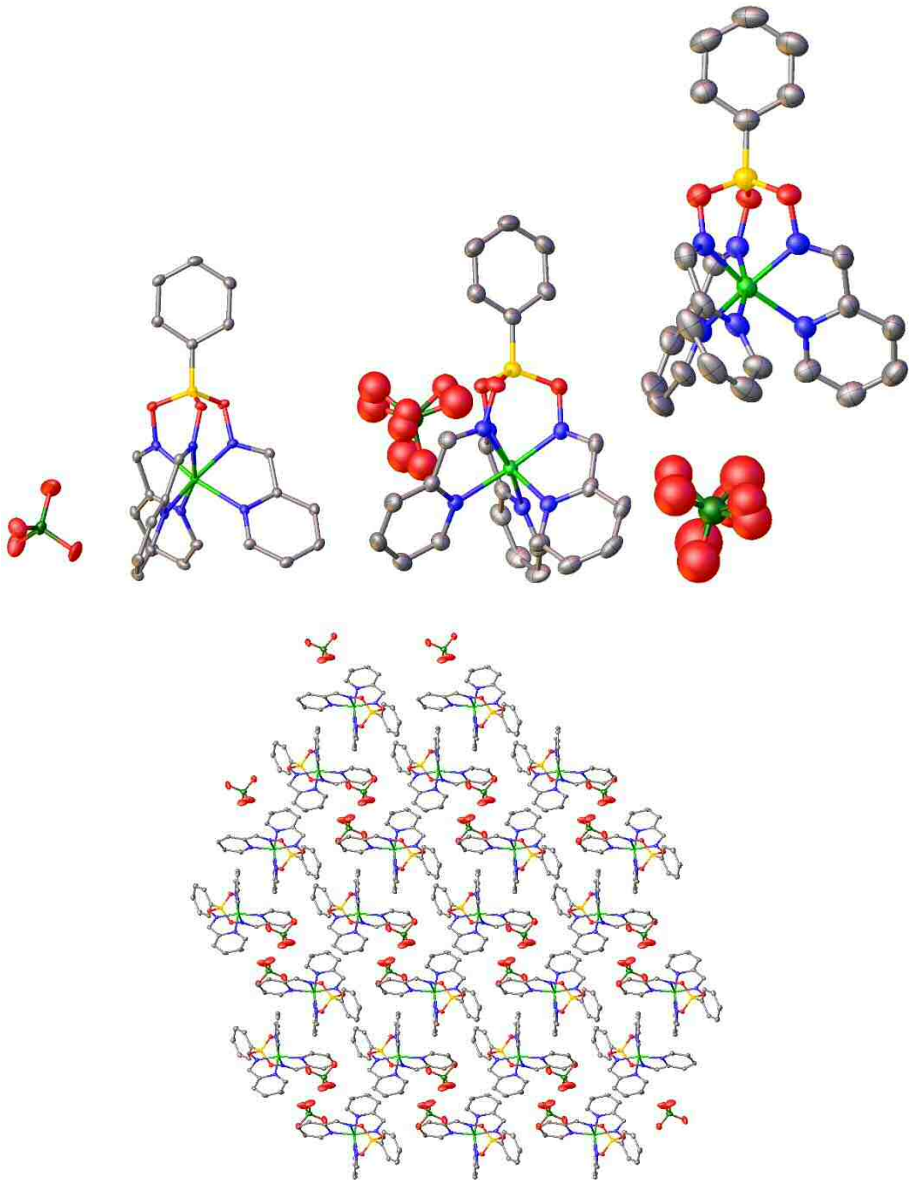

Figure 5.10 - Structure of 10 at 120 K (top left), 250 K (top middle) and 350 K (top right). Packing along the a axis of 10 at 120 K (bottom). As the packing at all temperatures is identical, only one image is included. Thermal ellipsoids are displayed at 50% probability. Hydrogen atoms are omitted for clarity.

Datasets of **11** were collected 120 K and 250 K and both solved in the triclinic P-1 space group. Both structures contain one complex cation and one perchlorate counterion in the asymmetric unit. At 120 K, no disorder was present and therefore no restraints were necessary. At 250 K, some disorder was seen in the counterion, which was modelled over two positions using oxygen occupancies of 0.5 and fixed bond restraints of Cl-O - 1.45 Å (2). Fe-N bond lengths at both temperatures indicate

complexes in their low-spin state. At both 120 and 250 K, the packing structure of **11** is identical to that of **10** and features the same offset π–π interactions.

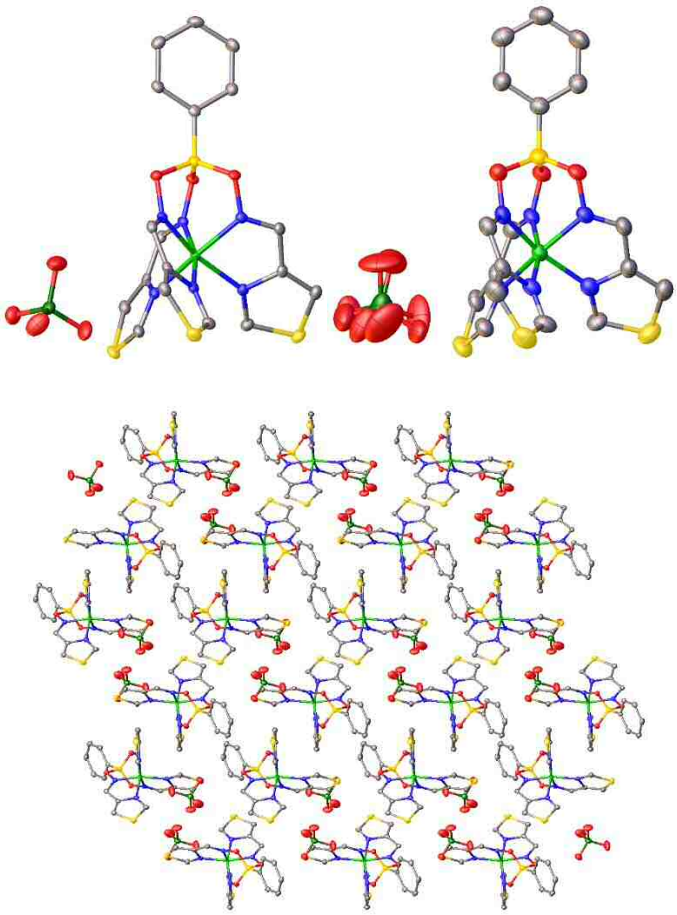

Figure 5.11 - Crystal structures of 11 at 120 K (top left) and 250 K (top right). Packing along a axis of 11 at 120 K (bottom). As the packing at both temperatures is identical, only one image is included. Thermal ellipsoids are displayed at 50% probability. Hydrogen atoms are omitted for clarity.

Despite numerous attempts in a range of solvents, complex **12** remained impervious to crystallisation.

A dataset of **13.MeCN** was collected 120 K and solved in the triclinic P-1 space group. The asymmetric unit contains one complex cation, one perchlorate counterion and one molecule of acetonitrile. Some disorder was seen in the counterion, which was refined anisotropically and modelled over two positions using oxygen occupancies of 0.5 and fixed bond restraints of Cl-O = 1.45 Å (2). Fe-N bond lengths show a high-spin complex. The location of the perchlorate counterion in this case is interesting; Voloshin

and co-workers reported a chloride ion aided self-assembly process in similar complexes, where the tripodal pendant ligand was a pyrazoloximate.[36] They report that the chloride ion forms hydrogen bonds with the pyrazole, templating the selective formation of the complex, even when large excesses of bromide or iodide ions are present. It is therefore possible that a similar templating effect occurs between the perchlorate ion and pyrazole hydrogen in **13.MeCN**, although this has not been observed in the other complexes in this chapter.

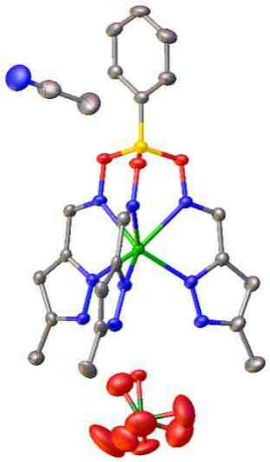

Figure 5.12 - Structure of 13 at 120 K. Thermal ellipsoids are displayed at 50% probability. Hydrogen atoms are omitted for clarity.

A structure of **14.0.5MeCN** was collected at Diamond Light Source at 100 K. The structure solved in the tetragonal $I4_1cd$ space group and contains one complex cation, one perchlorate counterion and half a molecule of acetonitrile in the asymmetric unit. The oxygen atoms in the perchlorate anion were modelled isotropically over two positions with half occupancies. The acetonitrile molecule was modelled isotropically at half occupancy. Fe-N bond lengths indicate a high-spin complex.

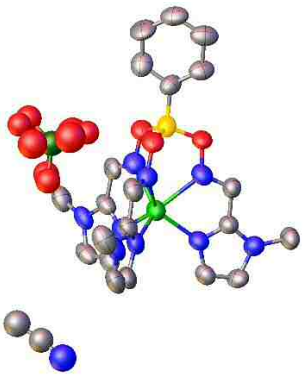

Figure 5.13 - Structure of 14 at 100 K. Thermal ellipsoids are displayed at 50% probability. Hydrogen atoms are omitted for clarity.

Table 5.1 - Selected crystallographic parameters for complexes 10 - 14.

Complex	10 (120 K)	10 (250 K)	10 (350 K)	11 (120)	11 (250)	13	14
Crystal system	Triclinic	Triclinic	Triclinic	Triclinic	Triclinic	Triclinic	Tetragonal
Space group	*P*-1	*P*-1	*P*-1	*P*-1	*P*-1	*P*-1	$I4_1cd$
a / Å	9.9332(4)	10.0218(6)	10.0858(4)	9.7149(3)	9.8237(11)	10.6613(4)	26.4281(13)
b / Å	10.5862(4)	10.6313(8)	10.6691(4)	10.5056(3)	10.5874(12)	11.8510(5)	26.4281(13)
c / Å	13.3041(6)	13.4764(7)	13.5777(6)	12.9970(3)	13.1199(14)	12.4063(6)	15.220(2)
α / Å	99.264(3)	98.983(5)	98.775(4)	100.654(2)	99.957(9)	107.984(4)	90
β / Å	108.848(4)	108.862(5)	108.908(4)	109.490(2)	109.810(11)	95.616(4)	90
γ / Å	105.453(3)	105.937(6)	106.125(3)	105.726(2)	106.338(10)	102.631(3)	90
Volume / Å^3	1228.41(9)	1258.30(15)	1279.67(10)	1146.94(6)	1176.3(2)	1431.55(11)	10630.1(14)
Fe-N(imine)	1.8882(16) - 1.8975(16)	1.887(3) - 1.901(3)	1.889(3) - 1.897(3)	1.8929(17) - 1.9076(17)	1.901(4) - 1.912(4)	2.181(2) - 2.221(3)	2.174(9) - 2.245(10)
Fe-N(aromatic)	1.9840(17) - 2.0037(16)	1.981(3) - 2.008(3)	1.991(4) - 2.008(3)	1.9867(18) - 1.9956(18)	1.994(4) - 1.997(4)	2.157(2) - 2.167(2)	2.103(10) - 2.154(11)
Bite angle (α)	79.94(7) - 80.03 (7)	79.85 (12) - 79.97 (13)	79.77 (14) - 80.18 15)	80.27(7) - 80.40(7)	80.09 (15) - 80.42(16)	72.67(9) - 73.79(9)	72.8(4) - 75.2(4)

5.5.3 Solid state magnetic susceptibility of iron(II) pseudoclathrochelate complexes

Solid state magnetic susceptibility data for complexes **10** - **14** were measured using a Super-Conducting Quantum Interference Device (SQUID) in a magnetic field of 0.5 T. These results are shown in Figure 5.14. Measurements were performed on freshly prepared powders which had been stored in the glovebox.

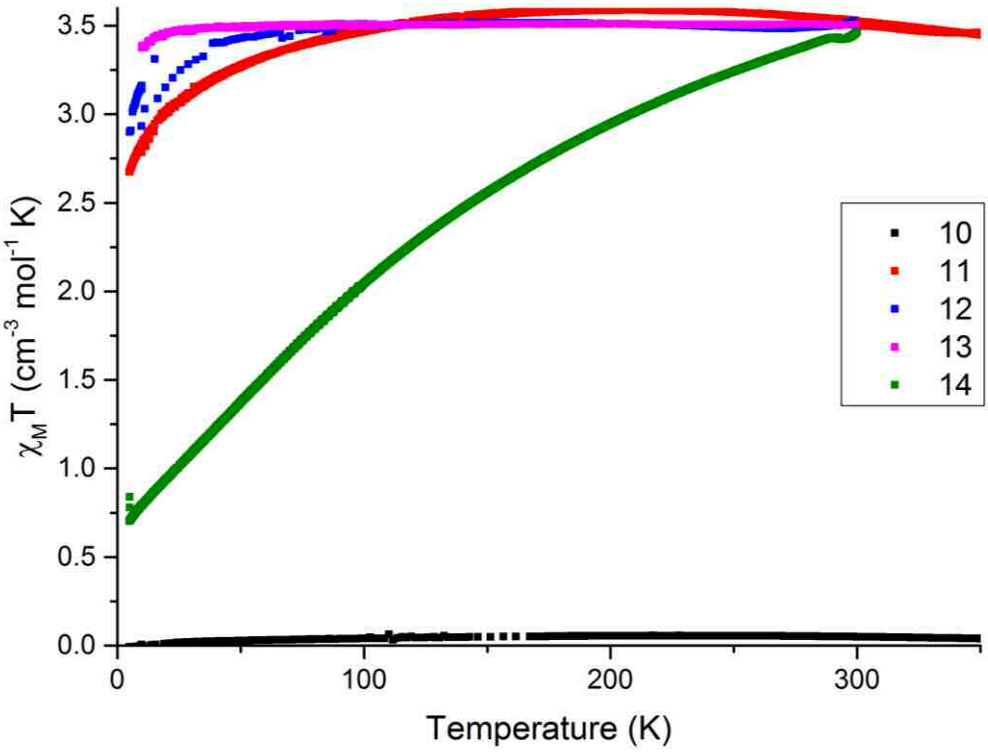

Figure 5.14 - Solid state magnetic susceptibility of complexes 10 (black), 11 (red), 12 (blue), 13 (pink) and 14 (green). Complexes 10 and 11 were measured from 5 - 350 K. 12, 13 and 14 were measured from 5 - 300 K.

Complexes **11**, **12** and **13** are high-spin, whilst complex **10** is low-spin, across the measured temperature range. Complex **14** appears to undergo SCO with a low $T_{1/2}$ temperature of 87 K, although the curve is unusual in shape.

5.5.1 Magneto-structural correlations of iron(II) pseudoclathrochelate complexes

The data described above establishes a clear magneto-structural correlation between the geometry of a complex and its potential to undergo SCO in the solid state.

Complexes **10** and **11** have distorted octahedral geometries (Figure 5.15). Magnetic susceptibility data show that **10** is fully low-spin; this is replicated in the crystallographic data. The two available crystal structures of **11** show the complex as low-spin at both 120 and 250 K, however the magnetic data indicate that the complex is undergoing spin-crossover. Complexes **13** and **14** are both high-spin, as indicated from both the crystal structures and the magnetic susceptibility data. In addition, they both show trigonal prismatic geometry (Figure 5.15). Given that **12** could not be crystallised, it is impossible to be certain of its geometry. That said, it could be inferred from its high-spin state that it would be crystallographically similar to **13** and **14**.

Table 5.1 shows the bite angles (defined as N(imine)-Fe-N(aromatic)) of **10** - **14.** Low-spin **10** and **11** show bite angles of 79 - 80°, whereas for high-spin **13** and **14** these angles are 72 - 75°. The smaller bite angles exhibited by **13** and **14** are indicative of the more constrained trigonal prismatic geometry, while the larger bite angles of the distorted octahedral **10** and **11** are comparatively relaxed.

Given that the capability of many complexes to undergo a solid state spin transition is governed by the rigidity of the crystal lattice, it is likely that complexes with the more rigid trigonal prismatic geometry are unable to go through Bailar's trigonal twist pathway[35] to switch to an octahedral geometry. This phenomenon has been seen in analogous tripodal iron(II) pseudoclathrochelate complexes.[34]

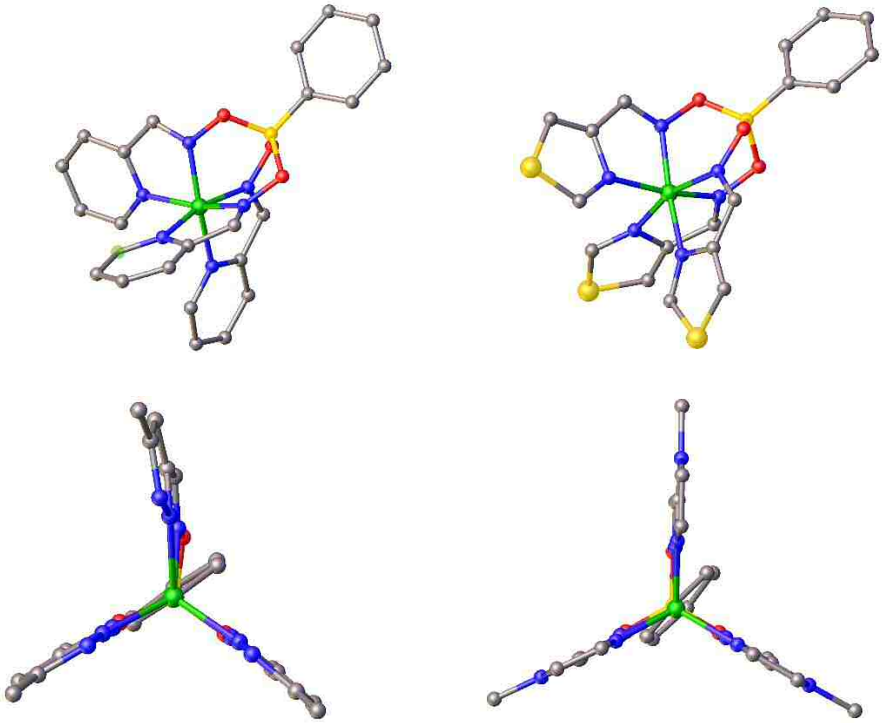

Figure 5.15 - Distorted octahedral geometry of complexes 10 (top left) and 11 (top right). Trigonal prismatic geometry of complexes 13 (bottom left) and 14 (bottom right). Counterions, solvent and hydrogen atoms are omitted for clarity.

5.6 Solution phase paramagnetic susceptibility of iron(II) pseudoclathrochelate complexes

The paramagnetic susceptibility of complexes **10** - **14** in solution was measured using variable temperature Evans' method NMR spectroscopy.[42, 43] The results of these experiments can be seen in Figure 5.16.

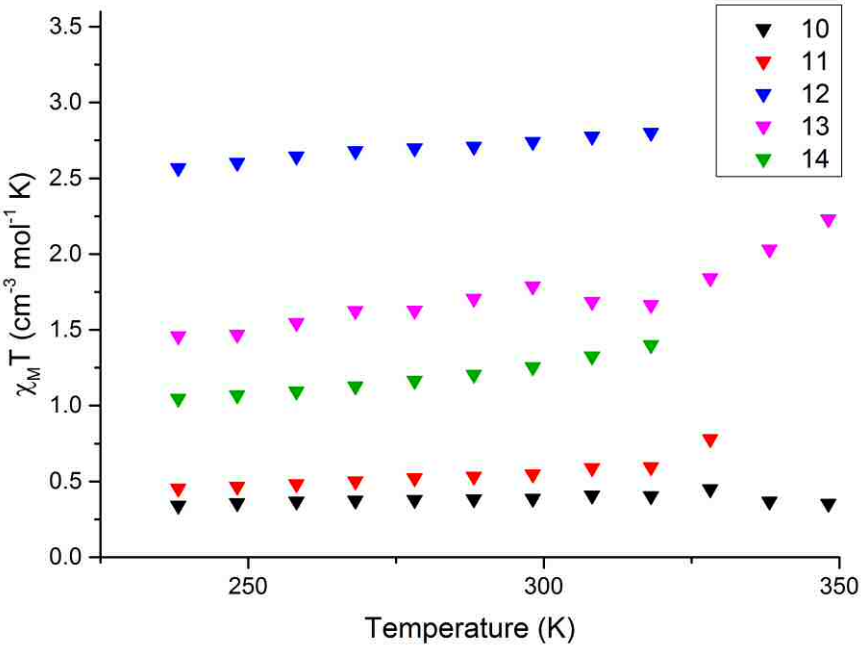

Figure 5.16 - Variable temperature Evans' method NMR spectroscopy of complexes 10 (black), 11 (red), 12 (blue), 13 (pink) and 14 (green). All complexes have been measured in acetonitrile-d_3.

Complexes **10** is low-spin across the measured temperature range. It is difficult to reliably define the spin state of **11**, given the available data. Difficulties with the NMR spectrometer used meant that higher temperature data could not be collected. There does appear to be an overall increase in the $\chi_M T$ which would imply a gradual transition, however without further data this cannot be confirmed. Complex **12** appears to show an extremely gradual thermal switch in solution; the $\chi_M T$ ranges from 2.5 cm^{-3} mol^{-1} K at 238 K to 2.8 cm^{-3} mol^{-1} K at 318 K. Due to instrumental difficulties with the NMR spectrometer and limited solubility in available deuterated solvents, a more extensive

temperature range of this sample could not be measured. The paramagnetic susceptibility of complex **13** was measured between 208 and 348 K. Initially, between 208 and 308 K, the spin-state switching is gradual, however the rate at which SCO occurs increases sharply between 318 and 348 K. Between the measured temperatures of 238 and 318 K, complex **14** is just under halfway through a gradual switch of spin state. It appears from the final few data points that the gradient of the transition is becoming sharper and thus it could be implied, although not concluded, that a more abrupt transition would follow, could higher temperatures be reached for measurement.

10 is low-spin in both solution and the solid state. **11** could be undergoing a transition from low to high-spin, which would be consistent with its behaviour in the solid state. Complexes **12** - **14** appear to show a very gradual spin transition in solution, in contrast to their solid state behaviour. This is most likely to be a result of the decreased rigidity in solution which allows a relaxation of the geometry and a change in spin state.

5.7 The serendipitous formation of multi-metallic cluster complexes

5.7.1 Synthesis of multi-metallic cluster complexes

Ligands **L15** and **L16** have very similar architecture; the aromatic portion of both is comprised of a pyridine ring with a substituent in the 6-pyridyl position. These ligands were chosen to increase the steric bulk close to the metal cation, with the aim of weakening the ligand field and making the complex more susceptible to undergoing SCO. This approach was successful in another class of tripodal iron(II) Schiff base complexes.[44]

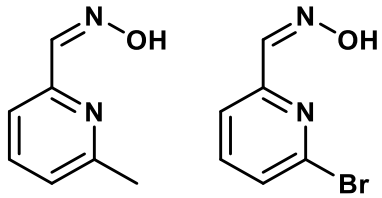

L15 L16

Figure 5.17 - Structure of L15 and L16.

As discussed in Section 5.4, the formation of tripodal pseudoclathrochelate complexes **15a** and **16a** (Figure 5.9) was never observed. The self-assembly reaction discussed in Section 5.4, which used 3 equivalents of oxime **L15** or **L16**, 1 equivalent of phenyl boronic acid and and 1 equivalent of iron(II) perchlorate in methanol under strict inert conditions was followed. Single crystals were grown from vapour diffusion of diethyl ether into a concentrated solution of the complex in acetonitrile. The crystal structures are discussed in Section 5.7.2.

5.7.2 X-ray crystallography of multi-metallic cluster complexes

The structure of **15** is shown in Figure 5.18. It consists of a planar region of three Fe^{3+} cations with an oxo bridge and three oximate ligands. The two nitrogen atoms in one oxime are both coordinated to the same iron centre, whilst the oxygen is coordinated to a second iron. Each Fe^{3+} has a coordinated terminal water and another oxo group, which extends the coordination up to a second type of co-planar complex. This second complex has one Fe^{2+} cation, coordinated to six nitrogen atoms from three oxime ligands. All four iron cations are in a slightly distorted octahedral geometry.

The multi-metallic cluster structure of **15** was refined in the monoclinic space group $P2_1/n$. The three perchlorate anions required different refinement. Perchlorate 1 successfully refined anisotropically, perchlorate 2 refined isotropically and perchlorate 3 was refined isotropically and modelled over two positions with 0.5 occupancy. In all counterions, the Cl-O bond lengths were restrained to 1.45 Å (2). The structure contains large solvent accessible voids (21% of the unit cell volume). Residual electron density

could not be meaningfully modelled as solvent therefore the SQUEEZE function of PLATON was used.

Selected bond lengths from **15** are shown in Table 5.2. The Fe^{2+}-N(imine) and Fe^{2+}-N(pyridine) bond lengths suggest that the segment of the cluster based around the iron(II) cation is low spin at 100 K. Fe^{3+}-N and Fe^{3+}-O bond lengths are similar to those in analogous multinuclear iron(III) based clusters.[45-48]

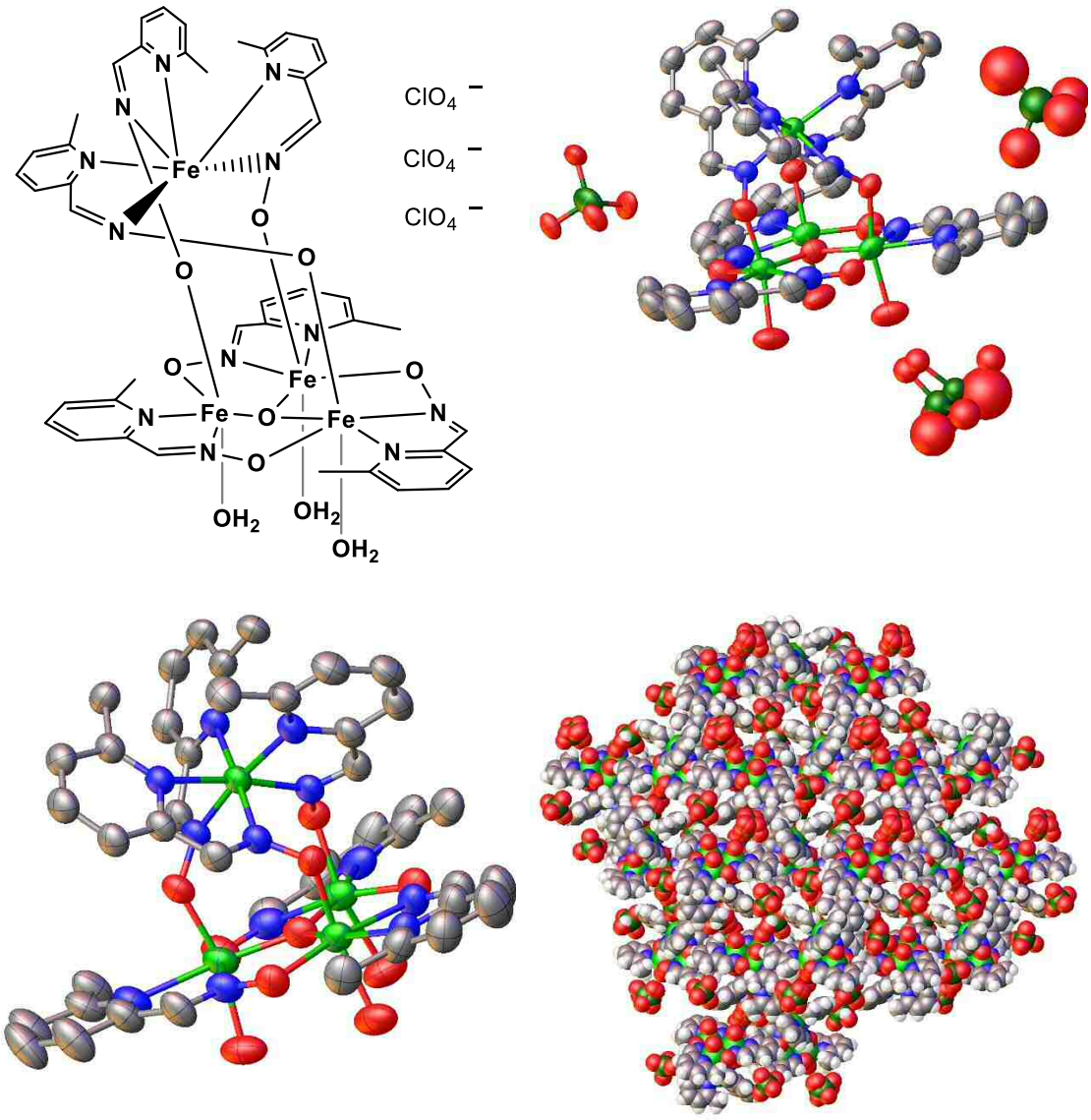

Figure 5.18 - Structure of 15 (top left). The asymmetric unit of 15 (top right). Hydrogen atoms are omitted for clarity. The cluster of 15 (bottom left). Counterions and hydrogen atoms are omitted for clarity. Packing down the a axis (bottom right) showing the large solvent accessible voids.

Table 5.2 - Selected crystallographic bonds lengths of 15.

Bond	Bond length / Å
Fe^{2+} - N(imine)	1.914(4) - 1.924(4)
Fe^{2+} - N(pyridine)	2.064(4) - 2.067(4)
Fe^{3+} - O(oxime)	1.955(4) - 1.960(4)
Fe^{3+} - N(imine)	2.130(4) - 2.144(4)
Fe^{3+} - N(pyridine)	2.234(5) - 2.256(4)
Fe^{3+} - O(bridging oxo)	1.934(4) - 1.951(4)
Fe^{3+} - O(water)	2.101(4) - 2.129(4)

The structure of **16** has four oximate ligands and four Fe^{3+} cations, each of which is coordinated to one terminal OH and two bridging OHs, as well as two nitrogen atoms and one oxygen atom from the oximate ligands. The x-ray diffraction data collected on this cluster were not of high enough quality to locate the hydrogen atoms on the terminal and bridging oxygen atoms. However the magnetic data (Section 5.5.3) are consistent with iron(III), which suggest that the oxygens atoms are terminal and bridging OH groups.

The multi-metallic cluster structure of **16** was refined in the monoclinic space group C2/c. The asymmetric unit contains half a cluster and one and two half perchlorate anions. The full occupancy perchlorate was modelled across two positions, each with 0.5 occupancy. Cl-O bond distances were restrained to 1.45 (2) Å and O-O distances were restrained to 2.09 (4) Å. One half counterion was modelled over two positions, each with 0.25 occupancy. The second half counterion sits with one Cl-O bond on a special position, with the other oxygen atoms in a 0.75 occupancy.

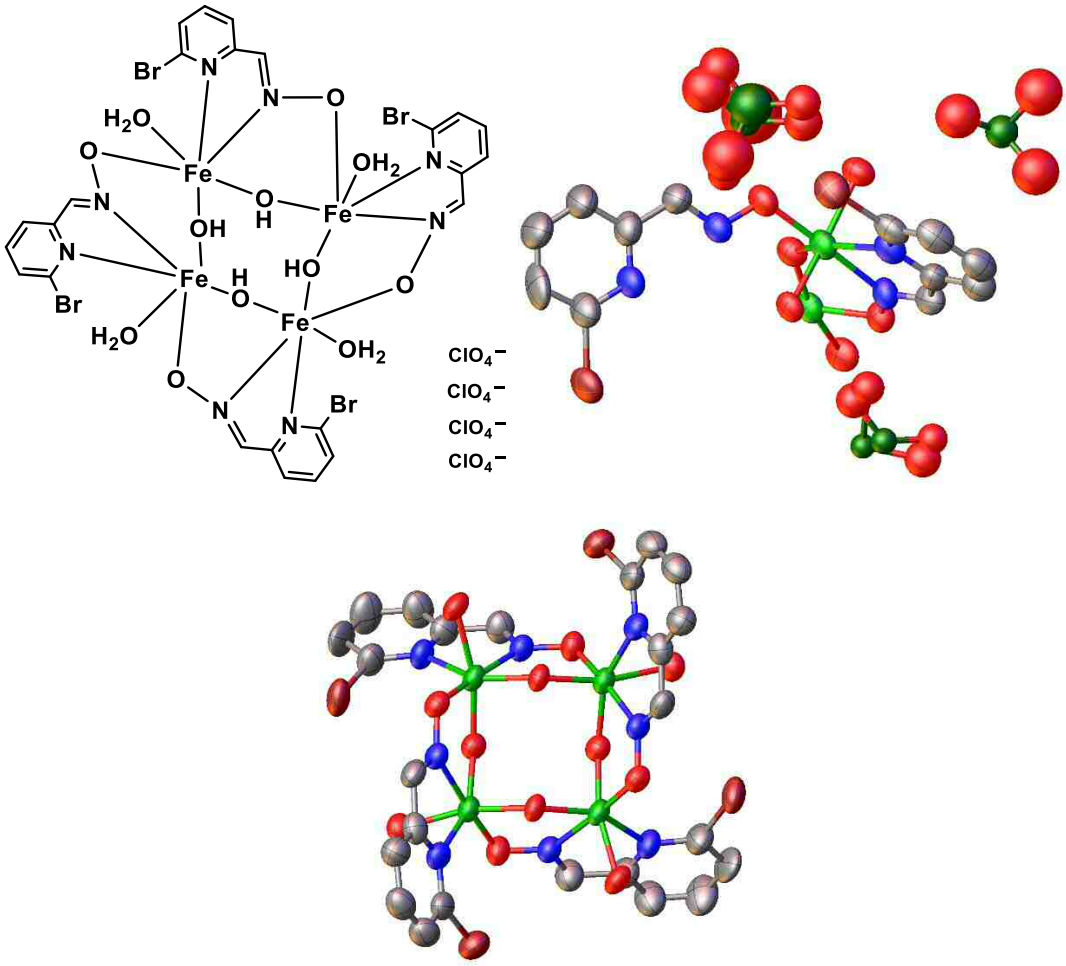

Figure 5.19 - Structure of 16 (top left). The asymmetric unit of 16 (top right). Hydrogen atoms are omitted for clarity. The structure of the full cluster of 16 (bottom). Counterions and hydrogen atoms are omitted for clarity.

Table 5.3 - Selected crystallographic bonds lengths of 16.

Bond	Bond length / Å
Fe^{3+} - O(oxime)	1.950 (7) - 1.978(7)
Fe^{3+} - N(imine)	2.167(8)
Fe^{3+} - N(pyridine)	2.200(9)
Fe^{3+} - O(bridging OH)	1.934(6) - 1.954 (7)
Fe^{3+} - O(terminal OH)	2.058 (7) - 2.059(7)

5.7.3 Other characterisation of complexes 15 and 16

A range of characterisation techniques, including NMR spectroscopy, mass spectrometry, elemental microanalysis and x-ray powder diffraction, were used to attempt to characterise complexes **15** and **16**. The complexes proved particularly difficult to characterise by any of these methods.

Attempts to collect a paramagnetic proton NMR spectrum for each complex proved unsuccessful, either due to an inability to properly shim the sample and the possibility of these structures being unstable in solution. To investigate the potential instability further, DOSY NMR spectroscopy experiments to assess the number of species in solution were attempted. However given the paramagnetic nature of these samples, the T1 relaxation times were too fast to capture spectra of either cluster.

Direct injection high-resolution electrospray mass spectra were obtained for **15** and **16**, however the data were inconclusive. It is speculated that this is due to the samples fragmenting inside the mass spectrometer.

Samples of both clusters were submitted for elemental microanalysis. However, despite several attempts, repeatable and reliable figures could not be obtained. It is hypothesised that this is due to either decomposition of the sample between removing it from the glovebox and it being tested at London Metropolitan University or a result of solvent loss in the same timeframe.

Similarly, samples were analysed by x-ray powder diffraction. Whilst these samples were run soon after removal from a nitrogen atmosphere, the grinding of the sample is likely to have caused lattice solvent to be lost. This means that the obtained powder diffraction data do not match the pattern simulated from the crystal structure.

5.7.4 Solid state magnetic susceptibility of cluster complexes

Solid state magnetic susceptibility measurements for complexes **15** and **16** were measured in a magnetic field of 0.5 T. These results are shown in Figure 5.20. Measurements were performed on freshly prepared powders which had been stored in the glovebox.

The magnetic data for both **15** and **16** are more complex than those of the tripodal pseudoclathrochelate complexes also presented in this chapter, which is to be expected given the presence of multiple iron centres. In the case of **15**, the shape is consistent with antiferromagnetic coupling between the three iron(III) cations and is as expected when compared with other iron(III)-oxo triangular clusters.[45-48] Given that there is no discontinuity in the susceptibility plot, there is no tangible evidence of any spin-crossover occurring at the iron(II) centre, although it is possible an extremely gradual transition may occur.

If **16** were fully low-spin, a magnetic susceptibility of ~2.0 cm^{-3} mol^{-1} K would be expected. However that data between 25-350 K show $\chi_M T$ = ~3.5 cm^{-3} mol^{-1} K, which is slightly higher than expected. However a fully high-spin cluster would have $\chi_M T$ = ~17.5 cm^{-3} mol^{-1} K, meaning that this cluster is certainly not approaching a fully high-spin state. This suggests that all four iron(III) atoms in this cluster are close low-spin.

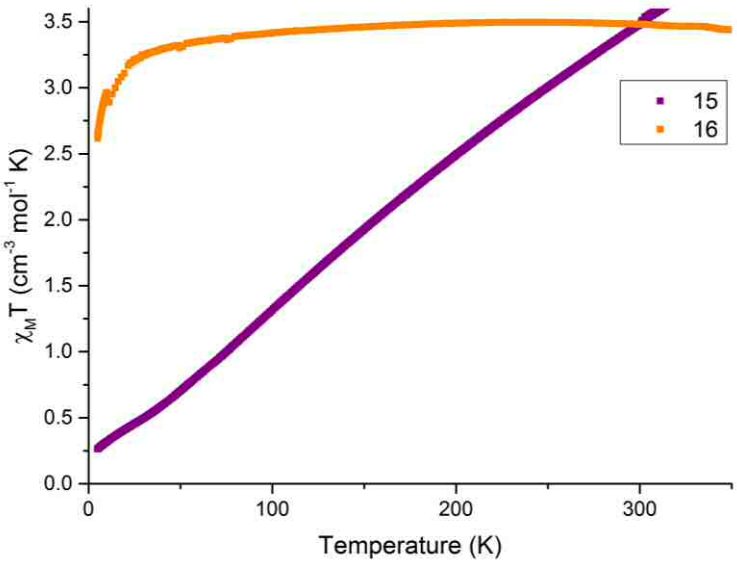

Figure 5.20 - Solid state magnetic susceptibility of complexes 15 (purple) and 16 (black). Complex 15 was measured from 5 - 300 K. Complex 16 was measured from 5 - 350 K.

5.7.5 Solution phase paramagnetic susceptibility of cluster complexes

The paramagnetic susceptibility of complexes **15** and **16** in solution were measured using variable temperature Evans' method NMR spectroscopy.[42, 43] The results of these experiments can be seen in Figure 5.21.

The solution phase paramagnetic susceptibility shows similar behaviour to that seen in the solid state. **16** remains close to low-spin across the measured temperature range, whilst **15** again shows antiferromagnetic coupling between iron(III) centres and no evidence of iron(II) spin-crossover.

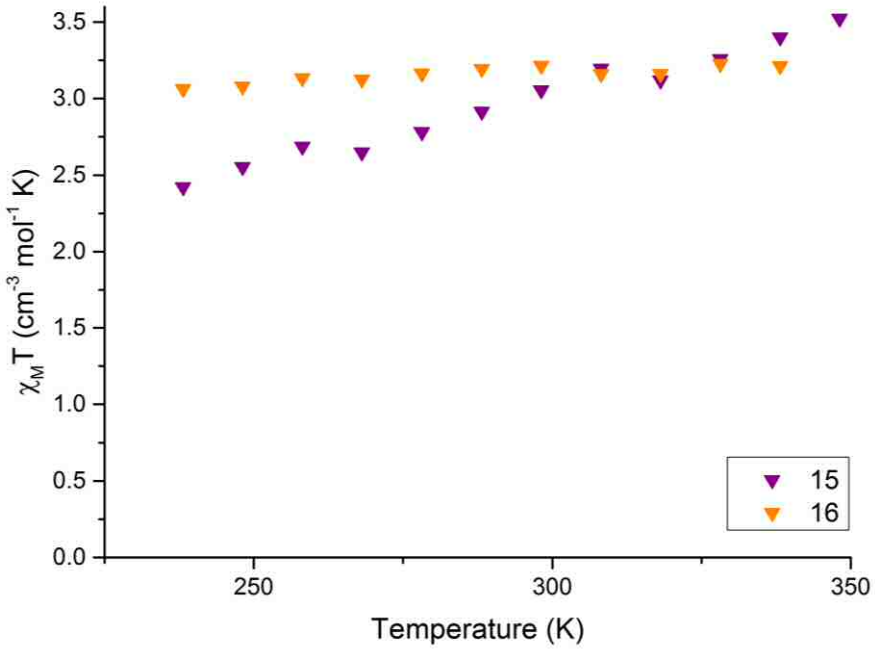

Figure 5.21 - Variable temperature Evans' method NMR spectroscopy of complexes 15 (purple) and 16 (orange). Both complexes have been measured in acetonitrile-d3.

5.8 Conclusions and further work

A family of tripodal iron(II) pseudoclathrochelate complexes has been synthesised and characterised. Whilst some of the complexes investigated remain either high or low-spin, some do undergo spin-crossover, making them candidates for future incorporation into polymeric materials. It is also clear that the size and

substituent of the aromatic moiety on the oxime ligand has a profound impact on the magnetic behaviour. Changes to transition temperatures could be effected by tuning this group. Functionalisation of this family of complexes to include a range of linkers attached to a polymerisable group, such as a vinyl group, would be synthetically facile given the ready availability of substituted phenyl boronic acid derivatives.

Whilst undertaking this study, a pair of multi-metallic clusters were serendipitously discovered and investigated. Although this proved challenging, given their inherent instability, it is evident that the chemistry behind the formation of the aforementioned pseudoclathrochelate complexes can be more complex than initially thought and should be the subject of further study.

5.9 References

1. C. Hu, B. C. Noll, C. E. Schulz and W. R. Scheidt, *Inorg. Chem.*, 2018, **57**, 793-803.
2. I. Hachem, M. S. Belkhiria, M. Giorgi, C. E. Schulz and H. Nasri, *Polyhedron*, 2009, **28**, 954-958.
3. C. G. Werncke, P. C. Bunting, C. Duhayon, J. R. Long, S. Bontemps and S. Sabo-Etienne, *Angew. Chem. Int. Ed.*, 2015, **54**, 245-248.
4. C. J. Qin, L. James, J. D. Chartres, L. J. Alcock, K. J. Davis, A. C. Willis, A. M. Sargeson, P. V. Bernhardt and S. F. Ralph, *Inorg. Chem.*, 2011, **50**, 9131-9140.
5. B. Dietrich, J. M. Lehn and J. P. Sauvage, *Tetrahedron Lett.*, 1969, **10**, 2899-2892.
6. S. O. Kang, J. M. Llinares, V. W. Day and K. Bowman-James, *Chem. Soc. Rev.*, 2010, **39**, 3980-4003.
7. Greaser, J. M. Harrowfield, A. J. Merit, A. M. Sargeson and J. Springborg, *J. Am. Chem. Soc.*, 1977, **99**, 3181-3182.
8. J. J. Grzybowski, R. D. Allen, J. A. Belinski, K. L. Bieda, T. A. Bish, P. A. Finnegan, M. L. Hartemstein, C. S. Regitz, D. M. Ryalls, M. E. Quires and H. J. Thomas, *Inorg. Chem.*, 1993, **32**, 5266-5272.
9. D. R. Boston and N. J. Rose, *J. Am. Chem. Soc.*, 1968, **90**, 6859-6860.
10. J. E. Parks, B. E. Wagner and R. H. Holm, *J. Am. Chem. Soc.*, 1970, **92**, 3500-3502.
11. V. L. Goedken and S.-M. Pen, *J. Chem. Soc., Chem. Commun.*, 1973, 62-63.
12. S. M. Jansze and K. Severin, *Acc. Chem. Res.*, 2018, **51**, 2139-2147.
13. K. L. Bieda, A. L. Kranitz and J. J. Grzybowski, *Inorg. Chem.*, 1993, **32**, 4209-4213.
14. Y. Z. Voloshin, O. A. Varzatskii, S. V. Korobko and Y. A. Maletin, *Inorg. Chem. Commun.*, 1998, **1**, 328-331.
15. Y. Z. Voloshina, A. I. Stasha, O. A. Varzatskiib, V. K. Belskya, Y. A. Maletinb and N. G. Strizhakovab, *Inorg. Chim. Acta*, 1999, **284**, 180-190.
16. Y. Z. Voloshin, O. A. Varzatskii, N. G. Strizhakova and E. Y. Tkachenko, *Inorg. Chim. Acta*, 2000, **299**, 104-111.

17. Y. Z. Voloshin, O. A. Varzatskii, A. I. Stash, V. K. Belsky, Y. N. Bubnov, I. I. Vorontsov, K. A. Potekhin, M. Y. Antipin and E. V. Polshin, *Polyhedron*, 2001, **20**, 2721-2733.
18. D. A. Henckel, Y. F. Lin, T. M. McCormick, W. Kaminsky and B. M. Cossairt, *Dalton Trans.*, 2016, **45**, 10068-10075.
19. V. V. Novikov, A. A. Pavlov, Y. V. Nelyubina, M. E. Boulon, O. A. Varzatskii, Y. Z. Voloshin and R. E. Winpenny, *J. Am. Chem. Soc.*, 2015, **137**, 9792-9795.
20. V. V. Novikov, I. V. Ananyev, A. A. Pavlov, M. V. Fedin, K. A. Lyssenko and Y. Z. Voloshin, *J. Phys. Chem. Lett*, 2014, **5**, 496-500.
21. Y. Z. Voloshin, O. A. Varzatskii, V. V. Novikov, N. G. Strizhakova, I. I. Vorontsov, A. V. Vologzhanina, K. A. Lyssenko, G. V. Romanenko, M. V. Fedin, V. I. Ovcharenko and Y. N. Bubnov, *Eur. J. Inorg. Chem.*, 2010, **2010**, 5401-5415.
22. Y. Z. Voloshin, O. A. Varzatskii, Vorontsov, II and M. Y. Antipin, *Angew. Chem. Int. Ed.*, 2005, **44**, 3400-3402.
23. Y. Z. Voloshin, V. V. Novikov, Y. V. Nelyubina, A. S. Belov, D. M. Roitershtein, A. Savitsky, A. Mokhir, J. Sutter, M. E. Miehlich and K. Meyer, *Chem. Commun.*, 2018, **54**, 3436-3439.
24. J. G. Muller, J. J. Grzybowski and K. J. Takeuchi, *Inorg. Chem.*, 1986, **25**, 2665-2667.
25. S. I. Shylin, M. V. Pavliuk, L. D'Amario, I. O. Fritsky and G. Berggren, *Faraday Discuss.*, 2019.
26. S. I. Shylin, M. V. Pavliuk, L. D'Amario, F. Mamedov, J. Sa, G. Berggren and I. O. Fritsky, *Chem. Commun. (Camb)*, 2019, **55**, 3335-3338.
27. A. V. Dolganov, O. V. Tarasova, A. Y. Ivleva, O. Y. Chernyaeva, K. A. Grigoryan and V. S. Ganz, *Int. J. Hydrogen Energy*, 2017, **42**, 27084-27093.
28. J. Al Cheikh, A. Villagra, A. Ranjbari, A. Pradon, M. Antuch, D. Dragoe, P. Millet and L. Assaud, *Appl. Catal. B*, 2019, **250**, 292-300.
29. J. Blechinger, O. A. Varzackii, V. Kovalska, G. E. Zelinskii, Y. Z. Voloshin, E. Kinski and A. Mokhir, *Bioorg. Med. Chem. Lett.*, 2016, **26**, 626-629.
30. J. L. Bila, J. Pijeat, A. Ramorini, F. Fadaei-Tirani, R. Scopelliti, E. Baudat and K. Severin, *Dalton Trans.*, 2019, **48**, 4582-4588.

31. B. Alameddine, S. Shetty, R. S. Anju, F. Al-Sagheer and S. Al-Mousawi, *Eur. Polym. J.*, 2017, **95**, 566-574.
32. M. Marmier, G. Cecot, A. V. Vologzhanina, J. L. Bila, I. Zivkovic, H. M. Ronnow, B. Nafradi, E. Solari, P. Pattison, R. Scopelliti and K. Severin, *Dalton Trans.*, 2016, **45**, 15507-15516.
33. R. M. Islamova and Y. B. Monakov, *Polymer Science Series C*, 2011, **53**, 27-34.
34. P. Stock, E. Deck, S. Hohnstein, J. Korzekwa, K. Meyer, F. W. Heinemann, F. Breher and G. Horner, *Inorg. Chem.*, 2016, **55**, 5254-5265.
35. J. C. B. Jr., *J. Inorg. Nucl. Chem.*, 1958, 165-175.
36. O. A. Varzatskii, L. V. Penkova, S. V. Kats, A. V. Dolganov, A. V. Vologzhanina, A. A. Pavlov, V. V. Novikov, A. S. Bogomyakov, V. N. Nemykin and Y. Z. Voloshin, *Inorg. Chem.*, 2014, **53**, 3062-3071.
37. O. A. Varzatskii, S. V. Kats, A. A. Pavlov, A. S. Belov, I. G. Belaya, Y. V. Nelyubina, V. V. Novikov and Y. Z. Voloshin, *Inorg. Chim. Acta*, 2018, **471**, 413-418.
38. O. A. Varzatskii, S. V. Kats Menkach, L. V. Penkova, S. V. Volkov, A. V. Dolganov, A. V. Vologzhanina, Y. N. Bubnov and Y. Z. Voloshin, *Eur. J. Inorg. Chem.*, 2013, **2013**, 1987-1992.
39. G. M. Sheldrick, *Acta Cryst. A*, 2015, **71**, 3-8.
40. G. M. Sheldrick, *Acta Cryst. C*, 2015, **71**, 3-8.
41. O. V. Dolomanov, L. J. Bourhis, R. J. Gildea, J. A. K. Howard and H. Puschmann, *J. Appl. Crystallogr.*, 2009, **42**, 339-341.
42. D. F. Evans, *J. Chem. Soc.*, 1959, 2003-2005.
43. E. M. Schubert, *J. Chem. Educ.*, 1992, 62.
44. M. A. Hoselton, L. J. Wilson and R. S. Drago, *J. Am. Chem. Soc.*, 1975, **97**, 1722-1729.
45. L. An, L.-j. Zhong, J. Feng, S.-z. Du and X.-m. Lu, *Inorg. Chem. Commun.*, 2012, **22**, 108-112.
46. K. Mason, I. A. Gass, S. Parsons, A. Collins, F. J. White, A. M. Slawin, E. K. Brechin and P. A. Tasker, *Dalton Trans.*, 2010, **39**, 2727-2734.
47. S. G. Sreerama and S. Pal, *Eur. J. Inorg. Chem.*, 2004, **2004**, 4718-4723.

48. M. Hołyńska, R. Clérac, T. Langer, R. Pöttgen and S. Dehnen, *Polyhedron*, 2013, **52**, 1425-1430.

Chapter 6 - Initial Studies on a New Class of Functionalised Polymers

6.1 Introduction

6.1.1 Introducing Reversible Addition-Fragmentation chain Transfer (RAFT) polymerisation

There is no doubt that polymeric materials have revolutionised the way that we live our lives. Since the invention of Bakelite in 1909,[1] polymers have become more and more prevalent, being used in applications in all fields of human endeavour. The demand for polymers is ever increasing and the design of novel materials is an active area of research.

Reversible Addition-Fragmentation chain Transfer (RAFT) polymerisation was pioneered at Australia's Commonwealth Scientific and Industrial Research Organisation (CSIRO) in the 1990s.[2] It is a remarkably versatile method of living polymerisation which will tolerate a wide range of functional groups and solvents, including common organic solvents, protic solvents (including water), as well as more unusual solvents, such as ionic liquids and supercritical carbon dioxide.[3]

RAFT polymerisation requires a monomer, an initiator, a RAFT charge transfer agent (CTA) and a solvent, although a solvent is not strictly required if the monomer is liquid. Common initiators are azobisisobutyronitrile (AIBN) and 4,4'-azobis(4-cyanovaleric acid) (ACVA). These agents provide the radical source needed to propagate the polymerisation. There is a plethora of available charge transfer agents, usually thiocarbonylthio compounds, and the choice of CTA for a particular type of reaction is the subject of intense research in its own right.

The mechanism of RAFT polymerisation is shown in Figure 6.1.[4] The initiation step involves the initiator decomposing into two radical fragments (I·), which react with a single monomer (M) to give a propagating radical species (Pn·) which has a chain length of one. The chain transfer step occurs when Pn· reacts with the CTA to form a RAFT adduct radical. This adduct can fragment forwards or backwards to give the starting CTA species or a leaving group radical (R·) and a polymeric-CTA agent (S=C(Z)S-Pn). Re-initiation occurs when the leaving group radical (R·) reacts with a monomer, which

starts a new active chain. The main RAFT equilibrium allows all the radicals to be distributed between all the species which have not undergone termination. In an ideal reaction, all the radicals are distributed evenly which gives each chain equal growth and a narrow polydispersity (PD) value. Termination of active chains undergo biradical termination which leaves 'dead' chains, which cannot react further. The ratio of CTA, initiator and monomer can control the charge transfer and main RAFT equilibrium steps, and thus control the properties of the resultant polymers.

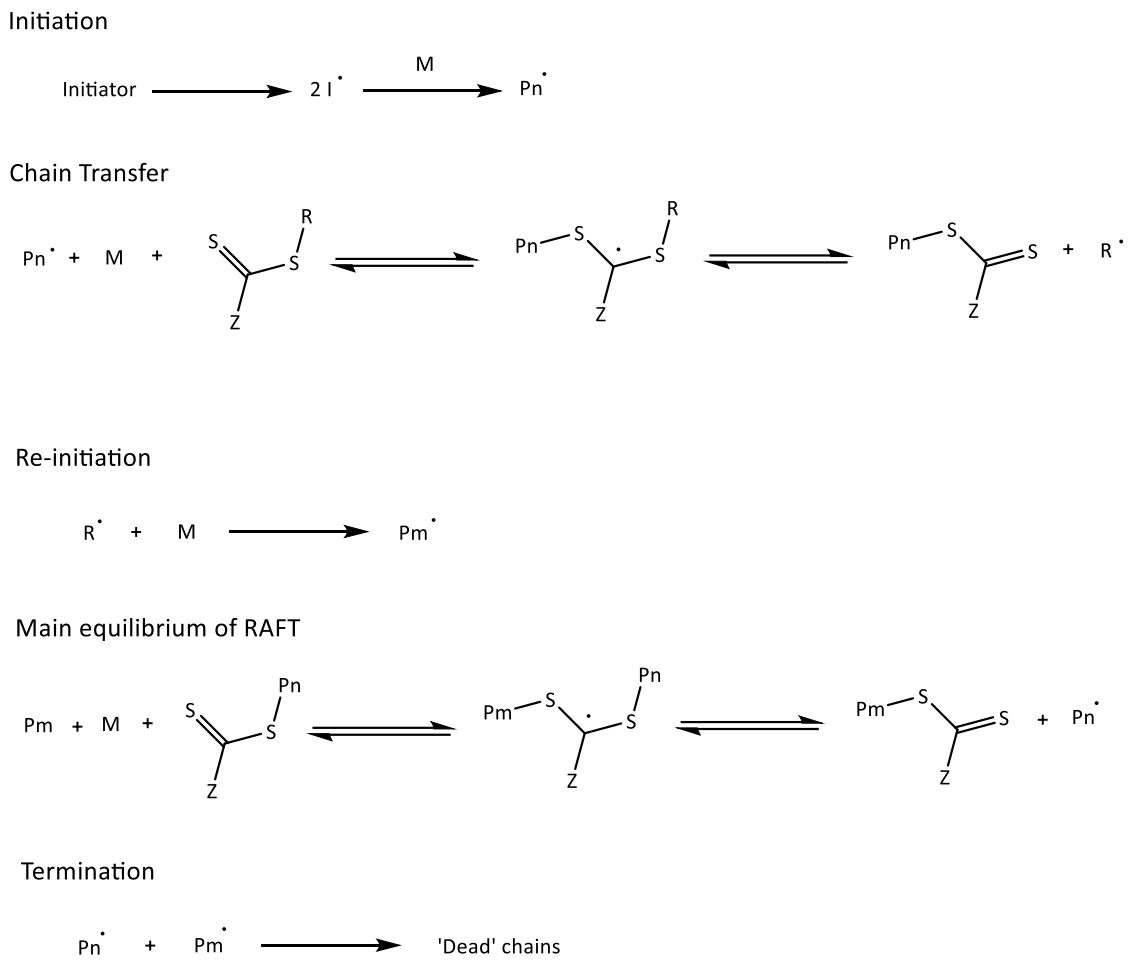

Figure 6.1 - Mechanism of RAFT polymerisation.[4]
M =monomer, Pn and Pm = polymer chains and I = initiator.

6.1.2 Metallosupramolecular polymers

Given the diverse properties of transition metals, it is unsurprising that research into stimuli-responsive polymers has grown to incorporate these elements. The inclusion of metal ions and the ligand architecture to which they are coordinated gives rise to a vast array of structures, geometries and coordination modes, as well as access to a range of magnetic, optical, electronic and catalytic properties.[6] In addition the ligand-metal interaction has an effect on the binding strength, reversibility of coordination and solubility of the polymer.[7] The power of such polymers, herein referred to as metallosupramolecular polymers (MSPs), lies in the inherently tuneable nature of all the above features. MSPs can have metal containing units either as part of the main chain or in the side chain of the polymer.

Many properties of MSPs rely on bonds that reversibly associate and dissociate as a result of external stimuli, such as temperature, light and the presence of competing ions.[8, 9] The presence of non-covalent bonds, such as π–π interactions, hydrogen bonding, and metal-ligand bonding, are crucial in this responsive process. The latter can be considered the most versatile as the strength of the bond is easily tuneable depending on ligand architecture, metal ion and counterion.

Just as the chelate effect has a profound influence in coordination chemistry, Dobrawa and Würthner showed the changes in binding constant in Zn^{2+} complexes with different pyridine ligands, where the complex was situated in the main chain of the poymer.[10] For a single Zn-pyridine system, the binding constant was $K > 10^3\ M^{-2}$. When this system was changed to a Zn-terpyridine system, the binding constant increased to $K > 10^{14}\ M^{-2}$.

Monomers which have been functionalised with multi-dentate ligand structures have been used to add diverse properties to polymer systems. These investigations have focused particularly on the use of terpyridine (terpy), phenanthroline (phen) or 2,6-bis(1'-alkylbenzimidazolyl)-pyridine structures, in particular a 2,6-bis(1'-methylbenzimidazolyl)-pyridine (Mebip) ligand. These ligand structures are shown in Figure 6.2.

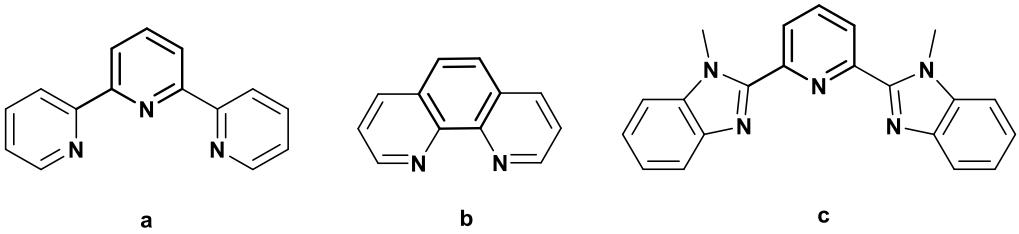

Figure 6.2 - Structures of terpyridine (a), phenanthroline (b) and 2,6-bis(1'-methylbenzimidazolyl)-pyridine (c).

Initially, polymers using terpy suffered from limited solubility. However, this problem was resolved by functionalising the terpy ligand with poly(oxytetramethylene) or poly(ethylene oxide) groups in the 4-pyridyl position. The formation of these one-dimensional MSPs was reversible when the pH, temperature or electrochemical potential was changed.[11-13]

Higuchi *et al.* investigated the electrochromic behaviour of a copper phenanthroline complex which had been functionalised with a fluorene derivative.[14] This one dimensional MSP formed a material which reversibly changed from green to colourless upon the redox reaction of the coordinated copper.

The above examples rely on the functionalisation of two tridentate ligands onto opposite ends of a linker group. Upon metal coordination, this leads to a linear, one dimensional structure, akin to a coordination polymer. However, another approach which leads to MSPs with a different structure can be taken.

A 2,6-bis(1'-methylbenzimidazolyl)-pyridine ligand (Figure 6.2) was functionalised with an acrylate monomer. This monomeric unit was copolymerised with butyl acrylate to form a polymer where the ligand is a pendant from the main chain. This polymer was reacted with copper, cobalt or zinc to form MSPs with fascinating mechanical properties. The MSPs were pressed into thin films, all of which had the same morphology regardless of the metal used. The mechanical properties were then tested. Given the comparative weakness of the copper-nitrogen bond, it is logical that the copper-based MSP had a lower modulus, tensile strength and yield strength than either the cobalt or the zinc MSP. A combination of both copper and cobalt in the same thin

film led to a material which combined the pliable nature of the copper MSP with the stiffness of the cobalt MSP. This indicates that the diversity of transition metals can be further explored by combining them in the same material.[8] Further work by the same group on zinc MSP materials have led to vesicles which formed due to the discrepancy between the polarity of the metal-ligand and backbone sections of the polymer chain. Initial studies show that these vesicles have self-healing properties.

6.2 Aims

This chapter aims to provide 'proof of concept' to a new method of incorporating spin-crossover modules into polymers. Most reported polymers which are designed with spin state switches in mind are based on a one dimensional coordination polymer structure.[5, 15-18] However, here a different structure is explored, which incorporates a polymeric backbone with an appended functionalised tridentate ligand.

The purpose of this chapter is not to explore the spin-crossover behaviour of such polymers, but rather to establish some knowledge of polymer chemistry and a synthetic strategy for functionalisation within the group, on which future research can expand.

The results discussed here are two-fold. Firstly, successful procedures for the RAFT polymerisation of acrylate monomers is explored and analysis on these polymerisations is provided. This has served to establish the expertise within the group to build upon this research project in the future. Secondly, a synthetic methodology has been established which allows the facile functionalisation of a 2,6-*bis*[pyrazol-1-yl]pyridine (bpp) ligand which is a central motif of spin-crossover research, especially within the Halcrow group. Once functionalised, the ligand can be polymerised, and copolymerised with other monomers, and subsequently complexed with iron(II) to provide a model system for future developments of spin-crossover active polymers.

6.3 The polymerisation of poly(butyl acrylate) and poly(benzylmethacrylate)

Since previous research in the Halcrow group has not explored polymers, a substantial amount of background work was undertaken to establish an understanding of the synthetic methodology needed to make polymers and copolymers *via* RAFT polymerisation.

As discussed in Section 6.1.1, RAFT polymerisation is tolerant to a wide range of functional groups and solvents which is of much use when exploring new pathways. Acrylate monomers were chosen as a test system, due their solubility, cheap and ready availability, prolific use in RAFT polymerisation and success in MSPs with similar tridentate ligand motifs.[8, 9]

Given the structure of the functionalised bpp ligand used here (Section 6.6), a polymer composed solely of bpp would be sterically bulky, which could make incorporation of a metal ion difficult. Therefore, copolymers with both butyl acrylate and benzylmethacrylate were identified as targets.

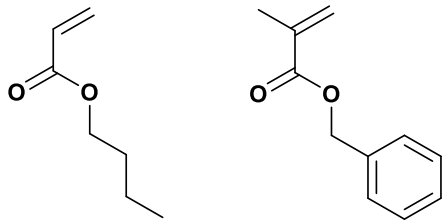

a b

Figure 6.3 - Structure of butyl acrylate (a) and benzyl methacrylate (b).

The choice of charge transfer agents in RAFT polymerisation is the subject of intense research in its own right, and there are a variety of substituents on these thiocarbonylthio molecules which can improve the polymerisation of particular functional groups. Given that this work is an initial study, rather than an in depth optimisation, 2-[[(butylthio)thioxomethyl]thio]propanoic acid (Figure 6.4) was chosen, as it is suitable for a broad range of functional groups. Azobisisobutyronitrile (AIBN), a

common initiator, was also used here. Dichloromethane and ethanol were chosen as solvents for poly(butyl acrylate) and poly(benzylmethacrylate) respectively, based on precedence in the literature.[4, 19]

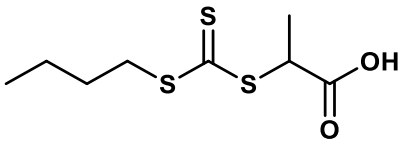

Figure 6.4 - Structure of 2-[[(butylthio)thioxomethyl]thio]propanoic acid.

A standard ratio of monomer : CTA : AIBN of 300:1:0.25 was chosen based on a literature example showing diblock polymers formed by RAFT polymerisation with low polydispersities.[20] Although alteration of this ratio would be relevant to optimising the properties of the polymers, it is beyond the scope of this exploratory work.

6.3.1 Synthesis of poly(butyl acrylate) (PBA)

Poly(butyl acrylate) was synthesised according to a modified literature procedure.[4] CTA, AIBN and butyl acrylate were dissolved in dichloromethane in a Schlenk flask under N_2. The solution was degassed for 30 minutes and placed in a pre-heated oil bath at 70 $^{\circ}$C for the allotted amount of time. Once the reaction was finished, the reaction was quenched by placing the flask in a water bath. A yellow, viscous liquid was precipitated by addition of excess methanol. This liquid was analysed by NMR spectroscopy to assess the conversion from monomer to polymer and by GPC to analyse the content of the polymer. The length of time for which the reactions were run was informed by literature methods.[4]

Figure 6.5 shows the ^{1}H NMR spectra of butyl acrylate (top, blue) and poly- (butyl acrylate) (bottom, red). From these spectra, the effects of polymerisation can clearly be seen. The three well-defined peaks from the vinyl protons of butyl acrylate at 6.37, 6.08 and 5.77 ppm all diminish upon polymerisation, indicating that the vinyl groups have reacted. Instead, broad peaks at 2.27 and 1.91 ppm which are attributable to the CH and CH_2 groups which form the backbone of the polymer are seen in the spectrum for

poly(butyl acrylate). In addition, the peaks for the CH_2 and CH_3 in the 'tail' of the poly(butyl acrylate) are much broader than those for the monomer, which is to be expected from an NMR spectrum of a polymer.

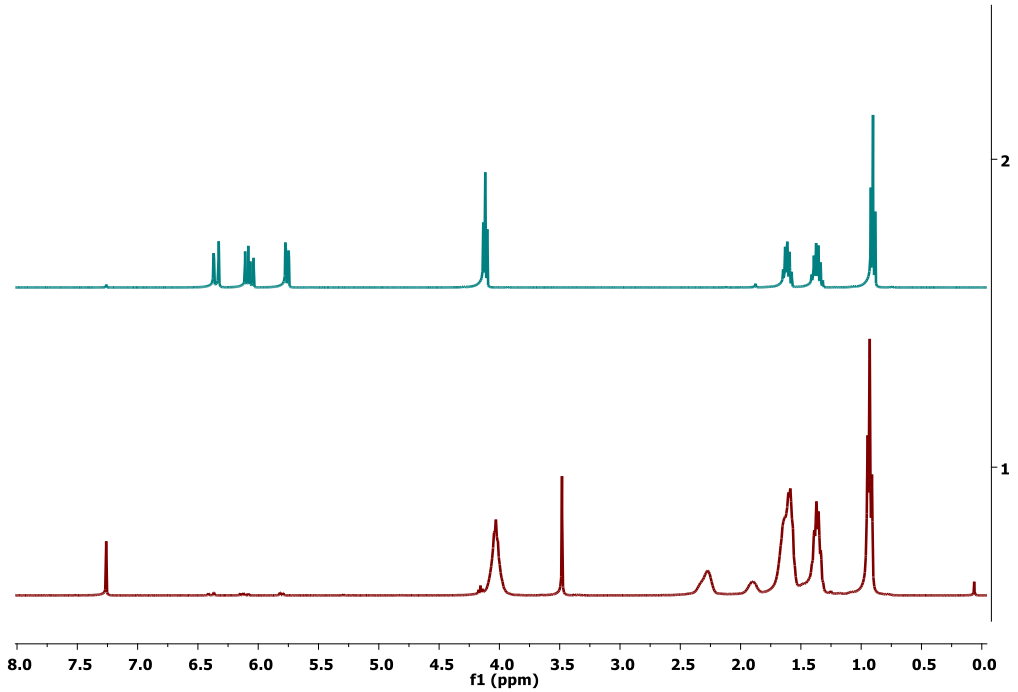

Figure 6.5 - ^{1}H NMR spectra of butyl acrylate (top, blue) and poly(butyl acrylate) (bottom, red), both in $CDCl_3$.

Table 6.1 shows the NMR and GPC analysis of each reaction. In general, all samples of poly(butyl acrylate) show excellent PD values of 1.13 - 1.39 and the conversion is good, where the lowest conversion rate is 73.5 %. Based on the results in Table 6.1, the 4 hour reaction gives the best combination of conversion and polydispersity (PD). Although the PD value is slightly lower for the 2 hour reaction, there was only 73.5% conversion. The conversion percentage shown by the 0.5, 1 and 2 hour reactions is interesting; the conversion appears to go down with increasing time. This observation is the opposite of what would be expected. However, this may be a result of the challenges of assessing conversion by NMR spectroscopy. This method relies on comparing the integration of vinyl peaks, which disappear as polymerisation occurs, and peaks from the polymer, which appear with polymerisation. There is some error

associated with the measurement of integration and this could account for the unusual trend seen here.

Table 6.1 - NMR and GPC analysis of poly(butyl acrylate)

Time (hours)	Conversion (%)	M_n (g mol^{-1})	M_w (g mol^{-1})	PD
0.5	81.8	16602	20980	1.26
1	75.6	17604	24531	1.39
2	73.5	17841	20153	1.13
4	90.1	21576	26607	1.23

6.3.2 Synthesis of poly (benzyl methacrylate) (PBzMA)

Poly(benzyl methacrylate) (PBzMA) was synthesised according to a modified literature procedure.[19] CTA, AIBN and benzyl methacrylate were dissolved in ethanol in a Schlenk flask under N_2. The solution was degassed for 30 minutes and placed in a pre-heated oil bath at 70 $^{\circ}$C for the allotted amount of time. Once the reaction was finished, the reaction was quenched by placing the flask in a water bath. A yellow, viscous liquid was precipitated by addition of excess diethyl ether. This liquid was analysed by NMR spectroscopy to assess the conversion from monomer to polymer and by GPC to analyse the content of the polymer. The length of time for which the reactions were run was informed by literature methods.[19]

Figure 6.6 shows the ^{1}H NMR spectra of benzyl methacrylate (top, blue) and poly(benzyl methacrylate) (bottom, red). For all of the peaks in these spectra there is a significant upfield shift upon polymerisation, making it obvious that a reaction has occurred. These changes are detailed in Table 6.2. There is also a broadening of peaks upon polymerisation. The vinyl peaks at 6.03 and 5.43 ppm disappear upon polymerisation and are replaced by CH_2 environments at 0.03 and 0.15 ppm.

Table 6.2 - Change in ^{1}H chemical shift in ppm upon conversion from benzyl methacrylate to poly(benzyl methacrylate).

	Monomer	Polymer
Benzyl	7.23	6.51
Methyl	1.84	0.81
OCH_2	5.06	4.11
Vinyl	6.03, 5.43	0.15, 0.03

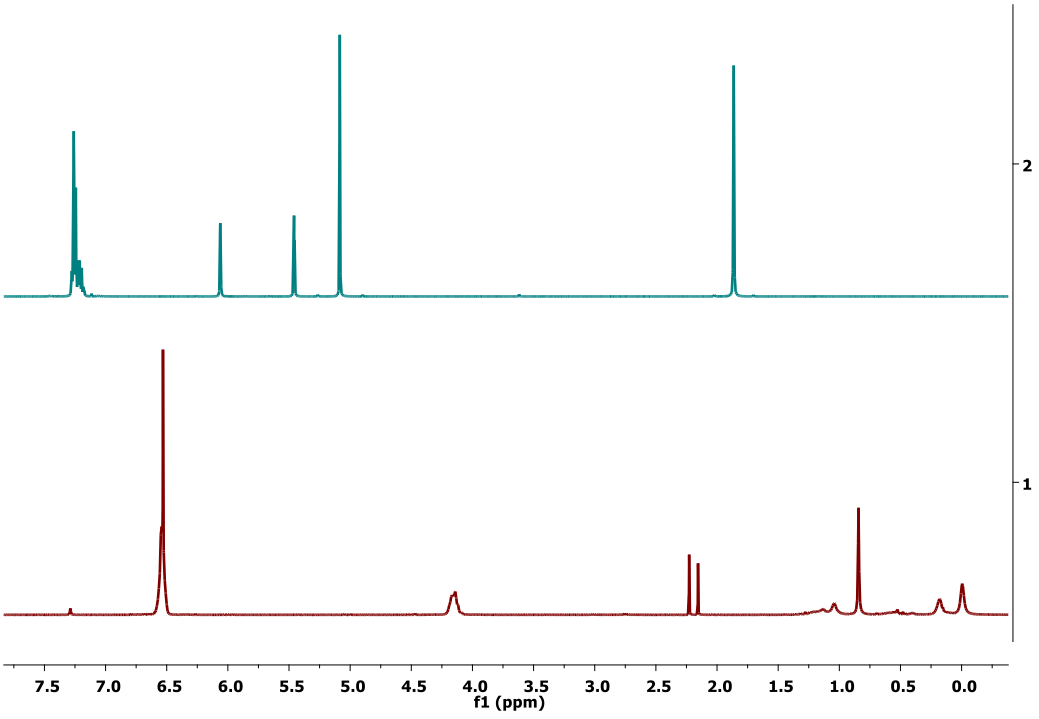

Figure 6.6 - ^{1}H NMR spectra of benzyl methacrylate (top, blue) and poly(benzyl methacrylate) (bottom, red), both in $CDCl_3$.

The results of these timed reactions of poly(benzyl methacrylate) are shown in Table 6.3. The reactions for 0.5 and 1 hour showed no conversion by NMR spectroscopy and 2 hour reaction showed only 11.7 % conversion. These conversions clearly indicate that longer time spans were necessary. The 4, 10, 18 and 24 hour reactions all showed

conversions which were broadly similar (98.9 - 99.7 %), however the PD values improved slightly with longer timescales, indicating that longer reactions narrow the distribution of molecular mass in a sample. However, the best PD value achieved here was 2.16, showing that the reaction would require optimisation in order to improve polydispersity.

Table 6.3 - NMR and GPC analysis of poly(benzyl methacrylate).

Time (hours)	Conversion (%)	M_n (g mol^{-1})	M_w (g mol^{-1})	PD
0.5	No conversion			
1	No conversion			
2	11.7	149879	318689	2.13
4	98.9	31897	773966	2.43
10	99.2	255474	607405	2.38
18	99.7	196976	435552	2.21
24	99.7	151689	327541	2.16

6.4 Synthesis of copolymers

6.4.1 Poly (butyl acrylate-benzyl methacrylate)

Poly(butyl acrylate-benzyl methacrylate) was synthesised according to the same modified literature procedure used for the synthesis of PBA.[4] CTA, AIBN, butyl acrylate and benzyl methacrylate were dissolved in dichloromethane in a Schlenk flask under N_2. The solution was degassed for 30 minutes and placed in a pre-heated oil bath at 70 °C for the allotted amount of time. Once the reaction was finished, the reaction was quenched by placing the flask in a water bath. A yellow, viscous liquid was precipitated by addition of excess diethyl ether. This liquid was analysed by NMR spectroscopy to assess the conversion from monomer to polymer and by GPC to analyse the content of

the polymer. Copolymerisation reactions were run for 2 and 4 hours. These times were chosen based on the time scales used for the synthesis of PBA and PBzMA.[19, 21] The NMR spectra showed peaks for both poly(butyl acrylate) and poly(benzyl methacrylate).

Table 6.4 - NMR and GPC analysis of poly(butyl acrylate-benzyl methacrylate).

Time (hours)	Conversion (%)	Ratio (PBzMA : PBA)	M_n (g mol^{-1})	M_w (g mol^{-1})	PD
2	98.8	2 : 1	21603	35988	1.57
4	96.6	2.25 : 1	22571	37177	1.65

6.5 Conclusions on polymer screening reactions

During the polymer screening investigations discussed previously in this chapter, a range of reaction times were investigated. As this chapter discusses only an exploratory study, it is strongly recommended that any follow up study should investigate the other variables which are key to RAFT polymerisation reactions, including the use of different CTAs, solvents and ratios of reagents. The results obtained from this screen informed the next step of the project; the polymerisation of a functionalised bpp ligand.

6.6 Synthesis of a functionalised bpp ligand

2,6-*Bis*[pyrazol-1-yl]pyridine has been intensively studied in the Halcrow group.[21-25] It is cheap and relatively quick to synthesise, although the initial step requires a long reaction time and a high temperature. It is also possible to synthesise on a relatively large scale, making it suitable for an exploratory project such as this.

The target bpp derivative, 4-carboxylic acid-2,6-*bis*[pyrazol-1-yl]pyridine, is shown in Figure 6.7. The carboxylic acid moiety allows simple functionalisation to add a monomer group to this ligand.

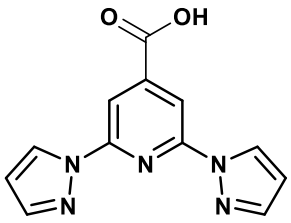

Figure 6.7 - Structure of 4-carboxylic acid-2,6-*bis*[pyrazol-1-yl]pyridine.

The synthesis of the final functionalised ligand (**21**) is shown in Figure 6.8. Step one was a nucleophilic substitution of 2 equivalents of pyrazole onto 4-carboxylic acid-2,6-dichloro pyridine (**17**), which forms 4-carboxylic acid-2,6-*bis*[pyrazol-1-yl]pyridine (**18**). Compound **19** was formed *via* an esterification of **18** using sulfuric acid and methanol. A short linker to impart flexibility upon the eventual polymer was attached by reacting ethanolamine with **19** to give **20**. Finally a polymerisable vinyl group was attached by nucleophilic substitution of **20** onto acryloyl chloride to give **21**.

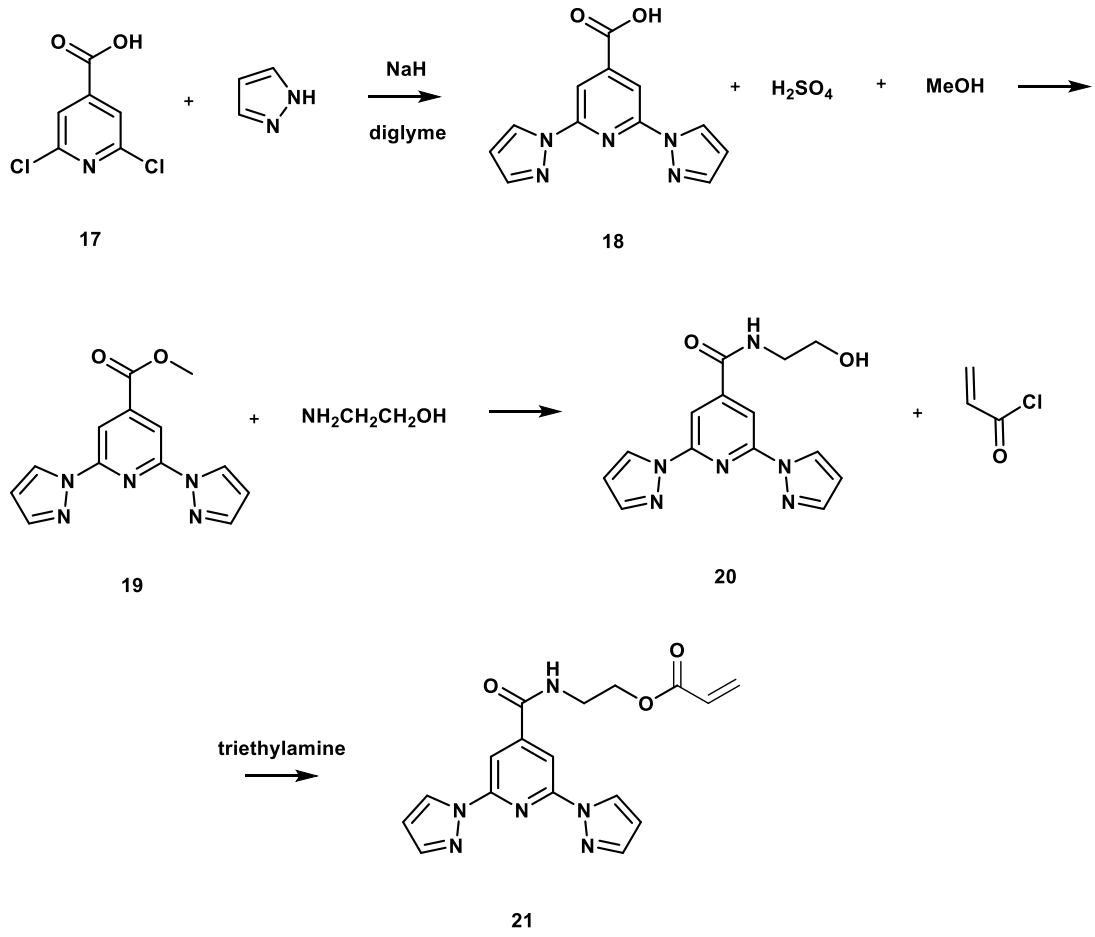

Figure 6.8 - Synthesis of functionalised bpp ligand.

This ligand (**21**) provides a starting point for incorporating spin-crossover modules into a polymeric material. Given that spin-crossover is governed by the relationship between the ligand field strength and temperature, suitable ligands can easily be tuned to alter the spin-crossover properties, for example by functionalising the pyrazoles prior to the reaction. The metal-ligand bond strength should also be affected by this tuning which could lead to a range of interesting properties, including tuneable mechanical and self-healing characteristics as well as spin-crossover.

6.7 Polymerisation and copolymerisation studies of 21

The choice of conditions used for reactions of the polymerisation of **21** and the copolymerisations between **21** and butyl acrylate or benzyl methacrylate were informed by the conditions discussed in Sections 6.3, 6.4 and 6.5. CTA, AIBN and **21**, and butyl acrylate or benzyl methacrylate where appropriate, were dissolved in dichloromethane in a Schlenk flask under N_2. The solution was degassed for 30 minutes and placed in a pre-heated oil bath at 70 °C for 4 hours. Once the reaction was finished, the reaction was quenched by placing the flask in a water bath. A yellow, viscous liquid was precipitated by addition of excess diethyl ether. This liquid was analysed by NMR spectroscopy to assess the conversion from monomer to polymer and by GPC to analyse the content of the polymer. The proposed structures of these compounds are shown Figure 6.9. **22** is the product of the polymerisation of **21**, whereas **23** and **24** are copolymers between **21** and butyl acrylate or benzyl methacrylate respectively.

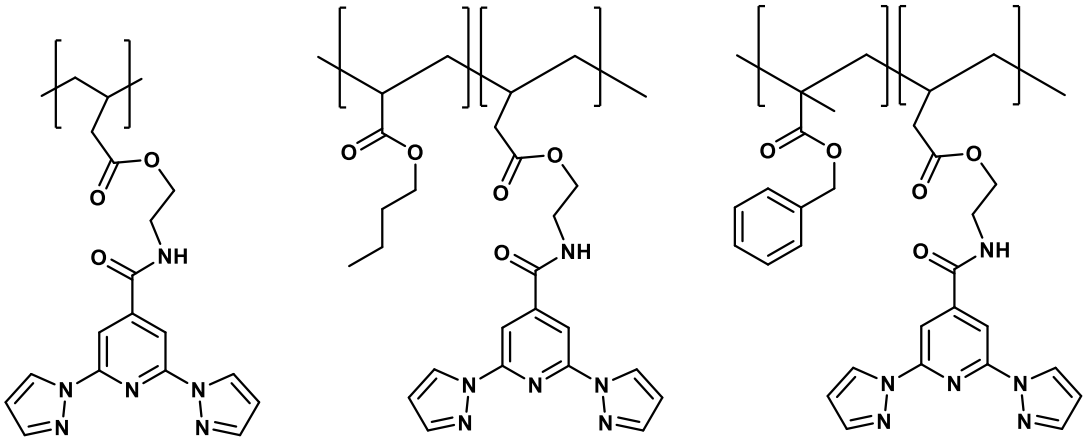

22 23 24

Figure 6.9 - Proposed structures of polymer 22 and copolymers 23 and 24.

Both the NMR and GPC results show that **21** did not undergo successful polymerisation to form **22**. The NMR spectra for **21** and the obtained reaction product are shown in Figure 6.10 and both are identical, showing that polymerisation has not occurred. Similarly the GPC results gave no data indicating that a polymer was present in the sample. This lack of polymerisation is almost certainly a result of the steric

properties of the tridentate bpp ligand, which hinder the approach of vinyl units necessary for a reaction to occur. During the planning stages of this aspect of the project, it was hypothesised that this polymerisation would be hindered by the sterics of the ligand, hence copolymerisations were planned.

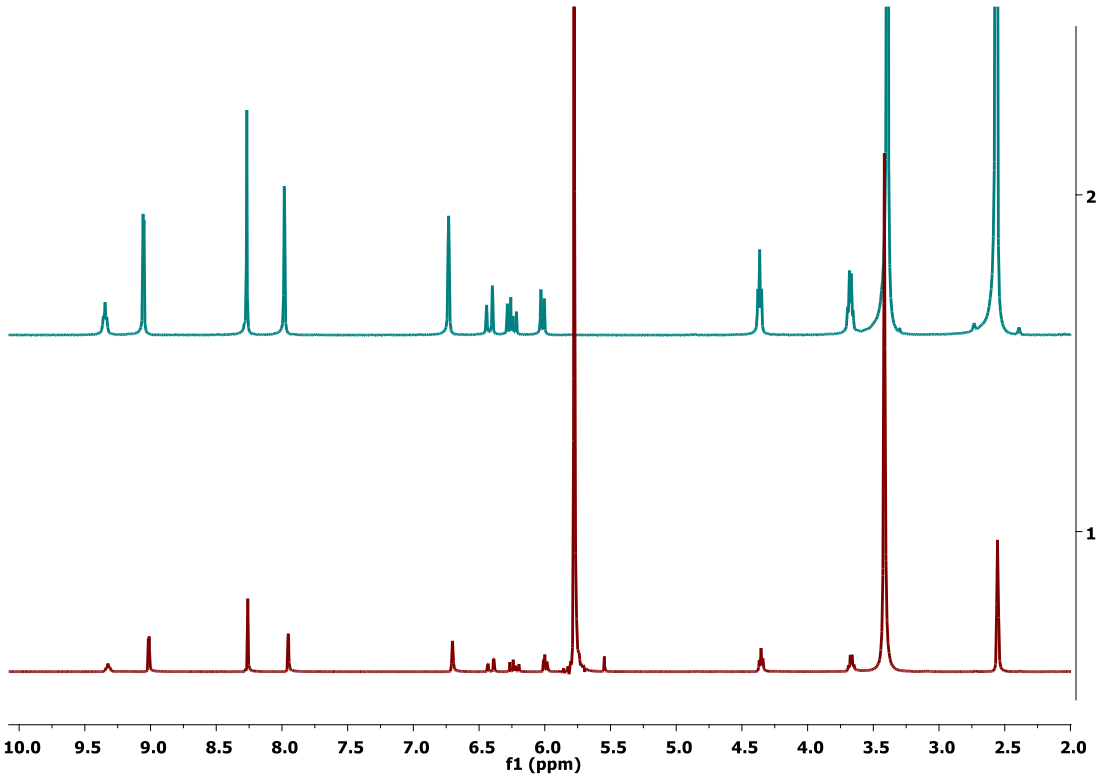

Figure 6.10 - The ^{1}H NMR spectra of 21 (top, blue) and obtained reaction product (bottom, red) in DMSO. The peak at 5.77 is residual DCM.

There is some discrepancy between the NMR and GPC data for **23**. The GPC data (Table 6.5) indicate that polymer has formed, suggesting that some reaction has taken place between the butyl acrylate monomer and **21**. However, this result is not corroborated by the NMR spectrum of **23** (Figure 6.11). The peaks between 5.75 and 6.5 ppm show that there a significant presence of vinyl groups in the material, as well as sharp multiplets between 1.0 and 2.0 ppm which suggest that the butyl group has undergone limited polymerisation. Furthermore there are no signals between 2.0 and 3.0 ppm which show CH and CH_2 peaks which have appeared as a result of the vinyl groups in the butyl acrylate monomer undergoing polymerisation.

It is reasonable to suggest that polymerisation may be much slower than in the screening reactions discussed previously. It is likely that this is a result of the size of butyl acrylate which does not provide enough space between the bulky bpp ligand. Longer reaction times or increased amount of CTA and initiator may help to promote polymerisation and should be the subject of further study.

Table 6.5 - GPC data for 23.

M_n (g mol^{-1})	M_w (g mol^{-1})	PD
32526	42965	1.32

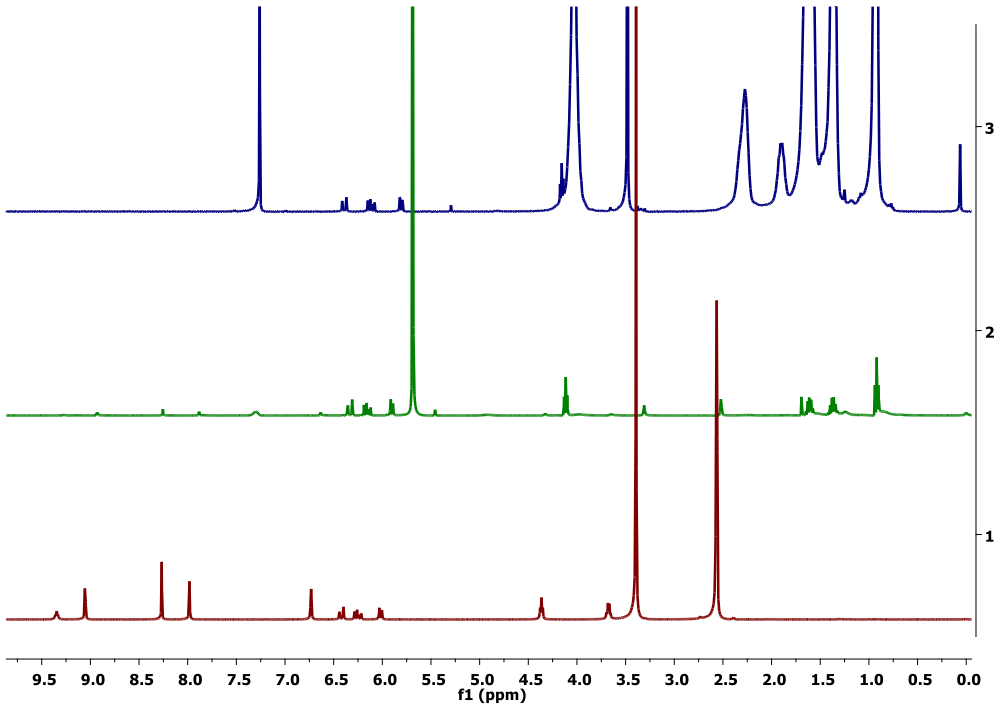

Figure 6.11 - ^{1}H NMR spectra of poly(butyl acrylate) in $CDCl_3$ (top, blue), 23 (middle, green) and 21 (bottom, red) in DMSO.

The formation of **24** was much more successful than either **22** or **23**. Both the NMR (Figure 6.12) and GPC (Table 6.6) data show that a polymer has formed. The chemical shift of the benzyl, methyl and OCH_2 groups show an upfield shift when polymerisation has occurred; Figure 6.12 shows that these signals are at the same chemical shift in **24** as in the spectrum for poly (benzyl methacrylate). Furthermore,

there is only a small trace of vinyl peaks from either benzyl methacrylate or **21** observed in the spectrum for **24**.

The success of this polymerisation, which used the same reaction conditions as those which proved unsuccessful in the case of **22** and only partially successful for **23**, indicate that it is the steric bulk of **21** which hinders these reactions, rather than an inability of the functionalised ligand itself to undergo polymerisation or copolymerisation. Benzyl methacrylate is more bulky than butyl acrylate, and therefore is likely to be a better spacer between units of **21** in a polymer.

Table 6.6 - GPC data for 24.

M_n (g mol^{-1})	M_w (g mol^{-1})	PD
54952	90240	1.64

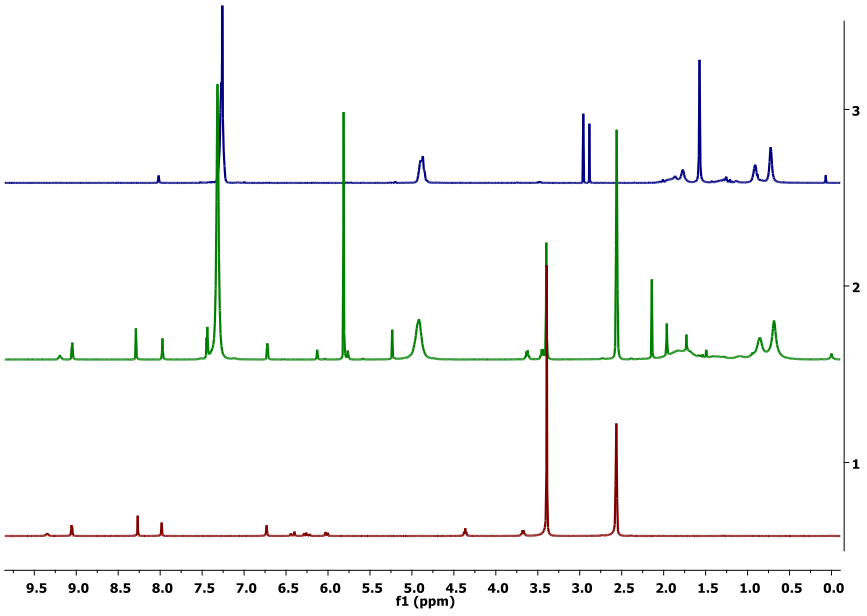

Figure 6.12 - ^{1}H NMR spectra of poly(benzyl methacrylate) (top, blue), 24 (middle, green) and 21 (bottom, red).

6.8 Conclusions

This chapter has shown the exploration of a new synthetic methodology which can be applied to spin-crossover research in the future. A functionalised bpp derivative, **21**, has been prepared in an easy four step synthesis utilising cheap, readily available reagents, meaning it would be possible to synthesise this ligand on a large enough scale for polymer chemistry and subsequent testing. In addition, RAFT polymerisation reactions have been used to form polymers and copolymers of butyl acrylate and benzyl methacrylate. The impact of reaction times on the composition of these polymers were investigated and this optimum reaction time of 4 hours was used when attempting to polymerise and copolymerise **21**. The polymerisation of **21** was unsuccessful, most likely due to the steric bulk of the ligand. Colpolymerisation of **21** and butyl acrylate to form **23** was of limited success. This is thought to be due to the small size of butyl acrylate being unable to provide enough space between units of **21**. The copolymerisation of **21** with benzyl methacrylate to form **24** was much more successful. Benzyl methacrylate is a much bulkier molecule and provides adequate space between **21** during polymerisation.

6.9 Future work

Given that this chapter has only scratched the surface of the chemistry involved with this project, the scope for future work is significant and diverse.

Firstly, the conditions used for forming polymers and copolymers should be further optimised. This is particularly in the case for benzyl methacrylate, which showed very high molecular weights and polydispersities. The ratio of CTA, initiator and monomer, as well as reaction times would be worthwhile endeavours to provide a thorough framework on which to base novel polymers. As an extension, other monomers, CTAs and solvents could be investigated. Similarly, further copolymerisation studies, investigating different ratios of monomers as well as different monomer feeding methods would give an insight into the incredible variation available and could introduce interesting morphologies and architectures to this project. Specifically, the

optimisation of the reaction to form **23** by increasing the ratio of butyl acrylate to **21** may allow this copolymer to form successfully. The incorporation of other monomers with varying size and steric properties would almost certainly be a fascinating way to provide differentiation in structure and behaviour. In addition, the formation of diblocks may also yield interesting structures, particularly micelles, which could improve the potential for the use of such polymers in functional materials.

The functionalised bpp derivative, **21**, discussed in the chapter is only one example of a ligand which could be used in this project. Different length linkers could alter the likelihood of polymerisation and different functional groups in the 4-pyridyl position or on the pyrazoles would alter the ligand field strength, allowing the SCO properties to be tuned. Given the expertise of the Halcrow group in this area, this aspect of future work would be readily achievable.

Finally, the incorporation of metals into the polymers prepared in this chapter has not been investigated, due to time constraints on this project. This is the most significant next step and certainly the most novel and exciting. The combination of SCO active complexes into polymers with different architectures could lead to functional materials with used in biomedical, catalytic, imaging and environmental applications. Furthermore, the physical properties, such as self-healing, mechanical and rheological behaviour, of such polymers should be investigated to further understand the potential used of such polymers.

6.10 References

1. G. D. Patterson, in *100+ Years of Plastics: Leo Backeland and Beyond*, eds. E. T. Strom and S. C. Rasmussen, ACS Publications, Editon edn., 2011, vol. 1080, pp. 21-29.
2. J. Chiefari, Y. K. Chong, F. Ercole, J. Krstina, J. Jeffery, T. P. T. Le, R. T. A. Mayadunne, G. F. Meijs, C. L. Moad, G. Moad, E. Rizzardo and S. H. Thang, *Macromolecules*, 1998, **31**, 5559-5562.
3. G. Moad, E. Rizzardo and S. H. Thang, *Polymer*, 2008, **49**, 1079-1131.
4. A. Favier and M.-T. Charreyre, *Macromol. Rapid Commun.*, 2006, **27**, 653-692.
5. O. Roubeau, *Chem. Eur. J.*, 2012, **18**, 15230-15244.
6. M. Rehahn, *Acta Polym.*, 1998, **49**, 201-224.
7. R. Dobrawa, M. Lysetska, P. B. Grune and F. Wurthner, *Macromolecules*, 2005, **38**, 1315-1325.
8. A. C. Jackson, F. L. Beyer, S. C. Price, B. C. Rinderspacher and R. H. Lambeth, *Macromolecules*, 2013, **46**, 5416-5422.
9. A. M. Savage, S. D. Walck, R. H. Lambeth and F. L. Beyer, *Macromolecules*, 2018, **51**, 1636-1643.
10. R. Dobrawa and F. Würthner, *J. Polym. Sci., Part A: Polym. Chem.*, 2005, **43**, 4981-4995.
11. S. Schmatloch, M. F. Gonzalez and U. S. Schubert, *Macromol. Rapid Commun.*, 2002, **23**, 957-961.
12. U. Mansfeld, A. Winter, M. D. Hager, W. Günther, E. Altuntaş and U. S. Schubert, *J. Polym. Sci., Part A: Polym. Chem.*, 2013, **51**, 2006-2015.
13. S. Schmatloch, A. M. J. v. d. Berg, A. S. Alexeev, H. Hofmeier and U. S. Schubert, *Macromolecules*, 2003, **36**, 9943-9949.
14. M. D. Hossain, T. Sato and M. Higuchi, *Chem. Asian. J.*, 2013, **8**, 76-79.
15. M. M. Dirtu, F. Schmit, A. D. Naik, I. Rusu, A. Rotaru, S. Rackwitz, J. A. Wolny, V. Schunemann, L. Spinu and Y. Garcia, *Chem. Eur. J.*, 2015, **21**, 5843-5855.

16. J. Y. Li, Y. C. Chen, Z. M. Zhang, W. Liu, Z. P. Ni and M. L. Tong, *Chem. Eur. J.*, 2015, **21**, 1645-1651.
17. T. Fujigaya, D.-L. Jiang and T. Aida, *J. Am. Chem. Soc.*, 2003, **125**, 14690-14691.
18. M. M. Dîrtu, D. Gillard, A. D. Naik, A. Rotaru and Y. Garcia, *Hyperfine Interact.*, 2011, **205**, 75-79.
19. E. R. Jones, M. Semsarilar, A. Blanazs and S. P. Armes, *Macromolecules*, 2012, **45**, 5091-5098.
20. M. Zamfir, C. S. Patrickios, F. Montagne, C. Abetz, V. Abetz, L. Oss-Ronen and Y. Talmon, *J. Polym. Sci., Part A: Polym. Chem.*, 2012, **50**, 1636-1644.
21. L. J. K. Cook, R. Kulmaczewski, R. Mohammed, S. Dudley, S. A. Barrett, M. A. Little, R. J. Deeth and M. A. Halcrow, *Angew. Chem. Int. Ed.*, 2016, **55**, 4327 - 4331
22. J. M. Holland, S. A. Barrett, C. A. Kilner and M. A. Halcrow, *Inorg. Chem. Commun.*, 2002, **5**, 328-332.
23. J. M. Holland, J. A. McAllister, C. A. Kilner, M. Thornton-Pett, A. J. Bridgeman and M. A. Halcrow, *J. Chem. Soc., Dalton Trans.*, 2002, 548-554.
24. L. J. Kershaw Cook, R. Mohammed, G. Sherborne, T. D. Roberts, S. Alvarez and M. A. Halcrow, *Coord. Chem. Rev.*, 2015, **289-290**, 2-12.
25. T. D. Roberts, M. A. Little, L. J. Kershaw Cook, S. A. Barrett, F. Tuna and M. A. Halcrow, *Polyhedron*, 2013, **64**, 4-12.

Chapter 7 - Experimental

7.1 General materials and methods

All reactions were performed under ambient conditions, unless otherwise noted, when standard Schlenk and inert atmosphere techniques were used. All commercially available reagents were used without further purification. Dry solvents were obtained from the University of Leeds Solvent Purification System. No problems have been experienced during the synthesis of complexes discussed in this thesis, however metal-organic perchlorates are potentially explosive and should be handled carefully and in small quantities.

^{1}H and ^{13}C NMR experiments were conducted on either a Bruker Avance DPX300 spectrometer (operating frequency 300.1 MHz for ^{1}H and 75.48 MHz for ^{13}C), a Bruker Avance 400 III HD-400 (operating frequency 400.13 MHz for ^{1}H and 100.613 MHz for ^{13}C), a Bruker Avance 500 or a Bruker Avance DRX500 (both with an operating frequency 500.13 MHz for ^{1}H and 125.80 MHz for ^{13}C). Single crystal X-ray data were collected by the author (unless otherwise noted) at the specified temperatures. A suitable crystal was selected, immersed in Fomblin and mounted on the goniometer head of an Agilent SuperNova diffractometer equipped with an Atlas CCD detector using mirror monochromated Mo-Kα (λ = 0.71073 Å) or Cu-Kα (λ = 1.54184 Å). The crystals were cooled using an Oxford Cryostream low temperature device. Elemental microanalysis was performed by Stephen Boyer at London Metropolitan University. Mass spectrometry was performed using a Bruker Daltonics (micro T.O.F) instrument operating in the positive ion electrospray mode and the spectra were acquired over the m/z range of 50 - 4000. All spectra were recorded using methanol, acetonitrile or DMSO as the eluent and a sodium formate solution to calibrate the system.

The computational methods and software used are described fully in Chapter 3.

7.2 Compounds in Chapter 2

7.2.1 Materials and methods for Chapter 2

2,6-*bis*(4-(*R*)-phenyloxazolinyl)pyridine, 2,6-*bis*(4-(*S*)-phenyloxazolinyl)pyridine, 2,6-*bis*(4-(*R*)-isopropyloxazolinyl)pyridine and 2,6-*bis*(4-(*S*)-isopropyloxazolinyl) pyridine, other starting materials, metal salts and solvents were purchased commercially and used as supplied, unless otherwise stated. All reactions were performed in ambient conditions. X-ray diffraction data for ***RS*-5** were collected by the author on Beamline I19 at the Diamond Light Source synchrotron (λ = 0.6998 Å) and processed using the in-house software Xia2. Evans' Method variable temperature solution based paramagnetic susceptibility measurements were performed by Mr. Simon Barrett on a Bruker Avance DRX500 500 MHz NMR spectrometer using TMS as a reference. Magnetic susceptibility measurements were collected by Dr. Rafal Kulmaczewski on a Quantum Design SQUID magnetometer, in an applied field of 1000 Oe.

7.2.2 Synthesis of PyBox ligands

7.2.2.1 Dimethyl 2,6-pyridinecarboximidate

This precursor was prepared according to a modified literature procedure.[2] Sodium (0.55 g, 2.3 mmol) was added to dry methanol under N_2 and stirred until the sodium dissolved. 2,6-Pyridinedicarbonitrile (2.10 g, 15.5 mmol) was added and the yellow solution was stirred for 28 hours. Acetic acid (0.13 mL, 2.3 mmol) was added and the solvent was removed *in vacuo*, leaving a yellow solid.

Yield: 2.82 g, 90%. **^{1}H NMR** (300 MHz, $CDCl_3$) δ 9.24 (d, 7.8Hz, 2H, H2), 7.93 (t, 7.8Hz, 1H, H1), 4.04 (s, 4H, H3/H4). **^{13}C NMR** (125 MHz, $CDCl_3$) δ 163.04 (C4), 147.03 (C3), 138.93 (C1), 122.60 (C2), 54.05 (C5). **HR-ESI MS**: Calculated [L] 193.0851. Found [LH^+] 194.20.

7.2.2.2 2,6-Bis(oxazolin-2-yl)pyridine) (L^H)

Dimethyl 2,6-pyridinecarboximidate (0.708 g, 3.65 mmol) was dissolved in dry chloroform (20 mL) under N_2. Ethanolamine (0.45 g, 7.3 mmol) was dissolved in chloroform (20 mL) and added to the dimethyl 2,6-pyridinecarboximidate solution. The reaction was heated to reflux for 5 days. The solvent was removed *in vacuo* and the residue washed with diethyl ether to purify the product.

Yield: 0.563 g, 71%. **^{1}H NMR** (400 MHz, $CDCl_3$) δ 8.16 (d, 7.8 Hz, 1H), 7.88 (t, 7.9 Hz, 1H), 4.54 (t, 9.7 Hz, 2H), 4.12 (t, 9.7 Hz, 2H). **^{13}C NMR** (125 MHz, $CDCl_3$) δ 163.49 (C4), 146.79 (C3), 137.37 (C1), 125.53 (C2), 68.36 (C5), 55.10 (C6). **HR-ESI MS**: Calculated [L] 217.09. Found [LH^+] 218.10.

7.2.2.3 2,6-Bis(4*R*-methyl-oxazolin-2-yl) pyridine (*R*-L^{Me})

Dimethyl 2,6-pyridinecarboximidate (0.70 g, 3.6 mmol) was dissolved in dry chloroform (20 mL) under N_2. *R*-2-Aminopropan-1-ol (0.55 g, 7.3 mmol) dissolved in dry chloroform (10 mL) was added and the reaction was heated to reflux for 4 days. The solvent was removed *in vacuo* and the resultant solid was dried in a dessicator for 24 hours, leaving a yellow powder.

Yield: 0.720 g, 81%. **^{1}H NMR** (300 MHz, $CDCl_3$) δ 8.18 (d, 2H, *J* = 7.7 Hz, H2), 7.87 (t, 1H, *J* = 7.6Hz, H1), 4.63 (dd, 2H, *J* = 9.6Hz, H3), 4.41-4.51 (m, 2H, H3/H4), 4.08 (t, 2H, *J* = 2.8Hz, H3/H4), 1.39 (d, 6H, *J* = 6.6Hz, H5). **^{13}C NMR** (125 MHz, $CDCl_3$) δ 162.29 (C4), 146.92 (C3), 137.29 (C1), 125.62 (C2), 62.29 (C5), 21.37 (C6). **HR-ESI MS**: Calculated [L] 245.12. Found [LH^+] 246.20.

7.2.2.4 2,6-Bis(N-(1S,2R)-indanol)-pyridyldiamide

Potassium carbonate (1.12 g, 0.008 mol) was dissolved in deionised water (10 mL). (1S,2R)-aminoindanol (1.0 g, 0.006 mol)) was dissolved in ethyl acetate (20 mL) and was added to the potassium carbonate solution. A solution of pyridine-2,6-dicarbonylchloride (0.8 g, 0.004 mol) in dichloromethane (15 mL) was added dropwise. This mixture was heated to reflux for 6 hours and then left to stir overnight at room

temperature. A hydrochloric acid solution was used to modify the pH from 8 to 2. At this pH, a beige precipitate appeared. This was isolated *via* vacuum filtration and was thoroughly washed with deionised water.

Yield: 0.82 g, 52%. The ^{1}H and ^{13}C NMR spectra were consistent with those previously reported in the literature.[1]

7.2.2.5 2,6-Bis(N-(1R,2S)-indanol)-pyridyldiamide

Potassium carbonate (1.12 g, 0.008 mol) was dissolved in deionised water (10 mL). (1R,2S)-aminoindanol (1.0 g, 0.006 mol)) was dissolved in ethyl acetate (20 mL) and was added to the potassium carbonate solution. A solution of pyridine-2,6-dicarbonylchloride (0.8 g, 0.004 mol) in dichloromethane (15 mL) was added dropwise. This mixture was heated to reflux for 6 hours and then left to stir overnight at room temperature. A hydrochloric acid solution was used to modify the pH from 8 to 2. At this pH, a beige precipitate appeared. This was isolated *via* vacuum filtration and was thoroughly washed with deionised water.

Yield: 1.06 g, 66%. The ^{1}H and ^{13}C NMR spectra were consistent with those previously reported in the literature.[1]

7.2.2.6 2,6-Bis(N-(1S,2R)-indanol-oxazolin-2-yl)-pyridine (1*S*2*R*-L^{Ind})

A solution of 2,6-Bis(N-(1S,2R)-indanol)-pyridyldiamide (0.35 g, 0.0008 mol) in BF_3Et_2O (5 mL, 0.008 mol) was placed in a flame dried Schlenk flask under N_2. The solution was heated to 120 °C for 6 hours. The solution was then cooled to room temperature, diluted with dichloromethane (50 mL) and poured onto a 1M sodium hydroxide solution. This was extracted with dichloromethane (3 x 50 mL) and the solvent removed *in vacuo*, leaving a beige powder. This was washed thoroughly with diethyl ether and water and dried in a dessicator.

Yield: 0.29 g, 93 %. **^{1}H NMR** (300 MHz, $CDCl_3$) δ 8.12 (d, 2H, *J* = 7.5 Hz, Py-*H*2), 7.75 (t, 1H, *J* = 7.4 Hz, Py-*H*3), 7.53-7.58 (m, 2H, Ph-*H*), 7.22-7.29 (m, 6H, Ph-*H*), 5.76 (d, 2H, *J* =

8.2 Hz, C*H*N), 5.60 (dt, 2H, *J* = 8.2, 4.0 Hz, C*H*O), 3.48-3.55 (m, 4H, CH_2). The ^{1}H and ^{13}C NMR spectra were consistent with those previously reported in the literature.[1]

7.2.2.7 2,6-Bis(N-(1R,2S)-indanol-oxazonlin-2-yl) pyridine (1*R*2*S*-L^{Ind})

A solution of 2,6-Bis(N-(1S,2R)-indanol)-pyridyldiamide (0.35 g, 0.0008 mol) in BF_3Et_2O (5 mL, 0.008 mol) was placed in a flame dried Schlenk flask under N_2. The solution was heated to 120 °C for 6 hours. The solution was then cooled to room temperature, diluted with dichloromethane (50 mL) and poured onto a sodium hydroxide solution. This was extracted with dichloromethane (3 x 50 mL) and the solvent removed *in vacuo*, leaving a beige powder. This was washed thoroughly with diethyl ether and water and dried in a dessicator.

Yield: 0.26 g, 83%. **^{1}H NMR** (300 MHz, $CDCl_3$) δ 8.11 (d, 2H, *J* = 7.5 Hz, Py-*H*2), 7.75 (t, 1H, *J* = 7.4 Hz, Py-*H*3), 7.23-7.57 (m, 2H, Ph-*H*), 7.22-7.27 (m, 6H, Ph-*H*), 5.74 (d, 2H, *J* = 8.2 Hz, C*H*N), 5.60 (dt, 2H, *J* = 8.2, 4.0 Hz, C*H*O), 3.49-3.55 (m, 4H, CH_2). The ^{1}H and ^{13}C NMR spectra were consistent with those previously reported in the literature.[1]

7.2.3 Synthesis of [Fe(PyBox)$_2$]$^{2+}$ complexes

7.2.3.1 Synthesis of [Fe((*R*)-L^{Ph})$_2$][ClO$_4$]$_2$ (*R*-1)

Iron(II) perchlorate hydrate (40mg, 0.135 mmol) was added to a solution of **(*R*)-L^{Ph}** (100mg, 0.27 mmol) in acetonitrile (25 mL). The resulting purple solution was stirred at room temperature for one hour, before the product was precipitated by an excess of diethyl ether. The dark purple precipitate was isolated using vacuum filtration, leaving a purple powder. Vapour diffusion of diethyl ether into a concentrated solution of the complex in nitromethane gave purple crystals of the nitromethane solvate suitable for X-ray diffraction.

Yield: 0.070 g, 52%. **^{1}H NMR** (300 MHz, CD_3CN) δ, 56.95 (4H, 3-py-*H*), 30.43 (4H, C*H*), 25.02 (2H, 4-py-*H*), 17.75 (4H, ph-*H*), 5.12 (4H, ox-*H*), 4.65 (4H, ox-*H*), 3.31 (8H, ph-*H*), -

3.11 (8H, ph-*H*). **Elemental microanalysis**: Calculated for $FeC_{46}H_{38}N_6O_{12}Cl_2$ C 55.61, H 3.86, N 8.46%. Found C 55.59, H 3.75, 8.43%.

7.2.3.2 Synthesis of [Fe(*R*)-L^{Ph})(*S*)-L^{Ph})][ClO_4]$_2$ (*RS*-1)

(*R*)-L^{Ph} (101.7 mg, 0.27 mmol) and **(*S*)-L^{Ph}** (100.2 mg, 0.27 mmol) were dissolved in acetonitrile (25 mL). Iron perchlorate hydrate (70.3 mg, 0.27 mmol) was added and stirred for one hour at room temperature. A colour change from a clear solution to dark purple was seen upon addition of the iron. A large excess of diethyl ether (400 mL) was added and a purple precipitate was observed. The precipitate was isolated by vacuum filtration giving a dark pink/purple powder. Single crystals suitable for X-ray diffraction analysis were grown by vapour diffusion of diethyl ether into a concentrated solution of the product in acetonitrile.

Yield: 177 mg, 87 %. **^{1}H NMR**: (300 MHz, CD_3CN): δ 43.43 (4H, 3-py-*H*), 26.26 (2H, 4-py-*H*), 7.78, 7.22, 6.84, 6.44 (20H, ph-*H*), 4.81 (4H, C*H*), 3.22 (8H, ox-*H*). **Elemental microanalysis:** Calculated for $C_{46}H_{38}N_6O_4FeB_2F_8.0.5Et_2O$ C 55.94, H 4.21, N 8.15. Found C 54.11, H 3.91, 8.78.

7.2.3.3 Synthesis of [Fe((*R*)-L^{iPr})$_2$][ClO_4]$_2$ (*R*-2)

(*R*)-L^{iPr} (100 mg, 0.033 mmol) was dissolved in acetonitrile (30 mL). Iron(II) perchlorate (40 mg, 0.0165 mmol) was added. The solution turned bright red. A large excess of diethyl ether (300 mL) was added and a red precipitate was observed. The precipitate was isolated by vacuum filtration giving a red powder. Single crystals suitable for X-ray diffraction analysis were grown by vapour diffusion of diethyl ether into a concentrated solution of the product in acetonitrile.

Yield: 0.0945 g, 87 %. **^{1}H NMR** (300 MHz, $(CD_3)_2CO$) δ -16.22 (4H, C*H*$(CH_3)_2$), -14.22 (12H, iPr-*H*), -13.63 (12H, iPr-*H*), 23.10 (4H, ox-*H*), 24.85 (2H, ox-*H*), 26.68 (4H, ox-*H*), 59.89 (2H, 3-py-*H*), 62.11 (1H, 4-py-*H*). **Elemental microanalysis**: Calculated for $C_{34}H_{46}N_6O_{12}FeCl_2$ C 47.62, H 5.41, N 9.80. Found C 47.57, H 5.38, N 9.86.

7.2.3.4 Synthesis of [Fe(*R*)-L^{iPr})(*S*)-L^{iPr})][ClO_4]$_2$ (*RS*-2)

(*R*)-L^{iPr} (50 mg, 0.0165 mmol) and **(*S*)-L^{iPr}** (50 mg, 0.0165 mmol) was dissolved in acetonitrile (30 mL). Iron(II) perchlorate (40 mg, 0.0165 mmol) was added. The solution turned bright red. A large excess of diethyl ether (300 mL) was added and a red precipitate was observed. The precipitate was isolated by vacuum filtration giving a red powder. Single crystals suitable for X-ray diffraction analysis were grown by vapour diffusion of diethyl ether into a concentrated solution of the product in acetonitrile.

Yield: 0.103 g, 95 %. **^{1}H NMR** (300 MHz, $(CD_3)_2CO$) δ -8.39 (12H, iPr-*H*), -3.52 (12H, iPr-*H*), -1.5 (4H, C*H*$(CH_3)_2$), 7.01 (2H, ox-*H*), 11.62 (2H, ox-*H*), 16.23 (2H, ox-*H*), 27.31 (1H, 4-py-*H*), 67.72 (2H, 3-py-*H*). **Elemental microanalysis**: Calculated for $C_{34}H_{46}N_6O_{12}FeCl_2$ C 47.62, H 5.41, N 9.80. Found C 47.70, H 5.40, N 9.97.

7.2.3.5 Synthesis of [Fe((*R*)-L^{Me})$_2$][ClO_4]$_2$ (*R*-3)

(*R*)-L^{Me} (100mg, 0.41mmol) was dissolved in nitromethane (20ml). Iron(II) perchlorate hexahydrate (73mg, 0.20mmol) was dissolved in nitromethane (25ml) and added to the colourless solution. This red solution was stirred at room temperature for one hour. An excess of diethyl ether (500ml) was added to produce a pink precipitate and this was left in the freezer to crystallise overnight. The solid was isolated *via* vacuum filtration to give a red powder (0.152g, 68%). Single crystals suitable for X-ray diffraction were produced using vapour diffusion of diethyl ether into a concentrated solution of the complex in acetonitrile.

Yield: 0.152 g, 68%. **^{1}H NMR** (500 MHz, (CD_3CN) δ 2.23 (12H, Me-*H*), 11.58 2H, ox-*H*), 13.49 (2H, ox-*H*), 24.84 2H, ox--*H*), 30.05 (2H, 4-py-*H*), 65.40 (4H, 3-py-*H*). **Elemental microanalysis**: Calculated for $C_{46}H_{38}N_6O_4FeB_2F_8$ C 41.90, H 4.06, N 11.28%. Found C 42.02, H 4.04, 11.25%.

7.2.3.6 Synthesis of [Fe(L^H)$_2$][ClO_4]$_2$ (4)

L^H (100 mg, 0.46 mmol) was dissolved in nitromethane (20 mL). Iron(II) perchlorate (83 mg, 0.23 mmol) was dissolved in nitromethane (10 mL) and this was added to the

colourless solution, resulting in a dark purple solution which was stirred for 30 minutes. Excess diethyl ether (150 mL) was added, causing a purple powder to precipitate. This was isolated using vacuum filtration. Single crystals suitable for x-ray diffraction were produced using a vapour diffusion of diethyl ether into a concentrated solution of the complex in acetonitrile.

Yield: 0.107 g, 95%. **^{1}H NMR** (500 MHz, (CD_3CN) δ 11.31 (8H, ox-*H*), 13.35 (4H, *H*), 24.86 (1H, 4-py-*H*), 56.06 (2H, 3-py-*H*). **Elemental microanalysis**: Calculated for $FeC_{28}H_{37}N_6O_{12}Cl_2$ C 38.34; H 3.22; N 12.19%. Found: C 36.81; H 3.13; N 11.42%.

7.2.3.7 Synthesis of [Fe((1*S*2*R*)-L^{Ind})$_2$][ClO$_4$]$_2$ (*R*-5)

(1*S*2*R*)-L^{Ind} (63 mg, 0.00016 mmol) was dissolved in acetonitrile (30 mL). Iron(II) perchlorate (20 mg, 0.00008 mmol) was added. The solution turned bright red. A large excess of diethyl ether (300 mL) was added and a red precipitate was observed. The precipitate was isolated by vacuum filtration giving a red powder. Single crystals suitable for X-ray diffraction analysis were grown by vapour diffusion of diethyl ether into a concentrated solution of the product in acetonitrile.

Yield: 0.18 g, 72 %.

7.2.3.8 Synthesis of [Fe(1*S*2*R*)-L^{Ind}) (1*R*2*S*)-L^{Ind})][ClO$_4$]$_2$ (*RS*-5)

(1*S*2*R*)-L^{Ind} (32 mg, 0.00008 mol) and **(1*R*2*S*)-L^{Ind}** (32 mg, 0.00008 mol) was dissolved in acetonitrile (30 mL). Iron(II) perchlorate (20 mg, 0.00008 mmol) was added. The solution turned bright red. A large excess of diethyl ether (300 mL) was added and a red precipitate was observed. The precipitate was isolated by vacuum filtration giving a red powder.

Yield: 0.16 g, 64 %.

7.3 Compounds in Chapter 4

7.3.1 Materials and methods for Chapter 4

2,6-*bis*(4-(*R*)-phenyloxazolinyl)pyridine, 2,6-*bis*(4-(*S*)-phenyloxazolinyl)pyridine, 2,6-*bis*(4-(*R*)-isopropyloxazolinyl)pyridine and 2,6-*bis*(4-(*S*)-isopropyloxazolinyl) pyridine, metal salts and solvents were purchased commercially and used as supplied, unless otherwise stated. All reactions were performed in ambient conditions. X-ray diffraction data for ***RS*-9** were collected by the author on Beamline I19 at the Diamond Light Source synchrotron (λ = 0.6998 Å) and processed using the in-house software Xia2. Evans' Method variable temperature solution based paramagnetic susceptibility measurements were performed by Mr. Simon Barrett on a Bruker Avance DRX500 500 MHz NMR spectrometer using TMS as a reference. Magnetic susceptibility measurements were collected by Dr. Rafal Kulmaczewski on a Quantum Design SQUID magnetometer, in an applied field of 1000 Oe.

7.3.1.1 Synthesis of $[Zn((R)\text{-}L^{Ph})_2][BF_4]_2$ (*R*-6)

Zinc(II) tetrafluoroborate hydrate (16 mg, 0.068 mmol) was added to a solution of (R)-L^{Ph} (50 mg, 0.135 mmol) in acetonitrile (15 mL). The resultant colourless solution was stirred at room temperature for one hour, before the product was precipitated using excess diethyl ether. The white precipitate was collected using vacuum filtration. Single crystals suitable for x-ray diffraction analysis were grown by vapour diffusion of diethyl ether into a concentrated solution of the product in acetonitrile.

Yield: 0.056 g, 84%. **^{1}H NMR** (CD_3CN) δ 8.47 (t, 2H, 7.9 Hz, 4-py-H), 8.04 (d, 4H, 7.9 Hz, 3-py- H). 7.22 (m, 4H, 4-Ph-H), 7.09 (t, 8H , 7.2 Hz, 3-Ph-H), 6.76 (d, 8H, 7.2 Hz, 2-Ph-H), 5.23 (dd (4H, 10.4, 8.9 Hz, ox-H), 5.15 (t, 4H, 10.6 Hz, C-H), 4.75 (dd, 4H, 10.8, 8,9 Hz, ox-H). **Elemental microanalysis**: Calculated for $ZnC_{46}H_{38}N_6O_4B_2F_8$ C 56.50 H 3.92 N 8.59. Found C 56.74 H 3.38 N 8.99.

7.3.1.2 Synthesis of [Zn((*R*)-L^{Ph})((*S*)-L^{Ph})][BF_4]$_2$ (*RS*-6)

Method as for ***R*-6**, but using a mixture of (R)-L^{Ph} (25 mg, 0.068 mmol), and (S)-L^{Ph} (25 mg, 0.068 mmol). The product was crystallised by vapour diffusion from acetonitrile/diethyl ether.

Yield: 0.06 g, 90 %. **^{1}H NMR**: (CD_3CN): δ 8.46 (t, 2H, 7.9 Hz, 4-py-H), 7.99 (d, 4H, 7.9 Hz, 3-py-H). 7.23-7.27 (m, 4H, 4-Ph-H), 7.16 (t, 8H, 7.2 Hz, 3-Ph-H), 6.93 (d, 8H, 8.2 Hz, 2-Ph-H), 4.99 (dd, 4H, 10.4, 9.5 Hz, ox-H), 4.79 (t, 4H, 9.2 Hz, C-H), 4.69 (dd, 4H, 10.4, 9.0 Hz, CH). **Elemental microanalysis**: Calculated for $ZnC_{46}H_{38}N_6O_4B_2F_8$ C 56.50 H 3.92 N 8.59. Found C 56.49 H 3.79 N 9.95.

7.3.1.3 Synthesis of [Zn((*R*)-L^{iPr})$_2$][BF_4]$_2$ (*R*-7)

(*R*)-L^{iPr} (50 mg, 0.165 mmol) was dissolved in acetonitrile (15 mL). Zinc(II) tetrafluoroborate hydrate (20 mg, 0.0825 mmol) was then added and the solution stirred at room temperature for one hour. A large excess of diethyl ether was added and the resulant precipitate was isolated by vacuum filtration leaving a white powder. Single crystals suitable for X-ray diffraction analysis were grown by vapour diffusion of diethyl ether into a concentrated solution of the product in acetonitrile.

Yield: 0.054 g, 78%. **^{1}H NMR** (CD_3CN) δ 8.66 (t, 2H, 7.9 Hz, 4-py-H), 8.40 (d, 4H, 7.9 Hz, 3-py-H), 4.97 (t, 4H, 9.7 Hz, ox-H), 4.67 (t, 4H, 8.9 Hz, ox-H), 3.89 (ddd, 4H, 10.0, 8.7, 6.6 Hz, ox-H), 1.40 (dq, 4H, 13.4, 6.7 Hz, iPr-CH), 0.63 (d, 12H, 6.7 Hz, iPr-H), 0.51 (d, 12H, 6.7 Hz, iPr-H). **Elemental microanalysis**: Calculated for $ZnC_{34}H_{46}N_6O_4B_2F_8$ C 48.51 H 5.51 N 9.98. Found C 48.36 H 5.39 N 10.04.

7.3.1.4 Synthesis of [Zn((*R*)-L^{iPr})((*S*)-L^{iPr})][BF_4]$_2$ (*RS*-7)

Method as for ***R*-7**, but using a mixture of (R)-L^{iPr} (25 mg, 0.0825 mmol) and (*S*)-L^{iPr} (25 mg, 0.0825 mmol). The product was crystallised using an acetonitrile/diethyl ether vapour diffusion method.

Yield: 0.06 g, 86 %. **^{1}H NMR** (CD_3CN) δ 8.63 (t, 2H, 7.9 Hz, 4-py-H), 8.37 (d, 4H, 7.9 Hz, 3-py-H), 4.82-4.70 (m, 8H, ox-H), 4.14 (ddd, 4H, 7.8, 3.8 Hz, ox-H), 1.29 (4H, qd, 10.7,6.8 Hz, iPr-CH), 0.68 (d, 12H, 3.2 Hz, iPr-H), 0.67 (d, 12H, 3.2 Hz, iPr-H). **Elemental microanalysis**: Calculated for $ZnC_{34}H_{46}N_6O_4B_2F_8$ C 48.51 H 5.51 N 9.98. Found C 48.37 H 5.43 N 10.03.

7.3.1.5 Synthesis of [Co((*R*)-L^{Ph})$_2$][BF$_4$]$_2$ (*R*-8)

Cobalt(II) tetrafluoroborate hydrate (25 mg, 0.0675 mmol) was added to a solution of (R)-L^{Ph} (50 mg, 0.135 mmol) in acetonitrile (15 mL). The resultant orange solution was stirred at room temperature for one hour. The product was precipitated using an excess of diethyl ether and the precipitate was collected by vacuum filtration, leaving an orange powder. A vapour diffusion of diethyl ether into a concentrated solution of the complex in acetonitrile gave orange crystals suitable for X-ray diffraction.

Yield: 0.056 g, 84%. **^{1}H NMR** (CD_3CN) δ 84.7(2H, 4-py-H), 40.5 (2H, ox-H), 36.8 (2H, ox-H), 20.0 (2H, ox-H), 7.7 (4H, 3-py-H), 3.0 (2H, Ph-H), 2.7 (4H, Ph-H), 2.65 (4H, Ph-H). **Elemental microanalysis**: Calculated for $CoC_{46}H_{38}N_6O_4B_2F_8$ C 56.88 H 3.94 N 8.65. Found C 56.63 H 3.81 N 8.53.

7.3.1.6 Synthesis of [Co((*R*)-L^{Ph})((*S*)-L^{Ph})][BF$_4$]$_2$ (*RS*-8)

Method as for ***RS*-1**, but using cobalt(II) tetrafluoroborate hydrate (25 mg, 0.0675 mmol). Single crystals suitable for X-ray diffraction analysis were grown by vapour diffusion of diethyl ether into a concentrated solution of the product in acetonitrile.

Yield: 0.06 g, 90 %. **^{1}H NMR** (CD_3CN): δ 72.4 (2H, 4-py-H), 37.9 (2H, ox-H), 28.3 (2H, ox-H), 26.9 (2H, ox-H), 16.2 (4H, 3-py-H), 8.0 (2H, Ph-H), 7.3 (4H, Ph-H), 1.7 (4H, Ph-H). **Elemental microanalysis**: Calculated for $CoC_{46}H_{38}N_6O_4B_2F_8$ C 56.88 H 3.94 N 8.65. Found C 56.73 H 4.03 N 8.79.

7.3.1.7 Synthesis of $[Co((R)\text{-}L^{iPr})_2][BF_4]_2$ (*R*-9)

Method as for ***RS*-4**, using cobalt(II) tetrafluoroborate hydrate (20 mg, 0.0825 mmol). Single crystals suitable for X-ray diffraction analysis were grown by vapour diffusion of diethyl ether into a concentrated solution of the orange complex in acetonitrile.

Yield: 0.054 g, 78%. **^{1}H NMR** (CD_3CN) δ 74.2 (2H, 4-py-H), 54.6 (4H, 3-py-H), 26.8 (4H, ox-H), 26.2 (4H, ox-H), 15.9 (4H, iPr-CH), 9.0 (4H, ox-H), –4.9 (12H, iPr- H), –17.3 (12H, iPr-H). **Elemental microanalysis**: Calculated for $CoC_{34}H_{46}N_6O_4B_2F_8$ C 48.89 H 5.55 N 10.06. Found C 48.97 H 5.40 N 10.13.

7.3.1.8 Synthesis of $[Co((R)\text{-}L^{iPr})((S)\text{-}L^{iPr})][BF_4]_2$ (*RS*-9)

Method as for ***RS*-2**, but using cobalt(II) tetrafluoroborate hydrate (20 mg, 0.0825 mmol). The product was crystallised using by vapour diffusion from acetonitrile/diethyl ether vapour diffusion.

Yield: 0.06 g, 86 %. **^{1}H NMR** (CD_3CN) δ 63.8 (2H, 4-py-H), 45.2 (4H, 3-py-H), 30.4 (4H, ox-H), 21.7 (4H, ox-H), 10.0 (4H, iPr-CH), –4.9 (12H, iPr-H), –17.3 (12H, iPr-H). **Elemental microanalysis**: Calculated for $CoC_{34}H_{46}N_6O_4B_2F_8$ C 48.89 H 5.55 N 10.06. Found C 48.71 H 5.65 N 9.98.

7.4 Compounds in Chapter 5

7.4.1 Materials and methods for Chapter 5

All complexes were synthesised under strict inert conditions and stored in a glovebox under nitrogen. X-ray diffraction data were collected by the author on an Agilent SuperNova diffractometer, except **15** and **16**, which were collected by the author on Beamline I19 at the Diamond Light Source synchrotron (λ = 0.6998 Å), and **14** which was collected by Dr Christopher Pask at Diamond Light Source. Structures collected at Diamond Light Source were processed using the in-house software Xia2. Evans' Method variable temperature solution based paramagnetic susceptibility measurements were performed by Dr Mark Howard on a JEOL 600 MHz ECAii NMR spectrometer using TMS as a reference. Magnetic susceptibility measurements were collected by Dr. Rafal Kulmaczewski, Izar Capel Berdiell or Namrah Shahid on a Quantum Design SQUID magnetometer in an applied field of 1000 Oe.

7.4.2 Synthesis of oxime ligands

7.4.2.1 2-pyridine oxime (L10)

Sodium acetate (1.47 g, 0.018 mol) was dissolved in deionised water (10 mL). Hydroxylamine hydrochloride (1.25 g, 0.018 mol) was added and the solution heated at 60°C for one hour. 2-pyridine carboxaldehyde (0.88 mL, 0.009 mol) dissolved in methanol (5 mL) was added and the reaction was heated overnight at 60°C. The mixture was cooled to 0°C, leaving a white precipitate which was isolated *via* vacuum filtration. The solid was washed repeatedly with deionised water and dried in a vacuum oven at 40°C overnight.

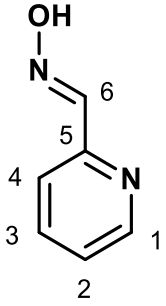

Yield: 0.95 g, 87%. **^{1}H NMR** (400 MHz, CH_3OD) δ 8.52 (dt, 1H, *J* = 4.8, 1.1Hz, H1), 8.10 (s, 1H, H6), 7.80-7.89 (m, 2H, H3 and H4), 7.38 (ddd, 1H, *J* = 6.9, 5.0, 1.7 Hz, H2). **^{13}C NMR** (101 MHz, CH_3OD) δ 153.6 (C5), 150.1 (C1), 149.5 (C6), 138.5 (C4), 125.3 (C2), 121.9 (C3).

7.4.2.2 2-thiazole oxime (L11)

Sodium acetate (1.80 g, 0.0215 mol) was dissolved in deionised water (15 mL). Hydroxylamine hydrochloride (0.72 g, 0.010 mol) was added and the solution heated at 60°C for one hour. 2-thiazole carboxaldehyde (1.0 g, 0.0086 mol) dissolved in methanol (10 mL) was added and the reaction was heated overnight at 60°C. The mixture was cooled to 0°C, leaving an off-white precipitate which was isolated *via* vacuum filtration. The solid was washed repeatedly with deionised water and dried in a vacuum oven at 40°C overnight.

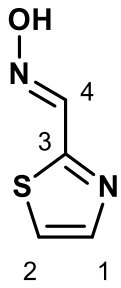

Yield: 0.79 g, 72 %. **^{1}H NMR** (400 MHz, CH_3OD) δ 8.26 (s, 1H, H4), 7.85 (d, 1H, *J* = 3.2, H1), 7.56 (d, 1H, *J* = 3.1, H2). **^{13}C NMR** (101 MHz, CH_3OD) δ 143.2 (C3), 142.6 (C4), 139.7 (C1), 123.4 (C2).

7.4.2.3 1H-pyrazole oxime (L12)

Sodium acetate (1.07 g, 0.013 mol) was dissolved in deionised water (10 mL). Hydroxylamine hydrochloride (0.44 g, 0.0064 mol) was added and the solution heated at 60°C for one hour. 1H-pyrazole carboxaldehyde (0.5 g, 0.0052 mol) dissolved in methanol (5 mL) was added and the reaction was heated overnight at 60°C. The mixture was cooled to 0°C, leaving an off-white precipitate which was isolated *via* vacuum filtration. The solid was washed repeatedly with deionised water and dried in a vacuum oven at 40°C overnight.

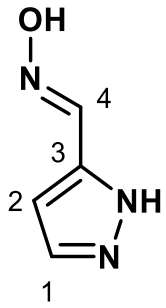

Yield: 0.156 g, 26%. **^{1}H NMR** (300 MHz, CH_3OD) δ 7.64 (s, 1H, H1), 7.45 (s, 1H, H4), 6.99 (s, 1H, H2). **^{13}C NMR** (101 MHz, CH_3OD) δ 150.5 (C1), 147.5 (C4), 143.4 (C3), 122.4 (C2).

7.4.2.4 5-methyl-1H-pyrazole-3-oxime (L13)

Sodium acetate (1.85 g, 0.023 mol) was dissolved in deionised water (15 mL). Hydroxylamine hydrochloride (0.75 g, 0.011 mol) was added and the solution heated at 60°C for one hour. 5-methyl-1H-pyrazole-3-carboxaldehyde (1.0 g, 0.009 mol) dissolved in methanol (10 mL) was added and the reaction was heated overnight at 60°C. The mixture was cooled to 0°C, leaving an off-white precipitate which was isolated *via* vacuum filtration. The solid was washed repeatedly with deionised water and dried in a vacuum oven at 40°C overnight.

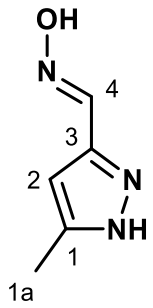

Yield: 0.76 g, 68%. **^{1}H NMR** (300 MHz, CH_3OD) δ 7.35 (s, 1H, H4), 6.98 (s, 1H, H2), 2.30 (s, 3H, H1a). **^{13}C NMR** (101 MHz, CH_3OD) δ 150.5 (C1), 139.2 (C4), 109.2 (C2), 11.5 (C1a).

7.4.2.5 1-methyl-2-imidazole oxime (L14)

Sodium acetate (1.84 g, 0.0225 mol) was dissolved in deionised water (15 mL). Hydroxylamine hydrochloride (0.74 g, 0.011 mol) was added and the solution heated at 60°C for one hour. 1-methyl-2-imidazole carboxaldehyde (1.0 g, 0.009 mol) dissolved in methanol (10 mL) was added and the reaction was heated overnight at 60°C. The mixture was cooled to 0°C, leaving an off-white precipitate which was isolated *via* vacuum filtration. The solid was washed repeatedly with deionised water and dried in a vacuum oven at 40°C overnight.

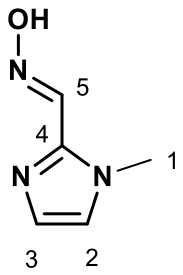

Yield: 0.61, 54% . **^{1}H NMR** 300 MHz, CH_3OD) δ 8.06 (s, 1H, H5), 7.13 (d, 1H, *J* = 0.8 Hz, H2), 7.01 (d, 1H, *J* = 1.2 Hz, H3), 3.88 (s, 3H, H1). **^{13}C NMR** (101 MHz, CH_3OD) δ 142.2 (C5), 141.7 (C4), 129.0 (C2), 125.6 (C3), 35.7 (C1).

7.4.2.6 6-methyl-2-pyridine oxime (L15)

Sodium acetate (0.65 g, 0.008 mol) was dissolved in deionised water (10 mL). Hydroxylamine hydrochloride (0.55 g, 0.008 mol) was added and the solution heated at 60°C for one hour. 6-methylpyridine-2-carboxaldehyde (0.5 g, 0.004 mol) dissolved in methanol (5 mL) was added and the reaction was heated overnight at 60°C. The mixture was cooled to 0°C, leaving a white precipitate which was isolated *via* vacuum filtration. The solid was washed repeatedly with deionised water and dried in a vacuum oven at 40°C overnight.

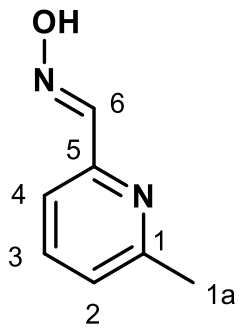

Yield: 0.51 g, 94%. **^{1}H NMR** (400 MHz, CH_3OD) 8.08 (1 H, s, H6), 7.71 - 7.62 (2 H, m, H3 and H4), 7.23 (1 H, dd, *J* 7.2, 1.1 Hz, H2), 2.52 (4 H, s, H1a). **^{13}C NMR** (125 MHz, CH_3OD) δ 159.4 (C5), 153.0 (C1), 149.7 (C6), 138.7 (C3/4), 124.9 (C2), 118.9 (C3/4), 23.8 (1a).

7.4.2.7 6-bromo-2-pyridine oxime (L16)

Sodium acetate (0.42 g, 0.0052 mol) was dissolved in deionised water (10 mL). Hydroxylamine hydrochloride (0.36 g, 0.0052 mol) was added and the solution heated at 60°C for one hour. 6-bromopyridine-2-carboxaldehyde (0.5 g, 0.0026 mol) dissolved in methanol (5 mL) was added and the reaction was heated overnight at 60°C. The mixture was cooled to 0°C, leaving a white precipitate which was isolated *via* vacuum filtration. The solid was washed repeatedly with deionised water and dried in a vacuum oven at 40°C overnight.

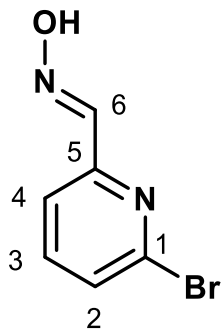

Yield: 0.47 g, 90%. **^{1}H NMR** (400 MHz, CH_3OD) δ 7.56 (d, 1H, H4, *J* = 7.8 Hz), 7.70 (t, 1H, H3, *J* = 7.8 Hz), 7.84 (d, 1H, H2, *J* = 7.8 Hz), 8.04 (s, 1H, H6). **^{13}C NMR** (101 MHz, CH_3OD) δ 118.9 (C2), 127.8 (C4), 139.2 (C3), 141.0 (C5) 147.4 (C6), 153.6 (C1).

7.4.3 Synthesis of iron(II) complexes

7.4.3.1 $[Fe(L10)_3(BC_6H_5)]ClO_4$ (10)

Phenyl boronic acid (0.16 g, 0.0013 mol), 2-pyridine oxime (0.5 g, 0.004 mol) and iron(II) perchlorate (0.33 g, 0.0013 mol) were added to a flame-dried Schlenk flask under N_2. The solids were dissolved in dry methanol (10 mL) and the solution was heated to reflux for 16 hours. Excess dry diethyl ether (100 mL) was transferred into the flask, causing a red solid to precipitate. This solid isolated *via* cannula filtration and the remaining solvent removed under vacuum. Single crystals suitable for x-ray diffraction were grown using a vapour diffusion of diethyl ether into a concentrated solution of the complex in acetonitrile.

Yield: 177 mg, 87 %. **^{1}H NMR**: (300 MHz, CD_3CN): δ 8.79 (3H, imine-*H*), 8.05 (5H, Ph-*H*), 7.67 (3H, py-*H*), 7.45 (3H, py-*H*) 7.35 (3H, py-*H*) 7.07 (3H, py-*H*). **$C_{46}H_{38}N_6O_4FeB_2F_8$.0.5 diethyl ether: Calcd**: C 55.94, H 4.21, N 8.15. **Found**: C 54.11, H 3.91, 8.78. **ES MS**: m/z (397.1146) 397.1175 [M^{2+}], 370.1555 [L-H^+], 761.2863 [2L-Na^+].

7.4.3.2 $[Fe(L11)_3(BC_6H_5)]ClO_4$ (11)

Phenyl boronic acid (0.06 g, 0. 0005mol), 2-thiazole oxime (0.5 g, 0.0016 mol) and iron(II) perchlorate (0.13 g, 0.0005 mol) were added to a flame-dried Schlenk flask under N_2. The solids were dissolved in dry methanol (10 mL) and the solution was heated to reflux for 16 hours. Excess dry diethyl ether (100 mL) was transferred into the flask, precipitating a brown solid. This solid was isolated *via* cannula filtration and the remaining solvent removed under vacuum. The sample was stored under nitrogen.

Yield: 150 mg, 48 %. **^{1}H NMR**: (300 MHz, CD_3CN): δ 10.03 (3H, N*H*), 9.01 (3H, thia-*H*), 8.41 (3H, thia-*H*), 7.77 (2H, Ph-*H*), 7.38 (2H, Ph-*H*), 5.99 (2H, Ph-*H*).

7.4.3.3 $[Fe(L12)_3(BC_6H_5)]ClO_4$ (12)

Phenyl boronic acid (0.07 g, 0. 0006mol), 1H-pyrazole oxime (0.3 g, 0.002 mol) and iron(II) perchlorate (0.15 g, 0.0006 mol) were added to a flame-dried Schlenk flask

under N_2. The solids were dissolved in dry methanol (10 mL) and the solution was heated to reflux for 16 hours. Excess dry diethyl ether (100 mL) was transferred into the flask, precipitating a brown solid. This solid was isolated *via* cannula filtration and the remaining solvent removed under vacuum. The sample was stored under nitrogen.

Yield: 127 mg, 38 %. **^{1}H NMR**: (300 MHz, CD_3CN): δ 11.98 (3H, imine-*H*), 7.73 - 8.10 (5H, Ph-*H*), 7.34 (3H, pyz-*H*), 6.96 (3H, pyz-*H*).

7.4.3.4 $[Fe(L13)_3(BC_6H_5)]ClO_4$ (13)

Phenyl boronic acid (0.03 g, 0.00027 mol), 5-methyl-1H-pyrazole-3-oxime (0.1 g, 0.0008 mol) and iron(II) perchlorate (0.07 g, 0.00027 mol) were added to a flame-dried Schlenk flask under N_2. The solids were dissolved in dry methanol (10 mL) and the solution was heated to reflux for 16 hours. Excess dry diethyl ether (100 mL) was transferred into the flask, precipitating a brown solid. This solid was isolated *via* cannula filtration and the remaining solvent removed under vacuum. The sample was stored under nitrogen.

Yield: 90 mg, 53 %. **^{1}H NMR**: (300 MHz, CD_3CN): δ 34.97(3H, imine-*H*), 11.57 (3H, pyz-*H*), 10.84 (9H, Me-*H*), 8.63 (1H, Ph-*H*), 6.96 (2H, Ph-*H*), 6.80 (2H, Ph-*H*).

7.4.3.5 $[Fe(L14)_3(BC_6H_5)]ClO_4$ (14)

Phenyl boronic acid (0.03 g, 0.00027 mol), 1-methyl-2-imidazole-oxime (d0.1 g, 0.0008 mol) and iron(II) perchlorate (0.07 g, 0.00027 mol) were added to a flame-dried Schlenk flask under N_2. The solids were dissolved in dry methanol (10 mL) and the solution was heated to reflux for 16 hours. Excess dry diethyl ether (100 mL) was transferred into the flask, precipitating a brown solid. This solid was isolated *via* cannula filtration and the remaining solvent removed under vacuum. The sample was stored under nitrogen.

Yield: 100 mg, 59 %. **^{1}H NMR**: (300 MHz, CD_3CN): δ 9.99 (3H, imine-*H*), 8.19 (2H, phenyl-*H*), 8.06 (2H, phenyl-*H*), 8.01 (H, phenyl-*H*), 7.76 (3H, imidazole-*H*), 7.38 (3H, imidazole-*H*). The peak for the methyl groups is hidden under the shoulders of the residual acetonitrile-d_3 peak as a result of poor shimming.

7.4.3.6 $[Fe(II)(L15)_3Fe(III)(L15)_3(H_2O)_3](ClO_4)_3$ (15)

Phenyl boronic acid (0.09 g, 0.0007 mol), 6-methyl-2-pyridine oxime (0.3 g, 0.0022 mol) and iron(II) perchlorate (0.18 g, 0.0007 mol) were added to a flame-dried Schlenk flask under N_2. The solids were dissolved in dry methanol (10 mL) and the solution was heated to reflux for 16 hours. Excess dry diethyl ether (100 mL) was transferred into the flask, precipitating a red solid. This solid was isolated *via* cannula filtration and the remaining solvent removed under vacuum. The sample was stored under nitrogen.

Yield: 100 mg, 59 %. **^{1}H NMR**: As discussed in in Chapter 5, Section 0, attempts to collect a paramagnetic proton NMR spectrum for this cluster proved unsuccessful, either inability to properly shim the sample and the possibility of these structures being unstable in solution.

7.4.3.7 $[Fe(II)_2(L16)_4(H_2O)_8](ClO_4)_4$ (16)

Phenyl boronic acid (0.036 g, 0.0003 mol), 6-bromo-2-pyridine oxime (0.2 g, 0.001 mol) and iron(II) perchlorate (0.076 g, 0.0003 mol) were added to a flame-dried Schlenk flask under N_2. The solids were dissolved in dry methanol (10 mL) and the solution was heated to reflux for 16 hours. Excess dry diethyl ether (100 mL) was transferred into the flask, precipitating a red/brown solid. This solid was isolated *via* cannula filtration and the remaining solvent removed under vacuum. The sample was stored under nitrogen.

Yield: 258 mg, 55 %. **^{1}H NMR**: As discussed in Chapter 5, Section 0, attempts to collect a paramagnetic proton NMR spectrum for this cluster proved unsuccessful, either inability to properly shim the sample and the possibility of these structures being unstable in solution.

7.5 Compounds in Chapter 6

7.5.1 Materials and methods for Chapter 6

GPC samples were run by Sam Parkinson in the School of Chemical and Process Engineering at the University of Leeds.

7.5.2 Synthesis of 18

Under an atmosphere of N_2, sodium hydride (60%) (2.3 g, 0.08 mol) was added to diglyme (100 mL). 1H-Pyrazole (2.18 g, 0.03 mol) was added and the reaction was stirred until hydrogen evolution had ceased (~ 20 mins). 4-carboxylic acid-2,6-dichloro-pyridine (3.0 g, 0.015 mol) was added slowly. Once added, the reaction was heated to 130 °C for 5 days. The brown solution was cooled to room temperature and poured into deionised water (~100 mL). This solution was acidified to pH 3 using hydrochloric acid, leaving a beige precipitate.

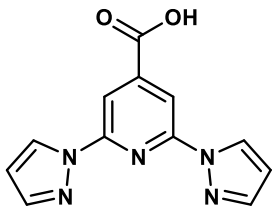

18

Yield: 2.67 g, 70 %**. ^{1}H NMR** (300 MHz, DMSO) δ 9.01 (d, 2H, *J* = 1.4 Hz, py-*H*), 8.15 (dd, 2H, *J* = 1.76, 0.85 Hz, pyz-*H*), 7.92 (dd, 2H, *J* = 1.76, 0.84 Hz, pyz-*H*), 6.67 (t, 2H, *J* = 1.76 Hz, pyz-*H*), 3.92 (s, 3H, OMe). **^{13}C NMR** (101 MHz, MeOD) δ 164.3 (COO), 151.2 (py-C), 143.7 (pyz-C), 143.1 (py-C), 128.5 (pyz-C), 109.3 (pyz-C), 107.9 (py-C), 53.8 (OMe).

7.5.3 Synthesis of 19

18 (1.0 g, mol) was dissolved in methanol (30 mL) and sulfuric acid (16 mL) added dropwise and heated to reflux for 24 hours. The reaction was cooled to room temperature and extracted into dichloromethane three times. The excess solvent was then removed *in vacuo*.

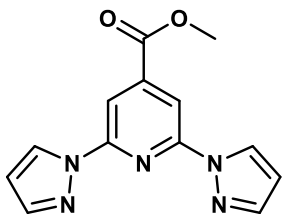

19

Yield: 0.89 g, 82%. **^{1}H NMR** (300 MHz, DMSO) δ 8.98 (d, 2H, *J* = 1.3 Hz, py-*H*), 8.13 (dd, 2H, *J* = 1.75, 0.85 Hz, pyz-*H*), 7.90 (dd, 2H, *J* = 1.75, 0.85 Hz, pyz-*H*), 6.67 (t, 2H, *J* = 1.75 Hz, pyz-*H*), 3.91 (s, 3H, OMe). **^{13}C NMR** (101 MHz, MeOD) δ 164.4 (COO), 150.8 (py-C), 143.72 (pyz-C), 143.3 (py-C), 128.9 (pyz-C), 109.4 (pyz-C), 108.2 (py-C), 53.6 (OMe).

7.5.4 Synthesis of 20

19 (0.7 g, 0.003 mol) was dissolved in ethanolamine (50 mL) and was heated to reflux for 24 hours. After cooling to room temperature, most of the solvent (~40 mL) was removed *in vacuo*. The solid beige product was precipitated with dichloromethane and washed thoroughly with water.

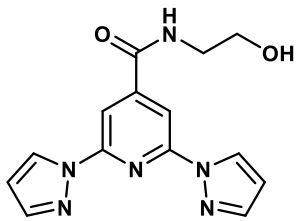

20

Yield: 0.75 g, 83 %. **^{1}H NMR** (400 MHz, DMSO) δ 8.99 (s, 2H, py-*H*), 8.22 (s, 2H, pyz-*H*), 7.91 (s, 2H, pyz-*H*), 6.66 (s, 2H, pyz-*H*), 3.56 (t, *J* = 6.0 Hz, 2H, CH_2), 3.37 (t, *J* = 6.0 Hz, 2H, CH_2). **^{13}C NMR** (101 MHz, MeOD) δ 164.2 (COO), 151.2 (py-C), 143.7 (pyz-C), 143.1 (py-C), 128.9 (pyz-C), 109.1 (pyz-C), 108.3 (py-C), 60.2 (CH_2), 41.9 (CH_2).

7.5.5 Synthesis of 21

20 (0.5 g, 0.0016 mol) was dissolved in chloroform (30 mL) and triethylamine (0.8 mL, 0.0064 mol) was added and the reaction was stirred for 30 minutes. Acryloyl chloride (0.26 mL, 0.0032 mol) was added and this solution was stirred at room temperature for 24 hours. The solution was then washed with a saturated sodium hydrogen carbonate solution (30 mL), deionised water (30 mL) and a saturated sodium chloride solution (30 mL). The organic layers were combined and the solvent removed *in vacuo*.

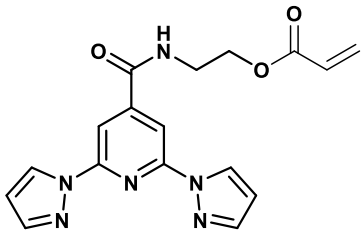

21

Yield: 0.39 g, 70 %. **^{1}H NMR** (400 MHz, $CDCl_3$) δ 8.45 (s, 2H, py-*H*), 8.11 (s, 2H, pyz-*H*), 7.27 (s, 2H, pyz-*H*), 6.43 (s, 2H, pyz-*H*), 6.20 (d, *J* = 2.0 Hz, 1H, vinyl-*H*), 6.14 - 6.08 (m, 2H, vinyl-*H*), 3.98 (t, *J* = 5.8, 3.5 Hz, 2H, CH_2), 3.49 (d, *J* = 5.7, 3.5 Hz, 2H, CH_2). **^{13}C NMR** (101 MHz, MeOD) δ 166.3 (COO), 150.3 (py-C), 140.9 (pyz-C), 144.2 (py-C), 137.8 (vinyl), 129.9 (pyz-C), 129.6 (vinyl), 110.0 (pyz-C), 109.7 (py-C), 58.9 (CH_2), 40.5 (CH_2).

7.5.6 Polymerisation of poly(butyl acrylate)

Butyl acrylate (11.2 mL, 0.075 mol) was filtered through basic alumina and added to a flame-dried Schlenk flask under N_2, with CTA (0.05 g, 0.0002 mol), AIBN (0.01 g, 0.00006 mol) and dichloromethane (10 mL). The flask was placed in a pre-heated oil bath at 70°C and heated for the allotted time. Once this was complete, the polymerisation reaction was quenched by placing the flask in a water bath. Addition of an excess of methanol precipitated a viscous, yellow liquid.

^{1}H NMR (300 MHz, $CDCl_3$) δ 4.03 (bs, 2H, OCH_2), 2.27 (bs, 2H, CH_2), 1.91 (bs, 1H, C*H*), 1.59 (bs, 2H, CH_2), 1.37 (bs, 2H, CH_2), 0.93 (bt, 3H, CH_3). **GPC** (DMF): **4 hours**: Conversion 90.1 %, M_n = 21576, PDI = 1.23. **2 hours**: Conversion 73.5 %, M_n = 17841, PDI = 1.13. **1 hour**: Conversion 75.6 %, M_n = 17604, PDI = 1.39. **0.5 hour**: Conversion 81.8 %, M_n = 16602, PDI = 1.26.

7.5.7 Polymerisation of poly(benzyl methacrylate)

Benzyl methacrylate (12.7 mL, 0.075 mol) was filtered through basic alumina and added to a flame-dried Schlenk flask under N_2, with CTA (0.05 g, 0.0002 mol), AIBN (0.008 g, 0.00006 mol) and ethanol (10 mL). The flask was placed in a pre-heated oil bath at 70°C and heated for the allotted time. Once this was complete, the polymerisation reaction was quenched by placing the flask in a water bath. Addition of an excess of methanol precipitated a viscous, yellow solid.

^{1}H NMR (300 MHz, $CDCl_3$) δ 7.27 (m, 5H, benzyl-*H*), 4.87 (bs, 2H, OC*H*$_2$), 1.57 (bs, 3H, C*H*$_3$), 0.91 (bs, 2H, C*H*$_2$). **GPC** (DMF): **24 hours**: Conversion 99.7 %, M_n = 151689, PDI = 2.16. **18 hours**: Conversion 99.7 %, M_n = 196976, PDI = 2.21. **10 hours**: Conversion 99.2 %, M_n = 255474, PDI = 2.38. **4 hours**: Conversion 98.9 %, M_n = 31897, PDI = 2.43. **2 hours**: Conversion 11.7 %, M_n = 318689, PDI = 2.13.

7.5.8 Copolymerisation of poly(butyl acrylate-benzyl methacrylate)

Benzyl methacrylate (12.7 mL, 0.075 mol) and butyl acrylate (11.2 mL, 0.075 mol) was filtered through basic alumina and added to a flame-dried Schlenk flask under N_2, with CTA (0.05 g, 0.0002 mol), AIBN (0.01 g) 0.00006 mol) and dichloromethane (10 mL). The flask was placed in a pre-heated oil bath at 70°C and heated for the allotted time. Once this was complete, the polymerisation reaction was quenched by placing the flask in a water bath. Addition of an excess of methanol precipitated a viscous, yellow solid.

^{1}H NMR (300 MHz, $CDCl_3$) δ 7.18 (m, 5H, PBzMA-benzyl-*H*), 4.81 (bs, 2H, PBzMA-OC*H*$_2$), 3.82 (bs, 2H, PBA-OC*H*$_2$), 1.86 (bs, 3H, PBzMA-C*H*$_3$), 1.67 (bs, 1H, PBA-C*H*), 1.41 (bs, 2H, PBA-C*H*$_2$), 1.29 - 1.16 (bs, 4H, 2xPBA-C*H*$_2$), 0.78 (bs, 2H, PBzMA-C*H*$_2$), 0.75 (bt, 3H, PBA-C*H*$_3$). **GPC** (DMF): **4 hours**: Conversion 96.7 % (PBzMA : PBA = 2.25 : 1), M_n = 22571, PDI = 1.65. **2 hours**: Conversion 98.8 % (PBzMA : PBA = 2 : 1), M_n = 21603, PDI = 1.57.

7.5.9 Polymerisation of 21

21 (0.6 g, 0.0017 mol) was added to a flame-dried Schlenk flask under N_2, with CTA (0.05 g, 0.0002 mol), AIBN (0.01 g, 0.00006 mol) and dichloromethane (10 mL) and was degassed for 30 minutes. The flask was then placed in a pre-heated oil bath at 70°C and heated for 4 hours. Once this was complete, the polymerisation reaction was quenched by placing the flask in a water bath. Addition of an excess of diethyl ether precipitated a viscous, yellow liquid.

^{1}H NMR (300 MHz, DMSO) δ 9.51 (s, 1H, NH), 8.96 (s, 2H, py-*H*), 8.21 (s, 2H, pyz-*H*), 7.90 (s, 2H, pyz-*H*), 6.65 (s, 2H, pyz-*H*), 6.33 (dd, *J* = 2.0 Hz, 1H, vinyl-*H*), 6.19 (q, *J* = 1.9 Hz,

1H, vinyl-*H*), 5.94 (m, *J* = 2.0 Hz 1H, vinyl-*H*), 4.30 (t, *J* = 5.8, 3.5 Hz, 2H, C*H*$_2$), 3.61 (d, *J* = 5.7, 3.5 Hz, 2H, C*H*$_2$). **GPC** (DMF): No polymer seen.

7.5.10 Copolymerisation of 21 and butyl acrylate

21 (0.6 g, 0.0017 mol), butyl acrylate (0.3 mL, 0.0017 mol) was added to a flame-dried Schlenk flask under N_2, with CTA (1.3 mg, 0.0000056 mol), AIBN (0.2 mg, 0.0000014 mol) and dichloromethane (10 mL) and degassed for 30 minutes. The flask was then placed in a pre-heated oil bath at 70°C and heated for 4 hours. Once this was complete, the polymerisation reaction was quenched by placing the flask in a water bath. Addition of an excess of diethyl ether precipitated a viscous, yellow liquid.

^{1}H NMR (300 MHz, DMSO) δ 9.27 (s, 1H, NH), 8.93 (s, 2H, py-*H*), 8.26 (s, 2H, pyz-*H*), 7.88 (s, 2H, pyz-*H*), 7.30 (s, 2H, pyz-*H*), 6.35 (dd, *J* = 2.0 Hz, 1H, vinyl-*H*), 6.16 (q, *J* = 1.9 Hz, 1H, vinyl-*H*), 5.92 (m, *J* = 2.0 Hz 1H, vinyl-*H*), 4.12 (t, *J* = 5.8, 3.5 Hz, 2H, OC*H*$_2$), 3.61 (d, *J* = 5.7, 3.5 Hz, 2H, C*H*$_2$), 1.66 - 1.56 (m, 1H, CH_2), 1.43 - 1.31 (m, 1H, CH_2), 0.96 - 0.87 (m, 1H, CH_3). **GPC** (DMF): M_n = 32526, PDI = 1.32.

7.5.11 Copolymerisation of 21 and benzyl methacrylate

21 (0.6 g, 0.0017 mol), benzyl methacrylate (0.3 mL, 0.0017 mol) was added to a flame-dried Schlenk flask under N_2, with CTA (1.3 mg, 0.0000056 mol), AIBN (0.2 mg, 0.0000014 mol) and dichloromethane (10 mL) and degassed for 30 minutes. The flask was then placed in a pre-heated oil bath at 70°C and heated for 4 hours. Once this was complete, the polymerisation reaction was quenched by placing the flask in a water bath. Addition of an excess of diethyl ether precipitated a yellow viscous semi-solid.

^{1}H NMR (300 MHz, DMSO) δ 9.14 (s, 1H, NH), 8.99 (s, 2H, py-*H*), 8.23 (s, 2H, pyz-*H*), 7.91 (s, 2H, pyz-*H*), 7.39 (s, 2H, pyz-*H*), 7.26 (m, 5H, PBzMA-benzyl-*H*), *(6.66 (bs, 1H, vinyl), 6.66 (bs, 1H, vinyl), 5.17 (bs, 1H, OCH_2)*, 4.86 (bs, 2H, PBzMA-OC*H*$_2$), 2.08 (bs, 3H, PBzMA-C*H*$_3$), 0.79 (bs, 2H, PBzMA-C*H*), 0.62 (bs, 1H, PBzMA-C*H*). * These protons are vinyl peaks from unreacted benzyl methacrylate monomer. **GPC** (DMF): M_n = 54952, PDI = 1.64.

7.6 References

1. M. Jiang, S. Dalgarno, C. A. Kilner, M. A. Halcrow and T. P. Kee, *Polyhedron*, 2001, **20**, 2151-2162.

2. M. K. Tse, S. Bhor, M. Klawonn, G. Anilkumar, H. Jiao, C. Dobler, A. Spannenberg, W. Magerlein, H. Hugl and M. Beller, *Chem. Eur. J.*, 2006, **12**, 1855-1874.

Appendices

Appendix A - X-ray crystallographic data for Chapter 2

A.1 Homochiral *R*-1

A.1.1 *R*-1 at 125 K

Empirical formula	$C_{47}H_{41}Cl_2FeN_7O_{14}$
Formula weight	1053.94
Temperature/K	125.03(10)
Crystal system	orthorhombic
Space group	$P2_12_12_1$
a/Å	13.5606(2)
b/Å	21.9177(3)
c/Å	46.1753(6)
α/°	90
β/°	90
γ/°	90
Volume/Å^3	13724.1(3)
Z	12
ρ_{calc}g/cm^3	1.530
μ/mm^{-1}	4.389
F(000)	6520.0
Crystal size/mm^3	0.2 × 0.2 × 0.2
Radiation	CuKα (λ = 1.54184)
2Θ range for data collection/°	6.794 to 147.586
Index ranges	-15 ≤ h ≤ 16, -20 ≤ k ≤ 27, -48 ≤ l ≤ 56
Reflections collected	38745
Independent reflections	23939 [R_{int} = 0.0345, R_{sigma} = 0.0519]
Data/restraints/parameters	23939/0/1928
Goodness-of-fit on F^2	0.586
Final R indexes [I>=2σ (I)]	R_1 = 0.0425, wR_2 = 0.1125
Final R indexes [all data]	R_1 = 0.0498, wR_2 = 0.1232
Largest diff. peak/hole / e Å^{-3}	0.53/-0.47
Flack parameter	-0.0018(16)

A.1.2 *R*-1 at 135 K

Empirical formula	$C_{47}H_{41}Cl_2FeN_7O_{14}$
Formula weight	1054.28
Temperature/K	135.01(10)
Crystal system	orthorhombic
Space group	$P2_12_12_1$
a/Å	13.5653(2)
b/Å	21.9353(3)
c/Å	46.2136(6)
α/°	90
β/°	90
γ/°	90
Volume/Å^3	13751.3(3)
Z	12
ρ_{calc}g/cm^3	1.528
μ/mm^{-1}	4.381
F(000)	6524.0
Crystal size/mm^3	0.2 × 0.2 × 0.2
Radiation	CuKα (λ = 1.54184)
2Θ range for data collection/°	6.792 to 147.628
Index ranges	-15 ≤ h ≤ 16, -20 ≤ k ≤ 27, -48 ≤ l ≤ 56
Reflections collected	38836
Independent reflections	24013 [R_{int} = 0.0396, R_{sigma} = 0.0569]
Data/restraints/parameters	24013/72/1916
Goodness-of-fit on F^2	1.018
Final R indexes [I>=2σ (I)]	R_1 = 0.0461, wR_2 = 0.1109
Final R indexes [all data]	R_1 = 0.0548, wR_2 = 0.1168
Largest diff. peak/hole / e Å^{-3}	0.95/-0.61
Flack parameter	-0.0029(18)

A.1.3 *R*-1 at 145 K

Empirical formula	$C_{47}H_{41}Cl_2FeN_7O_{14}$
Formula weight	1054.62
Temperature/K	145.01(10)
Crystal system	orthorhombic
Space group	$P2_12_12_1$
a/Å	13.5722(2)
b/Å	21.9562(3)
c/Å	46.2235(7)
α/°	90
β/°	90
γ/°	90
Volume/Å^3	13774.3(3)
Z	12
ρ_{calc}g/cm^3	1.526
μ/mm^{-1}	4.373
F(000)	6528.0
Crystal size/mm^3	0.2 × 0.2 × 0.2
Radiation	CuKα (λ = 1.54184)
2Θ range for data collection/°	6.788 to 147.692
Index ranges	-16 ≤ h ≤ 15, -27 ≤ k ≤ 20, -48 ≤ l ≤ 56
Reflections collected	38801
Independent reflections	24031 [R_{int} = 0.0403, R_{sigma} = 0.0579]
Data/restraints/parameters	24031/36/1921
Goodness-of-fit on F^2	1.017
Final R indexes [I>=2σ (I)]	R_1 = 0.0445, wR_2 = 0.1068
Final R indexes [all data]	R_1 = 0.0543, wR_2 = 0.1131
Largest diff. peak/hole / e Å^{-3}	0.53/-0.46
Flack parameter	-0.0041(18)

A.1.4 *R*-1 at 155K

Empirical formula	$C_{47}H_{41}Cl_2FeN_7O_{14}$
Formula weight	1054.62
Temperature/K	155.01(10)
Crystal system	orthorhombic
Space group	$P2_12_12_1$
a/Å	13.5830(3)
b/Å	21.9776(4)
c/Å	46.2647(10)
α/°	90
β/°	90
γ/°	90
Volume/Å^3	13811.0(5)
Z	12
ρ_{calc}g/cm^3	1.522
μ/mm^{-1}	4.362
F(000)	6528.0
Crystal size/mm^3	0.2 × 0.2 × 0.2
Radiation	CuKα (λ = 1.54184)
2Θ range for data collection/°	6.782 to 147.55
Index ranges	-15 ≤ h ≤ 16, -20 ≤ k ≤ 27, -48 ≤ l ≤ 56
Reflections collected	38806
Independent reflections	24078 [R_{int} = 0.0404, R_{sigma} = 0.0569]
Data/restraints/parameters	24078/36/1921
Goodness-of-fit on F^2	0.914
Final R indexes [I>=2σ (I)]	R_1 = 0.0468, wR_2 = 0.1265
Final R indexes [all data]	R_1 = 0.0578, wR_2 = 0.1370
Largest diff. peak/hole / e Å^{-3}	0.65/-0.50
Flack parameter	-0.0059(18)

A.1.5 *R*-1 at 165 K

Empirical formula	$C_{47}H_{41}Cl_2FeN_7O_{14}$
Formula weight	1054.62
Temperature/K	165.01(10)
Crystal system	orthorhombic
Space group	$P2_12_12_1$
a/Å	13.5894(2)
b/Å	21.9877(3)
c/Å	46.2804(6)
α/°	90
β/°	90
γ/°	90
Volume/Å^3	13828.6(3)
Z	12
ρ_{calc}g/cm^3	1.520
μ/mm^{-1}	4.356
F(000)	6528.0
Crystal size/mm^3	0.2 × 0.2 × 0.2
Radiation	CuKα (λ = 1.54184)
2Θ range for data collection/°	6.78 to 147.7
Index ranges	-15 ≤ h ≤ 16, -27 ≤ k ≤ 20, -56 ≤ l ≤ 48
Reflections collected	38922
Independent reflections	24127 [R_{int} = 0.0412, R_{sigma} = 0.0590]
Data/restraints/parameters	24127/0/1921
Goodness-of-fit on F^2	1.011
Final R indexes [I>=2σ (I)]	R_1 = 0.0491, wR_2 = 0.1163
Final R indexes [all data]	R_1 = 0.0618, wR_2 = 0.1253
Largest diff. peak/hole / e Å^{-3}	0.58/-0.48
Flack parameter	-0.006(2)

A.1.6 *R*-1 at 175K

Empirical formula	$C_{47}H_{41}Cl_2FeN_7O_{14}$
Formula weight	1054.62
Temperature/K	175(2)
Crystal system	orthorhombic
Space group	$C222_1$
a/Å	13.6091(7)
b/Å	15.4458(5)
c/Å	22.0008(6)
α/°	90.00
β/°	90.00
γ/°	90.00
Volume/Å^3	4624.6(3)
Z	4
ρ_{calc}g/cm^3	1.515
μ/mm^{-1}	4.342
F(000)	2176.0
Crystal size/mm^3	0.21 × 0.16 × 0.12
Radiation	CuKα (λ = 1.54184)
2Θ range for data collection/°	8.66 to 147.68
Index ranges	-16 ≤ h ≤ 15, -18 ≤ k ≤ 16, -27 ≤ l ≤ 20
Reflections collected	6473
Independent reflections	4049 [R_{int} = 0.0307]
Data/restraints/parameters	4049/52/348
Goodness-of-fit on F^2	1.045
Final R indexes [I>=2σ (I)]	R_1 = 0.0897, wR_2 = 0.2393
Final R indexes [all data]	R_1 = 0.1043, wR_2 = 0.2547
Largest diff. peak/hole / e Å^{-3}	0.42/-0.56
Flack parameter	0.022(12)

A.1.7 *R*-1 at 185K

Empirical formula	$C_{47}H_{41}Cl_2FeN_7O_{14}$
Formula weight	1054.62
Temperature/K	185(2)
Crystal system	orthorhombic
Space group	$C222_1$
a/Å	13.6121(5)
b/Å	15.4521(3)
c/Å	22.0403(4)
α/°	90.00
β/°	90.00
γ/°	90.00
Volume/Å^3	4635.9(2)
Z	4
ρ_{calc}g/cm^3	1.511
μ/mm^{-1}	4.331
F(000)	2176.0
Crystal size/mm^3	0.21 × 0.16 × 0.12
Radiation	CuKα (λ = 1.54184)
2Θ range for data collection/°	8.66 to 147.2
Index ranges	-16 ≤ h ≤ 15, -18 ≤ k ≤ 16, -27 ≤ l ≤ 20
Reflections collected	6497
Independent reflections	4047 [R_{int} = 0.0368]
Data/restraints/parameters	4047/42/328
Goodness-of-fit on F^2	1.058
Final R indexes [I>=2σ (I)]	R_1 = 0.0879, wR_2 = 0.2344
Final R indexes [all data]	R_1 = 0.0981, wR_2 = 0.2488
Largest diff. peak/hole / e Å^{-3}	0.48/-0.53
Flack parameter	0.008(10)

A.1.8 *R*-1 at 195K

Empirical formula	$C_{47}H_{41}Cl_2FeN_7O_{14}$
Formula weight	1054.62
Temperature/K	195(2)
Crystal system	orthorhombic
Space group	$C222_1$
a/Å	13.6440(7)
b/Å	15.4556(5)
c/Å	22.0532(9)
α/°	90.00
β/°	90.00
γ/°	90.00
Volume/Å^3	4650.5(3)
Z	4
ρ_{calc}g/cm^3	1.506
μ/mm^{-1}	4.318
F(000)	2176.0
Crystal size/mm^3	0.21 × 0.16 × 0.12
Radiation	CuKα (λ = 1.54184)
2Θ range for data collection/°	8.64 to 147.72
Index ranges	-15 ≤ h ≤ 16, -18 ≤ k ≤ 16, -20 ≤ l ≤ 27
Reflections collected	6423
Independent reflections	4042 [R_{int} = 0.0419, R_{sigma} = N/A]
Data/restraints/parameters	4042/36/323
Goodness-of-fit on F^2	1.099
Final R indexes [I>=2σ (I)]	R_1 = 0.0787, wR_2 = 0.2264
Final R indexes [all data]	R_1 = 0.0967, wR_2 = 0.2475
Largest diff. peak/hole / e Å^{-3}	0.45/-0.55
Flack parameter	0.003(10)

A.1.9 *R*-1 at 205K

Empirical formula	$C_{47}H_{41}Cl_2FeN_7O_{14}$
Formula weight	1045.59
Temperature/K	205.00(10)
Crystal system	orthorhombic
Space group	$C222_1$
a/Å	13.6394(4)
b/Å	15.4799(6)
c/Å	22.1071(7)
α/°	90
β/°	90
γ/°	90
Volume/Å^3	4667.6(3)
Z	4
ρ_{calc}g/cm^3	1.488
μ/mm^{-1}	4.294
F(000)	2154.0
Crystal size/mm^3	0.2 × 0.2 × 0.2
Radiation	CuKα (λ = 1.54184)
2Θ range for data collection/°	8.64 to 147.42
Index ranges	-15 ≤ h ≤ 16, -18 ≤ k ≤ 16, -20 ≤ l ≤ 27
Reflections collected	6584
Independent reflections	4062 [R_{int} = 0.0301, R_{sigma} = 0.0392]
Data/restraints/parameters	4062/94/365
Goodness-of-fit on F^2	1.061
Final R indexes [I>=2σ (I)]	R_1 = 0.0694, wR_2 = 0.1890
Final R indexes [all data]	R_1 = 0.0746, wR_2 = 0.1976
Largest diff. peak/hole / e Å^{-3}	0.45/-0.88
Flack parameter	0.003(4)

A.1.10 *R*-1 at 215K

Empirical formula	$C_{47}H_{41}Cl_2FeN_7O_{14}$
Formula weight	1041.92
Temperature/K	215.01(10)
Crystal system	orthorhombic
Space group	$C222_1$
a/Å	13.6536(8)
b/Å	15.5170(13)
c/Å	22.1583(15)
α/°	90
β/°	90
γ/°	90
Volume/Å^3	4694.5(6)
Z	4
ρ_{calc}g/cm^3	1.474
μ/mm^{-1}	4.260
F(000)	2147.0
Crystal size/mm^3	0.2 × 0.2 × 0.2
Radiation	CuKα (λ = 1.54184)
2Θ range for data collection/°	8.626 to 148.07
Index ranges	-16 ≤ h ≤ 15, -16 ≤ k ≤ 18, -20 ≤ l ≤ 27
Reflections collected	6622
Independent reflections	4067 [R_{int} = 0.0295, R_{sigma} = 0.0386]
Data/restraints/parameters	4067/20/323
Goodness-of-fit on F^2	1.043
Final R indexes [I>=2σ (I)]	R_1 = 0.0744, wR_2 = 0.1945
Final R indexes [all data]	R_1 = 0.0799, wR_2 = 0.2029
Largest diff. peak/hole / e Å^{-3}	0.52/-0.89
Flack parameter	0.004(5)

A.1.11 *R*-1 at 225K

Empirical formula	$C_{47}H_{41}Cl_2FeN_7O_{14}$
Formula weight	1048.57
Temperature/K	225.01(10)
Crystal system	orthorhombic
Space group	$C222_1$
a/Å	13.6597(2)
b/Å	15.5090(3)
c/Å	22.2122(3)
α/°	90
β/°	90
γ/°	90
Volume/Å^3	4705.62(13)
Z	4
ρ_{calc}g/cm^3	1.480
μ/mm^{-1}	4.267
F(000)	2152.0
Crystal size/mm^3	0.2 × 0.2 × 0.2
Radiation	CuKα (λ = 1.54184)
2Θ range for data collection/°	8.626 to 147.718
Index ranges	-16 ≤ h ≤ 15, -18 ≤ k ≤ 16, -27 ≤ l ≤ 20
Reflections collected	6628
Independent reflections	4081 [R_{int} = 0.0268, R_{sigma} = 0.0358]
Data/restraints/parameters	4081/26/356
Goodness-of-fit on F^2	1.006
Final R indexes [I>=2σ (I)]	R_1 = 0.0624, wR_2 = 0.1609
Final R indexes [all data]	R_1 = 0.0653, wR_2 = 0.1656
Largest diff. peak/hole / e Å^{-3}	0.53/-0.87
Flack parameter	0.006(4)

A.1.12 *R*-1 at 235K

Empirical formula	$C_{47}H_{41}Cl_2FeN_7O_{14}$
Formula weight	1030.30
Temperature/K	235.00(10)
Crystal system	orthorhombic
Space group	$C222_1$
a/Å	13.6774(2)
b/Å	15.5213(2)
c/Å	22.2671(3)
α/°	90
β/°	90
γ/°	90
Volume/Å^3	4727.11(11)
Z	4
ρ_{calc}g/cm^3	1.448
μ/mm^{-1}	4.218
F(000)	2126.0
Crystal size/mm^3	0.2 × 0.2 × 0.2
Radiation	CuKα (λ = 1.54184)
2Θ range for data collection/°	8.616 to 147.394
Index ranges	-15 ≤ h ≤ 16, -18 ≤ k ≤ 16, -20 ≤ l ≤ 27
Reflections collected	6665
Independent reflections	4091 [R_{int} = 0.0254, R_{sigma} = 0.0335]
Data/restraints/parameters	4091/21/340
Goodness-of-fit on F^2	1.046
Final R indexes [I>=2σ (I)]	R_1 = 0.0593, wR_2 = 0.1529
Final R indexes [all data]	R_1 = 0.0616, wR_2 = 0.1561
Largest diff. peak/hole / e Å^{-3}	0.70/-0.78
Flack parameter	0.001(3)

A.1.13 *R*-1 at 245 K

Empirical formula	$C_{47}H_{41}Cl_2FeN_7O_{14}$
Formula weight	1068.31
Temperature/K	245.00(10)
Crystal system	orthorhombic
Space group	$C222_1$
a/Å	13.6981(2)
b/Å	15.5267(2)
c/Å	22.2986(3)
α/°	90
β/°	90
γ/°	90
Volume/Å^3	4742.61(11)
Z	4
ρ_{calc}g/cm^3	1.496
μ/mm^{-1}	4.261
F(000)	2202.0
Crystal size/mm^3	0.2 × 0.2 × 0.2
Radiation	CuKα (λ = 1.54184)
2Θ range for data collection/°	8.608 to 147.57
Index ranges	-15 ≤ h ≤ 16, -18 ≤ k ≤ 16, -20 ≤ l ≤ 27
Reflections collected	6685
Independent reflections	4112 [R_{int} = 0.0254, R_{sigma} = 0.0331]
Data/restraints/parameters	4112/22/339
Goodness-of-fit on F^2	1.364
Final R indexes [I>=2σ (I)]	R_1 = 0.0613, wR_2 = 0.1631
Final R indexes [all data]	R_1 = 0.0638, wR_2 = 0.1670
Largest diff. peak/hole / e Å^{-3}	0.57/-0.99
Flack parameter	-0.003(3)

A.1.14 *R*-1 at 255 K

Empirical formula	$C_{47}H_{41}Cl_2FeN_7O_{14}$
Formula weight	1043.13
Temperature/K	255.00(10)
Crystal system	orthorhombic
Space group	$C222_1$
a/Å	13.7187(2)
b/Å	15.5385(2)
c/Å	22.3009(2)
α/°	90
β/°	90
γ/°	90
Volume/Å^3	4753.84(10)
Z	4
ρ_{calc}g/cm^3	1.457
μ/mm^{-1}	4.209
F(000)	2153.0
Crystal size/mm^3	0.2 × 0.2 × 0.2
Radiation	CuKα (λ = 1.54184)
2Θ range for data collection/°	8.598 to 147.5
Index ranges	-16 ≤ h ≤ 15, -16 ≤ k ≤ 18, -20 ≤ l ≤ 27
Reflections collected	6690
Independent reflections	4117 [R_{int} = 0.0256, R_{sigma} = 0.0330]
Data/restraints/parameters	4117/22/338
Goodness-of-fit on F^2	1.032
Final R indexes [I>=2σ (I)]	R_1 = 0.0632, wR_2 = 0.1654
Final R indexes [all data]	R_1 = 0.0657, wR_2 = 0.1692
Largest diff. peak/hole / e Å^{-3}	0.96/-0.70
Flack parameter	0.004(4)

A.1.15 *R*-1 at 265 K

Empirical formula	$C_{47}H_{41}Cl_2FeN_7O_{14}$
Formula weight	1041.53
Temperature/K	265.00(10)
Crystal system	orthorhombic
Space group	$C222_1$
a/Å	13.7381(2)
b/Å	15.5434(2)
c/Å	22.3120(2)
α/°	90
β/°	90
γ/°	90
Volume/Å^3	4764.43(10)
Z	4
ρ_{calc}g/cm^3	1.452
μ/mm^{-1}	4.198
F(000)	2150.0
Crystal size/mm^3	0.2 × 0.2 × 0.2
Radiation	CuKα (λ = 1.54184)
2Θ range for data collection/°	8.59 to 147.498
Index ranges	-15 ≤ h ≤ 16, -18 ≤ k ≤ 16, -20 ≤ l ≤ 27
Reflections collected	6711
Independent reflections	4123 [R_{int} = 0.0262, R_{sigma} = 0.0340]
Data/restraints/parameters	4123/20/338
Goodness-of-fit on F^2	1.069
Final R indexes [I>=2σ (I)]	R_1 = 0.0584, wR_2 = 0.1471
Final R indexes [all data]	R_1 = 0.0613, wR_2 = 0.1511
Largest diff. peak/hole / e Å^{-3}	0.66/-0.69
Flack parameter	-0.001(4)

A.1.16 *R*-1 at 275 K

Empirical formula	$C_{47}H_{41}Cl_2FeN_7O_{14}$
Formula weight	1044.83
Temperature/K	275.00(10)
Crystal system	orthorhombic
Space group	$C222_1$
a/Å	13.7609(2)
b/Å	15.5459(2)
c/Å	22.3234(3)
α/°	90
β/°	90
γ/°	90
Volume/Å^3	4775.55(11)
Z	4
ρ_{calc}g/cm^3	1.453
μ/mm^{-1}	4.194
F(000)	2155.0
Crystal size/mm^3	0.2 × 0.2 × 0.2
Radiation	CuKα (λ = 1.54184)
2Θ range for data collection/°	8.582 to 147.244
Index ranges	-17 ≤ h ≤ 15, -18 ≤ k ≤ 16, -27 ≤ l ≤ 20
Reflections collected	6749
Independent reflections	4124 [R_{int} = 0.0232, R_{sigma} = 0.0315]
Data/restraints/parameters	4124/22/338
Goodness-of-fit on F^2	1.051
Final R indexes [I>=2σ (I)]	R_1 = 0.0531, wR_2 = 0.1379
Final R indexes [all data]	R_1 = 0.0566, wR_2 = 0.1423
Largest diff. peak/hole / e Å^{-3}	0.28/-0.71
Flack parameter	-0.001(3)

A.1.17 *RS*-1 at 120 K

Empirical formula	$C_{52}H_{47}Cl_2FeN_9O_{12}$
Formula weight	1116.73
Temperature/K	119.99(14)
Crystal system	orthorhombic
Space group	Pbca
a/Å	20.58612(19)
b/Å	21.4992(2)
c/Å	22.5026(2)
α/°	90
β/°	90
γ/°	90
Volume/Å^3	9959.34(17)
Z	8
ρ_{calc}g/cm^3	1.490
μ/mm^{-1}	4.048
F(000)	4624.0
Crystal size/mm^3	0.3 × 0.1 × 0.05
Radiation	CuKα (λ = 1.54184)
2Θ range for data collection/°	7.126 to 147.65
Index ranges	-25 ≤ h ≤ 16, -26 ≤ k ≤ 22, -27 ≤ l ≤ 17
Reflections collected	27413
Independent reflections	9835 [R_{int} = 0.0318, R_{sigma} = 0.0326]
Data/restraints/parameters	9835/0/688
Goodness-of-fit on F^2	1.138
Final R indexes [I>=2σ (I)]	R_1 = 0.0444, wR_2 = 0.1406
Final R indexes [all data]	R_1 = 0.0506, wR_2 = 0.1462
Largest diff. peak/hole / e Å^{-3}	0.57/-0.49

A.1.18 *RS*-1 at 250 K

Empirical formula	$C_{52}H_{47}Cl_2FeN_9O_{12}$
Formula weight	1116.73
Temperature/K	250.00(10)
Crystal system	orthorhombic
Space group	Pbca
a/Å	20.7512(3)
b/Å	21.7685(4)
c/Å	22.6230(3)
α/°	90
β/°	90
γ/°	90
Volume/Å^3	10219.3(3)
Z	8
ρ_{calc}g/cm^3	1.452
μ/mm^{-1}	3.945
F(000)	4624.0
Crystal size/mm^3	0.4 × 0.2 × 0.05
Radiation	CuKα (λ = 1.54184)
2Θ range for data collection/°	7.064 to 148.024
Index ranges	-25 ≤ h ≤ 16, -26 ≤ k ≤ 25, -27 ≤ l ≤ 19
Reflections collected	27599
Independent reflections	10150 [R_{int} = 0.0326, R_{sigma} = 0.0347]
Data/restraints/parameters	10150/1/698
Goodness-of-fit on F^2	1.015
Final R indexes [I>=2σ (I)]	R_1 = 0.0496, wR_2 = 0.1329
Final R indexes [all data]	R_1 = 0.0642, wR_2 = 0.1440
Largest diff. peak/hole / e Å^{-3}	0.44/-0.42

A.1.19 *R*-2 at 120 K

Empirical formula	$C_{70}H_{95}Cl_4Fe_2N_{13}O_{24}$
Formula weight	1756.08
Temperature/K	120.00(13)
Crystal system	orthorhombic
Space group	$P2_12_12_1$
a/Å	12.61331(17)
b/Å	15.4887(3)
c/Å	41.0876(7)
α/°	90
β/°	90
γ/°	90
Volume/Å^3	8027.0(2)
Z	4
ρ_{calc}g/cm^3	1.453
μ/mm^{-1}	4.827
F(000)	3672.0
Crystal size/mm^3	0.45 × 0.23 × 0.08
Radiation	CuKα (λ = 1.54184)
2Θ range for data collection/°	6.098 to 147.598
Index ranges	-15 ≤ h ≤ 14, -18 ≤ k ≤ 16, -50 ≤ l ≤ 41
Reflections collected	34528
Independent reflections	15829 [R_{int} = 0.0595, R_{sigma} = 0.0792]
Data/restraints/parameters	15829/0/1073
Goodness-of-fit on F^2	1.003
Final R indexes [I>=2σ (I)]	R_1 = 0.0496, wR_2 = 0.1141
Final R indexes [all data]	R_1 = 0.0638, wR_2 = 0.1216
Largest diff. peak/hole / e Å^{-3}	1.43/-0.48
Flack parameter	-0.001(3)

A.1.20 *RS*-2 at 120 K

Empirical formula	$C_{34}H_{46}Cl_2FeN_6O_{12}$
Formula weight	857.52
Temperature/K	120.1(3)
Crystal system	monoclinic
Space group	$P2_1/n$
a/Å	9.21136(10)
b/Å	23.2381(2)
c/Å	17.78023(17)
α/°	90
β/°	95.5540(10)
γ/°	90
Volume/Å^3	3788.07(7)
Z	4
ρ_{calc}g/cm^3	1.504
μ/mm^{-1}	5.095
F(000)	1792.0
Crystal size/mm^3	0.22 × 0.18 × 0.1
Radiation	CuKα (λ = 1.54184)
2Θ range for data collection/°	6.278 to 147.46
Index ranges	-7 ≤ h ≤ 11, -28 ≤ k ≤ 26, -19 ≤ l ≤ 22
Reflections collected	16194
Independent reflections	7446 [R_{int} = 0.0297, R_{sigma} = 0.0360]
Data/restraints/parameters	7446/0/504
Goodness-of-fit on F^2	1.036
Final R indexes [I>=2σ (I)]	R_1 = 0.0323, wR_2 = 0.0779
Final R indexes [all data]	R_1 = 0.0388, wR_2 = 0.0820
Largest diff. peak/hole / e Å^{-3}	0.32/-0.41

A.1.21 *R*-3 at 130 K

Empirical formula	$C_{26}H_{30}Cl_2FeN_6O_{12}$
Formula weight	745.31
Temperature/K	130(2)
Crystal system	Trigonal
Space group	$P3_121$
a/Å	10.4565(2)
b/Å	10.4565(2)
c/Å	24.7573(4)
α/°	90.00
β/°	90.00
γ/°	120.00
Volume/Å^3	2344.26(7)
Z	3
ρ_{calc}g/cm^3	1.584
μ/mm^{-1}	6.082
F(000)	1152.0
Crystal size/mm^3	0.24 × 0.16 × 0.10
Radiation	CuKα (λ = 1.54184)
2Θ range for data collection/°	9.76 to 147.44
Index ranges	-5 ≤ h ≤ 13, -12 ≤ k ≤ 8, -20 ≤ l ≤ 27
Reflections collected	5805
Independent reflections	2813 [R_{int} = 0.0285, R_{sigma} = N/A]
Data/restraints/parameters	2813/0/215
Goodness-of-fit on F^2	1.042
Final R indexes [I>=2σ (I)]	R_1 = 0.0357, wR_2 = 0.0962
Final R indexes [all data]	R_1 = 0.0363, wR_2 = 0.0968
Largest diff. peak/hole / e Å^{-3}	0.49/-0.53
Flack parameter	-0.006(4)

A.1.22 4 at 240 K

Empirical formula	$C_{22}H_{22}Cl_2FeN_6O_{12}$
Formula weight	689.21
Temperature/K	240(2)
Crystal system	Monoclinic
Space group	$P2_1/n$
a/Å	15.4989(2)
b/Å	10.7135(1)
c/Å	17.0653(2)
α/°	90.00
β/°	103.426(1)
γ/°	90.00
Volume/Å^3	2756.21(5)
Z	4
ρ_{calc}g/cm^3	1.661
μ/mm^{-1}	6.844
F(000)	1408.0
Crystal size/mm^3	0.28 × 0.16 × 0.07
Radiation	CuKα (λ = 1.54184)
2Θ range for data collection/°	6.94 to 147.66
Index ranges	-19 ≤ h ≤ 18, -12 ≤ k ≤ 8, -20 ≤ l ≤ 20
Reflections collected	8520
Independent reflections	5280 [R_{int} = 0.0369, R_{sigma} = N/A]
Data/restraints/parameters	5280/20/395
Goodness-of-fit on F^2	1.041
Final R indexes [I>=2σ (I)]	R_1 = 0.0580, wR_2 = 0.1492
Final R indexes [all data]	R_1 = 0.0625, wR_2 = 0.1548
Largest diff. peak/hole / e Å^{-3}	0.72/-0.94

A.1.23 4 at 350 K

Empirical formula	$C_{22}H_{22}Cl_2FeN_6O_{12}$
Formula weight	689.21
Temperature/K	350(2)
Crystal system	Monoclinic
Space group	$P2_1/n$
a/Å	15.8967(5)
b/Å	10.8528(3)
c/Å	17.1038(6)
α/°	90.00
β/°	103.323(4)
γ/°	90.00
Volume/Å^3	2871.39(16)
Z	4
ρ_{calc}g/cm^3	1.594
μ/mm^{-1}	6.569
F(000)	1408.0
Crystal size/mm^3	0.28 × 0.16 × 0.07
Radiation	CuKα (λ = 1.54184)
2Θ range for data collection/°	6.84 to 148.44
Index ranges	-15 ≤ h ≤ 19, -13 ≤ k ≤ 8, -21 ≤ l ≤ 19
Reflections collected	9500
Independent reflections	5563 [R_{int} = 0.0433, R_{sigma} =]
Data/restraints/parameters	5563/20/395
Goodness-of-fit on F^2	1.034
Final R indexes [I>=2σ (I)]	R_1 = 0.0893, wR_2 = 0.2245
Final R indexes [all data]	R_1 = 0.1142, wR_2 = 0.2553
Largest diff. peak/hole / e Å^{-3}	0.74/-0.90

A.1.24 *R*-5 at 125 K

Empirical formula	$C_{50}H_{36}Cl_2FeN_6O_{12}$
Formula weight	1039.60
Temperature/K	124.97(11)
Crystal system	trigonal
Space group	$P3_121$
a/Å	14.64476(13)
b/Å	14.64476(13)
c/Å	38.2045(4)
α/°	90
β/°	90
γ/°	120
Volume/Å^3	7095.92(14)
Z	6
ρ_{calc}g/cm^3	1.460
μ/mm^{-1}	4.201
F(000)	3204.0
Crystal size/mm^3	0.1 × 0.1 × 0.1
Radiation	CuKα (λ = 1.54184)
2Θ range for data collection/°	6.942 to 147.152
Index ranges	-16 ≤ h ≤ 18, -17 ≤ k ≤ 13, -42 ≤ l ≤ 44
Reflections collected	55477
Independent reflections	9332 [R_{int} = 0.0393, R_{sigma} = 0.0247]
Data/restraints/parameters	9332/0/645
Goodness-of-fit on F^2	1.050
Final R indexes [I>=2σ (I)]	R_1 = 0.0508, wR_2 = 0.1462
Final R indexes [all data]	R_1 = 0.0558, wR_2 = 0.1519
Largest diff. peak/hole / e Å^{-3}	1.00/-0.51
Flack parameter	-0.0013(18)

Appendix B - X-ray crystallographic data for Chapter 4

B.1 *R*-6

Empirical formula	$B_2C_{46}F_8N_6O_4Zn$
Formula weight	939.51
Temperature/K	119.97(19)
Crystal system	monoclinic
Space group	$P2_1$
a/Å	11.1727(2)
b/Å	16.6495(3)
c/Å	12.4524(3)
α/°	90
β/°	111.611(2)
γ/°	90
Volume/Å^3	2153.56(8)
Z	2
ρ_{calc}g/cm^3	1.449
μ/mm^{-1}	1.555
F(000)	924.0
Crystal size/mm^3	0.5 × 0.15 × 0.1
Radiation	CuKα (λ = 1.54184)
2Θ range for data collection/°	7.636 to 147.718
Index ranges	-11 ≤ h ≤ 13, -20 ≤ k ≤ 20, -15 ≤ l ≤ 10
Reflections collected	17482
Independent reflections	8122 [R_{int} = 0.0289, R_{sigma} = 0.0346]
Data/restraints/parameters	8122/1/604
Goodness-of-fit on F^2	1.100
Final R indexes [I>=2σ (I)]	R_1 = 0.0429, wR_2 = 0.1258
Final R indexes [all data]	R_1 = 0.0440, wR_2 = 0.1288
Largest diff. peak/hole / e Å^{-3}	0.49/-0.34
Flack parameter	-0.016(10)

B.2 *RS*-6

Empirical formula	$C_{51}H_{45.25}B_2F_8N_{8.5}O_4Zn$
Formula weight	1080.20
Temperature/K	293.15
Crystal system	monoclinic
Space group	Pc
a/Å	21.25726(19)
b/Å	22.4616(2)
c/Å	20.7784(2)
α/°	90
β/°	91.4956(9)
γ/°	90
Volume/Å^3	9917.72(17)
Z	8
ρ_{calc}g/cm^3	1.447
μ/mm^{-1}	1.424
F(000)	4438.0
Crystal size/mm^3	0.33 × 0.19 × 0.05
Radiation	CuKα (λ = 1.54184)
2Θ range for data collection/°	7.07 to 147.65
Index ranges	-24 ≤ h ≤ 26, -26 ≤ k ≤ 27, -25 ≤ l ≤ 25
Reflections collected	97869
Independent reflections	34965 [R_{int} = 0.0449, R_{sigma} = 0.0422]
Data/restraints/parameters	34965/22/2725
Goodness-of-fit on F^2	1.267
Final R indexes [I>=2σ (I)]	R_1 = 0.0909, wR_2 = 0.2736
Final R indexes [all data]	R_1 = 0.0982, wR_2 = 0.2848
Largest diff. peak/hole / e Å^{-3}	3.12/-0.96
Flack parameter	0.00(5)

B.3 *R*-7

Empirical formula	$C_{35}H_{47.5}B_2F_{8.03}N_{6.5}O_4Zn$
Formula weight	1725.57
Temperature/K	120.00(10)
Crystal system	orthorhombic
Space group	$P2_12_12_1$
a/Å	12.61158(13)
b/Å	15.39473(15)
c/Å	40.6472(4)
α/°	90
β/°	90
γ/°	90
Volume/Å^3	7891.73(14)
Z	8
ρ_{calc}g/cm^3	1.452
μ/mm^{-1}	1.609
F(000)	3580.0
Crystal size/mm^3	0.3907 × 0.228 × 0.0659
Radiation	CuKα (λ = 1.54184)
2Θ range for data collection/°	6.14 to 147.818
Index ranges	-14 ≤ h ≤ 10, -18 ≤ k ≤ 18, -50 ≤ l ≤ 47
Reflections collected	34841
Independent reflections	15076 [R_{int} = 0.0352, R_{sigma} = 0.0433]
Data/restraints/parameters	15076/0/1053
Goodness-of-fit on F^2	1.028
Final R indexes [I>=2σ (I)]	R_1 = 0.0371, wR_2 = 0.0871
Final R indexes [all data]	R_1 = 0.0407, wR_2 = 0.0892
Largest diff. peak/hole / e Å^{-3}	0.97/-0.49
Flack parameter	-0.002(10)

B.4 *RS*-7

Empirical formula	$C_{34}H_{46}B_2F_8N_6O_4Zn$
Formula weight	841.76
Temperature/K	120.03(16)
Crystal system	monoclinic
Space group	$P2_1/n$
a/Å	9.16507(8)
b/Å	23.11363(16)
c/Å	17.77946(14)
α/°	90
β/°	95.7046(8)
γ/°	90
Volume/Å^3	3747.71(5)
Z	4
ρ_{calc}g/cm^3	1.492
μ/mm^{-1}	1.675
F(000)	1744.0
Crystal size/mm^3	0.4351 × 0.2085 × 0.0672
Radiation	CuKα (λ = 1.54184)
2Θ range for data collection/°	6.292 to 147.412
Index ranges	-10 ≤ h ≤ 11, -28 ≤ k ≤ 28, -21 ≤ l ≤ 22
Reflections collected	34739
Independent reflections	7398 [R_{int} = 0.0290, R_{sigma} = 0.0200]
Data/restraints/parameters	7398/0/504
Goodness-of-fit on F^2	1.033
Final R indexes [I>=2σ (I)]	R_1 = 0.0288, wR_2 = 0.0717
Final R indexes [all data]	R_1 = 0.0309, wR_2 = 0.0733
Largest diff. peak/hole / e Å^{-3}	0.55/-0.34

B.5 *R*-8

Empirical formula	$C_{52}H_{47}B_2CoF_8N_9O_4$
Formula weight	1094.53
Temperature/K	120.01(10)
Crystal system	monoclinic
Space group	$P2_1$
a/Å	10.81668(11)
b/Å	21.36754(16)
c/Å	11.76292(12)
α/°	90
β/°	112.5126(12)
γ/°	90
Volume/Å^3	2511.54(5)
Z	2
ρ_{calc}g/cm^3	1.447
μ/mm^{-1}	3.420
F(000)	1126.0
Crystal size/mm^3	0.1682 × 0.0958 × 0.0749
Radiation	CuKα (λ = 1.54184)
2Θ range for data collection/°	8.136 to 147.626
Index ranges	-13 ≤ h ≤ 11, -26 ≤ k ≤ 26, -14 ≤ l ≤ 14
Reflections collected	19234
Independent reflections	9866 [R_{int} = 0.0283, R_{sigma} = 0.0359]
Data/restraints/parameters	9866/1/688
Goodness-of-fit on F^2	1.003
Final R indexes [I>=2σ (I)]	R_1 = 0.0305, wR_2 = 0.0753
Final R indexes [all data]	R_1 = 0.0322, wR_2 = 0.0765
Largest diff. peak/hole / e Å^{-3}	0.62/-0.28
Flack parameter	-0.0208(12)

B.6 *RS*-8

Empirical formula	$B_2C_{51}CoF_8N_{8.5}O_4$
Formula weight	1028.13
Temperature/K	119.99(10)
Crystal system	monoclinic
Space group	Pc
a/Å	21.2207(3)
b/Å	22.4647(5)
c/Å	20.7348(3)
α/°	90
β/°	91.6760(10)
γ/°	90
Volume/Å^3	9880.4(3)
Z	8
ρ_{calc}g/cm^3	1.382
μ/mm^{-1}	3.460
F(000)	4052.0
Crystal size/mm^3	0.2 × 0.1 × 0.1
Radiation	CuKα (λ = 1.54184)
2Θ range for data collection/°	7.072 to 148.06
Index ranges	-26 ≤ h ≤ 26, -26 ≤ k ≤ 26, -25 ≤ l ≤ 24
Reflections collected	30486
Independent reflections	30486 [R_{int} = ?, R_{sigma} = 0.0528]
Data/restraints/parameters	30486/56/2693
Goodness-of-fit on F^2	1.043
Final R indexes [I>=2σ (I)]	R_1 = 0.0843, wR_2 = 0.2326
Final R indexes [all data]	R_1 = 0.1002, wR_2 = 0.2490
Largest diff. peak/hole / e Å^{-3}	1.36/-0.69
Flack parameter	0.359(3)

Appendix C – X-ray crystallographic data for Chapter 5

C.1.1 10 (120 K)

Empirical formula	$C_{24}H_{20}BClFeN_6O_7$
Formula weight	606.57
Temperature/K	120.01(10)
Crystal system	triclinic
Space group	P-1
a/Å	9.9332(4)
b/Å	10.5862(4)
c/Å	13.3041(6)
α/°	99.264(3)
β/°	108.848(4)
γ/°	105.453(3)
Volume/Å^3	1228.41(9)
Z	2
ρ_{calc}g/cm^3	1.640
μ/mm^{-1}	6.450
F(000)	620.0
Crystal size/mm^3	0.3 × 0.25 × 0.2
Radiation	CuKα (λ = 1.54184)
2Θ range for data collection/°	7.294 to 147.62
Index ranges	-11 ≤ h ≤ 12, -12 ≤ k ≤ 11, -16 ≤ l ≤ 16
Reflections collected	9183
Independent reflections	4635 [R_{int} = 0.0272, R_{sigma} = 0.0338]
Data/restraints/parameters	4635/0/361
Goodness-of-fit on F^2	0.913
Final R indexes [I>=2σ (I)]	R_1 = 0.0346, wR_2 = 0.1075
Final R indexes [all data]	R_1 = 0.0359, wR_2 = 0.1096
Largest diff. peak/hole / e Å^{-3}	0.53/-0.62

C.1.2 10 (250 K)

Empirical formula	$C_{24}H_{20}BClFeN_6O_7$
Formula weight	606.57
Temperature/K	250.00(10)
Crystal system	triclinic
Space group	P-1
a/Å	10.0218(6)
b/Å	10.6313(8)
c/Å	13.4764(7)
α/°	98.983(5)
β/°	108.862(5)
γ/°	105.937(6)
Volume/Å^3	1258.30(15)
Z	2
ρ_{calc}g/cm^3	1.601
μ/mm^{-1}	6.297
F(000)	620.0
Crystal size/mm^3	0.3 × 0.25 × 0.2
Radiation	CuKα (λ = 1.54184)
2Θ range for data collection/°	7.198 to 147.788
Index ranges	-12 ≤ h ≤ 12, -13 ≤ k ≤ 10, -14 ≤ l ≤ 16
Reflections collected	8965
Independent reflections	4703 [R_{int} = 0.0270, R_{sigma} = 0.0336]
Data/restraints/parameters	4703/8/352
Goodness-of-fit on F^2	1.057
Final R indexes [I>=2σ (I)]	R_1 = 0.0593, wR_2 = 0.1592
Final R indexes [all data]	R_1 = 0.0624, wR_2 = 0.1623
Largest diff. peak/hole / e Å^{-3}	0.92/-1.69

C.1.3 10 (350 K)

Empirical formula	$C_{24}H_{20}BClFeN_6O_7$
Formula weight	606.57
Temperature/K	350.00(10)
Crystal system	triclinic
Space group	P-1
a/Å	10.0858(4)
b/Å	10.6691(4)
c/Å	13.5777(6)
α/°	98.775(4)
β/°	108.908(4)
γ/°	106.125(3)
Volume/Å^3	1279.67(10)
Z	2
ρ_{calc}g/cm^3	1.574
μ/mm^{-1}	6.192
F(000)	620.0
Crystal size/mm^3	0.3 × 0.25 × 0.2
Radiation	CuKα (λ = 1.54184)
2Θ range for data collection/°	7.14 to 147.538
Index ranges	-12 ≤ h ≤ 12, -13 ≤ k ≤ 9, -16 ≤ l ≤ 16
Reflections collected	8817
Independent reflections	4815 [R_{int} = 0.0996, R_{sigma} = 0.0895]
Data/restraints/parameters	4815/8/352
Goodness-of-fit on F^2	1.045
Final R indexes [I>=2σ (I)]	R_1 = 0.0715, wR_2 = 0.2081
Final R indexes [all data]	R_1 = 0.0884, wR_2 = 0.2337
Largest diff. peak/hole / e Å^{-3}	1.00/-1.47

C.1.4 11 (120 K)

Empirical formula	$C_{18}H_{14}BClFeN_6O_7S_3$
Formula weight	624.64
Temperature/K	119.97(12)
Crystal system	triclinic
Space group	P-1
a/Å	9.7149(3)
b/Å	10.5056(3)
c/Å	12.9970(3)
α/°	100.654(2)
β/°	109.490(2)
γ/°	105.726(2)
Volume/Å^3	1146.94(6)
Z	2
ρ_{calc}g/cm^3	1.809
μ/mm^{-1}	9.414
F(000)	632.0
Crystal size/mm^3	0.5 × 0.2 × 0.2
Radiation	CuKα (λ = 1.54184)
2Θ range for data collection/°	7.572 to 147.78
Index ranges	-12 ≤ h ≤ 11, -13 ≤ k ≤ 11, -16 ≤ l ≤ 14
Reflections collected	8563
Independent reflections	4302 [R_{int} = 0.0242, R_{sigma} = 0.0303]
Data/restraints/parameters	4302/0/334
Goodness-of-fit on F^2	1.037
Final R indexes [I>=2σ (I)]	R_1 = 0.0291, wR_2 = 0.0722
Final R indexes [all data]	R_1 = 0.0314, wR_2 = 0.0739
Largest diff. peak/hole / e Å^{-3}	0.49/-0.42

C.1.5 11 (250 K)

Empirical formula	$C_{18}H_{14}BClFeN_6O_7S_3$
Formula weight	624.64
Temperature/K	250.01(10)
Crystal system	triclinic
Space group	P-1
a/Å	9.8237(11)
b/Å	10.5874(12)
c/Å	13.1199(14)
α/°	99.957(9)
β/°	109.810(11)
γ/°	106.338(10)
Volume/Å^3	1176.3(2)
Z	2
ρ_{calc}g/cm^3	1.763
μ/mm^{-1}	9.178
F(000)	632.0
Crystal size/mm^3	0.5 × 0.2 × 0.2
Radiation	CuKα (λ = 1.54184)
2Θ range for data collection/°	7.5 to 146.88
Index ranges	-11 ≤ h ≤ 12, -12 ≤ k ≤ 13, -15 ≤ l ≤ 10
Reflections collected	8134
Independent reflections	4381 [R_{int} = 0.0549, R_{sigma} = 0.0570]
Data/restraints/parameters	4381/32/379
Goodness-of-fit on F^2	1.164
Final R indexes [I>=2σ (I)]	R_1 = 0.0583, wR_2 = 0.1653
Final R indexes [all data]	R_1 = 0.0681, wR_2 = 0.1967
Largest diff. peak/hole / e Å^{-3}	0.81/-0.82

C.1.6 13

Empirical formula	$C_{23}H_{26}BClFeN_{10}O_7$
Formula weight	656.65
Temperature/K	150.01(10)
Crystal system	triclinic
Space group	P-1
a/Å	10.6613(4)
b/Å	11.8510(5)
c/Å	12.4063(6)
α/°	107.984(4)
β/°	95.616(4)
γ/°	102.631(3)
Volume/Å^3	1431.55(11)
Z	2
ρ_{calc}g/cm^3	1.523
μ/mm^{-1}	5.620
F(000)	676.0
Crystal size/mm^3	0.3 × 0.2 × 0.15
Radiation	CuKα (λ = 1.54184)
2Θ range for data collection/°	8.13 to 146.894
Index ranges	-12 ≤ h ≤ 13, -14 ≤ k ≤ 14, -14 ≤ l ≤ 10
Reflections collected	10449
Independent reflections	5366 [R_{int} = 0.0294, R_{sigma} = 0.0372]
Data/restraints/parameters	5366/111/428
Goodness-of-fit on F^2	1.030
Final R indexes [I>=2σ (I)]	R_1 = 0.0482, wR_2 = 0.1272
Final R indexes [all data]	R_1 = 0.0519, wR_2 = 0.1307
Largest diff. peak/hole / e Å^{-3}	1.00/-0.82

C.1.7 14

Empirical formula	$C_{22}H_{25}BClFeN_{9.5}O_7$
Formula weight	632.62
Temperature/K	100 K
Crystal system	tetragonal
Space group	$I4_1cd$
a/Å	26.428
b/Å	26.428
c/Å	15.220
α/°	90
β/°	90
γ/°	90
Volume/Å^3	10630.0
Z	16
ρ_{calc}g/cm^3	1.581
μ/mm^{-1}	0.724
F(000)	5204.0
Crystal size/mm^3	0.4 × 0.3 × 0.2
Radiation	Synchrotron (λ = 0.6889)
2Θ range for data collection/°	4.226 to 48.416
Index ranges	-31 ≤ h ≤ 31, -31 ≤ k ≤ 31, -18 ≤ l ≤ 18
Reflections collected	61294
Independent reflections	4686 [R_{int} = 0.2466, R_{sigma} = 0.0984]
Data/restraints/parameters	4686/9/365
Goodness-of-fit on F^2	0.960
Final R indexes [I>=2σ (I)]	R_1 = 0.0800, wR_2 = 0.2079
Final R indexes [all data]	R_1 = 0.1152, wR_2 = 0.2261
Largest diff. peak/hole / e Å^{-3}	0.49/-0.60
Flack parameter	0.06(3)

C.1.8 15

Empirical formula	$C_{42}H_{48}Cl_3Fe_4N_{12}O_{20}$
Formula weight	1370.67
Temperature/K	100 K
Crystal system	monoclinic
Space group	$P2_1/n$
a/Å	14.5136(2)
b/Å	18.7778(4)
c/Å	23.7712(3)
α/°	90
β/°	91.7920(10)
γ/°	90
Volume/Å^3	6475.28(18)
Z	4
ρ_{calc}g/cm^3	1.406
μ/mm^{-1}	1.069
F(000)	2796.0
Crystal size/mm^3	0.15 × 0.1 × 0.08
Radiation	Synchrotron (λ = 0.6889)
2Θ range for data collection/°	2.68 to 54.678
Index ranges	-19 ≤ h ≤ 19, -25 ≤ k ≤ 25, -31 ≤ l ≤ 31
Reflections collected	93353
Independent reflections	16077 [R_{int} = 0.0883, R_{sigma} = 0.0609]
Data/restraints/parameters	16077/31/728
Goodness-of-fit on F^2	1.238
Final R indexes [I>=2σ (I)]	R_1 = 0.0941, wR_2 = 0.3068
Final R indexes [all data]	R_1 = 0.1140, wR_2 = 0.3261
Largest diff. peak/hole / e Å^{-3}	2.32/-1.80

C.1.9 16

Empirical formula	$C_{24}H_{24}Br_4Cl_4Fe_4N_8O_{28}$
Formula weight	1557.35
Temperature/K	100 K
Crystal system	monoclinic
Space group	C2/c
a/Å	14.8176(8)
b/Å	23.1339(15)
c/Å	14.9421(7)
α/°	90
β/°	108.794(5)
γ/°	90
Volume/Å^3	4848.9(5)
Z	4
ρ_{calc}g/cm^3	2.133
μ/mm^{-1}	4.505
F(000)	3040.0
Crystal size/mm^3	0.053 × 0.012 × 0.01
Radiation	Synchrotron (λ = 0.6889)
2Θ range for data collection/°	3.292 to 49.618
Index ranges	-17 ≤ h ≤ 17, -26 ≤ k ≤ 25, -18 ≤ l ≤ 17
Reflections collected	9941
Independent reflections	3486 [R_{int} = 0.0769, R_{sigma} = 0.1106]
Data/restraints/parameters	3486/14/313
Goodness-of-fit on F^2	1.045
Final R indexes [I>=2σ (I)]	R_1 = 0.0795, wR_2 = 0.2240
Final R indexes [all data]	R_1 = 0.1005, wR_2 = 0.2454
Largest diff. peak/hole / e Å^{-3}	1.29/-1.26